UCRL-ID-136635

Signal and Imaging Sciences Workshop 1998 Proceedings

J.V. Candy

November 4, 1999

U.S. Department of Energy
Lawrence Livermore National Laboratory

Approved for public release; further dissemination unlimited

DISCLAIMER

This document was prepared as an account of work sponsored by an agency of the United States Government. Neither the United States Government nor the University of California nor any of their employees, makes any warranty, express or implied, or assumes any legal liability or responsibility for the accuracy, completeness, or usefulness of any information, apparatus, product, or process disclosed, or represents that its use would not infringe privately owned rights. Reference herein to any specific commercial product, process, or service by trade name, trademark, manufacturer, or otherwise, does not necessarily constitute or imply its endorsement, recommendation, or favoring by the United States Government or the University of California. The views and opinions of authors expressed herein do not necessarily state or reflect those of the United States Government or the University of California, and shall not be used for advertising or product endorsement purposes.

This work was performed under the auspices of the U. S. Department of Energy by the University of California, Lawrence Livermore National Laboratory under Contract No. W-7405-Eng-48.

Table of Contents

NOVEMBER 12 OPENING PRESENTATIONS

An Update on Engineering New Initiatives and Technology Development
Spiros Dimolitsas – Associate Director, Engineering 00

Diffraction Tomography – *Anthony Devaney, Keynote Speaker* 00

COMPUTED TOMOGRAPHY

Land Mine Detection – *Steve Azevedo* 00

HERMES Bridge Deck Inspection System Current
Results and Future Research – *Holger Jones* 00

Active and Passive Computed Tomography with a Constrained
Conjugate Gradient Solution – *Jesse Jackson* 00

Applying Optimization Tomography Problems – *Dennis Goodman* 00

Can We Cure Osteoporosis? – *John Kinney* 00

Spectral Partitioning of the Object Function in
Diffraction Tomography – *Sean Lehman* 00

RADAR-ACOUSTIC APPLICATIONS

Introduction to Low Power Radars for Acoustics Applications:
Speech and Object Characterization – *John Holzrichter* 00

Excitation Function of Human Speech – *Greg Burnett* 00

Accurate EM/Acoustic Pitch Estimation – *Larry Ng* 00

EM/Acoustic Speaker Verification – *Todd Gable* 00

Object Identification Using Low Power Radars – *Randy Roberts* 00

SIGNAL/IMAGE PROCESSING FOR NON-DESTRUCTIVE MEASUREMENT

Overview of Center for NDE – *Harry Martz* 00

Ultrasonic Compound B-scan Imaging – *Tyler Gomm, Jason A. Mauseth* 00

Gigahertz Photodetector Modules: Faster, Smaller, Cheaper – *Ken Froeschner* 00

InGaAs Linescan Camera System for Paper Web
Moisture Measurements – *Jose Hernandez* 00

Evaluation of an Amorphous Selenium Array
for Industrial X-Ray Imaging – *Clint Logan* 00

Matched Field Imaging of Laser-Based
Ultrasound Data – *Robert Huber* 00

NOVEMBER 13 OPENING PRESENTATIONS

An introduction to the Information Sciences & Technology Program:
Sheila Vaidya – Program Leader for IS&T 00

Detection of Nonsolar Planets by Spinning Infrared
Interferometer – *Ronald Bracewell, Keynote Speaker* 00

ASTRONOMICAL IMAGING

Novel Interferometer-Spectrometer for Sensitive Doppler Planet Detection – *Dave Erskine* 00

Resolution Enhancement of Adaptive Optics Corrected Astronomical Images – *Jim Brase* 00

LBNL/Lick Observatory Fully-Depleted CCD Image Sensor Development – *Steve Holland* 00

Extrasolar Planet Search With Adaptive Optics Spectrometer with R = 200,000 – *Jian Ge* 00

Micro-Satellite Technology for the 21st Century – *Larry Ng* 00

Detecting Massed Troops with the French SPOT Satellites – *Vipin Gupta* 00

ACOUSTICAL PROCESSING AND IMAGING

Combined Sensing and Simulation for Enhanced
Evaluation of Large Structures – *Dave McCallen* 00

Failure Detection for Mechanical Structures:
A State-Space Model-Based Approach – *Greg Clark* 00

Parametric Time-Frequency Estimation of Prosthetic
Heart Valve Sounds – *Skip Perkins* 00

Near Field / Far Field Transition Distance for
Broad Band Acoustic Pulses – *Dave Chambers* 00

Optimization of Array Generated Fields for
Broad Frequency Band Width – *Kent Lewis* 00

Automated Event Picking for Seismic Oil Exploration – *Peter K-Z. Cheng* 00

MATERIALS DETECTION AND IDENTIFICATION

Explosive Detection and Discriminant Research for
Civil Aviation Security – *Harry Martz* 00

Grain Identification and Analysis of Shock Induced
Damage of Sandstone – *Carl Hagelberg* 00

Signal Design for Lithography – *Jesse Kolman* 00

Fluoro Immuno Sensors for Biological Warfare Agents
Detection and Identification – *Kodumudi Venkateswaran* 00

Day 1
Opening Presentations

Engineering: An Update on Engineering New Initiatives and Technology Development

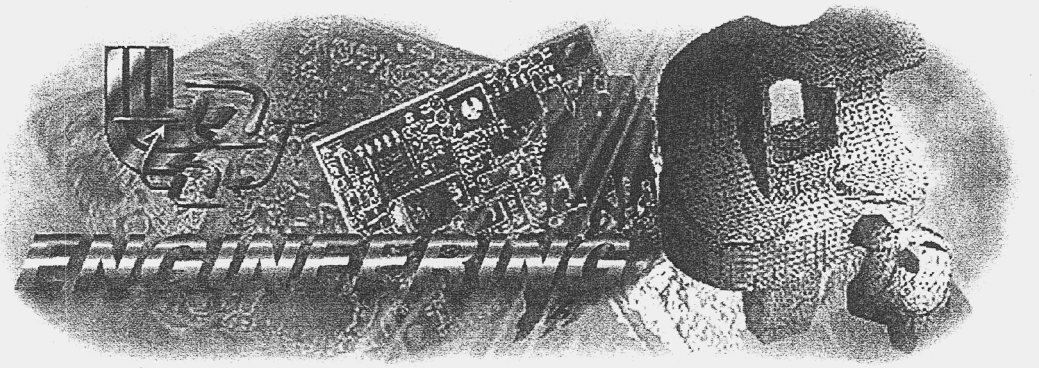

Spiros Dimolitsas
Associate Director for Engineering

ENGINEERING

LLNL Organization

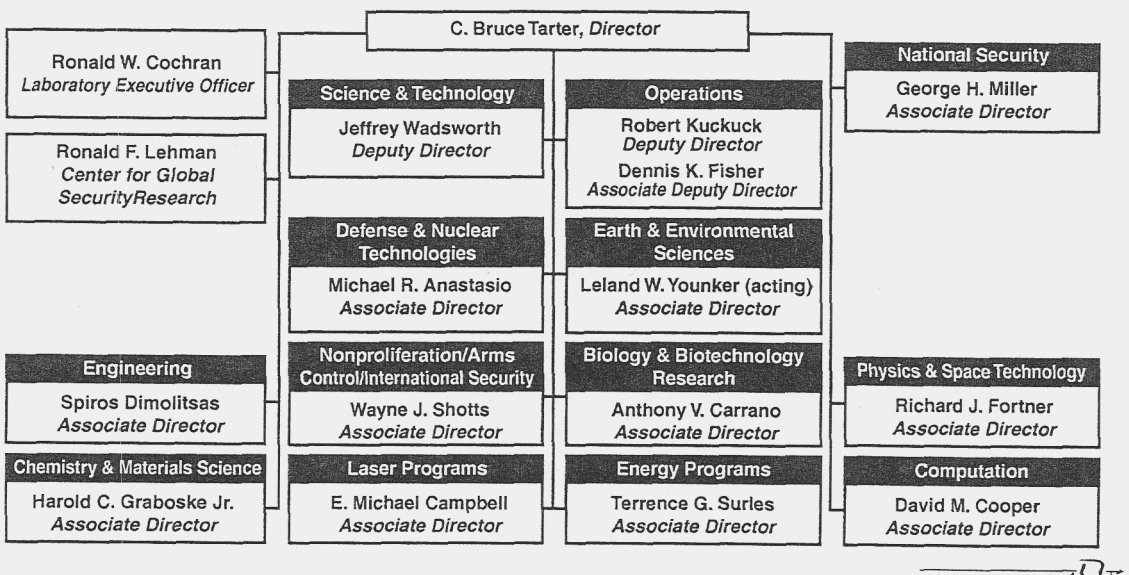

ENGINEERING

DOE Lawrence Livermore National Laboratory

- Employees
  - Staff: 7,300
  - Other: 1,200
- Capital Plant: $4B
- Annual operating and capital funds: ~$1B/yr

Managed by the University of California since 1952

ENGINEERING

Global Security

LLNL's defining mission is national security

- Dismantling the nuclear arsenals
- Stockpile stewardship
  - Focused on the enduring stockpile
  - Science-based (no underground testing)
  - Production capability rather than capacity
- Dealing with the proliferation threat
  - Detect
  - Inhibit
  - Respond

We have helped develop single, integrated multi-Lab programs in concert with DOE and others; execution of LLNL's part is through our Council on National Security

ENGINEERING

Characteristics of Lawrence Livermore National Laboratory

- Strong focus on problems of national importance
- Intentionally and intensely multi-disciplinary
- Science and technology are mostly programmatically driven
- Entrepreneurial, with an emphasis on high risk, high leverage technological solutions
- Utilizes teams on projects, not individuals on grants

ENGINEERING

Our Core Competencies allow us to solve problems involving multiple extreme dimensionalities simultaneously

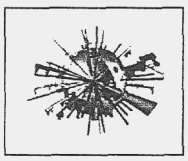

Integrated Engineering of Large-Scale Complex Applied Physics Systems

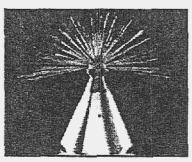

Measurement Science at Extreme Dimensionalities

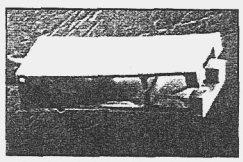

Microscale Engineering

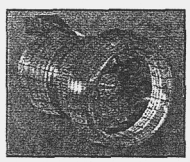

Large-Capacity Computational Modeling and Simulation

Integrated/Multidisciplinary • Couplex • Precise • Modelled

ENGINEERING

LLNL's Programmatic Evolution

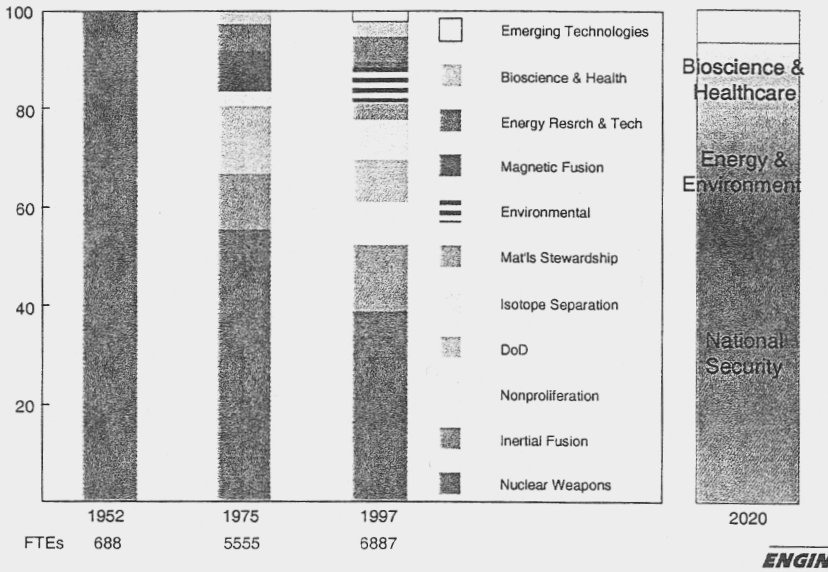

ENGINEERING

A complex football-stadium-sized structure delivers 700 tera watts of laser power with 50 μm (rms) accuracy

- 4000 tons of steel
- 2700 class-100 assemblies
- 35,000 control points
- 42,500 optical elements
- 18,000 ft² of optical surfaces
- 1.8 mega joules of energy
- 1 nanosecond event duration
- < 20nm surface finish requirements

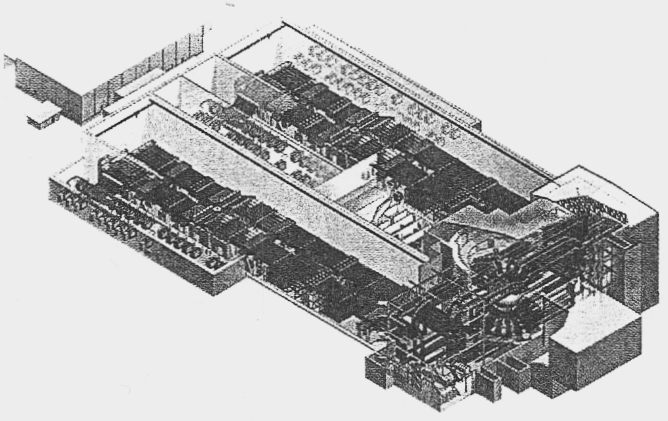

ENGINEERING

DYNA3D simulations are critical to the process of design/analysis/experiment

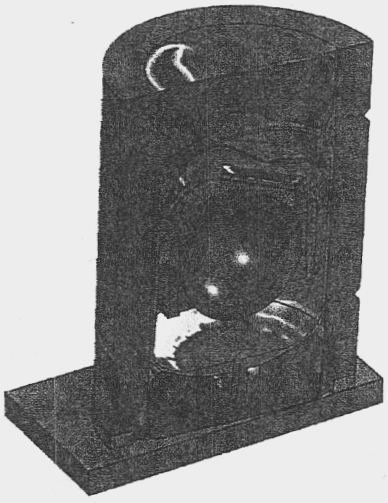

AT400A shipping container

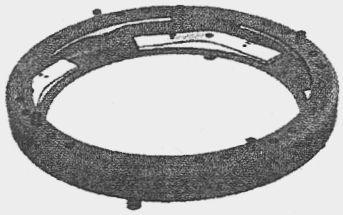

An energy absorption requirement demanded an analysis-driven flange design

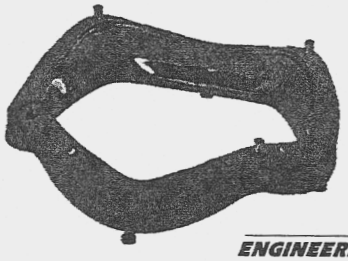

ENGINEERING

Our tiltmeter can detect 1-inch gap formations 10,000 ft. below the earth's surface and sense nanoradian earth-induced movement

1997 R&D-100 winner

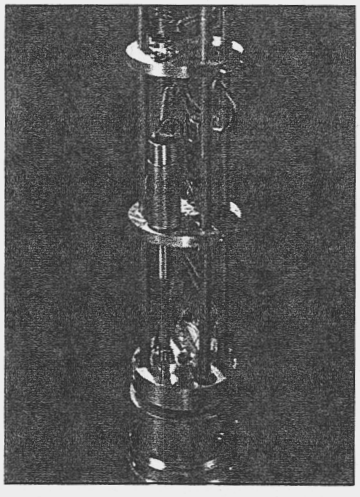

ENGINEERING

High-resolution, ultra-high speed, multi-frame stereoscopic imaging is a capability unique to LLNL

Image-converter camera

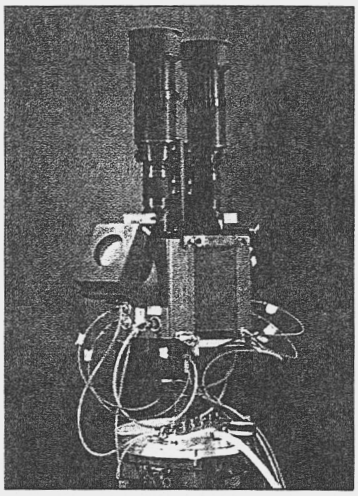

ENGINEERING

Explosively-driven conical shell collapsing and squirting out at 9.2 km/sec (Mach number 27)

to + 17.1 μsec

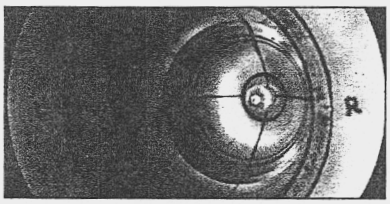

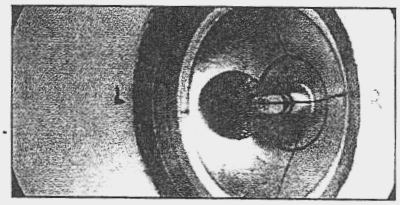

to + 24.1 μsec

to + 31.5 μsec

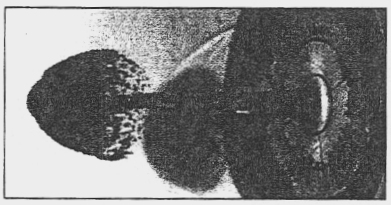

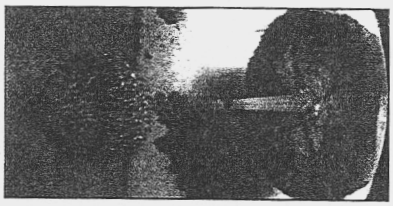

to + 40.8 μsec

20 nsec exposures

ENGINEERING

Engineering's Technology Strategy
• Implementation Plan •

ENGINEERING

A layered-structure can be defined to facilitate understanding and management of our core technologies and competencies

- Engineering competencies – definitions (. . . What we do)
- Engineering technologies – definitions (. . . How we do it)

ENGINEERING

Engineering's Competencies as of August 1998

Over-Arching Competence	Core Competencies	Application Competencies
Extreme Engineering: Engineering of systems involving the concurrent integration of multiple technologies driven to their extreme	Integrated engineering of large-scale, complex applied physics systems	Nuclear and conventional weapons engineering Nuclear materials disposition Laser systems engineering Isotope separator engineering Safety-critical control systems High-integrity systems Accelerator and particle detector systems engineering Field engineering Security control systems Adaptive optics Electronic commerce and concurrent engineering systems
	Large, complex computational modeling and simulation	Structural, thermal, and fluid system analysis and design Nonlinear systems modeling Bio/human system modeling Accelerator and microwave electronics analysis and design Antenna modeling Nuclear and electromagnetic radiation effects Integrated photonics Information systems vulnerability analysis and operations Transportation vehicles, systems, and infrastructure Natural hazards assessment and mitigation
	Microscale engineering	Precision, brittle material fabrication High-precision optics High precision assemblies Miniaturized, integrated analytical bio/chemical systems Medial micro-instruments and micro-tools Genome sequencing instrumentation Opto-electronic communication devices
	Measurement science at extreme dimensionalities	Real-time data acquisition and processing Transient diagnostics Remote characterization and detection systems Ultra low-power, precision proximity radar Adaptive sensors and networks Nondestructive evaluation Accelerated materials aging Biomedical imaging Geologic signal processing and analysis Sub-surface (including underground) imaging Environmental monitoring and characterization

ENGINEERING

Engineering's Technologies as of August 1998

Core Technologies	Enabling Technologies	Supporting Technologies
Systems engineering	Mechanical systems design Electronics and electrical systems design Computer controls design Optical engineering High power electro-optics Software engineering Power conditioning and pulse power Reliability, availability, and maintainability analysis Probabilistic risk analysis Sparse data analysis	Project management Real time, large-scale/multi-point control systems Real time acquisition and tracking Nuclear engineering Intelligent automation Energetic materials engineering Systems science High pressure engineering Communication network design and integration High-performance computer systems engineering RF engineering Superconducting magnet technology Flight systems engineering Discrete event simulation Economic systems modeling
Computational engineering	Computational structural mechanics Computational thermal transport Computational fluid dynamics Continuum material modeling Coupled, multi-physics code integration Fabrication process modeling Time-domain electromagnetics Massively parallel software implementation	Computational tools for analysis and design Mesh generation Visualization Numerical analysis Large code architecture and design Micro-scale mechanics and fluidics

ENGINEERING

Engineering's Technologies as of August 1998 (continued)

Core Technologies	Enabling Technologies	Supporting Technologies
Precision engineering	Deterministic manufacturing Machine design and analysis Precision positioning and control Brittle materials processing Diamond turning Precision grinding and polishing Manufacturing process development and control (casting, spin-forming welding, etc.)	Metal turning, shaping and forming Composite and anisotropic materials fabrication Metrology Coatings and deposition Multi-layer fabrication
Microsystems technology	Microsystems integration and packaging Opto-electronic materials processing High-aspect ratio micromachining Controlled stress thin-film fabrication Microfluidics engineering Material deposition Integrated micro-actuators Fusion bonding	Microsystems process development III-V material systems
Signal acquisition and characterization	High-speed electronics and opto-electronics Laser-driven ultrasonics Model-based digital signal processing Feature-based image restoration Computed tomography Array signal processing Remote sensing and multi-spectral imaging Micro-impulse, spread spectrum radar High velocity experimentation	Electrical resistance tomography Magnetic field imaging Seismic signal processing Environmental testing of systems Neural network integration Digital/film radiography, ultrasonic testing, and IR imaging Material testing and characterization

ENGINEERING

Engineering Organization

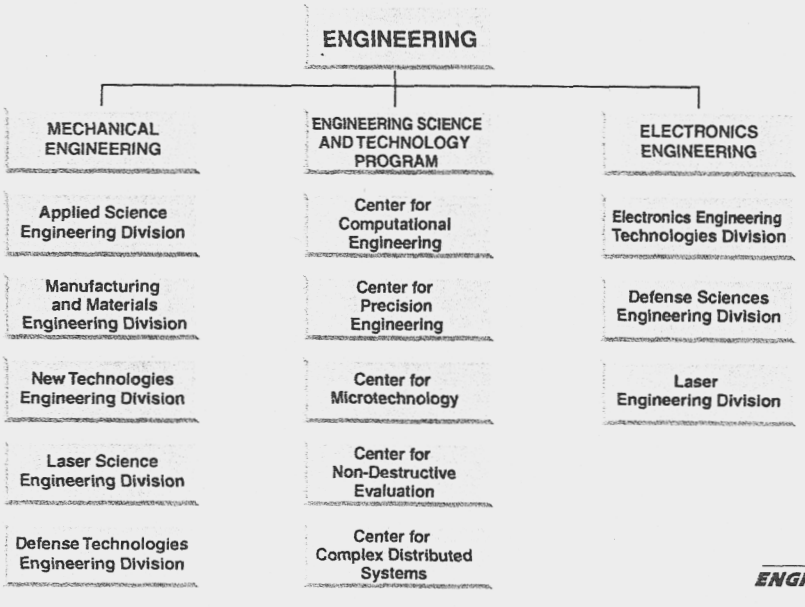

ENGINEERING

Center mission

An Engineering Center is the focus at LLNL for the core technology represented.

- An Engineering Center has been delegated by the Directorate the responsibility for the vitality and growth of the core technology it represents. Hence, it focuses and guides investments in enabling technologies and supporting capabilities.
- A Center is an Engineering R&D "program" whose output is technology.
- When a Center has a focus that is narrower than the core technology it is most closely related to, the Center will in addition provide a forum for the discussion of issues related to the broader core technology area (e.g. the Center on NDE will provide a forum for the discussion of issues related to "signal acquisition and characterization")

ENGINEERING

A successful Engineering Center . . .

- Solves compelling problems that require breakthrough innovation.
- Is world class, or is on a path to become world class, and put Engineering on the national map.
- Broadly impacts the Laboratory, enables new programs (one technology focus, many program applications).
- Requires and drives mechanical and electrical engineering enabling technologies to advance (is cross cutting).
- Is enabled and is critically dependent on unique LLNL capabilities (to create a sustainable differential advantage).
- Has close and/or significant University affiliations.
- Facilitates the introduction of new technology to applications (programs) and provides an avenue to facilitate access to engineering enabling technologies.
- Develops a significant intellectual property base.
- Can attract external sponsorship.

A robust Center solves compelling problems that require world-class innovation

ENGINEERING

Diffraction Tomography

By A.J. Devaney
Department of Electrical Engineering
Northeastern University
Boston, MA 02115

This talk will trace the evolution of diffraction tomography (DT) from its foundations in X-ray Crystallography to its current status as a rigorous solution to a host of linearized inverse problems involving acoustic, electromagnetic and optical wavefields. Special attention will be devoted to applications of DT to statistically based problems such as target detection and identification and parameter estimation from noisy wavefield data. The talk will review a number of example applications of modern DT that include imaging and parameter estimation from ground penetrating radar (GPR), ultrasound tomography, and optical diffraction microscopy. Current commercial ventures aimed at developing a high resolution optical microscope based on the concepts of optical diffraction microscopy and the development of a fast and efficient GPR system capable of mapping underground utility lines will be reviewed.

Diffraction Tomography

A.J. Devaney
Department of Electrical and Computer Engineering
Northeastern University
Boston, MA 02115
tonydev2@aol.com

- Brief history
- Mathematical formulation
- Examples
- Summary and comments

Physics based signal processing

Problems addressed by DT

Geophysical

Electromagnetic
Acoustic

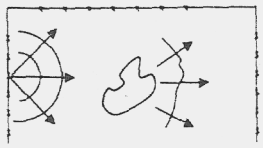

Off-set VSP/ cross-well tomography
GPR surface imaging
induction imaging

Medical

Ultrasonic
Optical

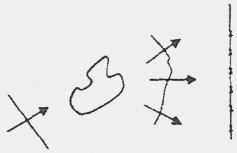

Ultrasound tomography
optical microscopy
photon imaging

Industrial

Electromagnetic
Ultrasonic
Optical

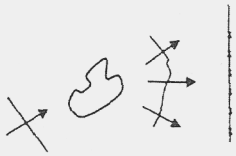

Ultrasound tomography
optical microscopy
induction imaging

Historical survey

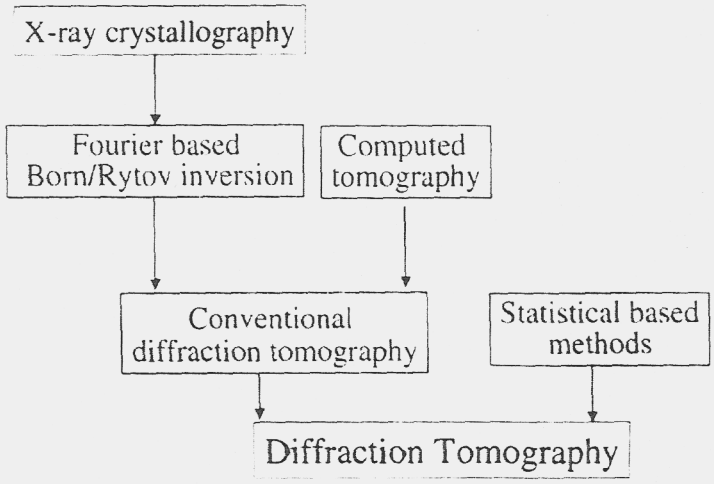

Canonical scattering configuration

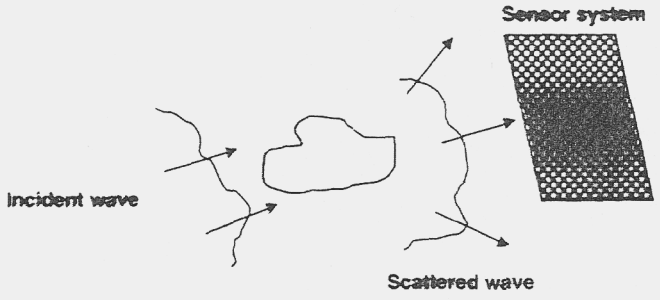

$$(\nabla^2 + k^2)\,\psi(\mathbf{r},\omega) = O(\mathbf{r},\omega)\,\psi(\mathbf{r},\omega)$$

$$O(\mathbf{r},\omega) = k^2[1 - n^2(\mathbf{r},\omega)]$$

Inverse scattering problem: Given set of scattered field measurements determine object function

Scattering models

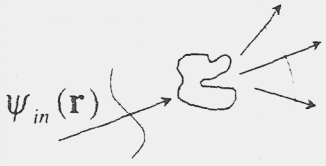

$$(\nabla^2 + k^2)\psi(\mathbf{r}) = \overbrace{k^2[1 - n^2(\mathbf{r})]}^{O(\mathbf{r})}\psi(\mathbf{r})$$

$$\psi^{(s)}(\mathbf{r}) = -\frac{1}{4\pi}\int d^3r'\,O(\mathbf{r}')\psi(\mathbf{r}')\frac{e^{ik|\mathbf{r}-\mathbf{r}'|}}{|\mathbf{r}-\mathbf{r}'|}$$

Born Model $$\psi_B^{(s)}(\mathbf{r}) = -\frac{1}{4\pi}\int d^3r'\,O(\mathbf{r}')\psi_{in}(\mathbf{r}')\frac{e^{ik|\mathbf{r}-\mathbf{r}'|}}{|\mathbf{r}-\mathbf{r}'|}$$

Rytov Model $$\psi = e^{ik[W_0(\mathbf{r})+\delta W(\mathbf{r})]}$$

$$\delta W_R(\mathbf{r}) = \frac{i}{4\pi k}\int d^3r'\,O(\mathbf{r}')e^{-ik[W_0(\mathbf{r})-W_0(\mathbf{r}')]}\frac{e^{ik|\mathbf{r}-\mathbf{r}'|}}{|\mathbf{r}-\mathbf{r}'|}$$

$$\psi_B^{(s)}(\mathbf{r}) = ike^{ikW_0(\mathbf{r})}\delta W_R(\mathbf{r})$$

Accuracy of Rytov approximation

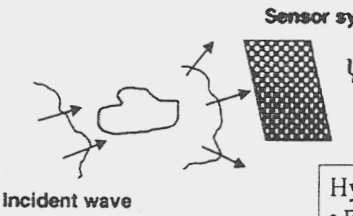

$$\psi_R = e^{ik[W_0(r)+\delta W_R(r)]} \rightarrow \psi_B \text{ as } kr \rightarrow \infty$$

Hybrid approximation:
- Exact from measurement plane to near field
- Rytov from near field to object

Simulation and experiment:
- optical fiber illuminated by red laser
- ray trace followed by free space propagation
- Rytov
- Hybrid
- Experiment

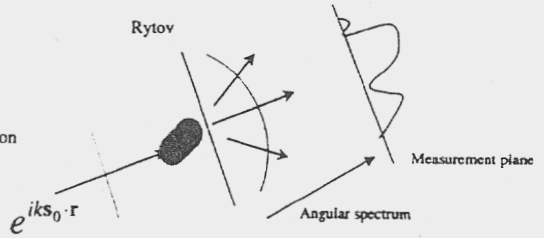

Ray trace, hybrid and Rytov

Optical fiber: a=25 μm, b= 65 μm, δna=.016, δnb=.0065

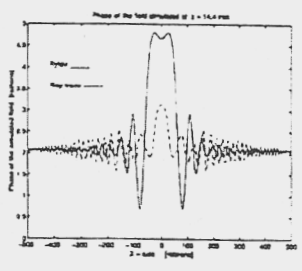

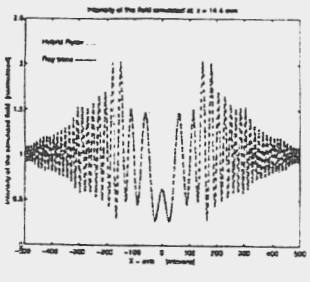

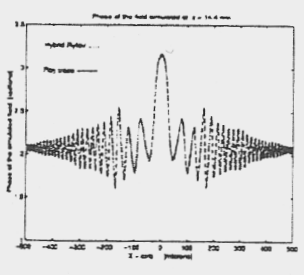

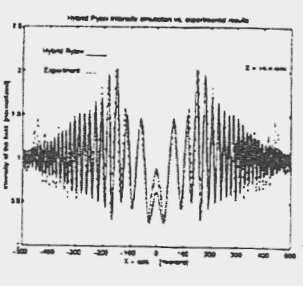

Rytov vs hybrid model

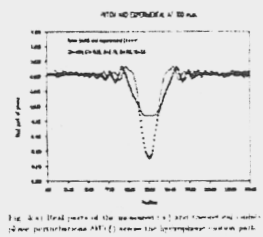

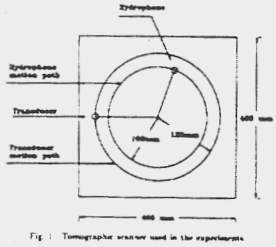

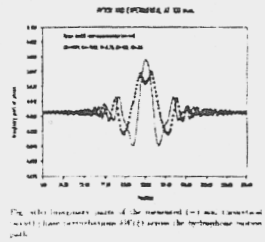

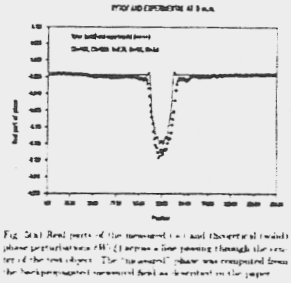

N. Sponheim, I. Johansen, A.J. Devaney, *Acoustical Imaging* Vol. 18 ed. H. Lee and G. Wade, 1989

Inverse problem

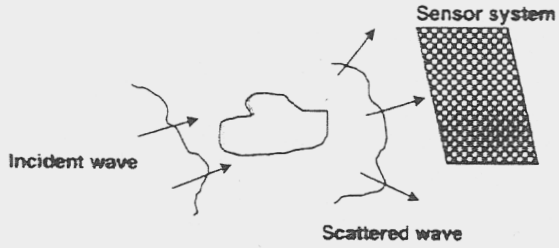

$$\Rightarrow \begin{cases} \psi_B^{(s)}(\mathbf{r}_0) \\ \delta W_R(\mathbf{r}_0) \end{cases}$$

Inversion Algorithm $\left.\begin{matrix} \psi_B^{(s)}(\mathbf{r}_0) \\ \delta W_R(\mathbf{r}_0) \end{matrix}\right\} \Rightarrow O(\mathbf{r},\omega)$

Problem reduces to solving set of coupled linear integral equations

Why tomography?

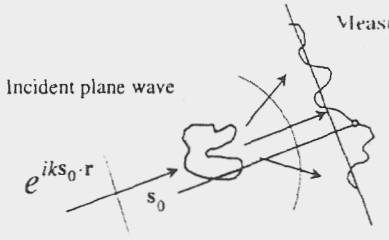

$$\delta W_R(\mathbf{r}_p) = \frac{i}{4\pi k}\int d^3r' O(\mathbf{r}') e^{-ik\mathbf{s}_0\cdot(\mathbf{r}_p-\mathbf{r}')}\frac{e^{ik|\mathbf{r}_p-\mathbf{r}'|}}{|\mathbf{r}_p-\mathbf{r}'|}$$

$$\rightarrow \int d^3r' O(\mathbf{r}')\delta(\mathbf{r}_p-\mathbf{u}_0\cdot\mathbf{r}')$$

Integral along straightline ray path: Inversion via CT

Diffraction tomography (DT) is generalization of CT to diffracting wavefields

- **Filtered back*propagation***
- **Generalized ART and SIRT**
- **Various limited view algorithms**

Born approximation imaging

$$\psi_b^s(\mathbf{r},\omega) = -\tfrac{1}{4\pi}\int d^3r' O(\mathbf{r}',\omega)\psi_{in}(\mathbf{r}',\omega)\frac{e^{ik|\mathbf{r}-\mathbf{r}'|}}{|\mathbf{r}-\mathbf{r}'|}$$

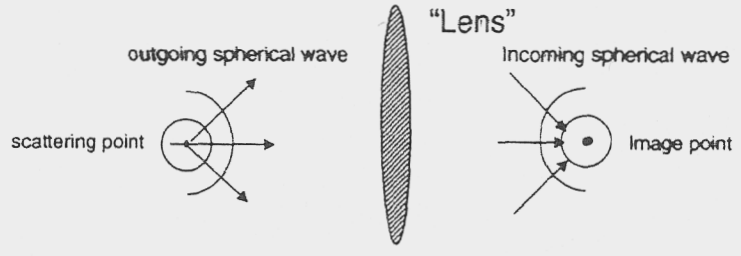

$$-\frac{1}{4\pi}\frac{e^{ik|\mathbf{r}-\mathbf{r}'|}}{|\mathbf{r}-\mathbf{r}'|} \Rightarrow h(\mathbf{r}-\mathbf{r}',\omega)$$

$$\psi_b^s(\mathbf{r},\omega) \Rightarrow \psi_I(\mathbf{r},\omega) = \int d^3r' O(\mathbf{r}',\omega)\psi_{in}(\mathbf{r}',\omega)h(\mathbf{r}-\mathbf{r}',\omega)$$

Backpropagation-the digital lens

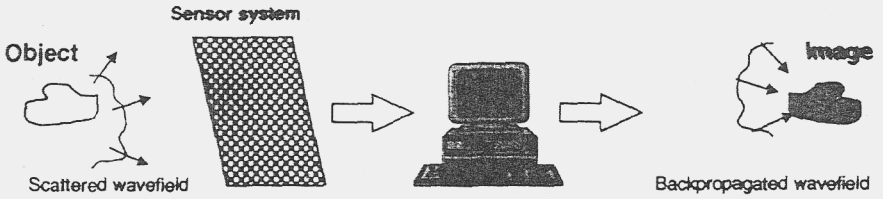

$$\psi_I(\mathbf{r},\omega) = \int d^3r' O(\mathbf{r}',\omega)\psi_{in}(\mathbf{r}',\omega)h(\mathbf{r}-\mathbf{r}',\omega)$$

Single experiment generates image of the product $O(\mathbf{r}',\omega)\,\psi_{in}(\mathbf{r}',\omega)$

The backpropagation algorithm

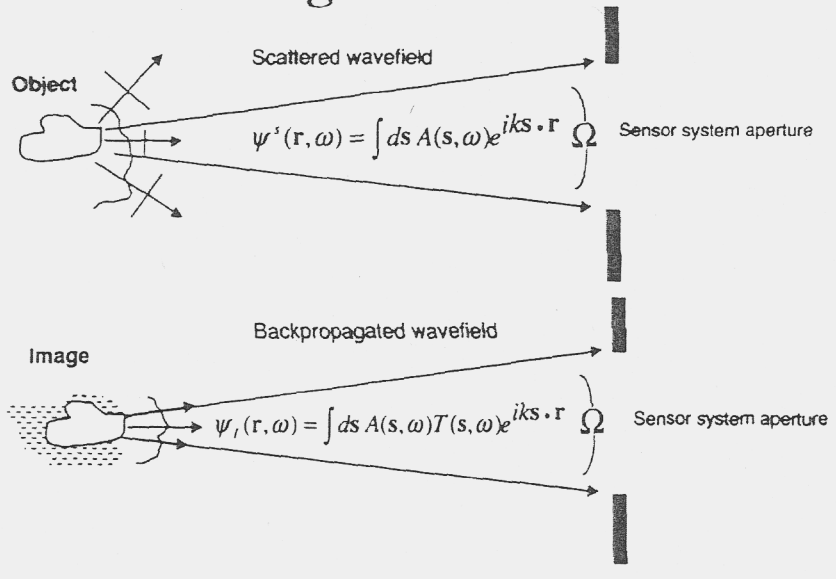

The backpropagation point spread function

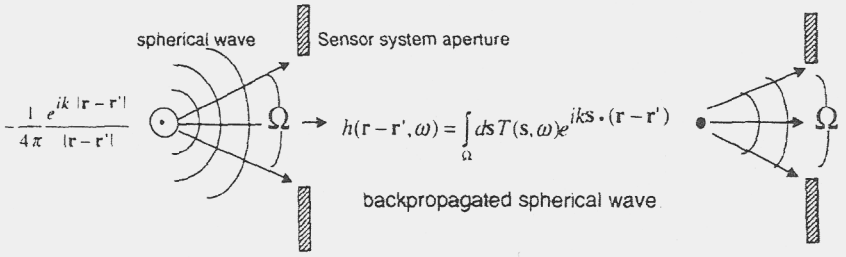

Point spread function is the image of a point (delta function) scatterer

Aperture function $T(\mathbf{s},\omega)$ models sensor and computational inaccuracies

Point spread function

$$h(\mathbf{R},\omega)=\int_{\Omega} ds\,T(\mathbf{s},\omega)e^{ik\mathbf{s}\cdot\mathbf{R}}$$

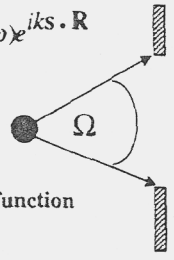

Ideal Case :

Zero aberration and $\Omega = 4\pi$ steradians

$$h(\mathbf{R},\omega)=\frac{\sin kR}{kR}=\mathrm{sinc}(kR)$$

Point spread function

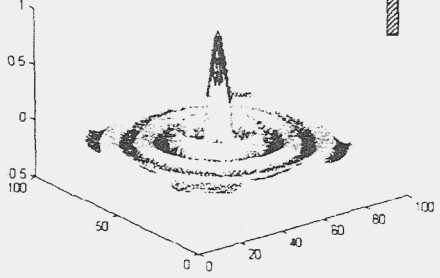

Coherent transfer function

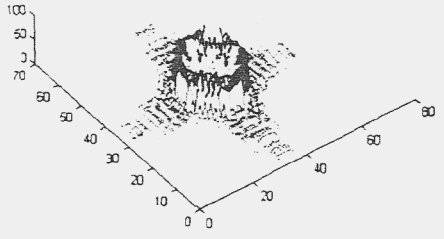

Plane wave diffraction tomography

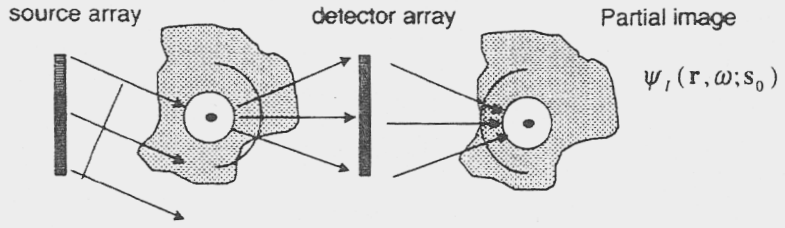

$$\psi_I(\mathbf{r},\omega;\mathbf{s}_0) = \int d^3r' O(\mathbf{r}',\omega)\, e^{ik\mathbf{s}_0 \cdot \mathbf{r}'} h(\mathbf{r}-\mathbf{r}',\omega)$$

$$h^*(\mathbf{r}-\mathbf{r}',\omega) = \int_\Omega ds_0 e^{ik\mathbf{s}_0 \bullet (\mathbf{r}'-\mathbf{r})}$$

$$\boxed{\psi_I(\mathbf{r},\omega) = \int_\Omega ds_0\, e^{-ik\mathbf{s}_0 \cdot \mathbf{r}} \psi_I(\mathbf{r},\omega;\mathbf{s}_0) = \int d^3r' O(\mathbf{r}',\omega)\left|h(\mathbf{r}-\mathbf{r}',\omega)\right|^2}$$

Image quality

$$\psi_I(\mathbf{r},\omega) = \int d^3r' O(\mathbf{r}',\omega)\left|h(\mathbf{r}-\mathbf{r}',\omega)\right|^2$$

$$\left|h(\mathbf{R},\omega)\right|^2 = \left(\frac{\sin(kR)}{kR}\right)^2$$

Point spread function

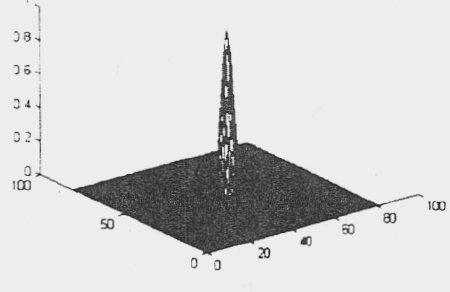

Transfer function

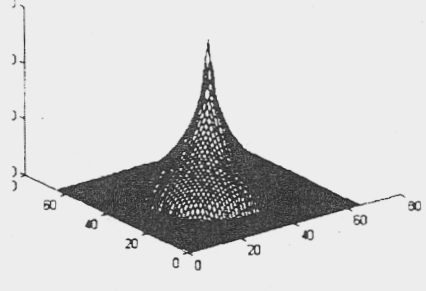

Image processing

$$|h(\mathbf{R},\omega)|^2 = \left(\frac{\sin(kR)}{kR}\right)^2$$

$$H(\mathbf{K}) = \frac{1}{K} \quad \text{for} \quad K < 2k \Rightarrow H^{-1}(\mathbf{K}) = K$$

$$\psi_I(\mathbf{r},\omega) = \int d^3r' O(\mathbf{r}',\omega)\left|h(\mathbf{r}-\mathbf{r}',\omega)\right|^2$$

$$\hat{O}(\mathbf{r},\omega) = H^{-1} \otimes \psi_I(\mathbf{r},\omega) = \int d^3r' O(\mathbf{r}',\omega)\Delta(\mathbf{r}-\mathbf{r}',\omega)$$

Filtered backpropagation algorithm

$$\hat{O}(\mathbf{r},\omega) = \sum_{\mathbf{s}_0} \mathrm{BP}\left\{Q_{\mathbf{s}_0} \otimes \psi^s_{\mathbf{s}_0}\right\}(\mathbf{r},\omega)$$

Filtered backpropagation algorithm

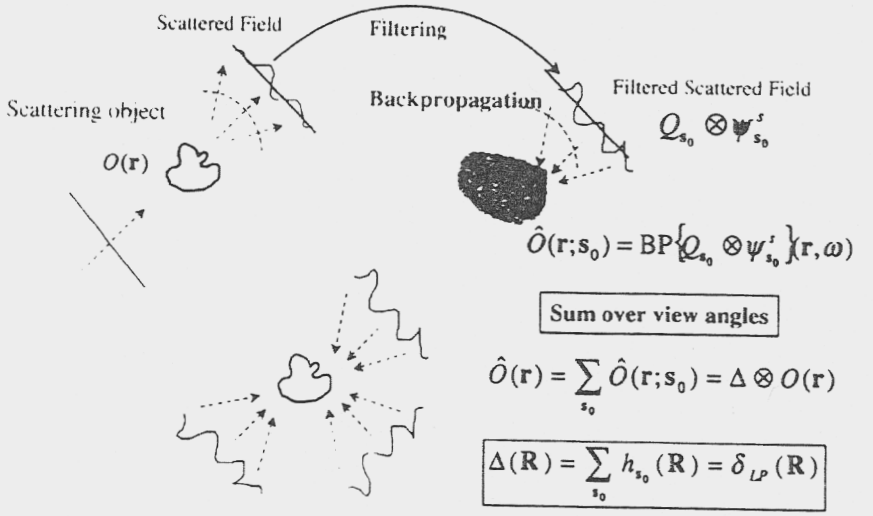

Simulations

2D objects: objects composed of superposition of cylinders

- Single view as function of wavelength
- multiple view at fixed wavelength
- Comparison of CT versus DT with DT data
- multiple view as function of wavelength

Simulations test DT algorithms and *not* Rytov model

Image quality as function of number of views

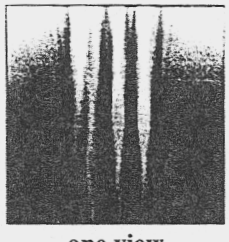

one view

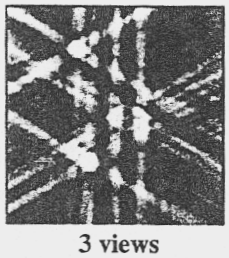

3 views

5 views

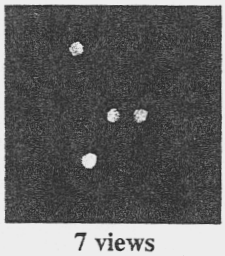

7 views

Backpropagation as a function of wavelength

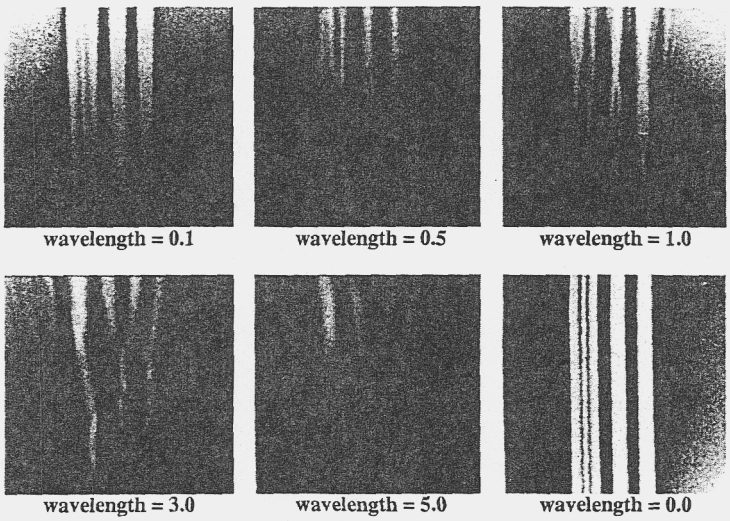

Filtered backprojection and backpropagation algorithms applied to scattered field data

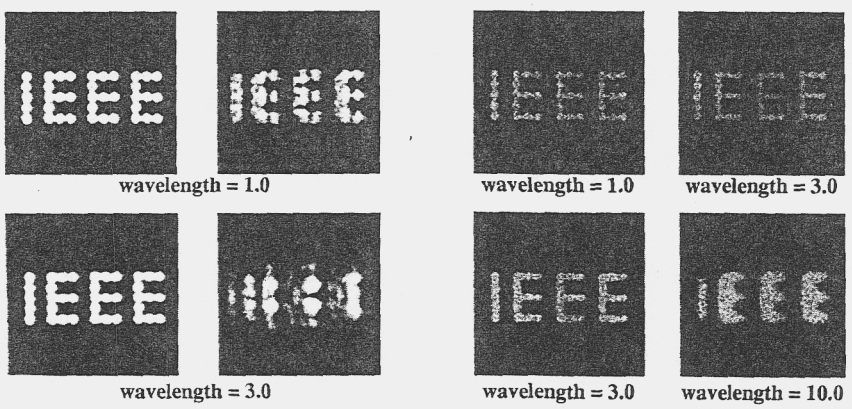

Filtered backpropagation versus filtered backprojection

Filtered backpropagation as function of wavelength

Norwegian ultrasound tomography system

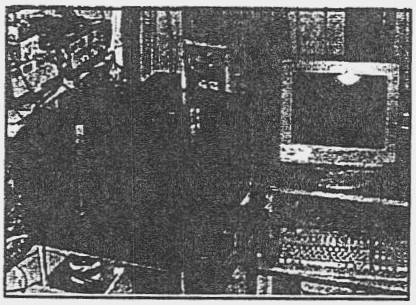

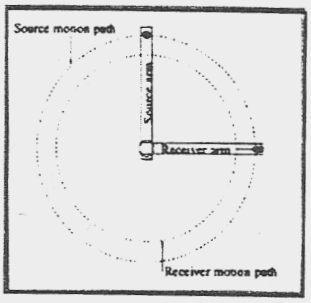

Tor Standnes, *Experimental investigation of ultrasound diffraction tomography*
Ph.D. Thesis, 1998,
University of Belgium

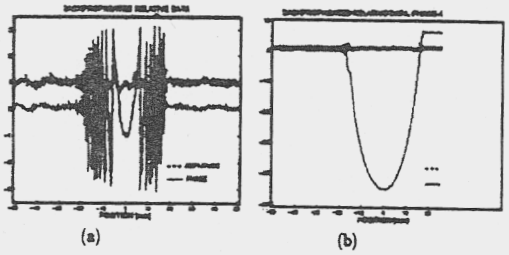

Ultrasound simulations: Born vs Rytov

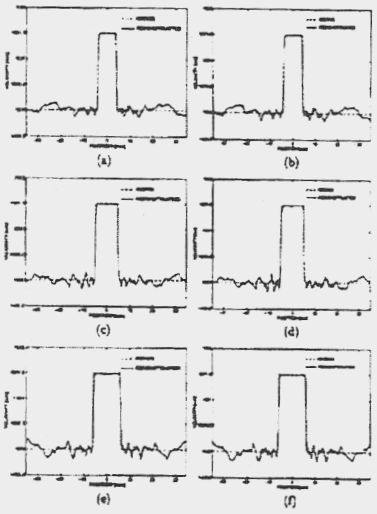

Figure 7.7: Reconstructed diametrical sections of cylindrical objects with circular cross section based on simulated data for a velocity difference of 0.1 % and radius a. (a) Born data; a = 4.0 mm; (b) Rytov data; a = 4.0 mm; (c) Born data; a = 5.0 mm; (d) Rytov data; a = 5.0 mm; (e) Born data; a = 6.0 mm; (f) Rytov data; a = 6.0 mm.

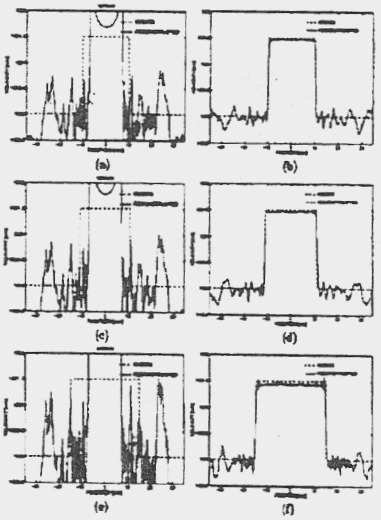

Figure 7.9: Reconstructed diametrical sections of cylindrical objects with circular cross section based on simulated data for a velocity difference of 0.1 % and radius a. (a) Born data; a = 10.0 mm; (b) Rytov data; a = 10.0 mm; (c) Born data; a = 11.0 mm; (d) Rytov data; a = 11.0 mm; (e) Born data; a = 15.0 mm; (f) Rytov data; a = 15.0 mm.

Ultrasound reconstructions from real data

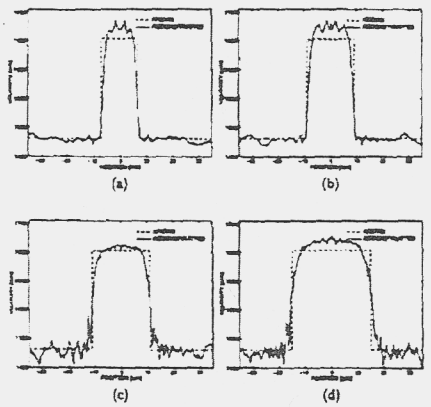

Figure 7.35: Reconstructed diametrical sections of cylindrical objects with circular cross section based on measured data for a velocity difference of 11.6 % and radius a. (a) Rytov data; a = 7.0 mm; (b) Rytov data; a = 9.0 mm; (c) Rytov data; a = 11.0 mm; (d) Rytov data; a = 15.0 mm.

Tor Standnes, *Experimental investigation of ultrasound diffraction tomography*
Ph.D Thesis, 1998, University of Bergen

FBP vs ART reconstructions from ultrasound data

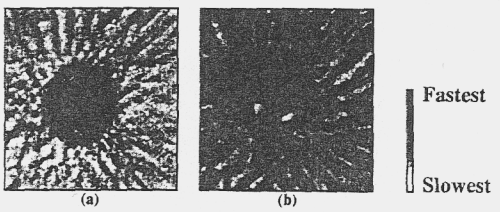

Fig. 5 (a) Real part of the reconstruction generated from the FBP algorithm from data taken at 26 equally spaced view angles. (b) Imaginary part of the reconstruction generated from the FBP algorithm from data taken at 26 equally spaced view angles.

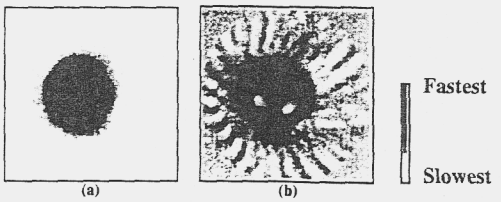

Fig. 6 (a) Real part of the reconstruction generated from the DT-ART algorithm from data taken at 26 equally spaced view angles. (b) Imaginary part of the reconstruction generated from the DT-ART algorithm from data taken at 26 equally spaced view angles.

What's Wrong with Optical Microscopy?

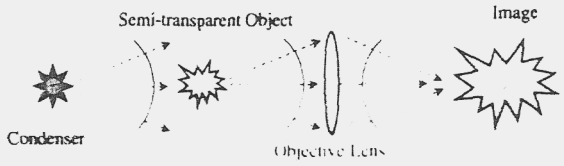

- **Illuminating light spatially coherent over small scale:**
  - Poor image quality for 3D objects
  - Need to thin slice
- **Cannot image phase only objects:**
  - Need to stain
  - Need to use special phase contrast methods
- **Require high quality optics**

Inverse Problem

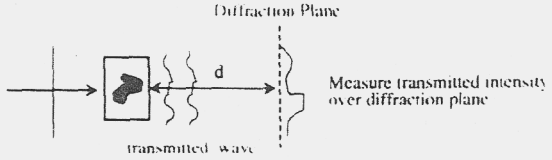

Inverse Problem: Given intensity of transmitted wave estimate the complex index of refraction distribution of the object.

Difficulties

- Phase Problem
  - Phase retrieval
  - Holography
- Quantitative Inversion
  - Diffraction tomography
    - Born Model
    - Rytov Model
- Limited Data
  - Multiple experiments

Experimental systems for optical diffraction tomography

Torolf Wedberg, *Quantitative phase microscopy by two-dimensional optical diffraction tomography*, Ph.D. Thesis, 1994, University of Bergen

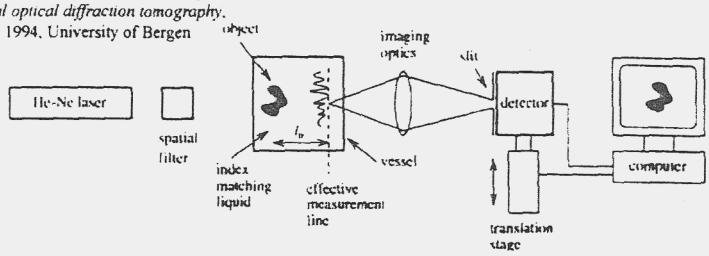

Mohammad Maleki, *Optical diffraction tomography*, Ph.D. Thesis, 1994, Northeastern University, Boston

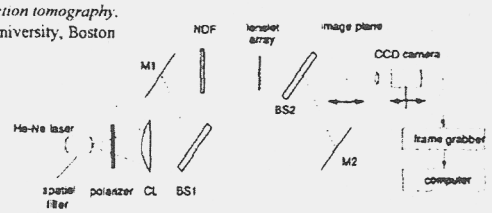

Fig. 6 Experimental setup where CL is the collimating lens, BS is the beam splitter, M is the mirror, and NDF is the neutral-density filter.

ODT reconstructions directly from intensity

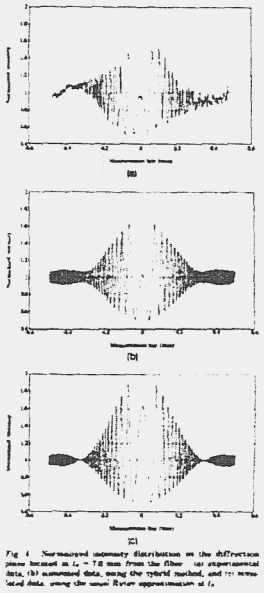

Fig. 4 Normalized intensity distribution on the diffraction plane located at $z_0 = 7.6$ mm from the fiber (a) experimental data, (b) simulated data, using the hybrid method, and (c) simulated data, using the usual Rytov approximation at z_0.

Optical fiber: a=1.2 μm, b= 6.22 μm, $\delta n = 11.5 \times 10^{-3}$

M. Maleki, A.J. Devaney, A. Schatzberg, JOSA A, Vol. 9, 1992

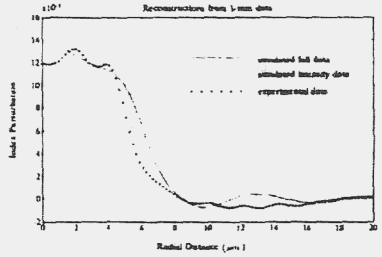

Fig. 5 Reconstruction from experimental and hybrid scattering data. The dotted curve shows the ideal fiber profile, and the solid curve gives the reconstruction obtained from the full (amplitude and phase) simulated data. The dashed curve is the reconstruction obtained from the hybrid intensity data, and the reconstruction from the experimental intensity data is displayed with pluses (+).

Experimental results from ODT

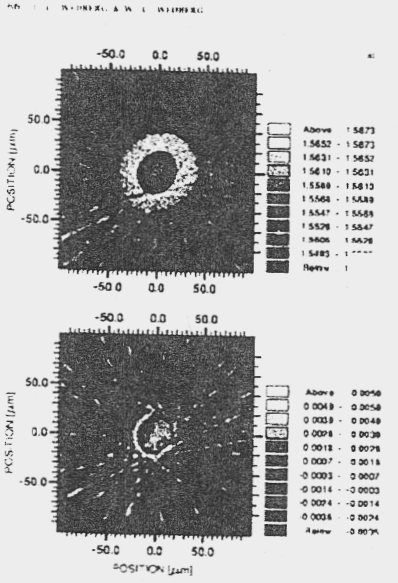

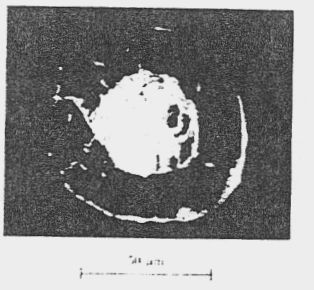

T. Wedberg and W. Wedberg, "Tomographic reconstruction of the cross-section refractive index distribution in semi-transparent, birefringent fibres," *Journal of Microscopy*, Vol. 177, 1995.

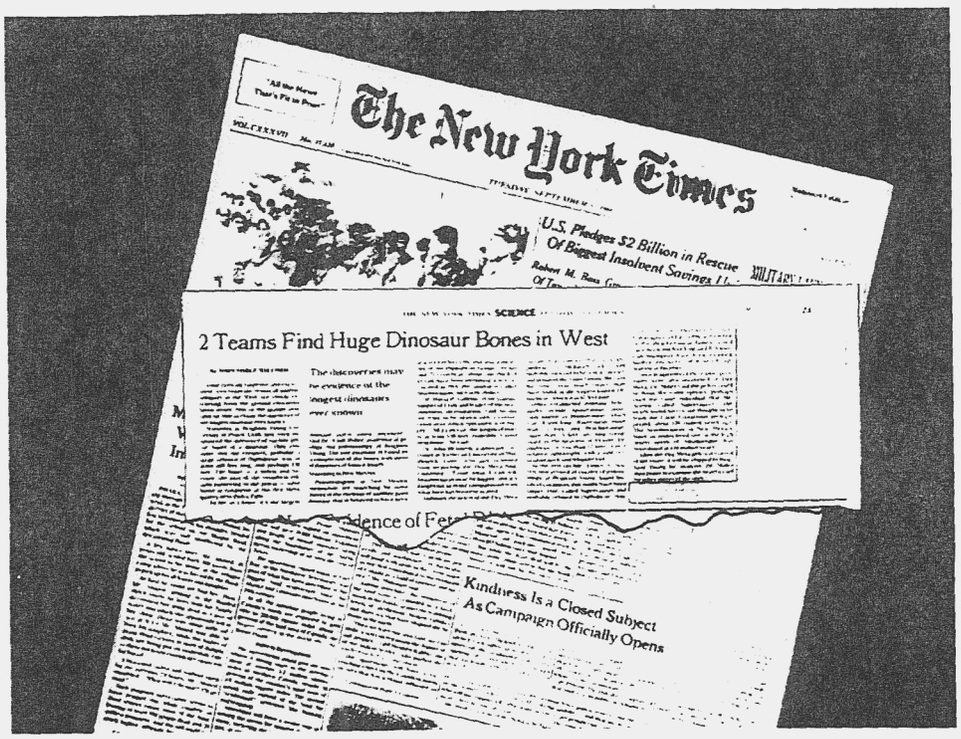

GDT survey lines and results

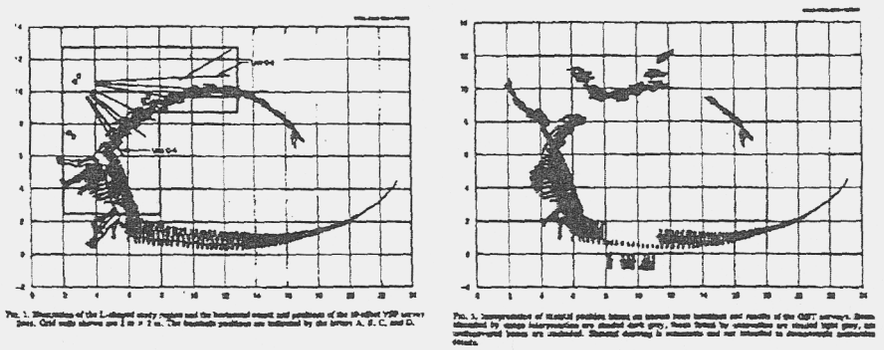

A. Witten, D. Gillette, J. Sypniewski, and W.C. King, " Geophysical diffraction tomography at a dinosaur site", *Geophysics*, Vol. 57, 1992

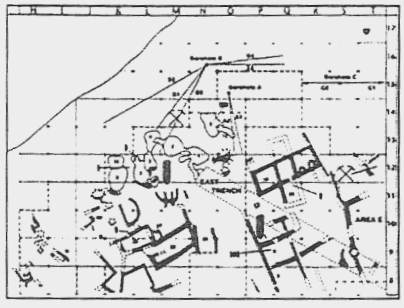

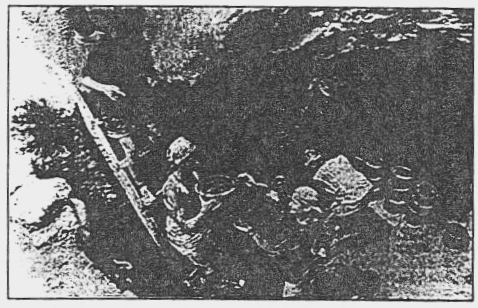

WITTEN ET AL.

Figure 5. The 1992 Shiqmim study area as illustrated by (a) the site plan showing the excavated surface and subterranean features and (b) a photograph of the Sub-room 8 excavation.

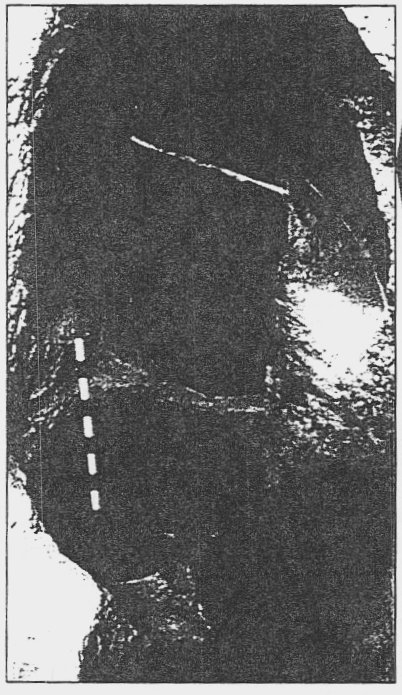

A photograph of a portion of an excavated subterranean room showing several small storage facilities dug into the floor (left) and a GDT image of a portion of an unexcavated room displaying a single storage pit in the floor (below).

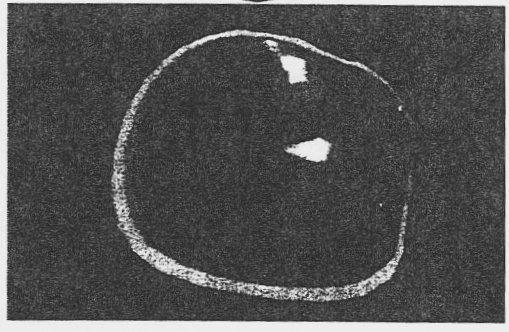

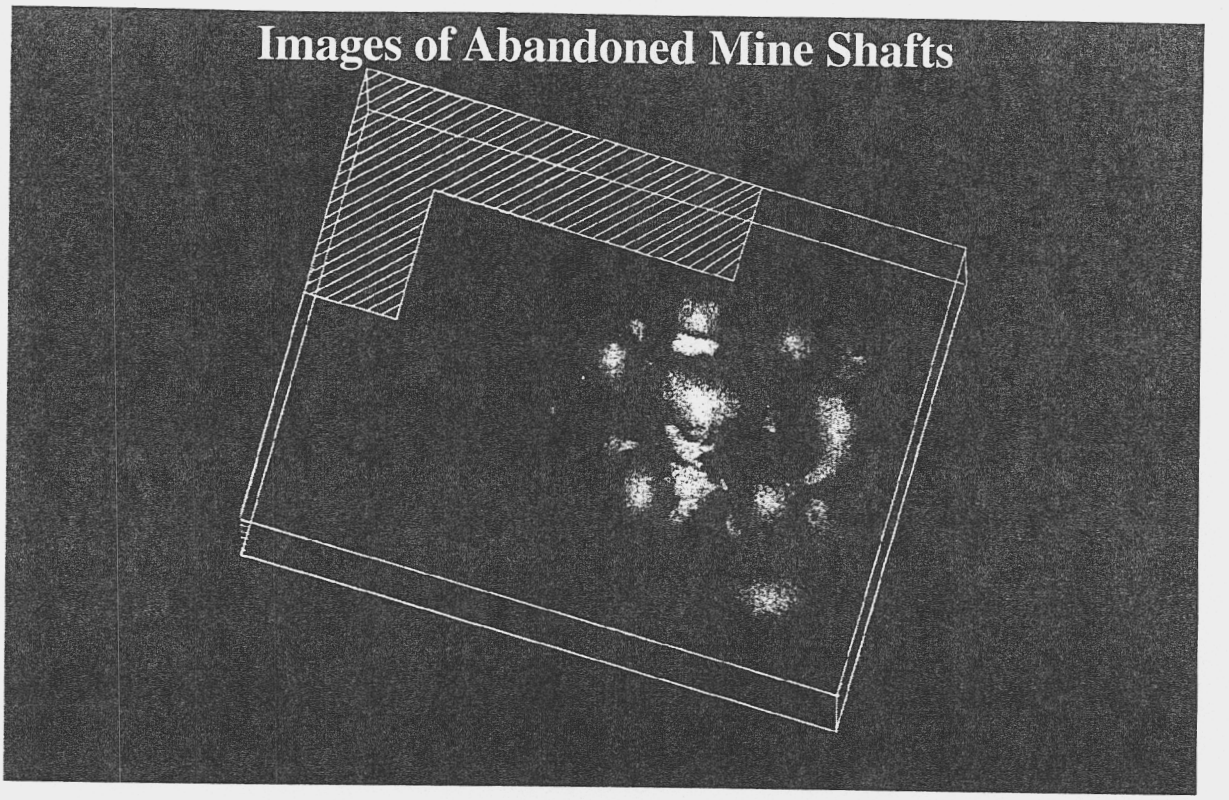

Statistical based DT

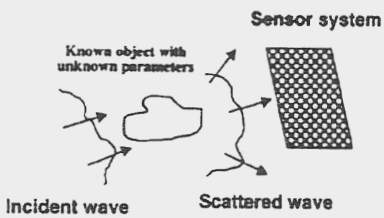

$$\Rightarrow y(\mathbf{r}_0,\omega) = d(\mathbf{r}_0,\omega) + W(\mathbf{r},\omega)$$

Maximum Likelihood Location Estimation

$$f(\mathbf{s},\mathbf{s}_0;\mathbf{R}) = f(\mathbf{s},\mathbf{s}_0;\mathbf{R}=\mathbf{0})e^{-ik\mathbf{s}_0\cdot\mathbf{R}}$$

Algorithm generates image of log likelihood function

- Exact for p.w. illumination and AWGN
- Solution in form of FBP algorithm for data rich cases
- Can be employed for target ID and target classification
- Applies to limited data
- Yields CR bounds

DTMLE using multi-monostatic GPR

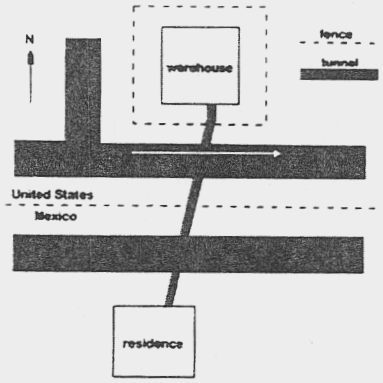

Figure 5. Illustration of the tunnel site in Douglas, AZ (not to scale). Measurements were made along the l axis.

For noise free data, such as that used here, this function is more properly referred to as the ambiguity function.

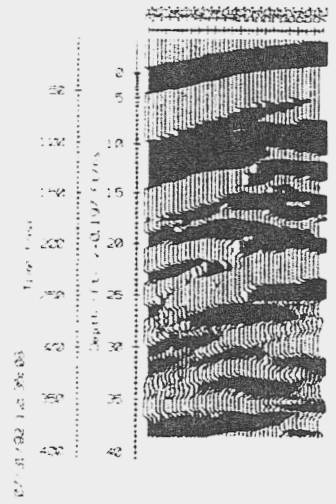

Figure 6. Plot of 25 MHz data for the *TE* polarization.

A. Witten, A. Schatzberg, A.J. Devaney, *J.Env.&Eng. Geophysics*, Vol. 0, 1996

MLE estimates of tunnel location

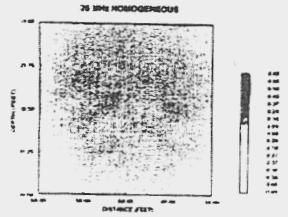

Figure 8. Spatial distribution of the log likelihood function, displayed as gray levels, for the 25 MHz homogeneous case.

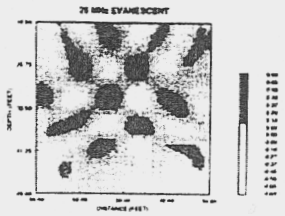

Figure 9. Spatial distribution of the log likelihood function, displayed as gray levels, for the 25 MHz evanescent case.

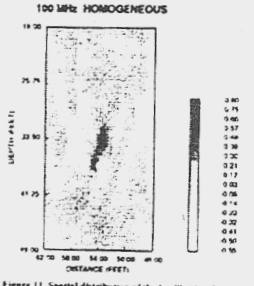

Figure 11. Spatial distribution of the log likelihood function, displayed as gray levels, for the 100 MHz homogeneous case.

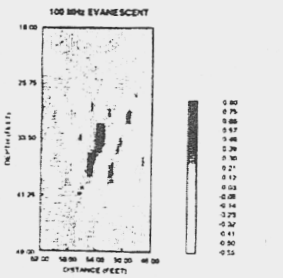

Figure 12. Spatial distribution of the log likelihood function, displayed as gray levels, for the 100 MHz evanescent case.

Future

- APPLICATIONS
- NON-LINEAR EXTENSIONS
- NOISE—INCLUDING CLUTTER
- ADAPTIVE SYSTEMS

Computed Tomography

The LANDMARC Project: Land-mine Detection with Advanced Radar Systems

Stephen Azevedo
Laser Engineering Division, EE
Information Science and Technology Program
Laser Programs Directorate

CASIS Workshop
Lawrence Livermore National Laboratory
November 12-13, 1998

The problem we are addressing is radar detection of landmines

- Objective: Develop and demonstrate the key technologies to prove the efficacy of a landmine detection system based on radar
- Importance: Demining operations to reclaim land and save lives are currently slow and inefficient (estimated 1000 years to clear)
  - Current methods are low-tech and dangerous
  - New LLNL-technologies can be applied and can be cost-effective

The LANDMARC technical team has experience with radar imaging

- Stephen G. Azevedo, Project Leader for MIR, Ph.D. in reconstructive imaging
- James M. Brase, Deputy Program Leader AMP, Image and signal processing
- E. Tom Rosenbury, Microwave hardware design
- Jeffrey E. Mast, Ph.D. Microwave diffraction tomographic imaging
- Sean Lehman, Ph.D. candidate at U.C. Davis
- Paul Walker, Ph.D. candidate at Purdue University
- Robert Greenwalt (Lt.Col., U.S. Army, ret.), Consultant
- Douglas Rake for Japan-US interactions, Consultant

Lawrence Livermore National Laboratory

Micropower Impulse Radar

MIR/SGA/6-98-0005 6 LANDMARC EE-SGA_Prop 99

AP NM M14 Antipersonnel Mine

Manufacturing Country:	India
Using Country:	India
Case:	Plastic
Type:	Antipersonnel
Shape:	Cylinder

Remarks:
The Indian AP NM M-14 is a copy of the US M14 pressure initiated, blast antipersonnel mine. When pressure is applied to the top of the mine, a belleville spring is inverted, snapping the striker into the detonator and setting off the mine. The plastic body does provide the mine with a non-metallic construction, thereby limiting the total metal in the mine to the striker and detonator.

DETAILED INFORMATION

All | Description | General Info | Characteristics | Components
Performance | Analyst's Info | Neutralization | Detectability

SOLUTIONS

Countermine Solutions

Return to Search Results

Mine Highlighted

TS-50

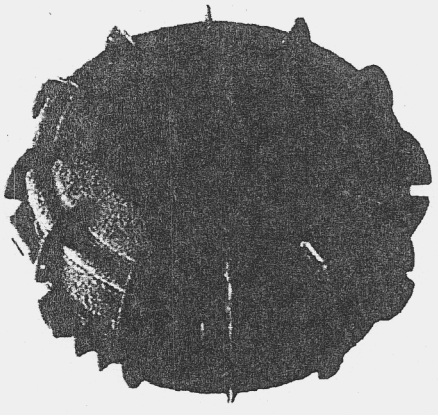

The TS-50 is a small, anti-personnel blast mine that can either be placed by hand or scattered from helicopters. The mine is blast-resistant and is designed to defeat most explosive countermeasures. This mine is found in Georgia, Iraq, Lebanon and Rwanda.

Existing mine detection R&D programs are largely directed to the military mission

Military Countermine	Humanitarian Demining
• Clearing and marking safe lanes	• Detect and destroy all land mines
• Avoiding mined areas	• Post conflict endeavor
• Requires rapid detection any time, weather, environment, enemy activity	• Detection of individual mines more important than speed of movement
• Some casualties accepted	• Conducted by the host country organization or outside assistance
• Mines not necessarily destroyed	• Detection and safety are critical (approach 100%)
• Objective taken; continue the battle	• Promote mine awareness of returning refugees
• Preserve the force	• Reestablish economy and infrastructure

University of California
Lawrence Livermore
National Laboratory

MIR/sga/10-3-98-4

Micropower
Impulse Radar

Santa Cruz Red Cross Conf.

Humanitarian demining goals and requirements are rigorous

— Once a minefield is located

- 100% removal of mines/UXO to plough-depth (20 cm)
- Do not make the mines more dangerous:
  - Don't bury them deeper
  - Don't leave any damaged mines
  - Don't modify them chemicaly etc.
- Locate every mine
  - Approach 100% detection
  - Reduce false alarms
- Speed overall removal process
  - Speed brush removal
  - Without hitting tripwires or booby traps
  - Clear each square meter quickly/reliably

— Plastic anti-personal (AP) mines are the main problem

In Cambodia: 1 acre produced 70 mines... but 500,000 metal fragments

University of California
Lawrence Livermore
National Laboratory

MIR/SGA/6-98-0005

Micropower Impulse
Radar

LANDMARC EE-SGA Prop

Current demining operations are done with simple tools

- Large-scale survey – Locate fields, prioritize them
- Narrow the search – Not yet done; will use dogs and mechanical systems
- Careful demining – Remove all metal from field to 20cm depth
  - Establish safe lanes
  - Teams of 2, in platoons of 30 (separated)
  - Calibrate metal detectors (one per team)
  - Over sections 1-by-0.5m:
    - Clear brush (1-30 minutes)
    - Pass detector over surface (15 sec.)
    - Probe for objects (many minutes)
- When found, remove or detonate mine
- Validation – often none

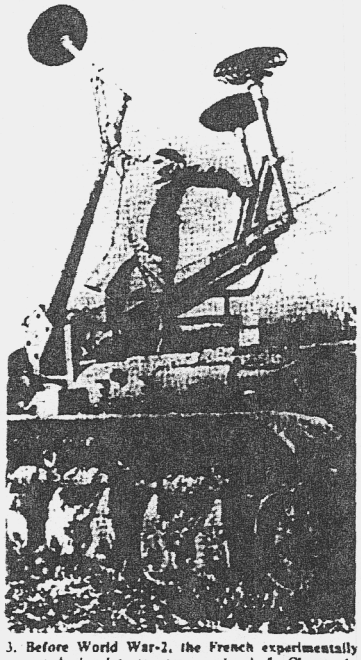

3. Before World War-2, the French experimentally mounted mine detectors to scan ahead of a Char tank. Development never advanced beyond this prototype

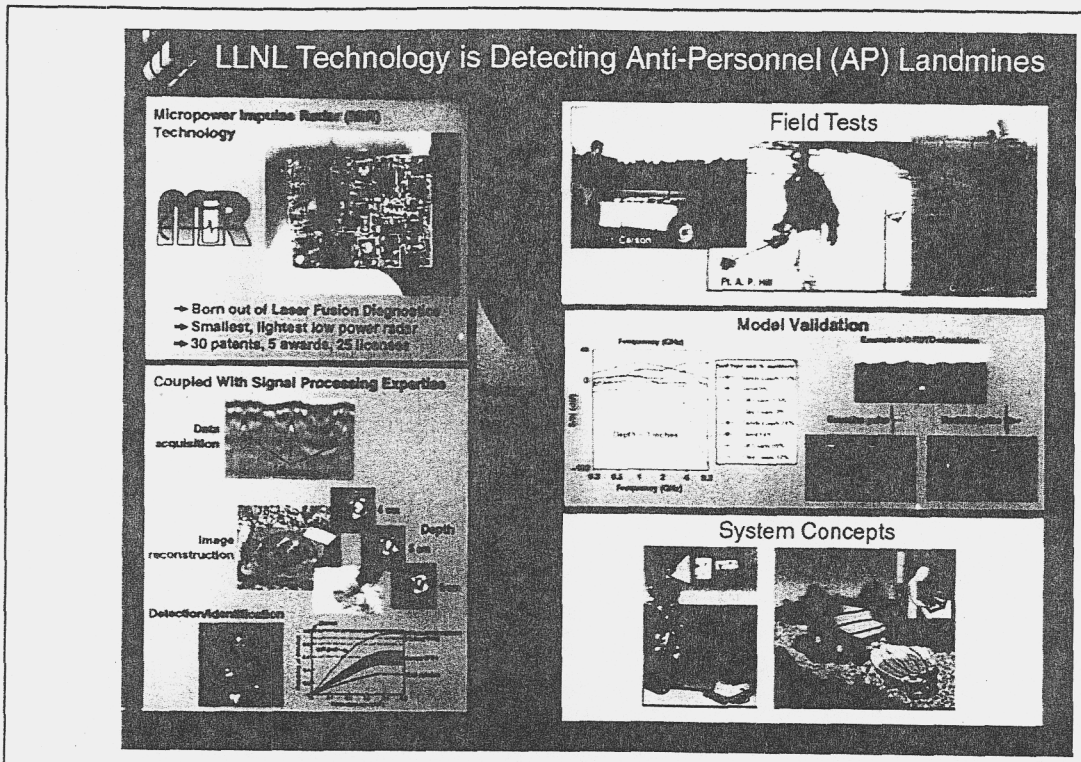
LLNL Technology is Detecting Anti-Personnel (AP) Landmines
Micropower Impulse Radar (MIR) Technology
MIR
→ Born out of Laser Fusion Diagnostics
→ Smallest, lightest low power radar
→ 30 patents, 5 awards, 25 licenses
Coupled With Signal Processing Expertise
Data acquisition
Image reconstruction
Depth
Detection/identification
Field Tests
Model Validation
System Concepts

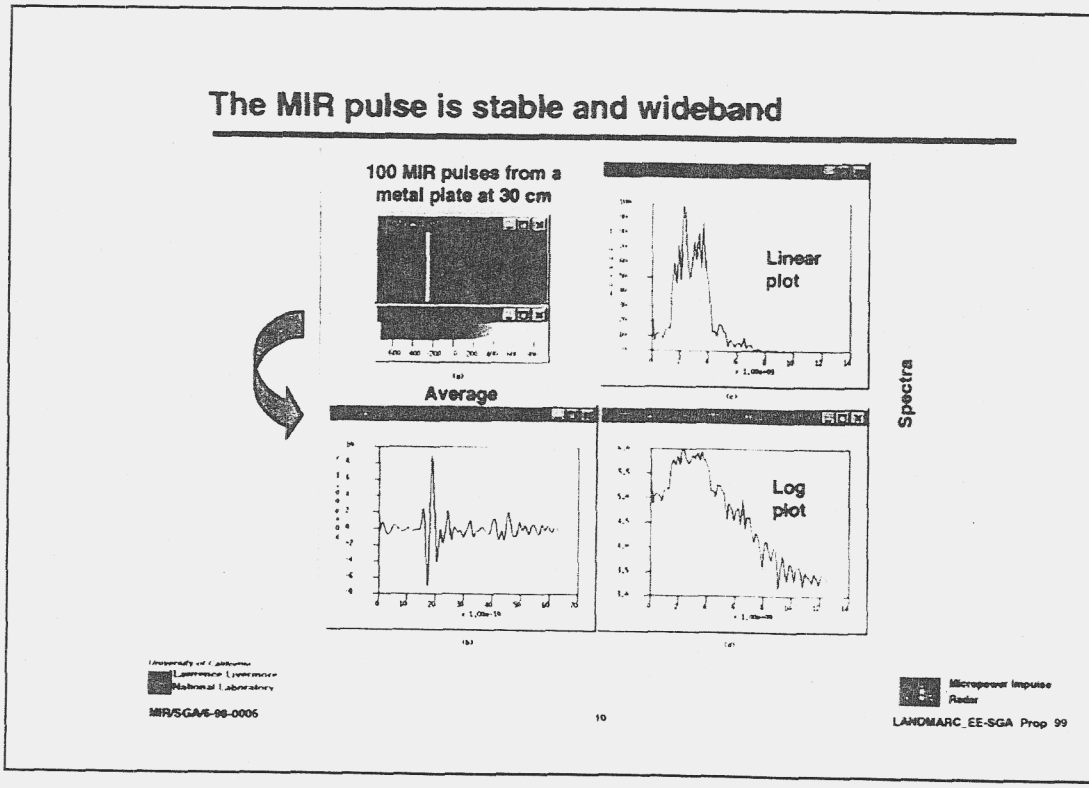
The MIR pulse is stable and wideband
100 MIR pulses from a metal plate at 30 cm
Linear plot
Average
Log plot
Spectra
Micropower Impulse Radar
MIR/SGA6-98-0006
10
LANDMARC_EE-SGA Prop 99

High Performance Robotic Radar Imaging System

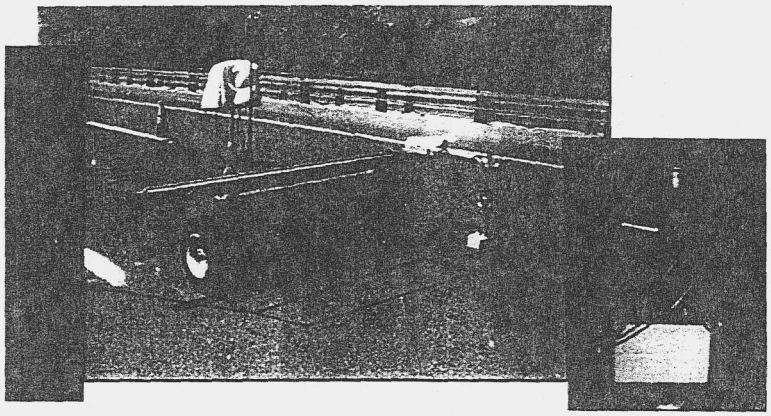

An MIR based NDE imaging system would be suitable for applications where a robotic vehicle is needed, e.g. inspection of large and tall vertical structures.

Surface Removal is done in several steps

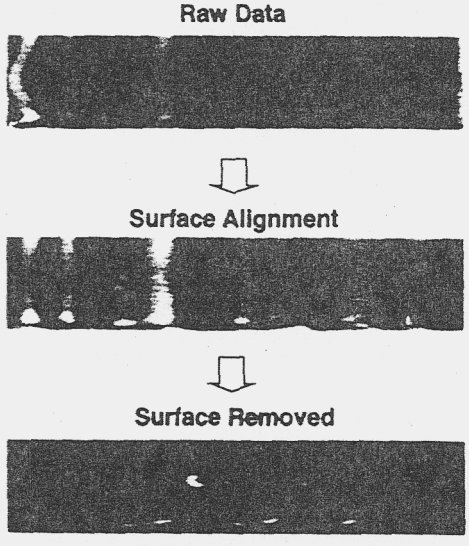

University of California Lawrence Livermore National Laboratory

Micropower Impulse Radar

A rough surface is a significant source of clutter in mine reconstructions and can distort the image of the mine

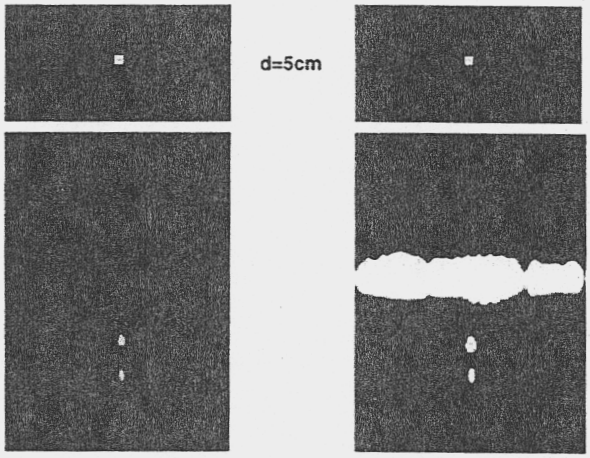

We will refine the simulation to reflect actual conditions based on real data

Jeff Mast 7 Micropower Impulse Radar 11/21-97 CASIS Workshop

Surface clutter is dominant for shallow mines however attenuation is the primary problem for deeper mines

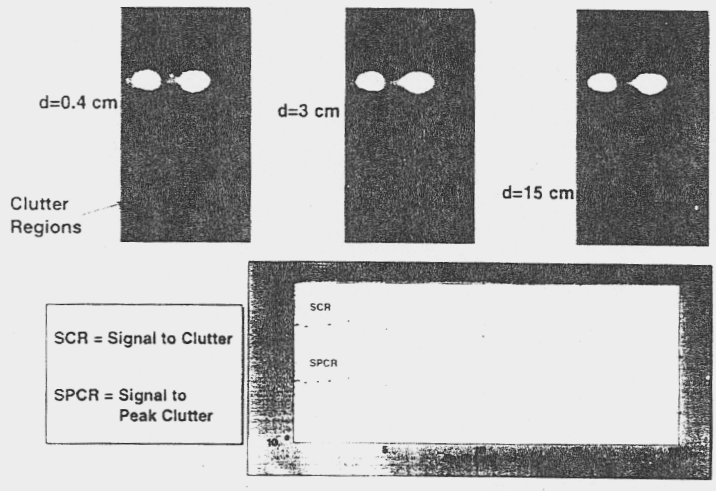

Jeff Mast Micropower Impulse Radar

The DSWA/LLNL mine detection system is based on needs of the humanitarian deminers

Carry/roll to the clearance site

Calibrate to known targets

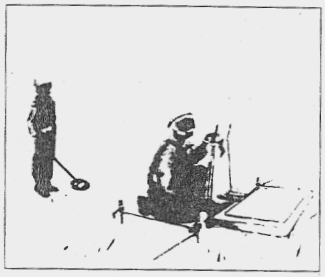

Image a 1m-squared area

Operational scenario:

- "Safe lanes" pre-marked
- Brush/foliage cleared to 5cm in a 1mX.5m area
- Detector brought into find subsurface mines
- Clear mines
- Move markers and repeat

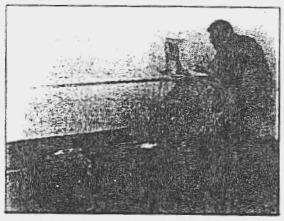

Lab prototype detector

Results to date (April 1998)

Average of 18 tests	AN/PSS-12	MIR
Detection rate	44%	85%
False alarms (Per detected mine)	31.8	14.6

Sponsors: LLNL, Defense Special Weapons Agency (DSWA), U.S. Army Humanitarian Demining R&D

University of California
Lawrence Livermore
National Laboratory

MIR/SGA/6-98-0005

11

Micropower Impulse Radar

LANDMARC EE-SGA Prop 99

MIR Mine Detection Program Status

Completed	Partially Completed	Planned
MIR single-sensor operational	EM model of mines and soils	Automatic Target Recognition
3D image display/analysis	Clutter discrimination	Mine discrimination in:
Anomaly detection in soil	Surface roughness removal	Variety of soils
Precision 3D positioning	Wider bandwidth (1-10 GHz)	Heterogeneous soils
MIR scanning array operational		Various climates
Mine detection in 3 soil types		Vegetation
Detection in presence of clutter		Field ready:
		Rugged, miniaturized
		Man-machine interface
		Low-cost

Micropower Impulse Radar

Developmental MIR mine detection experiments were performed in April '98

The experimental set up was as follows:

- MIR system: 4-element impulse radar array with ridged-horn antennas (1 to 5 GHz)
- 3 soil types: top soil, gravel, sand; homogeneous with flat surface
- Mines used: Extremely low metal-content mines (M-14's) with initiator removed and dielectrically filled (~.75 mines per m^2); mines laid within 1cm of the surface
- Intentional clutter: Small metal pieces in known moveable locations (~10 per m^2)
- Environment: From dry to rain-soaked
- Independent Test Control: Blind experiments with AN/PSS-12 (metal detector) and the new MIR mine detector. Both with trained operators in identical lanes.

Micropower Impulse Radar

Signal processing approach for imaging detection

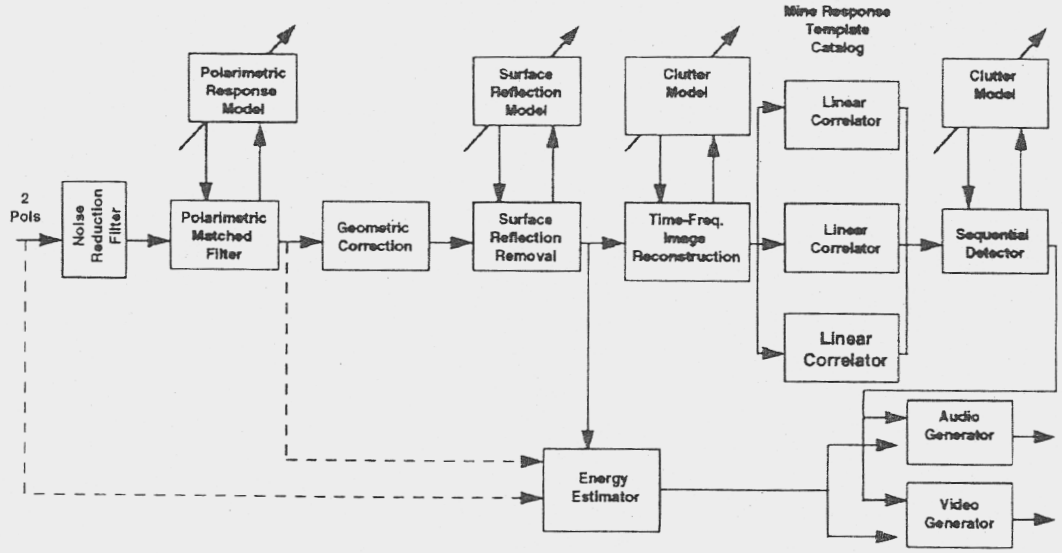

University of California
Lawrence Livermore
National Laboratory

MIR/SGA/6-98-0005

12

Micropower Impulse Radar

LANDMARC_EE-SGA_Prop 99

The goal is to develop a radar subsystem that has the best chance of finding buried mines

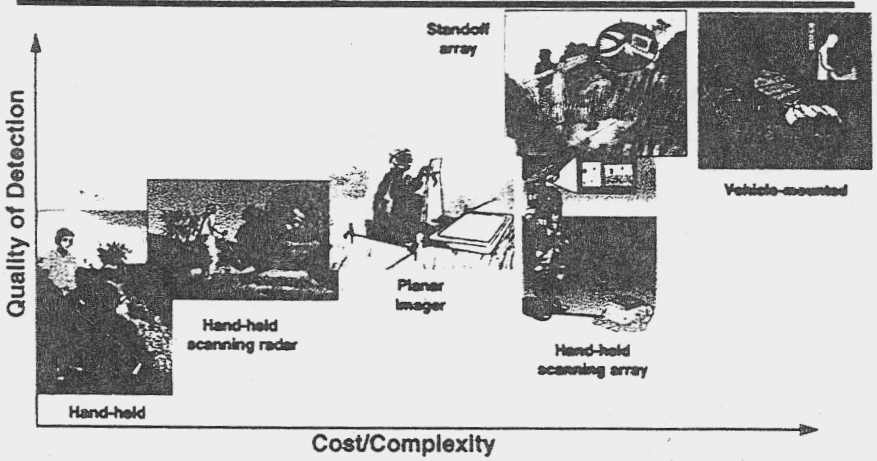

A series of trade-offs determine the type of system and its performance

University of California
Lawrence Livermore
National Laboratory

MIR/SA/3-98/0001

18

Micropower Impulse Radar

4/3/98 - Portable Landmine Det_Final

LANDMARC fits into the "big picture" of MIR mine detection

	LANDMARC	EE Tech Base	Lasers	External DARPA, DSWA, Army
Model development	✔			
Experimental validation	✔			
Incorporate in optimal processing	✔			
Detection/discrimination	✔			
Radar refinement		✔	✔	✔
Development testing			✔	
Program development			✔	
System design and implementation				✔
Deployment				✔
Sensor Fusion				
Automated detection				

University of California Lawrence Livermore National Laboratory

Micropower Impulse Radar

MIR/SGA/6-98-0005 6 LANDMARC_EE-SGA Prop 99

Summary: AP mine detection can be vastly improved with MIR technology

- Humanitarian demining and countermines are important global issues
- Detection in clutter is the key unresolved issue; MIR is an important enabling technology for a high-resolution 3D imaging approach
- Laboratory technology and expertise can and should be directed to this problem
  - MIR and systems
  - Radar modeling & simulation
  - Imaging techniques and detection
- Plans for future support and deployment include
  - U.S. Gov't sources and teaming with industry
  - Japanese interactions with gov't and companies
  - Non-governmental organizations

US-based technology will be directly applied to saving lives

MIR/04-97/08-SGA/mal

HERMES Bridge Deck Inspection System Current Results and Future Research

Holger E. Jones Lawrence Livermore National Laboratory

As a recent R&D 100 award winner, HERMES (High-Performance Electromagnetic Roadway Measurement and Evaluation System) showcases the multidisciplinary expertise, which LLNL can bring to bear on complex projects. Having completed acceptance testing by FHWA officials, HERMES enters into a new phase of research that will tie radar phenomenology to physical understanding. FHWA will survey many different bridges over the coming year, and collaborative efforts will focus on supporting field experiments, performing correlation studies of deck samples, and implementing techniques to increase image quality. This talk will highlight some of these efforts.

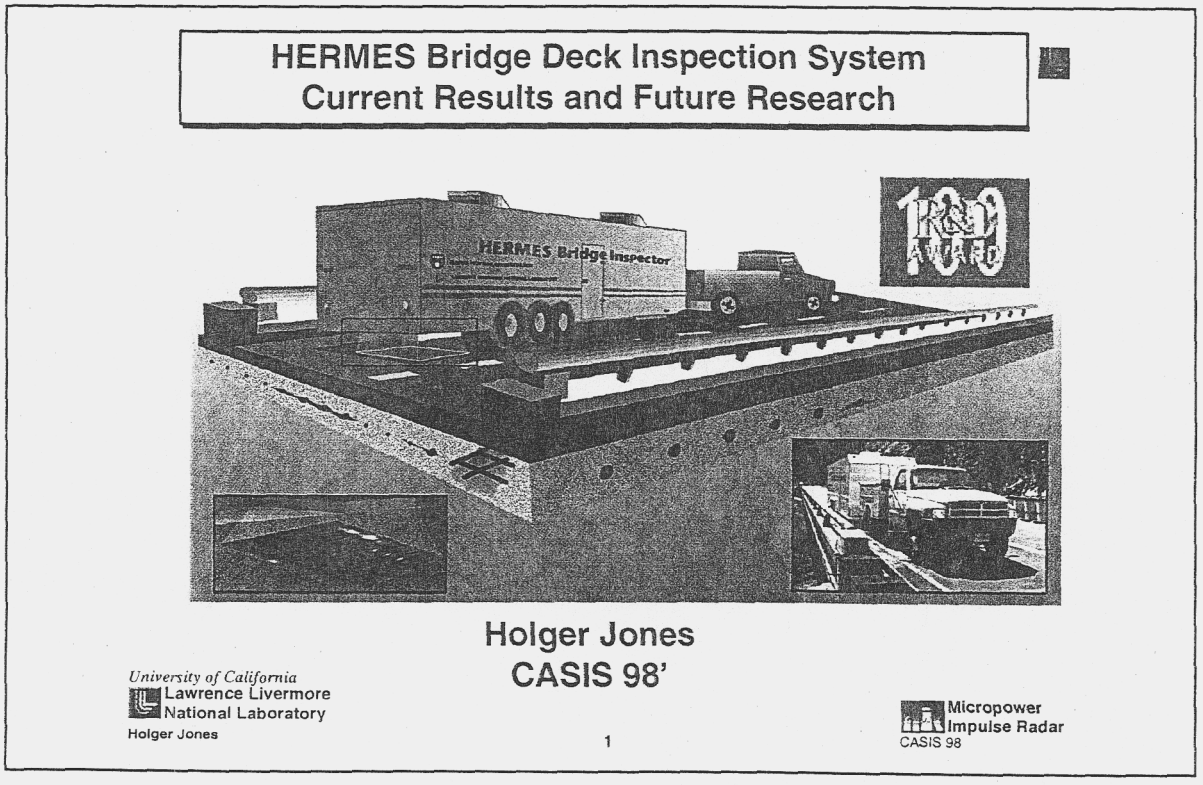

LLNL has a wide range of capabilities for development of radar based NDE

- Electromagnetic effects and modeling
  - Modeling and simulation
  - Source specifications and requirements
  - Antenna and array design
  - Experimental analysis
- Signal and image processing
  - Algorithm development
  - System specification and design
  - Detection and identification
  - Data analysis
- System development and integration
  - Custom source development
  - Custom software and data acquisition systems
- Examples
  - LLNL patented Micropower Impulse Radar (MIR) technology
  - GPR technology
    - Bridge deck inspection (shallow depths)
    - Surface to borehole imaging (deep depths)

University of California Lawrence Livermore National Laboratory
Holger Jones

2

Micropower Impulse Radar

Existing Inspection Technique

University of California Lawrence Livermore National Laboratory
Holger Jones

3

Micropower Impulse Radar

Hermes Array Implementation

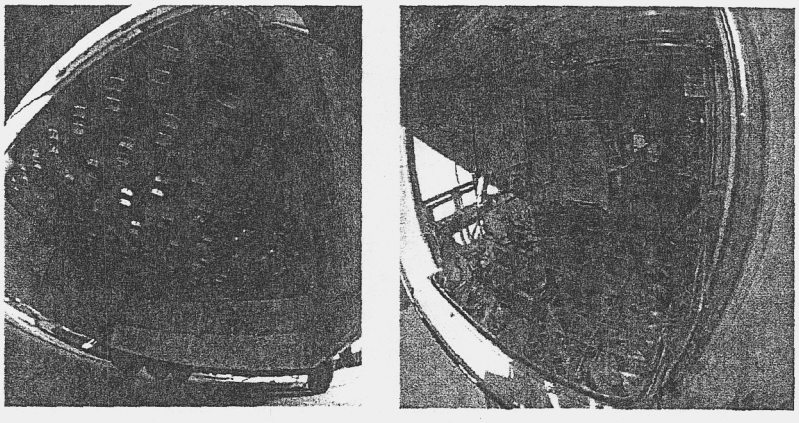

University of California Lawrence Livermore National Laboratory
Holger Jones

4

Micropower Impulse Radar

Frequency Domain Technique: A flow diagram

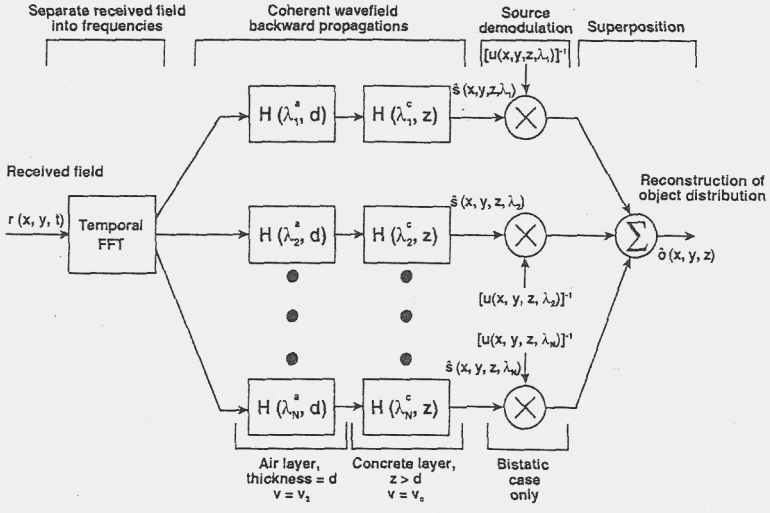

University of California Lawrence Livermore National Laboratory
Holger Jones

5

Micropower Impulse Radar

Effect of Height at Rebar Layer

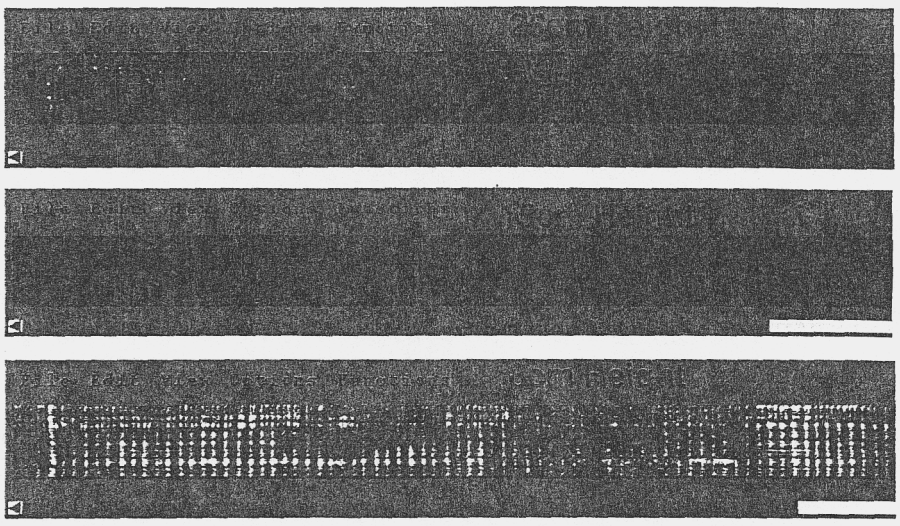

University of California
Lawrence Livermore
National Laboratory
Holger Jones

6

Micropower
Impulse Radar
CASIS 98

HERMES Inspecting Floriston Bridge

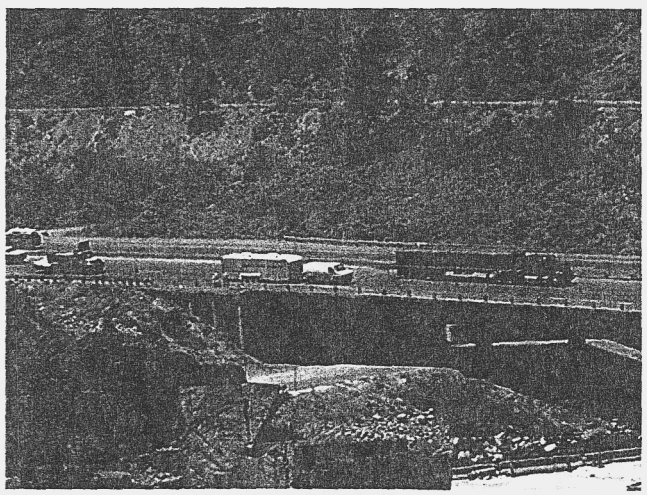

University of California
Lawrence Livermore
National Laboratory
Holger Jones

7

Micropower
Impulse Radar
CASIS 98

Data Post-Processing Efforts

- Surface Clutter is our worst problem
  - Mitigate this with
    - Advanced Surface Removal Algorithms
    - Cleaner Pulse Signature
  - Aggravated by platform motion
    - Ambiguity in depth cues
    - Use accelerometers for motion sensing
- Auto-focus Algorithm development
- Block-Processing Artifact Removal , Multi-lane montage
- 3-D Rendering Techniques, (opengl)
- Advanced Imaging Techniques
  - iterative
  - multi-monostatic correction
  - feedback from core-sample dielectric and contaminant profile
  - feedback from modeling efforts

Rebar Fade Phenomenon :

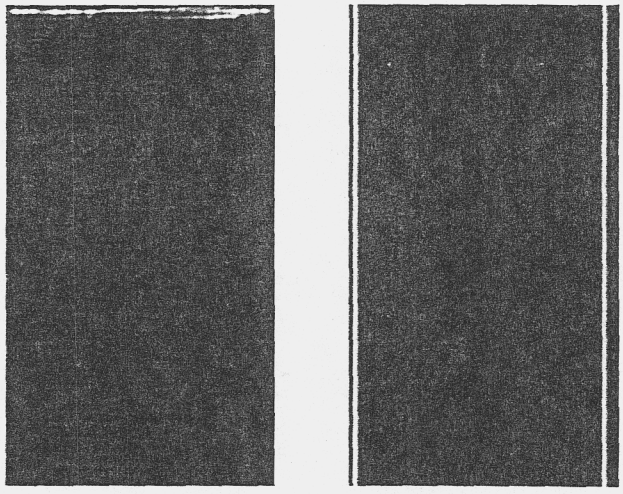

Radar Phenomenology Studies

- Collaborate with Universities
  - Models (contaminant diffusion, corrosion chemistry, etc)
  - PERES based controlled experiments
- Leverage deck-rehabilitation projects as data goldmines
  - Before/After study of RCS during deck planing (hydro-demolition)
  - Cores analyzed (dielectric/attenuation profiles, corrosion products, etc)
- High Power and Ground-coupled radar augmentation

Features Obscured/Aliased by Surface Clutter Ringing

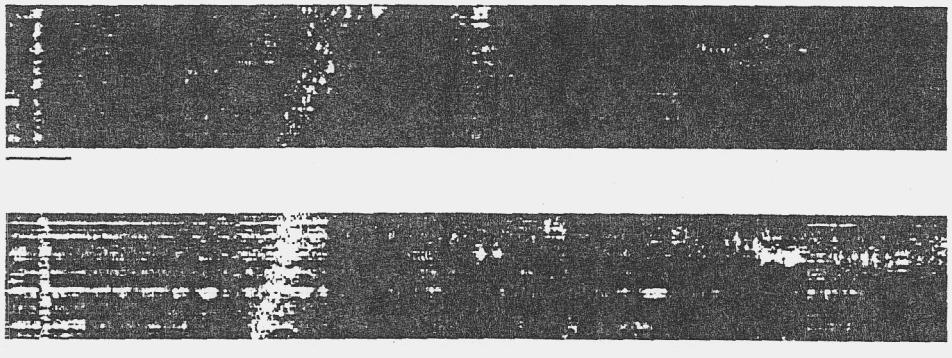

Effect of Permittivity Parameter

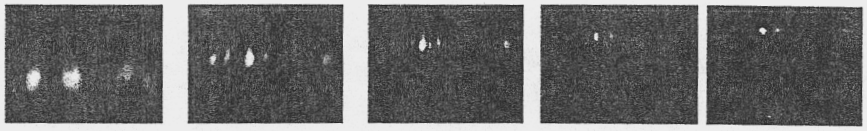

er =1.0 er=2.0 er=4.0 er=8.0 er=16.0

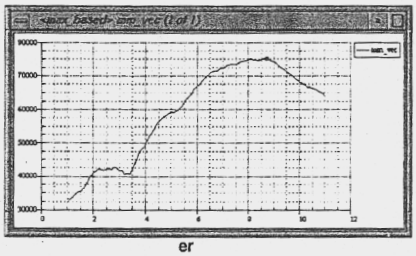

er

Peak Intensity

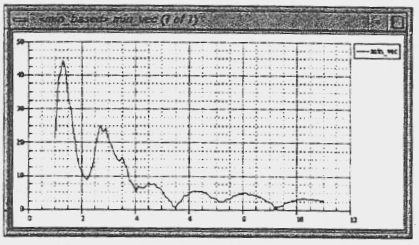

er

Normalized then summed

University of California Lawrence Livermore National Laboratory Holger Jones

12

Micropower Impulse Radar CASIS 98

3D Alpha Rendered (BoB)

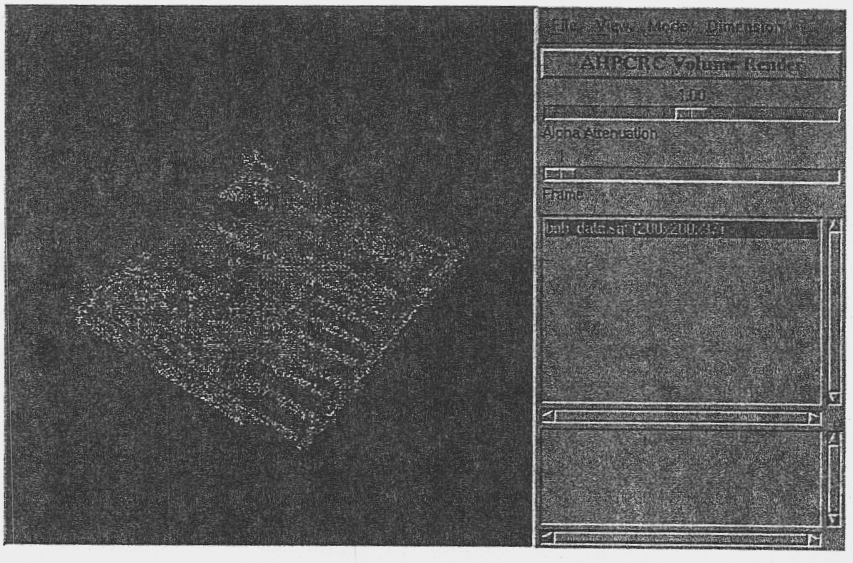

University of California Lawrence Livermore National Laboratory Holger Jones

13

Micropower Impulse Radar CASIS 98

Signal processing approach - image formation and analysis

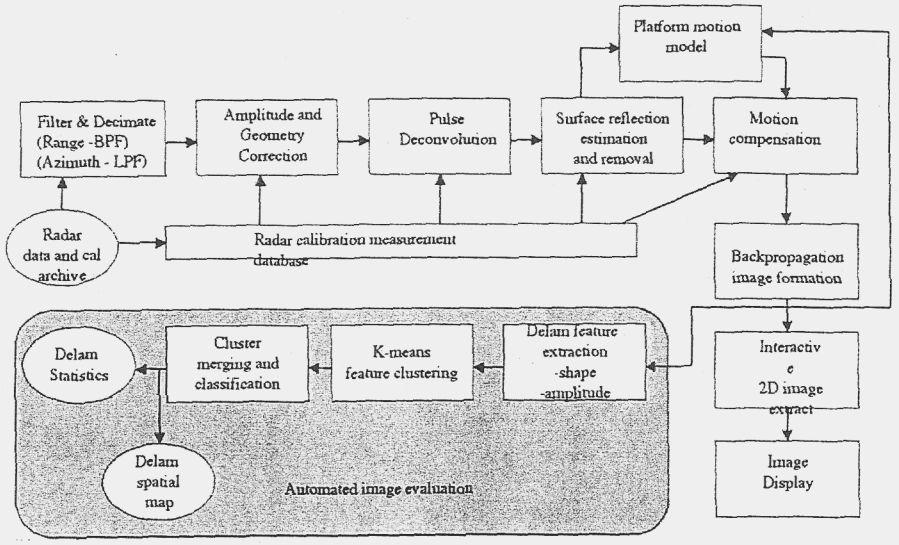

Connected Displays

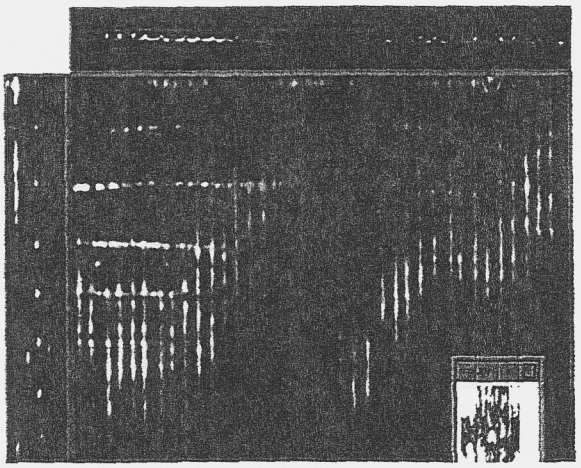

Connected Displays (different depth)

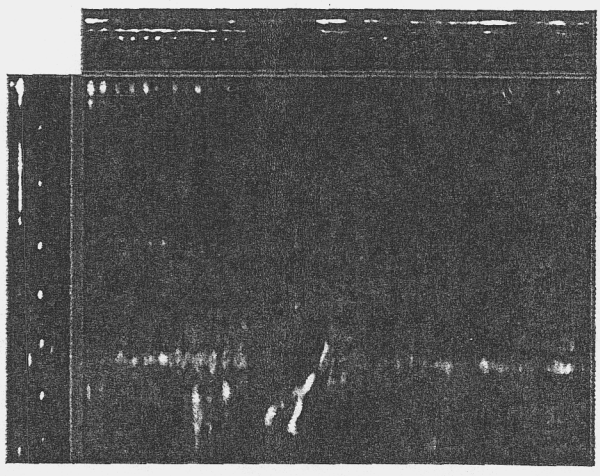

University of California
Lawrence Livermore
National Laboratory
Holger Jones

16

Micropower
Impulse Radar

Beowulf is a commodity parts based approach to cost-effective high performance computing

Highest performance computational components now arrive in PC's first --- this drives us to look at networked PC's for computationally dominated applications

Parallel computing based entirely on commodity components:
400MHz PII 256MB Ram 4GB EIDE
Dual Processor Capable Backplanes
100Mbit Ethernet
Point-to-point interconnect via switch
OS: Linux , GNU, X , PVM, MPICH

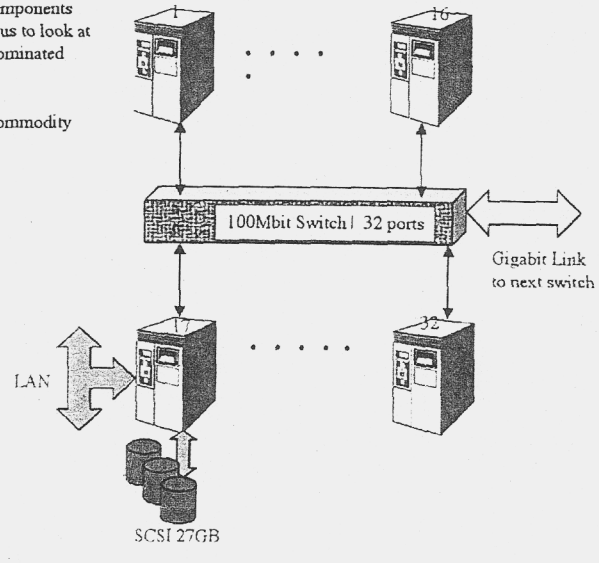

University of California
Lawrence Livermore
National Laboratory
Holger Jones

17

Micropower
Impulse Radar

Conclusion

- HERMES is entering its experimental phase
- FHWA will undertake its own studies this fall
- Maintain LLNL as Center for Inspection Studies
- Start on 2nd Prototype?
- Commercialization is key

ACTIVE AND PASSIVE COMPUTED TOMOGRAPHY WITH A CONSTRAINED CONJUGATE GRADIENT SOLUTION

By Jessie A. Jackson, Dennis Goodman,

An active and passive computed tomographic technique (A&PCT) has been developed at the Lawrence Livermore National Laboratory (LLNL). The technique uses an external radioactive source and active tomography to map the attenuation within a waste drum as a function of mono-energetic gamma-ray energy. Passive tomography is used to localize and identify specific radioactive waste within the same container., The passive data is corrected for attenuation using the active data and this yields a quantitative assay of drum activity.

A&PCT involves the development of a detailed system model that combines the data from the active scans with the geometry of the imaging system. Using the system model, iterative optimization techniques are used to reconstruct the image from the passive data. Requirements for high throughput yield measured emission levels in waste barrels that are too low to apply optimization techniques involving the usual Gaussian statistics. In this situation a Poisson distribution, typically used for cases with low counting statistics, is used to create an effective maximum likelihood estimation function. An optimization algorithm, Constrained Conjugate Gradient (CCG), is used to determine a solution for A&PCT quantitative assay. CCG, which was developed at LLNL, has proven to be an efficient and effective optimization method to solve limited-data problems. An overview of the algorithms used in developing the model and optimization codes will be given.

UCRL-JC-130818 abs

Active and Passive Computed Tomography with a Constrained Conjugate Gradient Solution

Jessie A. Jackson, Dennis Goodman,
G. Patrick Roberson, Harry E. Martz

November 12, 1998

Lawrence Livermore National Laboratory

Agenda

- Background and Goals of A&PCT Project
- Overview of the Passive Reconstruction Code
  - System Model
  - Cost Function
  - Optimization
- Results
- Summary

2

Schematic Design of A&PCT Data Processing

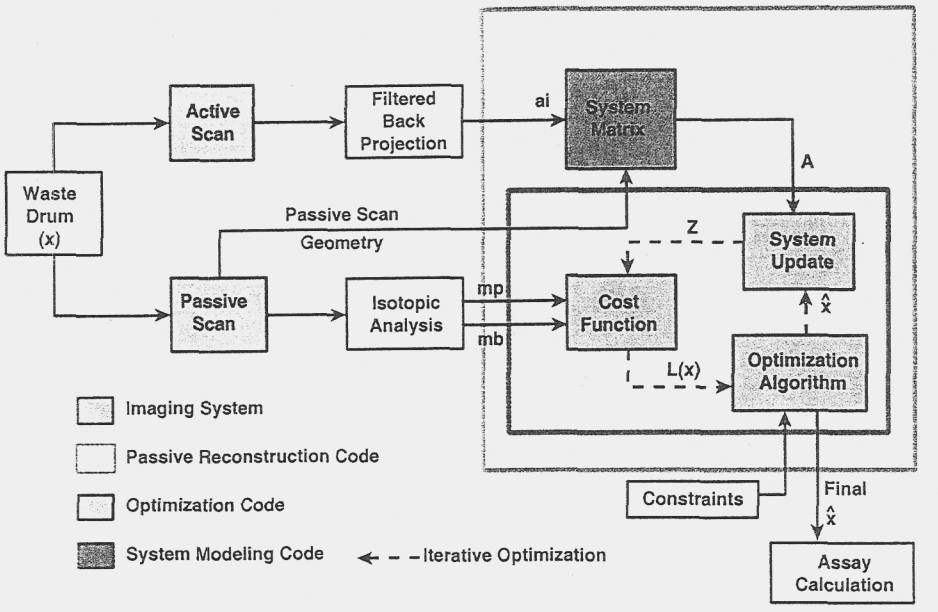

3

We combine active and passive computed tomography to more accurately assay wastes

Active CT (ACT)

ACT quantitatively maps the attenuation of the drum's contents to a specific volume element

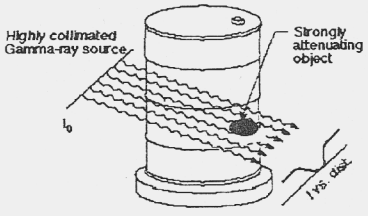

Passive CT (PCT)

PCT localizes and identifies the radioactivity to a specific volume element in the drum

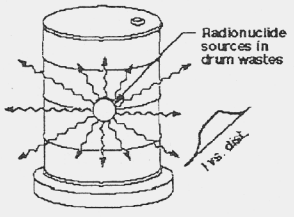

4

A&PCT Imaging System

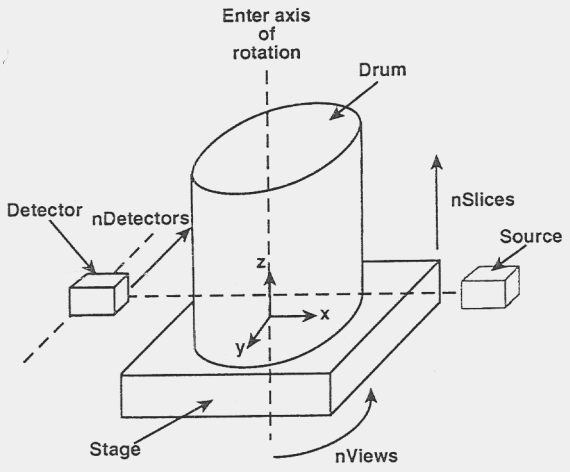

Typical Active Image
- 17 slices
- each slice has
  - 14x14 voxels

Total Voxels = 3332

Typical Passive Scan
- 7 detector positions
- 10 rotational views
- 17 slices

Total detectors =1190

5

Spectra Sample from a Passive Scan

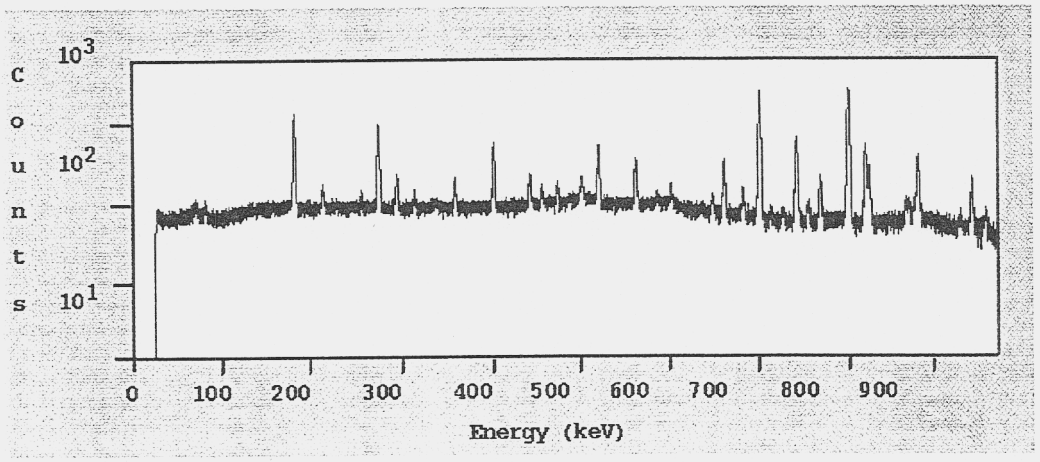

6

A&PCT Reconstruction Code Development

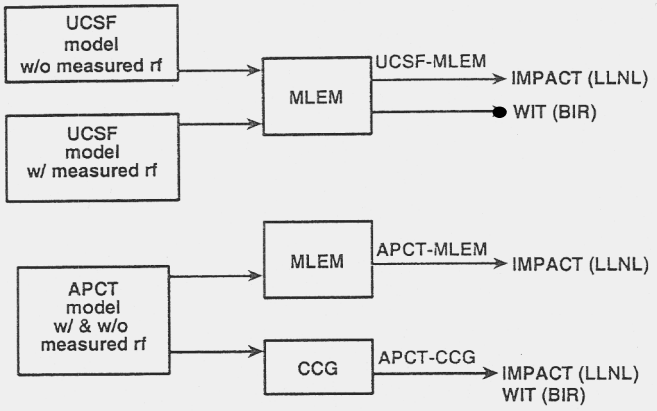

MLEM - Maximum Likelihood Expectation Maximizer
CCG - Constrained Conjugate Gradient

IMPACT - Isotope Measurements by Passive and Active Computed Tomography
BIR - Bio-Imaging Research Inc.
WIT - Waste Inspection Tomography

rf - response function of the detector-collimator

7

Spectral Signal at a Detector

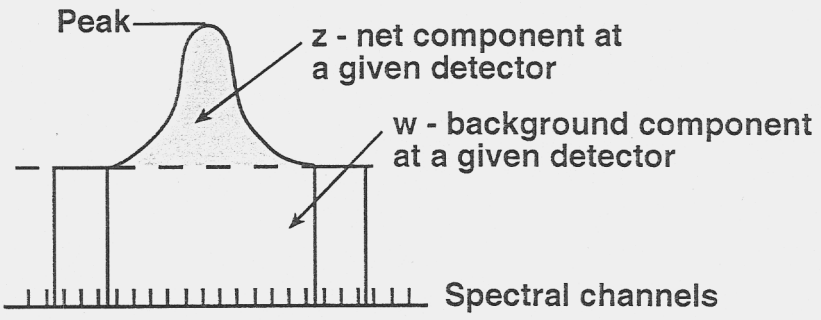

$$z = Ax$$

z - vector of net counts per detector

x - vector of emissions per image voxel

A - system Matrix

8

General Iterative Solution Technique

$$y = Ax$$

y - vector of measured values
x - vector of unknowns
A - system matrix

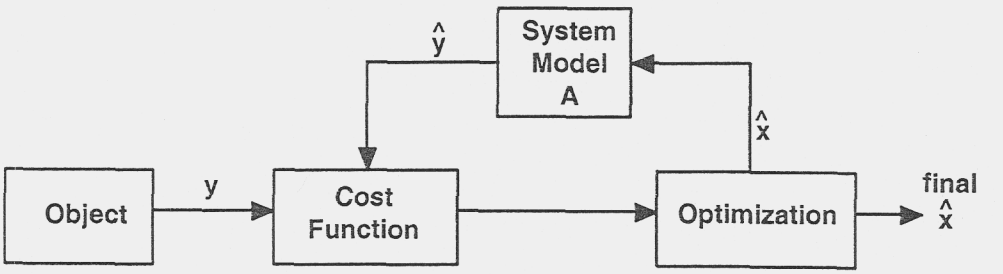

9

Passive Scan Measurements

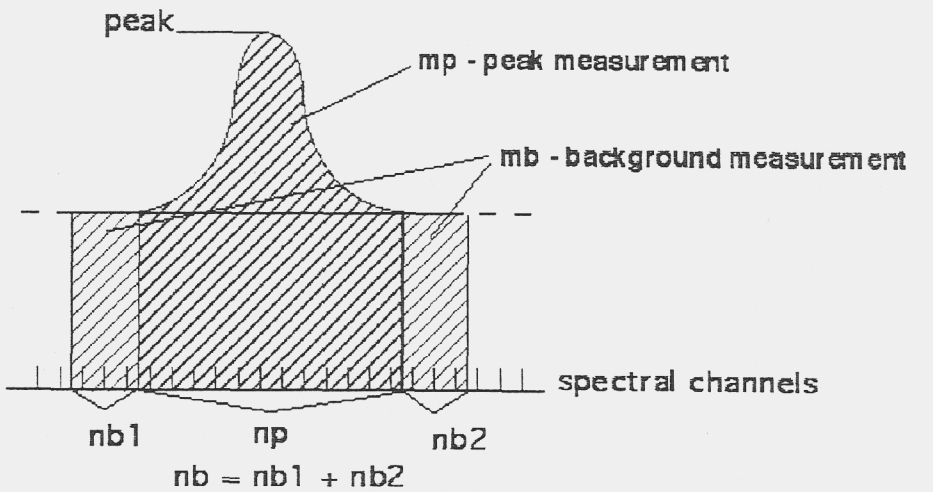

10

Iterative Solution for A&PCT

$$z = Ax$$

mp - vector of peak counts per detector
mb - vector of background counts per detector
z - vector of net counts per detector
x - vector of emissions per voxel
A - system matrix

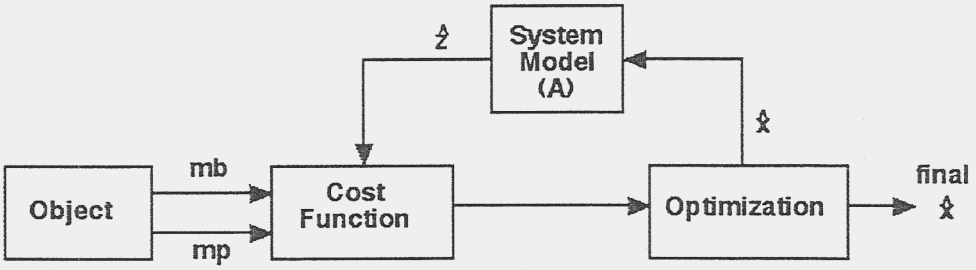

11

Cost Function - Poisson Distribution

$$\Pr\{n\} = \frac{1}{n!} a^n \exp(-a)$$

- observed value
Pr{n} - probabilty that is observed
- the expected value (mean) of Pr{n}

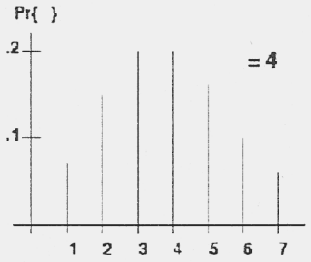

characterizes or defines a particular Poisson process

12

Cost Function - A&PCT Poisson Expectation Definition

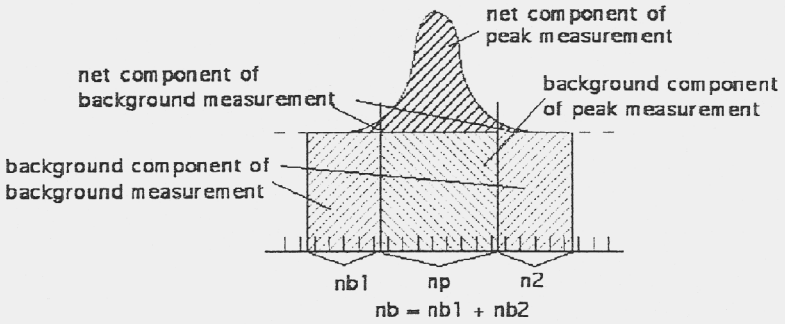

$$E\{mb\} = \tau_1 w + \tau_3 z$$

$$E\{mp\} = \tau_2 w + \tau_4 z$$

13

Comparison of Optimization Methods (MLEM and CCG) with Simulated Data

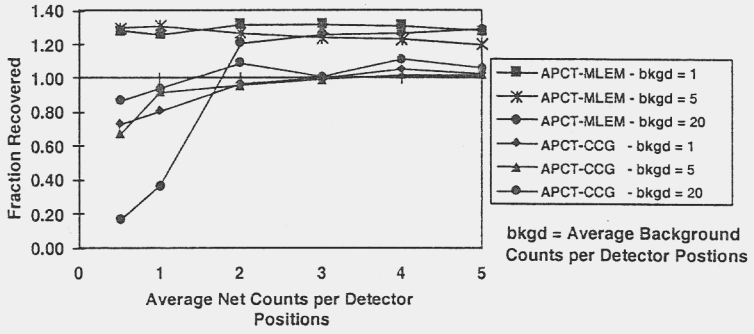

14

Comparison of Reconstruction Methods

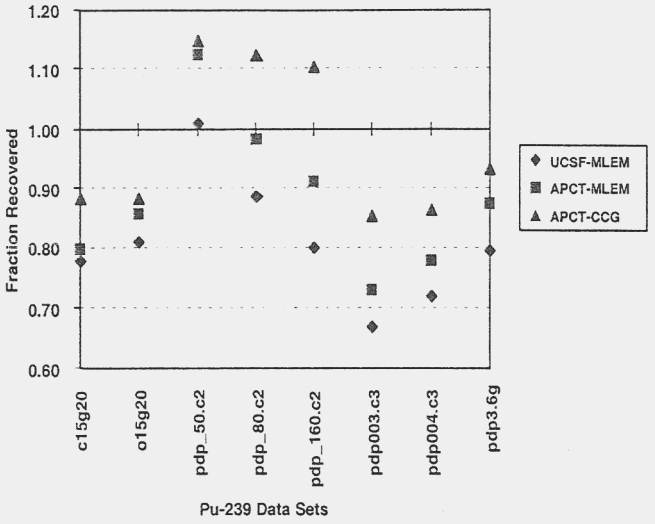

15

Simulated Comparison of MLEM and CCG

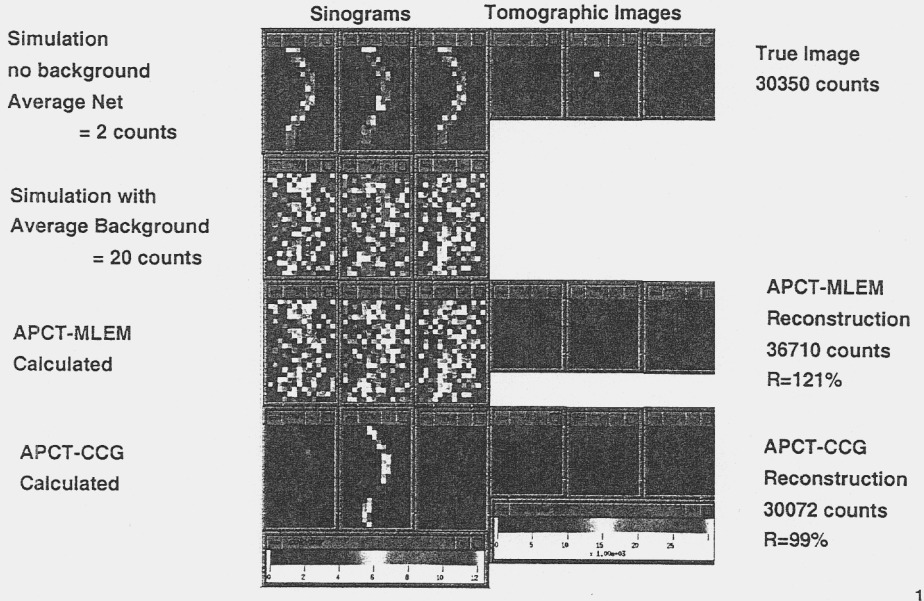

16

Applying Optimization to Tomography Problems

Dennis M. Goodman

Laser Engineering Division
Lawrence Livermore National Laboratory
Livermore, CA 94550

Outline

- Present basic ideas
- Show pretty pictures

Basic Ideas:

- Develop flexible tools for new problems (avoid ad hoc algorithms).
- Linear attenuation (transmission, etc.) model: $\hat{y} = A\hat{x}$.
- Fitting function based on statistics: $f = (y, \hat{y})$.
  - Data is y, Model of what data is $\hat{y}$.
- Optimize fit of model to data: minimize $L(y, \hat{x}) = f(y, A\hat{x})$.

Usually L is Negative log-likelihood or a robust (outlier resistant) fitting function.

Basic Ideas (Contd.):

- Model described above is called Generalized Linear Model in statistics. Lots of applicable theory that should be investigated.
- Can apply our methods to more general models as well.
- Two optimization methods to solve: both use bending linesearch.
  - Constrained Conjugate Gradients (CCG): if cols. of A easy
  - Constrained Limited Memory Quasi Newton (QN): if not

Fitting function depends on statistics:

Our algorithms let you use whatever is appropriate (or try several)

- Gaussian data leads to least squares for max. likelihood:

$$f(\mathbf{y},\hat{\mathbf{y}}) \;=\; \sum r_i^2, \quad \text{where} \quad r_i \;=\; y_i - \hat{y}_i \quad \text{(residuals)}.$$

- Least squares sensitive to outliers, use *robust* technique, e.g.:

$$f(\mathbf{y},\hat{\mathbf{y}}) \;=\; \sum g(r_i) \qquad \text{where} \quad g(r) = \begin{cases} r^2 & \text{if } |r| \le c \\ 2c|r| - c^2 & \text{if } |r| > c \end{cases}$$

- For counting data (emission tomography), max. likelihood assuming Poisson statistics leads to (we use $\mathbf{n}$ for vector of integer counts):

$$f(\mathbf{n},\hat{\mathbf{y}}) \;=\; \sum g(n_i,\hat{y}_i) \qquad \text{where} \quad g(n,\hat{y}) = \hat{y} \;-\; n \log \hat{y}$$

Both CCG and QN Algorithms solve:

$$\hat{\mathbf{x}} \;=\; \underset{\mathbf{x}\in S}{\text{Argmin}} \left\{ L(\mathbf{x},\mathbf{y}) \;+\; \nu\|\mathbf{x}\|_1 \;+\; \lambda\|\mathbf{x}\|_2 \;+\; \delta g(\mathbf{x}) \right\}$$

- The set S defines "Box" constraints: $S \;=\; \{\mathbf{x} : \mathbf{l} \le \mathbf{x} \le \mathbf{u}\}$.
- These constraints are very useful in imposing prior information about the unknown object: nonnegativity, regions of known absorption voids, occlusions, etc.
- The ℓ_1 and ℓ_2 norm terms penalize size of unknown (regularization).
  - ℓ_2 same as Gaussian prior; may oversmooth.
  - ℓ_1 same as Laplacian prior; good for "spiky" unknown.
- $g(\mathbf{x})$ arbitrary penalty term: entropy, Good's roughness, derivative penalties, etc.

During an iteration CCG and QN pick a direction, then they use a linesearch to optimize the function along that direction.

- Let $\underline{h(x)}$ = function being minimized.
- CCG picks new direction: $d_{i+1} = -\Delta_x \underline{h}(x_i) + \beta_{i+1} d_i$
  i.e.: Negative gradient plus scaled old direction.
- QN picks new direction: $d_{i+1} = -H\Delta_x \underline{h}(x_i)$ where H is a low order approximation to inverse Hessian matrix. Hessian = second partial matrix of $\underline{h}(x_i)$.
- "Bending" linesearch does not stop when face of $\underline{S}$ is hit:

$$\tilde{x}_{i+1} = Median\{1, x_i + \alpha d_i, u\}$$

$$\alpha_i = Arg\min_{\alpha>0}\left\{h\left[\tilde{x}_{i+1}(\alpha)\right]\right\}$$

Bending linesearch advantages over more common methods.

- Conventional optimization algorithms pick good search directions, but stop when hit first constraint: can hit only one face of box per iteration
- Common limited data CT methods (POCS, ART, EM, etc.) usually are steepest descent, project back to box with no linesearch.
- Our algorithms get good search directions. Uses bending to hit many faces of box per iteration. If cols. of $\underline{A}$ available, bending linesearch is very fast, use CCG; else use QN to minimize function evaluations in linesearch.

A bending linesearch approach is more efficient when many variables are bounded.

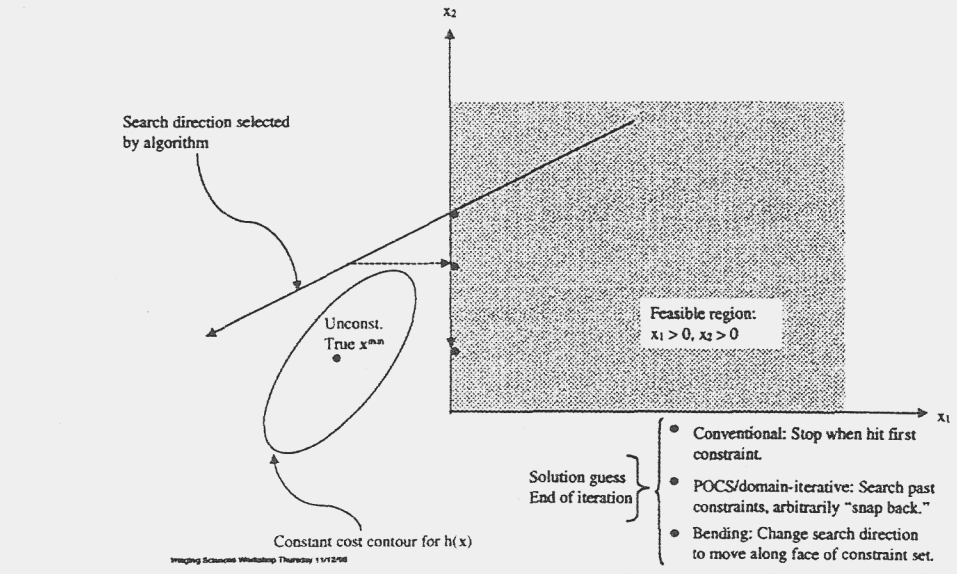

Now for the pretty pictures . . . We show six examples using CCG:

- Reconstruction from outlier-corrupted sinogram.
- Reconstruction from neutron CT data.
- Waste drum assay from counting (Poisson) data.
- Cone beam tomography for the Advanced Hydrotest Facility (AHF)
- Improved reconstruction using prior information.
- Pulsed photothermal tomography (invert heat equation).

Robust Example

- Sinogram data corrupted Gaussian mixture noise.
  - Outlier occurs with 1% probability
  - $\sigma_{outlier} = 100 \times \sigma_{regular}$
- Many problems at LLNL are outlier corrupted.
- CCG handled robust function very well.
- Reduced rms error by factors of 2-3.

Robust example: Sinogram data is corrupted with Gaussian mixture noise

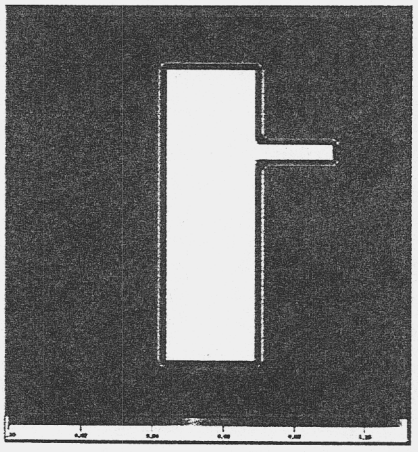

Original object

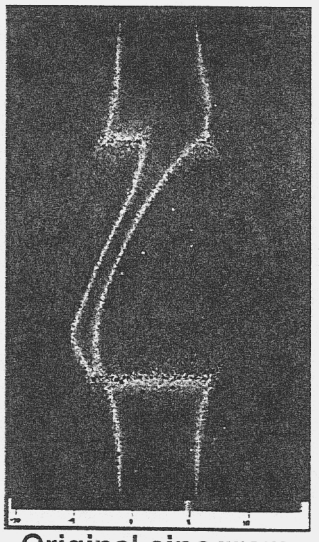

Original sinogram with noise added

CCG reconstruction using the least-squares fitting function is very sensitive to outliers

Least squares fit reconstruction

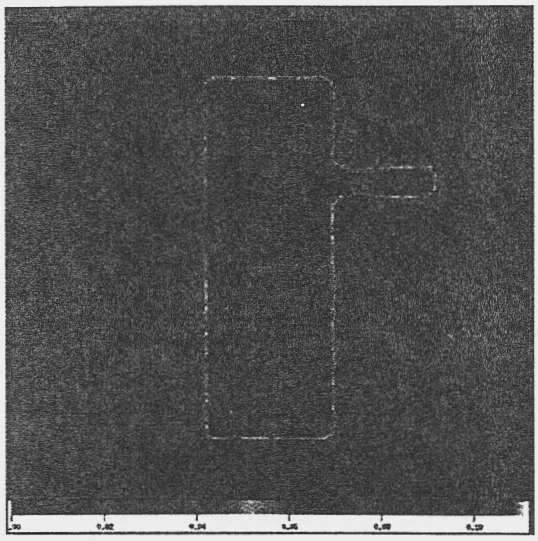

CCG reconstruction using robust fitting function reduces outlier sensitivity: lowers rms estimation error by factor of 2-3.

Robust (Huber Function) reconstruction

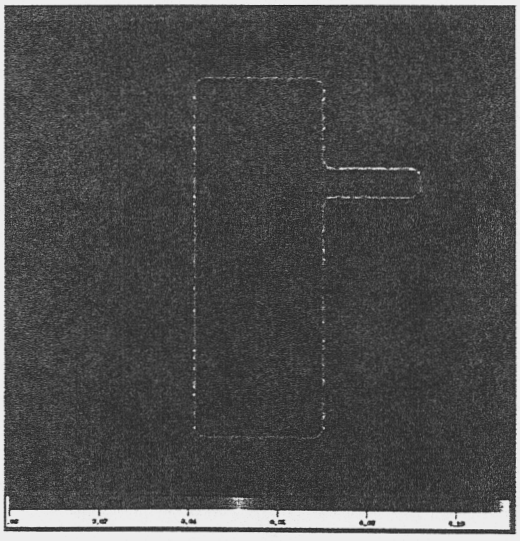

Neutron Imaging

- Important to ESP: image through dense stuff.
- CCG forced nonnegativity.
- Used least-squares, should have used counting statistics.
- Full of outliers due to external radiation.
  - Outliers removed by preprocessing.
  - Our robust model-based approach will be much better.

Summary of the LANL/LLNL experiments at LANSCE

- LANL/LLNL experiments at LANSCE first demonstrated the potential of neutron radiography for stockpile surveillance applications.
  - Incident neutron energies up to 400 MeV
  - Uranium and LiD test object assembly
  - Tungsten converter with multiwire detector
    - Sensitive to neutrons 40 MeV

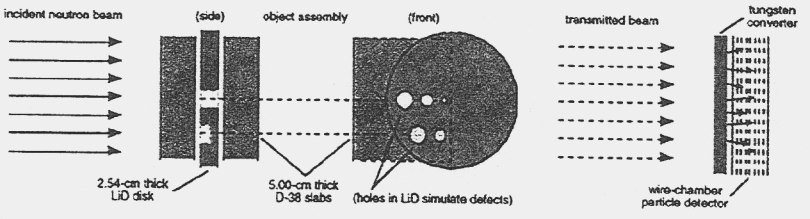

Experimental setup used to acquire the neutron CT data

- The lead/poly-cylinder phantom was imaged using 10 MeV neutrons produced at the Ohio University Accelerator Laboratory
  - 64 separate radiographic images
  - 10 minute exposures

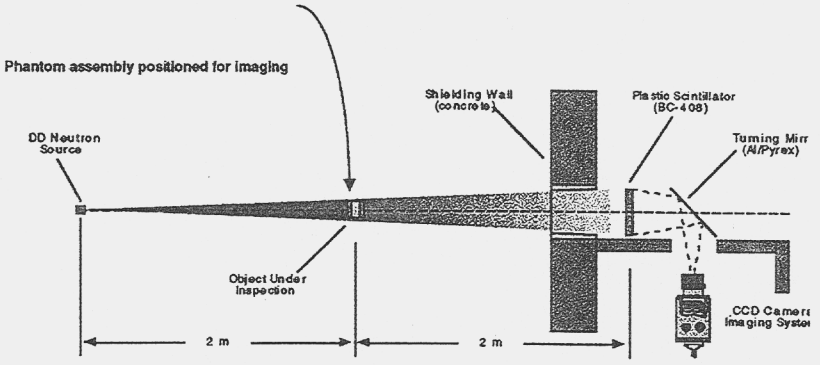

Lead/poly-cylinder phantom ~ 10 MeV neutron imaging

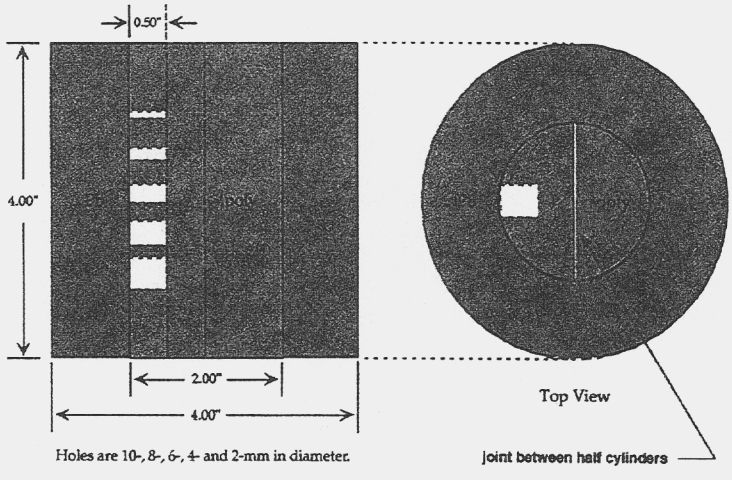

CCG reconstruction gave better results than conventional FBP for 10 MeV neutron imaging

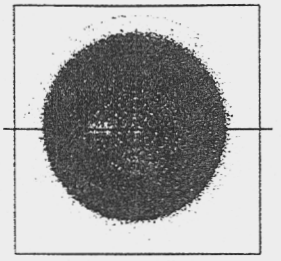

Constrained Conjugate Gradient (CCG)

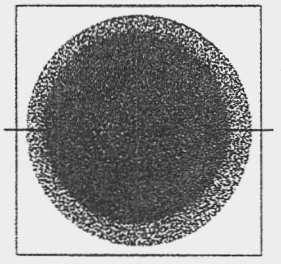

Standard Filtered Back Projection (FBP)

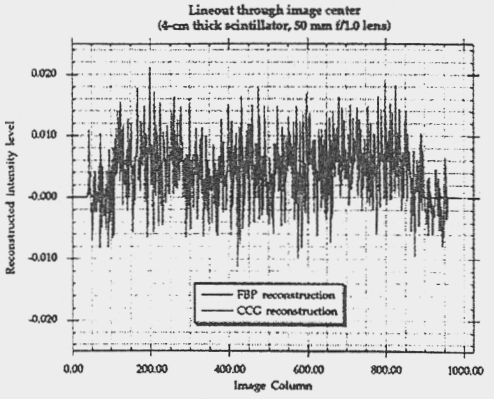

The CCG algorithm reduces pixel noise in reconstructed images by a factor of 3 - 5 compared to conventional FBP techniques

Enlarged view of horizontal slice through 6 cm hole

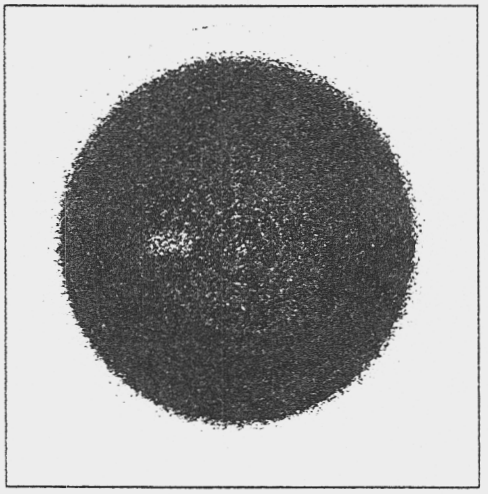

Constrained Conjugate Gradient (CCG) tomographic reconstruction

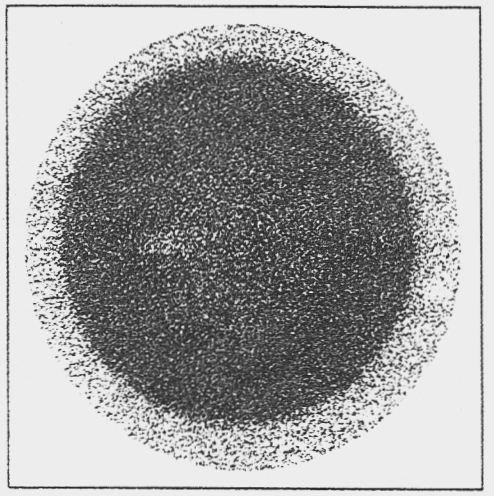

Standard Filtered Back Projection (FBP) tomographic reconstruction

Waste Drum Assay

- Complicated model: two measurements at each location.
  - Background.
  - Spectral peak.
- MLEM not flexible enough: used net = peak - background.
  - Statistically incorrect: net is not Poisson distributed.
  - Physically incorrect: net count may be negative.
- CCG implemented true likelihood.
  - Better assay.
  - Better pictures.

Comparison of CCG and MLEM reconstruction using simulated A&PCT data

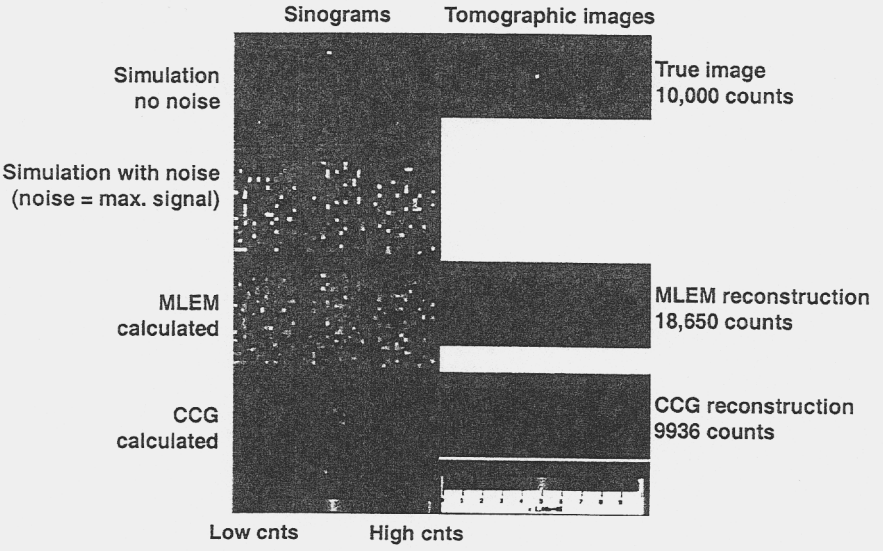

Comparison of CCG and MLEM reconstructions from actual low count A&PCT data

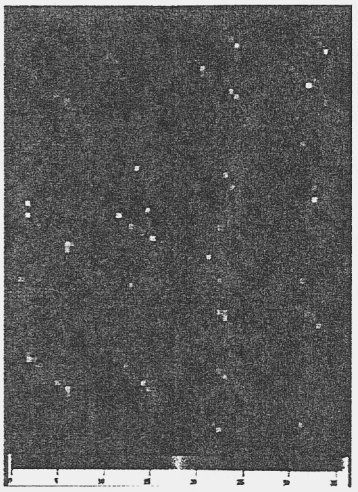

Imaging Sciences Workshop Thursday 11/12/98

Page 23

The 3D cone-beam CCG reconstructor shows significant improvement over conventional Feldkamp CT

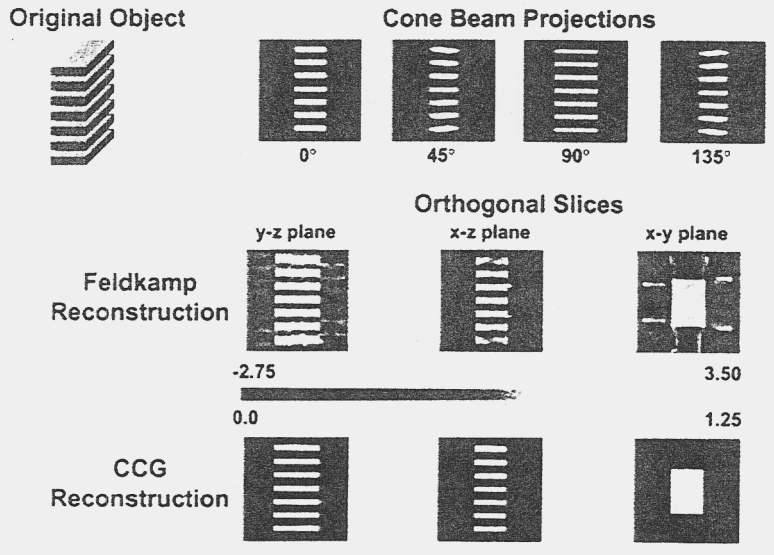

Imaging Sciences Workshop Thursday 11/12/98

Page 24

Applying prior information about known void and occlusion improved reconstruction quality outside these regions as well: total rms error reduced by factor of 3.

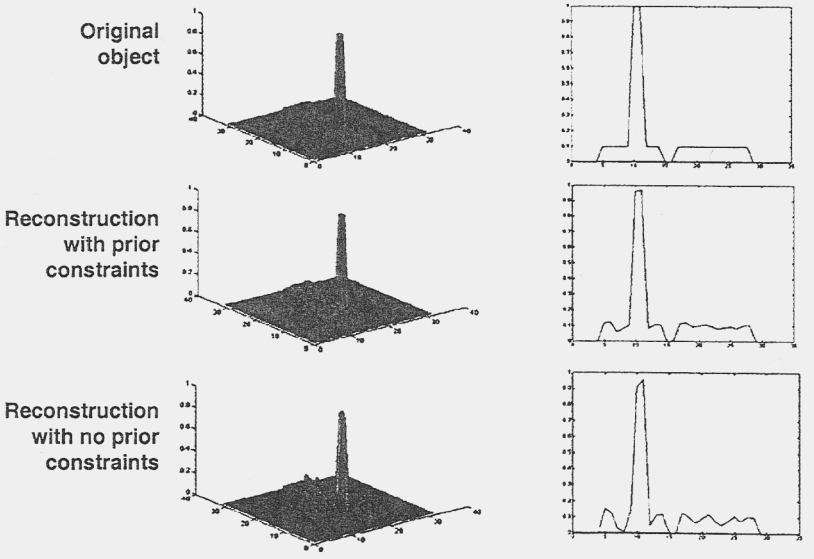

Pulsed photo-thermal tomography reconstructs 3-D absorption map of object from time-sequenced IR images of its surface heat following a laser pulse.

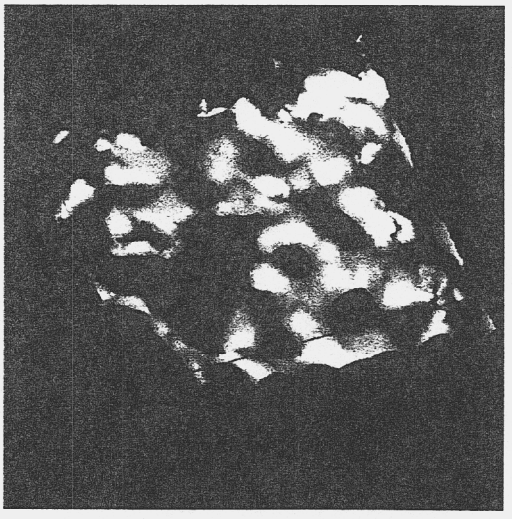

3-D reconstruction of in vivo port wine stain blood vessels of human subject.

Image dimension is 1.6 x 1.6 x .6 mm.

Blood vessels are ~ 100 microns in diameter

Can We Cure Osteoporosis?

J.H. Kinney, Dept. of Chemistry and Materials Science
Lawrence Livermore National Laboratory;
Division of Biomaterials, University of California, San Francisco

D.L. Haupt, Center for Nondestructive Evaluation
Lawrence Livermore National Laboratory

Osteoporosis is a serious public health problem. It is known that fracture risk is strongly correlated with the loss of bone mass at menopause, so current treatments are targeted at bone mass maintenance. Estrogen replacement therapy and anti–resorptive bisphosphonates are the first line treatments for preventing bone loss. None of these treatments, however, are anabolic–that is, they do not restore bone mass or strength to premenopausal levels.

By taking advantage of the high intensity, collimation, and monochromaticity of synchrotron radiation, we have been able to image the three–dimensional trabecular bone structure in living rats, thus providing serial data on the earliest architectural changes that occur with estrogen loss.

Results from these in vivo animal experiments demonstrated that one of the earliest manifestations of estrogen loss, in addition to a decrease in the amount of trabecular bone, was decreased connectivity.

We hypothesized that estrogen, if administered in a cyclic manner, could increase the thickness of the remaining trabecular bone by suppressing osteoclast (bone resorbing) activity while stimulating osteoblast (bone forming) activity. Our experiments demonstrated that estrogen replacement therapy, when initiated in this cyclic manner, restored bone mass to baseline levels but did not recover the trabecular connectivity. Even without an associated recovery in trabecular connectivity, finite element calculations on the three–dimensional images suggested that cyclic estrogen can recover the original structural modulus of elasticity. We believe the recovery of the elastic properties is due to an increase in trabecular thickness above baseline values. This is the first demonstration of an anabolic behavior of estrogen replacement, and points the way to new treatments to restore lost bone mass, either with estrogen or the new class of selective estrogen receptor modulators.

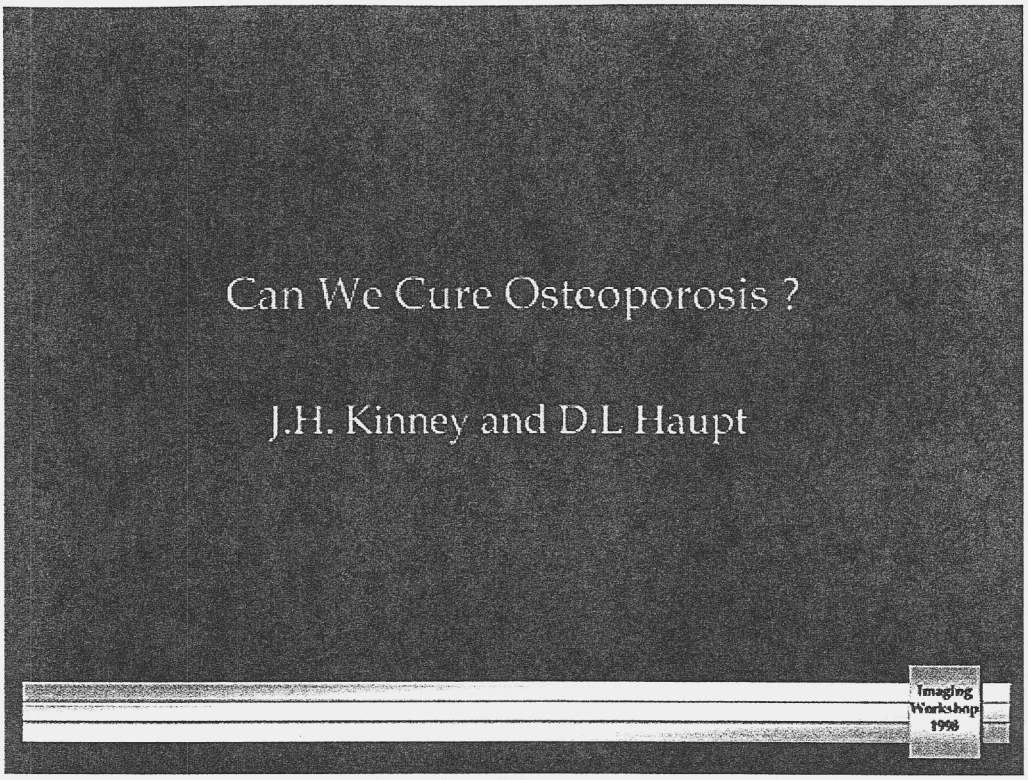
Can We Cure Osteoporosis ?
J.H. Kinney and D.L Haupt
Imaging Workshop 1998

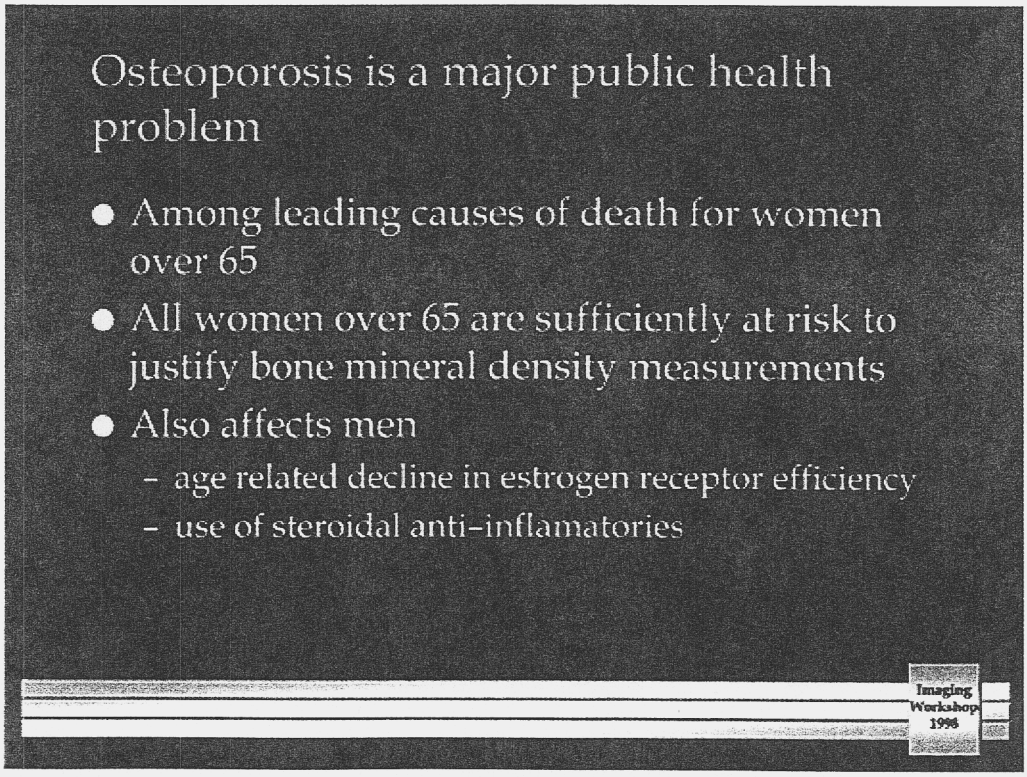
Osteoporosis is a major public health problem
Among leading causes of death for women over 65
All women over 65 are sufficiently at risk to justify bone mineral density measurements
Also affects men
- age related decline in estrogen receptor efficiency
- use of steroidal anti-inflamatories
Imaging Workshop 1998

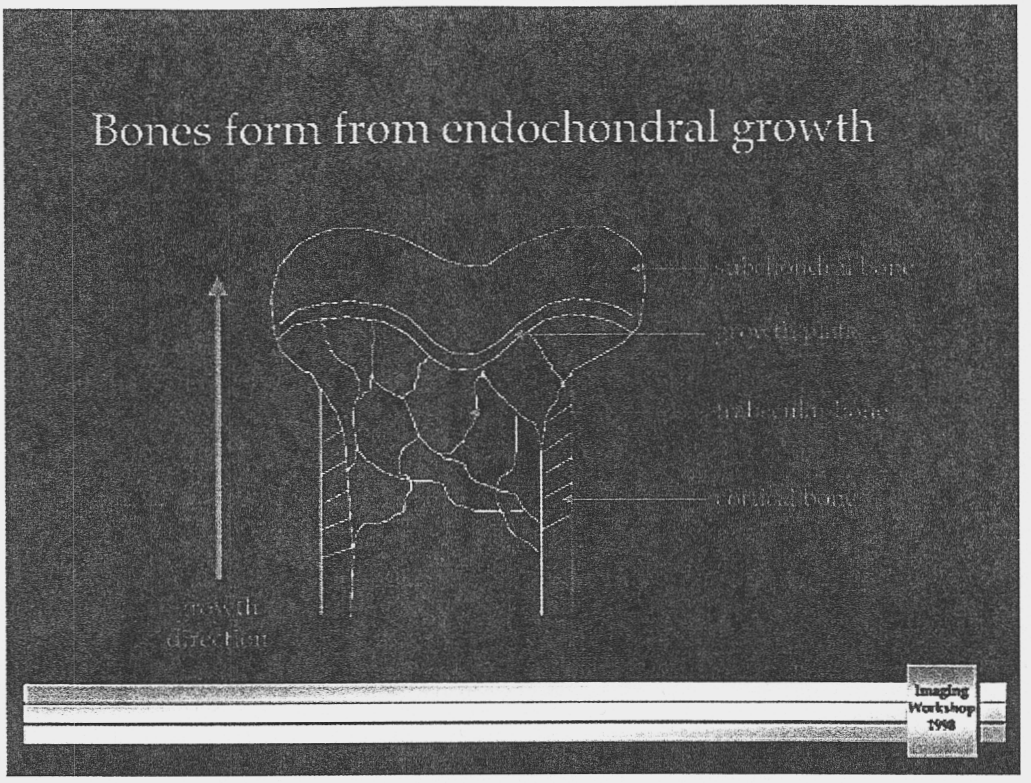
Bones form from endochondral growth
growth direction
Imaging Workshop 1998

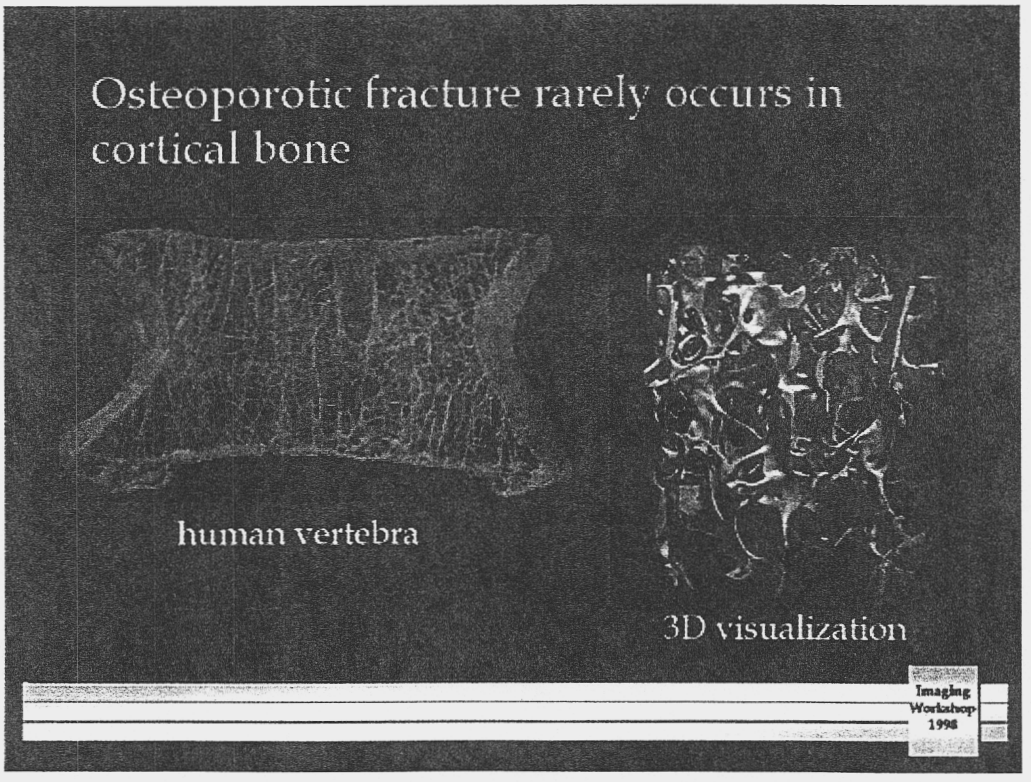
Osteoporotic fracture rarely occurs in cortical bone
human vertebra
3D visualization
Imaging Workshop 1998

Femoral neck is also largely composed of trabecular bone

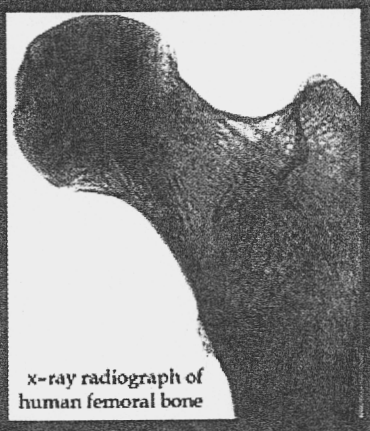

x-ray radiograph of human femoral bone

Imaging Workshop 1998

Understanding bone structure/properties is complicated by remodeling

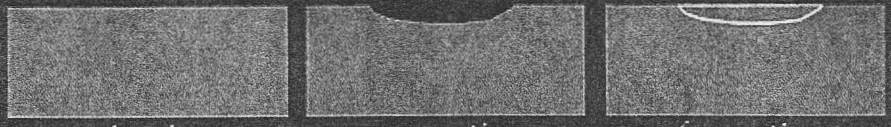

activation resorption formation

In healthy bone, remodeling is controlled by the need to : 1) maintain mineral balance, 2) repair tissue damage, and 3) respond to mechanical usage. Trabecular bone does not follow simple scaling laws of regular cellular structures, nor the typical scaling laws of random networks.

Imaging Workshop 1998

What happens at menopause?

- activation of remodeling increases
- bone formation is inhibited
- net loss of bone
- strength decreases with loss of bone mass

present treatments for osteoporosis attempt to suppress activation: estrogen, anti-resorptives, calcitonin.

Imaging Workshop 1998

How can imaging science help cure osteoporosis?

- In vivo imaging
  - provides structural information
  - provides mineral density information
- large scale finite element modeling
  - images can be used to compute fracture risk

Imaging Workshop 1998

CT imaging provides 3D structural information

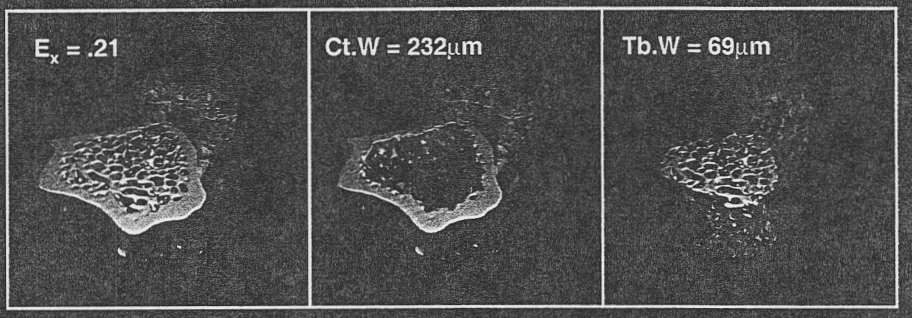

3D CT images provide structural information such as trabecular bone volume, cortical/trabecular width, and connectivity. With finite–element method, the strength of the structure can also be determined.

Imaging Workshop 1998

Monochromatic synchrotron radiation enables compositional analysis to be performed in vivo

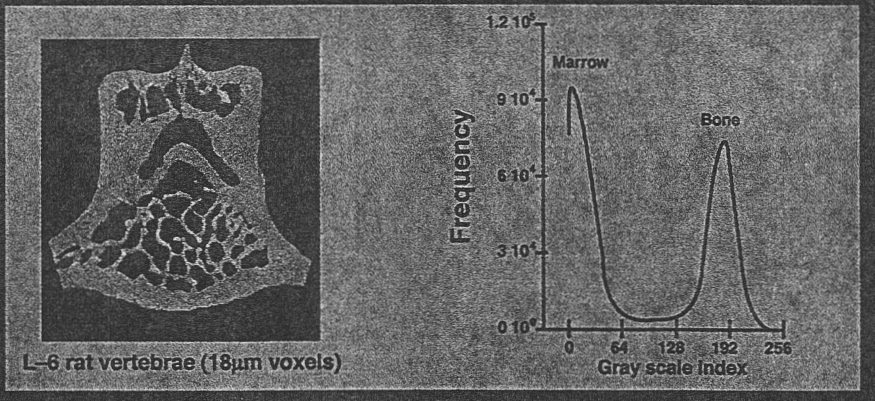

L–6 rat vertebrae (18μm voxels)

Imaging Workshop 1998

Mineral density distribution can be easily determined from the images

With monochromatic radiation, the concentration of mineral can be simply related to the gray scale value of the image:

$$V_i = \frac{a(GSI) - c}{m - c}$$

$$m - \rho_m \mu_m \quad c = \rho_0 \mu_0$$

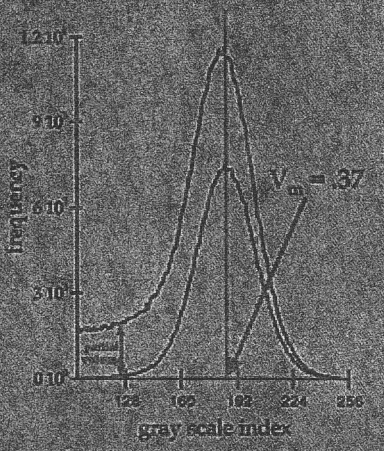

Imaging Workshop 1998

In vivo characterization of trabecular bone

anesthetized

Imaging Workshop 1998

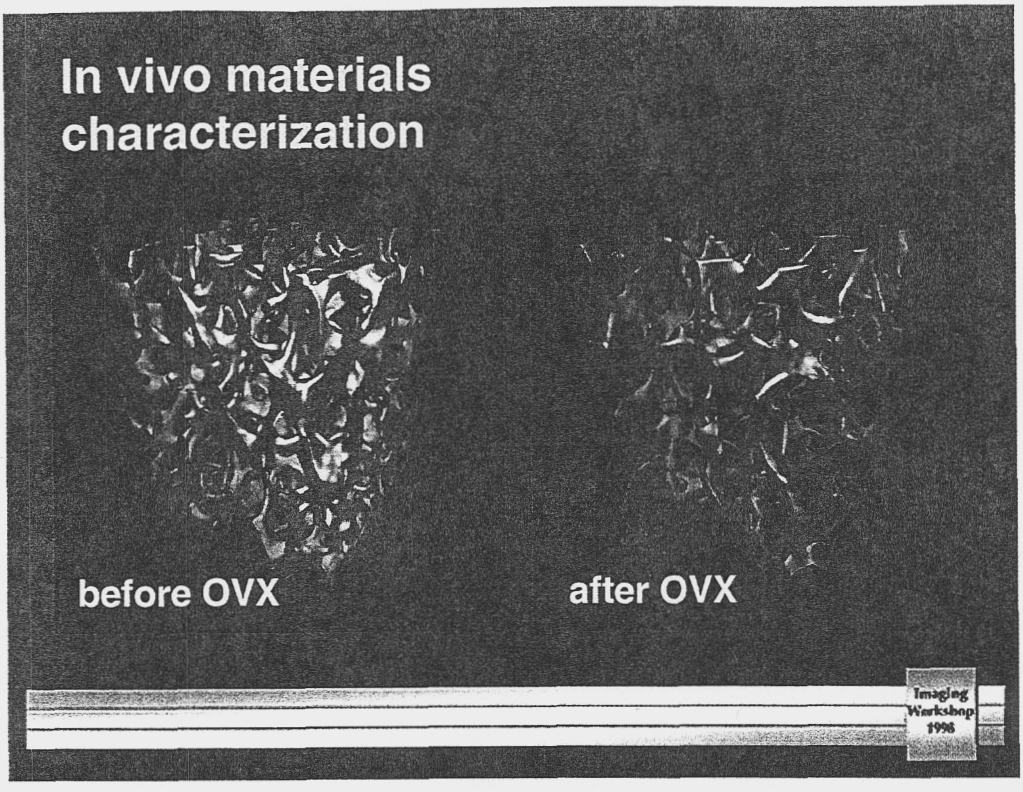
In vivo materials characterization
before OVX
after OVX
Imaging Workshop 1998

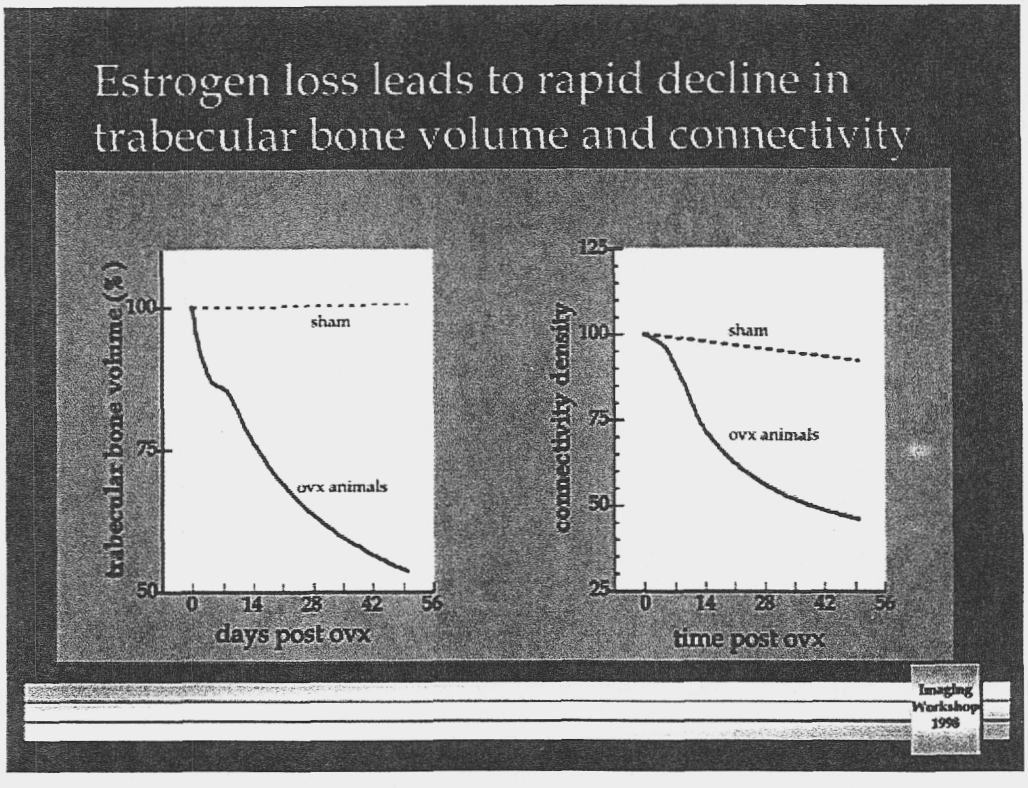
Estrogen loss leads to rapid decline in trabecular bone volume and connectivity
trabecular bone volume (%)
100
75
50
sham
ovx animals
0
14
28
42
56
days post ovx
connectivity density
125
100
75
50
25
sham
ovx animals
0
14
28
42
56
time post ovx
Imaging Workshop 1998

Element by element meshing

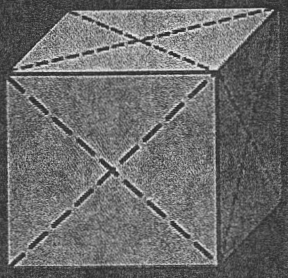

image voxel

$$H = \sum_i \frac{p_i^2}{2m} + \frac{K}{2}\sum_{i>j} g_{ij}\left[(u_i - u_j)\cdot \hat{x}_{ij}\right]^2$$

$$F = -K\sum_{n=1}^{b} g_n\left[(u - u_n)\cdot \hat{x}_n\right]\hat{x}_n$$

assume that on 1 μm scale, material is isotropic, and that architecture dominates material behavior

Imaging Workshop 1998

FE modeling reproduces the elastic properties within experimental error

Numerous problems with testing bone:

- boundary conditions
- small specimen size
- non physiological

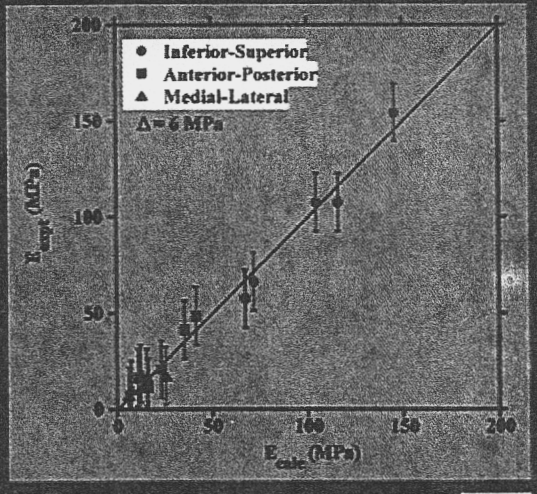

Imaging Workshop 1998

Hypothesis: cyclic administration of estrogen can reverse established OP

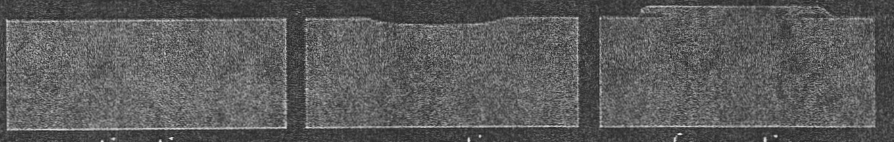

activation resorption formation

low estrogen levels increase active remodeling sites

elevated estrogen stops resporption, stimulates formation

net effect: increased trabecular bone volume

Imaging Workshop 1998

Mass is recovered, but connectivity is not

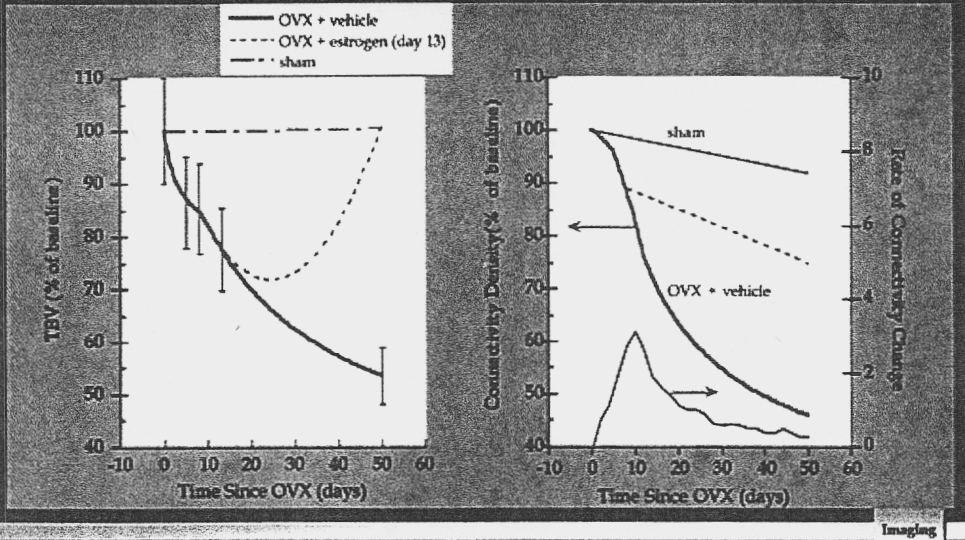

Imaging Workshop 1998

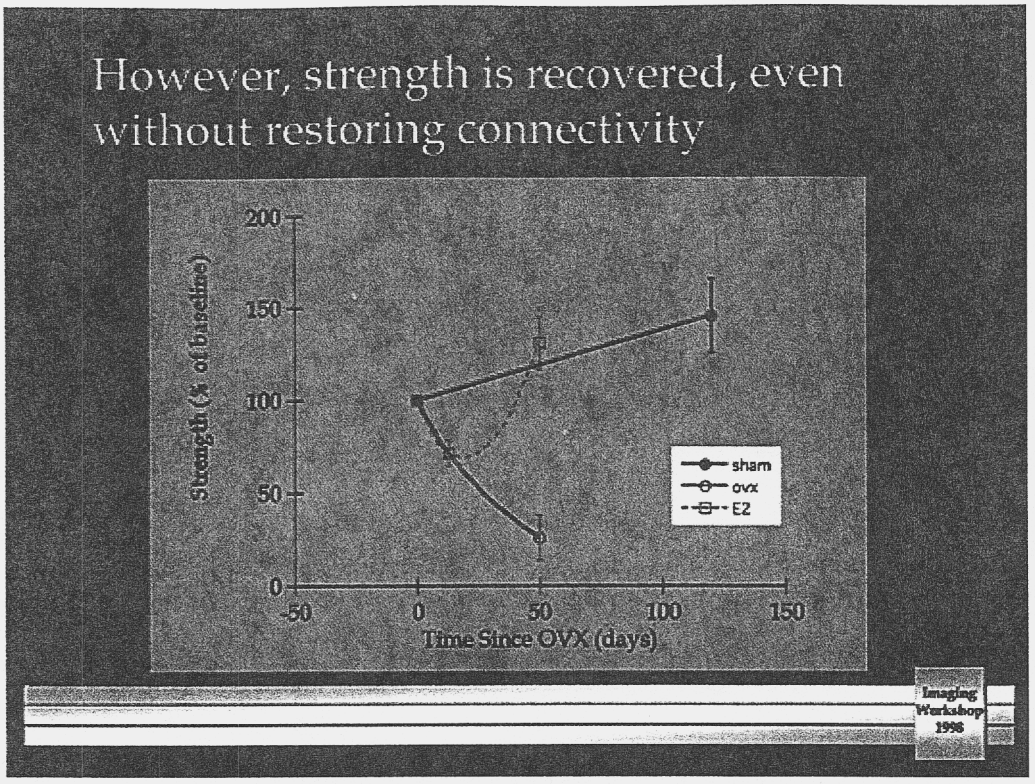
However, strength is recovered, even without restoring connectivity
Strength (% of baseline)
200
150
100
50
0
-50
0
50
100
150
Time Since OVX (days)
sham
ovx
E2
Imaging Workshop 1998

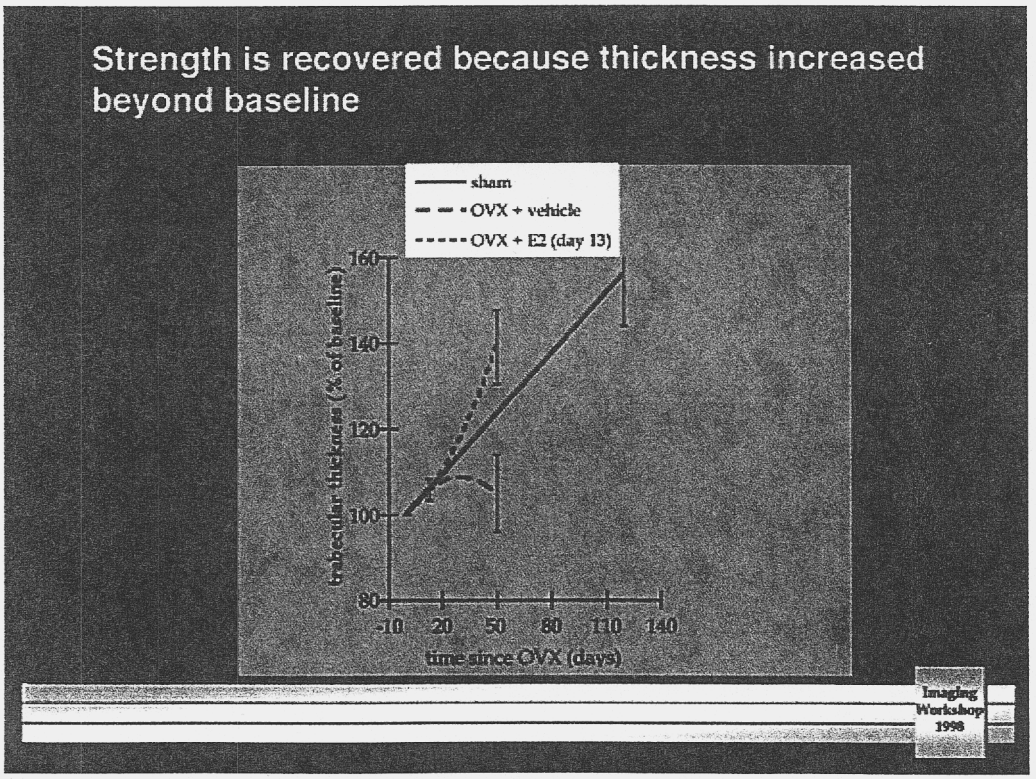
Strength is recovered because thickness increased beyond baseline
sham
OVX + vehicle
OVX + E2 (day 13)
trabecular thickness (% of baseline)
160
140
120
100
80
-10
20
50
80
110
140
time since OVX (days)
Imaging Workshop 1998

These are important results, suggesting potential monotherapies for treating established osteoporosis

- Estrogen replacement therapy:
- cyclic administration to build bone mass
- continuous administration to maintain
- Selective estrogen receptor modulators
- cyclic administration to build bone mass
- continuous administration to maintain

Imaging Workshop 1998

There are important implications for treating osteoporosis

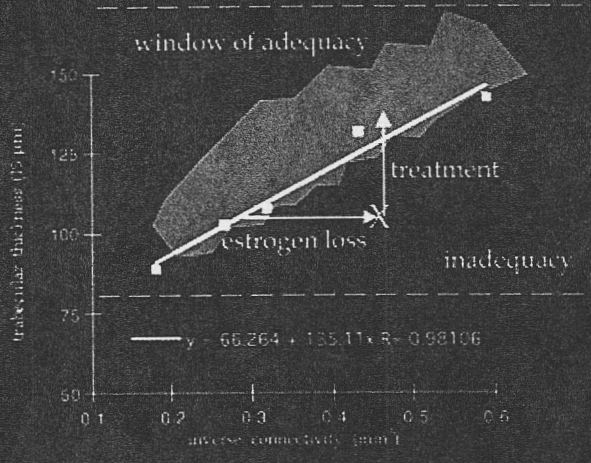

Imaging Workshop 1998

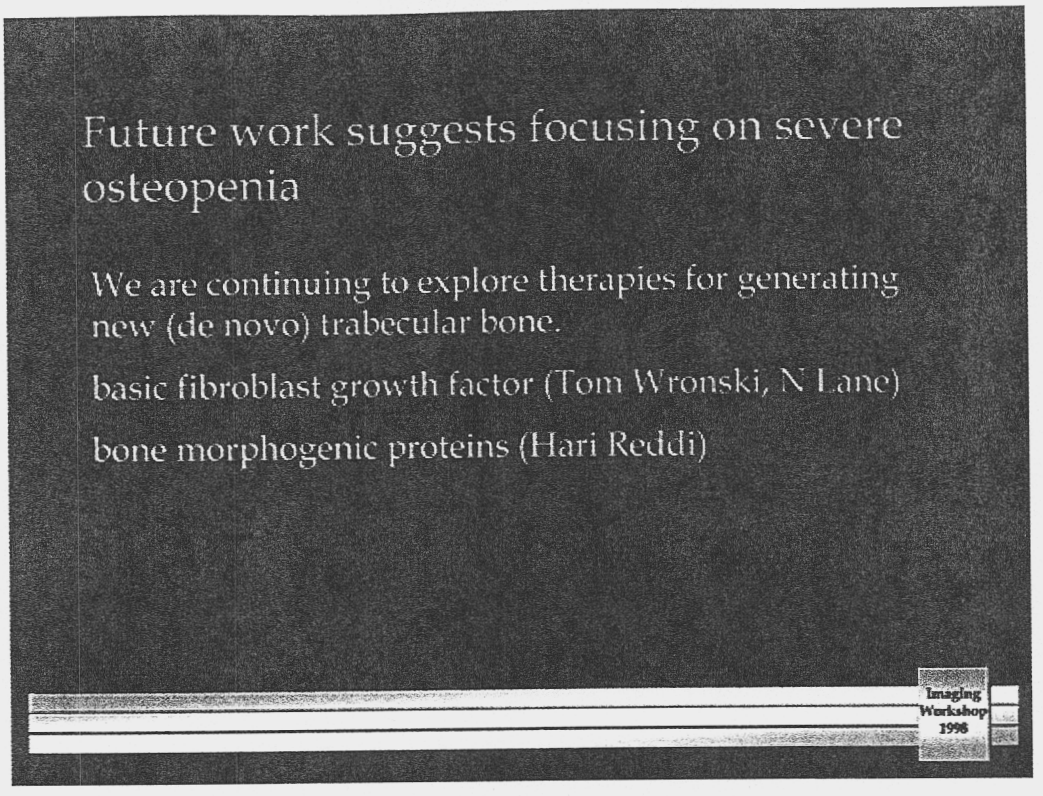
Future work suggests focusing on severe osteopenia
We are continuing to explore therapies for generating new (de novo) trabecular bone.
basic fibroblast growth factor (Tom Wronski, N Lane)
bone morphogenic proteins (Hari Reddi)
Imaging Workshop 1998

SPECTRAL PARTITIONING OF THE OBJECT FUNCTION IN DIFFRACTION TOMOGRAPHY

By Sean K. Lehman

Tomography is a method of producing (reconstructing) two-dimensional slices of the internal structures of a solid object such as the human body, a mechanical part, or the layered earth, by the observation and recording of the transmitted and/or reflected wave energy, either electromagnetic or acoustic, impinging on those structures. We distinguish between projection tomography which is diffractionless, and diffraction tomography. In the former, the irradiating wavelengths are such that the fields pass through the structures without being scattered. The only effect the object under evaluation has on the waves is that of attenuation. In diffraction tomography the fields are both attenuated and scattered.

The scattering mechanism of diffraction tomography is described by the integral form of the Helmholtz equation. The goal of diffraction tomography is to invert this equation in order to reconstruct the object function from the measured scattered fields.

In performing this reconstruction, care must be taken in how the evanescent (non-propagating) fields are used. If not handled correctly, these information carrying fields will be considered noise terms and this will reduce the quality and resolution of the reconstruction.

The object spectrum can be partitioned into resolvable and non-resolvable parts based upon the cutoff between the propagating and evanescent fields. We present near-field data showing how much of the measured scattered field consists of evanescent energy (energy which most current reconstruction techniques consider noise), and how non-resolvable object spectral information is converted to the propagating part of the field spectrum which can be used for reconstructions.

This work was performed under the auspices of the Department of Energy by the Lawrence Livermore National Laboratory under contract W-7405-Eng-48.

UCRL-JC-132314 Abs

Spectral Partitioning of the Object Function in Diffraction Tomography

Sean K. Lehman

CASIS Workshop

November 12, 1998

Introduction

- Definition of forward problem
- Projection vs diffraction tomography
- Operator development of diffraction tomography*
- Importance of evanescent information
- Partitioning of terms
- Partitioning of Helmhotz Equation
- Examples
- Conclusion

*Part of Ph.D. thesis, "Superresolution of Buried Objects in Layered Media by Near-Field Electromagnetic Imaging," at U.C. Davis, Dept. of Applied Science

Definition of Problem

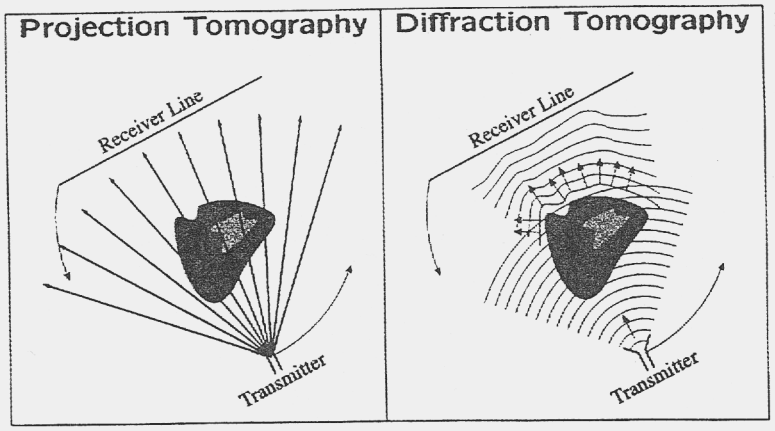

Projection vs Diffraction Tomography — I

Both Projection and Diffraction tomography fall under the category of Computed Tomography

Projection Tomography	Diffraction tomography
– Geometrical optics	– Physical optics
– Time delay & attenuation	– Phase & amplitude
– Diffractionless	– Diffraction
– Reconstruction through *Backprojection*	– Reconstruction through *Backpropagation*

Projection vs Diffraction Tomography — II

Governing Equations

Projection Tomography

$$P_\theta(l, z_0, \omega) \;=\; U^i(\omega) \int d\mathbf{r}\; o(\mathbf{r}, \omega)\; ds(\mathbf{r}, l)$$

Diffraction tomography (Integral form of Helmholtz equation)

$$\mathbf{E}_{scat}(\mathbf{r}_\perp, z_0, \omega) \;=$$
$$k_0^2(\omega) \int d\mathbf{r}'_\perp \int dz'\; \overleftrightarrow{\mathbf{G}}\,(\mathbf{r}_\perp - \mathbf{r}'_\perp, z_0 - z', \omega) \cdot \mathbf{E}(\mathbf{r}'_\perp, z', \omega)\; o(\mathbf{r}'_\perp, z', \omega)$$

Operator Development of Forward Problem

In operator notation, the Helmholtz equation can be expressed as:

$$\mathbf{E}_{scat}(\mathbf{r}_\perp, z_0, \omega) \;=\; \mathcal{G}(\mathbf{r}_\perp, z, \omega) * [\mathbf{E}(\mathbf{r}_\perp, z, \omega)\; o(\mathbf{r}_\perp, z, \omega)]$$

$$\mathbf{E}_{scat} \;=\; \mathcal{G} * [\mathbf{E}\; o]$$

Computing a planar Fourier transform w.r.t. $\mathbf{r}_\perp$:

$$\tilde{\mathbf{E}}_{scat} \;=\; \tilde{\mathcal{G}}\left[\tilde{\mathbf{E}} * \tilde{O}\right]$$

Partitioning of the Field Spectra

The spectrum of the wave operator, $\tilde{\mathcal{G}}$, and the spectra of the fields, $\tilde{\mathbf{E}}_{scat}$ and $\tilde{\mathbf{E}}$, are naturally partitioned into *propagating* and *evanescent* parts depending upon the wavenumber cutoff:

$$k_0(\omega) = \frac{\omega}{c}$$

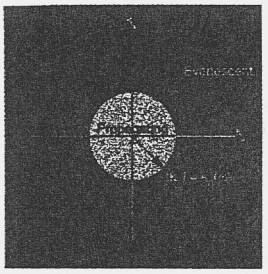

Imaging Sciences Workshop Thursday 11/12/98

Page 7

Importance of Evanescent Region in the Near Field

- Carries higher object spatial frequency information:
- Object spectrum is "smeared" across the propagating and evanescent regions via the convolution, even in the far field:
- Reconstruction schemes that take this into account will achieve superresolution and feature enhancements.

Imaging Sciences Workshop Thursday 11/12/98

Page 8

Partitioning of the Field Spectra — II

We express the wave operator and field spectra terms as:

$$\begin{aligned} \tilde{\mathcal{G}} &= \tilde{\mathcal{G}}_{<} + \tilde{\mathcal{G}}_{>} \\ \tilde{\mathbf{E}}_{scat} &= \tilde{\mathbf{E}}_{scat<} + \tilde{\mathbf{E}}_{scat>} \\ \tilde{\mathbf{E}} &= \tilde{\mathbf{E}}_{<} + \tilde{\mathbf{E}}_{>} \end{aligned}$$

where

$$\tilde{F}_{<}(\mathbf{k}_{\perp}, z, \omega) \equiv \left\{ \tilde{F}(\mathbf{k}_{\perp}, z, \omega) \;\middle|\; |\mathbf{k}_{\perp}| \leq k_0(\omega) \right\}$$

$$\tilde{F}_{>}(\mathbf{k}_{\perp}, z, \omega) \equiv \left\{ \tilde{F}(\mathbf{k}_{\perp}, z, \omega) \;\middle|\; |\mathbf{k}_{\perp}| > k_0(\omega) \right\}$$

Note: For any field term $\lim_{z \to \infty} \tilde{F}_{>} = 0$

Partitioning of the Object Spectrum

The object, however, not being a field, does not have propagating and evanescent parts. It does have *resolvable* and *non-resolvable* parts depending upon the wavenumber cutoff of the field measurement system.

Thus we write:

$$\tilde{O} = \underbrace{\tilde{O}_{\leq}}_{\text{resolvable}} + \underbrace{\tilde{O}_{>}}_{\text{non-resolvable}}$$

Partitioning of the Helmholz Equation

Combining the partitioned terms, the Helmholtz equation,

$$\tilde{\mathbf{E}}_{scat} = \tilde{\mathcal{G}}\left[\tilde{\mathbf{E}} * \tilde{O}\right]$$

becomes:

$$\tilde{\mathbf{E}}_{scat<} + \tilde{\mathbf{E}}_{scat>} = \left(\tilde{\mathcal{G}}_{<} + \tilde{\mathcal{G}}_{>}\right)\left[\left(\tilde{\mathbf{E}}_{<} + \tilde{\mathbf{E}}_{>}\right) * \left(\tilde{O}_{<} + \tilde{O}_{>}\right)\right]$$

Further partition this into *far field* and *near field* terms using the

$$\lim_{z\to\infty} \tilde{F}_{>} = 0$$

property of the field terms.

Partitioning of the Helmholz Equation — Far Field

Far Field $(z \to \infty)$

$$\tilde{\mathbf{E}}_{scat<} = \tilde{\mathcal{G}}_{<}\left[\tilde{\mathbf{E}}_{<} * \left(\tilde{O}_{<} + \tilde{O}_{>}\right)\right]$$

$$= \underbrace{\tilde{\mathcal{G}}_{<}\left[\tilde{\mathbf{E}}_{<} * \tilde{O}_{<}\right]}_{\text{current techniques}} + \underbrace{\tilde{\mathcal{G}}_{<}\left[\tilde{\mathbf{E}}_{<} * \tilde{O}_{>}\right]}_{\text{currently treated as noise}}$$

$$\tilde{\mathbf{E}}_{scat>} = 0$$

Partitioning of the Helmholz Equation — Near Field

Near Field

$$\tilde{\mathrm{E}}_{scat<} = \tilde{g}_{<}\left[\tilde{\mathrm{E}}_{<} * \left(\tilde{O}_{<} + \tilde{O}_{>}\right)\right] + \tilde{g}_{<}\left[\tilde{\mathrm{E}}_{>} * \left(\tilde{O}_{<} + \tilde{O}_{>}\right)\right]$$

$$\tilde{\mathrm{E}}_{scat>} = \underbrace{\tilde{g}_{>}\left[\tilde{\mathrm{E}}_{<} * \left(\tilde{O}_{<} + \tilde{O}_{>}\right)\right] + \tilde{g}_{>}\left[\tilde{\mathrm{E}}_{>} * \left(\tilde{O}_{<} + \tilde{O}_{>}\right)\right]}_{\text{currently ignored}}$$

Partitioning of the Helmholz Equation — Comments

- There are two physical effects occurring:
  - A "smearing" of object spectral information due to the convolution with the field;
  - A conversion between propagating and evanescent information via the wave operator.
- Reconstruction algorithms which take these effects into to account will result in imaging enhancements and superresolution.

Partitioning of the Helmholz Equation — Far Field

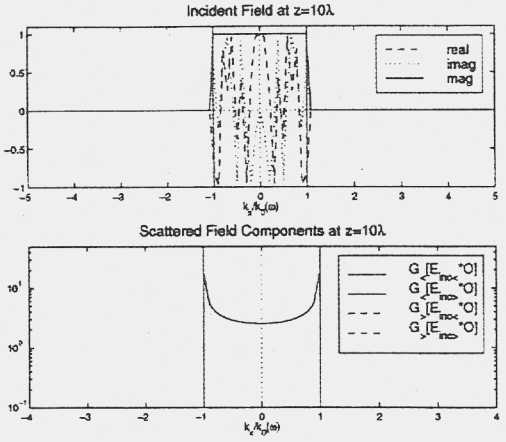

Partitioning of the Helmholz Equation — Near Field

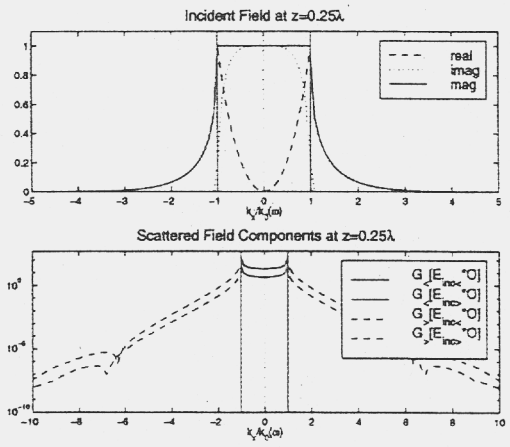

Partitioning of the Helmholz Equation — Far Field Details

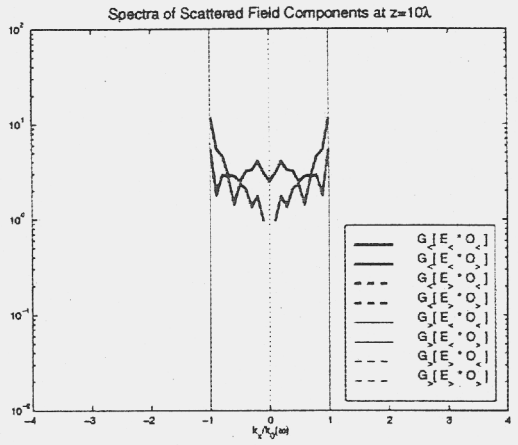

Partitioning of the Helmholz Equation — Near Field Details

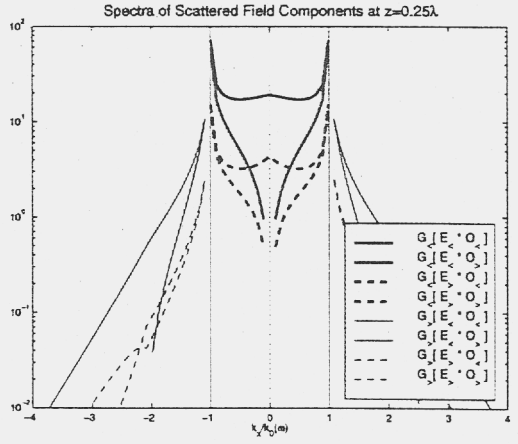

FDTD Mine Simulation

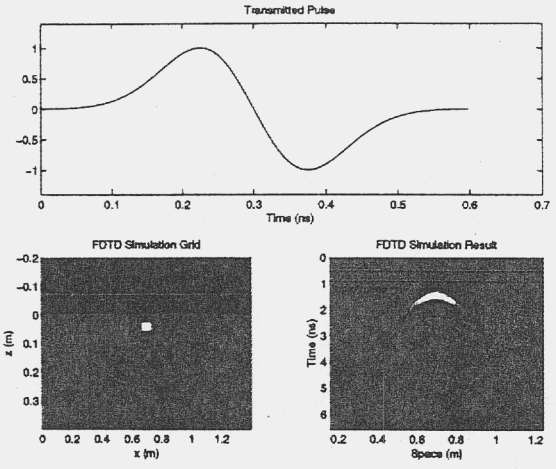

FDTD Mine Simulation

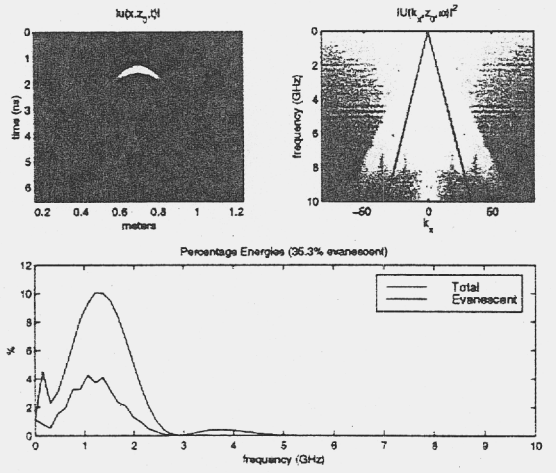

Real Mine Data

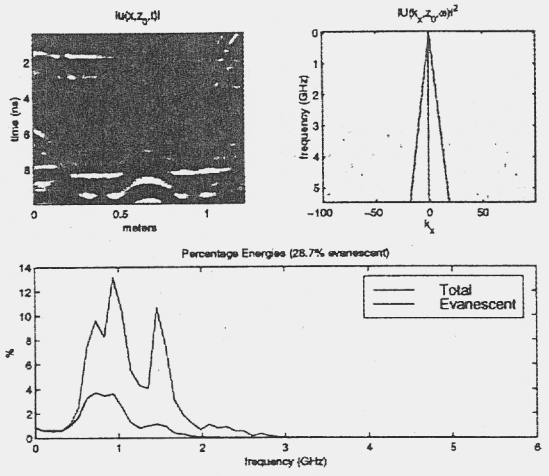

Conclusions

- Mine simulations show within the near field up to 30% of the measured energy is evanescent;
- The forward scattering operator shows there is a "smearing" of object spectral information across the measurement system's propagating and evanescent regions;
- Reconstruction schemes must take this into account. If not, object spectral information will be treated as noise and there will be a loss of detail and resolution.

Radar-Acoustic Applications

Introduction to Low Power Radars for Acoustic Applications: Speech and Object Characterization

John F. Holzrichter

The use of radar (and related propagating wave Electro Magnetic wave devices) for acoustic research and applications has not been well developed. LLNL's suite of low power radars, e.g., the MIRs, are making possible many applications where low power, portability, and low cost are dominant factors. They make possible accurate amplitude measurements, ranging from centimeters to micrometers, of moving mechanical elements. The measurements can be performed at meter distances from the antenna, and through surrounding dielectric media such as skin and water. Several such examples relating to human speech recognition and coding (Burnett), to speaker verification (Gable), to pitch determination (Ng), and to structural vibration detection and identification (Roberts) will be given in the accompany talks.

Radar-Acoustic Applications:
Speech Characterization and Object Identification

CASIS Signal and Imaging Sciences Workshop

Session on Radar/Acoustic Applications
John F. Holzrichter
LLNL

November 12, 1998

Two applications of EM Sensors and Acoustics are human speech and object characterization

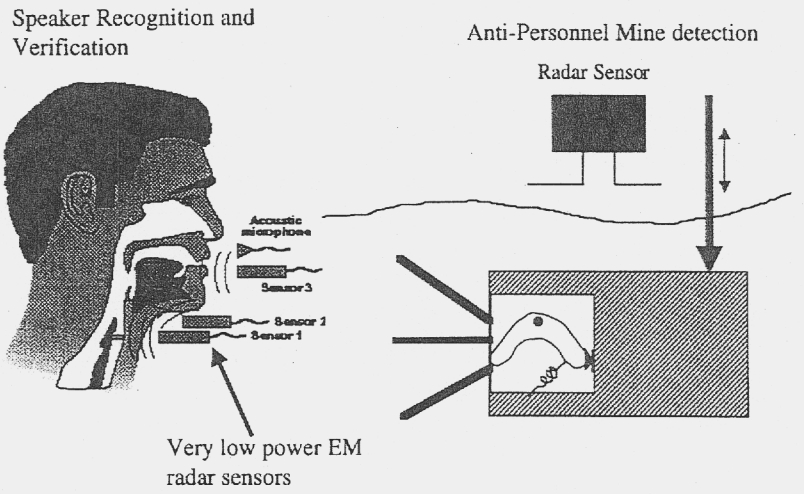

JFH:11/12/98:pt.2tlb

The Radar/Acoustic Session will include the following topics (see agenda for details)

- The use of micro-power homodyne radar to measure in real-time, an excitation function of human speech
  - Greg Burnett et al, LLNL, UCD/DAS
- Using excitation function information to obtain instant "pitch" of voiced speech and to enable "pole/zero" (e.g., ARMA) techniques to be used to estimate transfer functions
  - Lawrence Ng et al, LLNL/EE
- Using human vocal tract articulator information, obtained with micro-power EM radar sensors, to verify the identity of a speaker
  - Todd Gable et al, LLNL, UCD/DAS
- Using homodyne radar to measure the acoustic response of unknown objects (e.g., antipersonnel land mines) for purposes of identification
  - Roger Perry/Randy Roberts et al, LLNL/EE

JFH:11/12/98:pt.3tlb

We would like to thank many LLNL, UC and other researchers for their assistance and support

- Signal Processing:
  - Drs. Greg Clark, Farid Dowla and Jim Candy
  - Dr. Mark Duchaineau, LLNL/Comp. Dept.
- Micro-power EM Sensors:
  - Dr. Stephen Azevedo, Tom Rosenbury, Doug Poland, Bob Stever, Greg Dallum, Pat Welsh — MIR Group
  - Don Mullenhoff — NAI
- UC System Collaborations:
  - Dr. Rebecca Leonard, UCD Medical Center, Sacramento
  - Profs. R. Freeman and R. Vermuri — DAS
  - Prof. N. Luhmann, C. Domier and Mr. C. Liang — UCD/EE
- Dr. Wayne Lea (consultant)

JFH:11/12/98:pt.4tlb

The interpretation of EM Sensor information depends upon its use in near, intermediate or far field modes

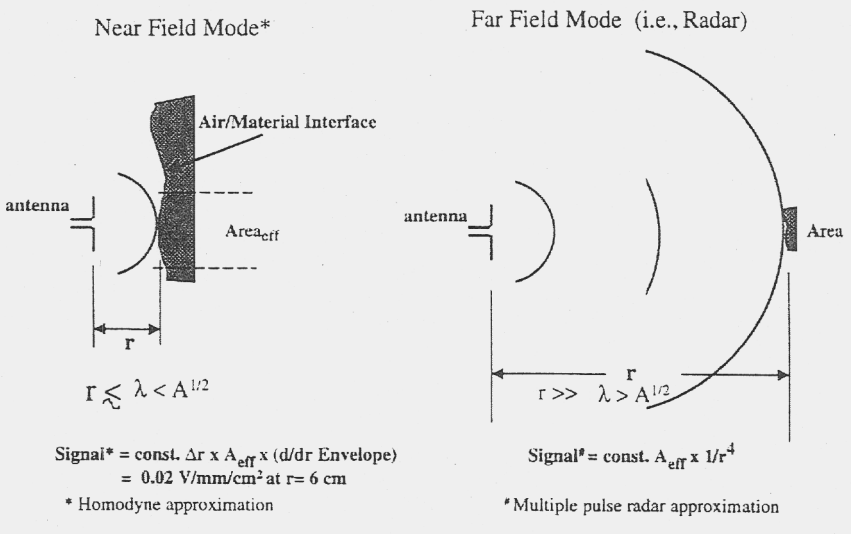

JFH:11/12/98:pt.5tlb

The human vocal tract has excitation source(s), E, followed by a sequence of tubes and resonators that can be described as H, using linear equations

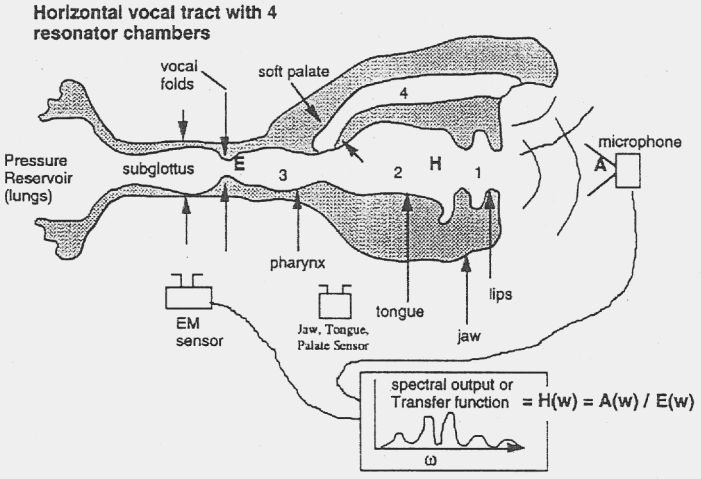

JFH:11/12/98:pt.6tlb

One or more miniature micropower EM sensors (reducible to one or two $2 chips) can be used

This image shows the present MIR sensor, which costs about $15 dollars in parts and about $200 to replicate (margin costs). Most sensors for speech are used in the homodyne "filed disturbance" mode.

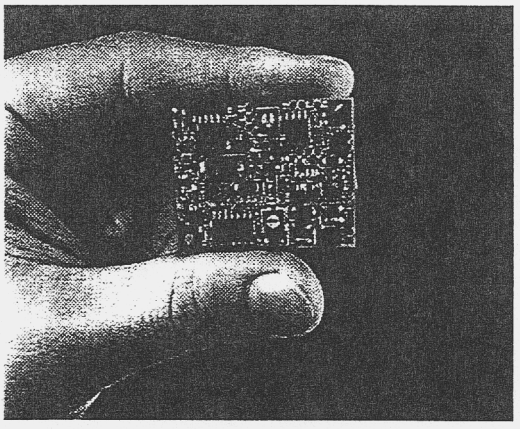

JFH:11/12/98:pt.7tlb

Audio and EM sensors measure several speech articulator motions simultaneously, e.g., "print"

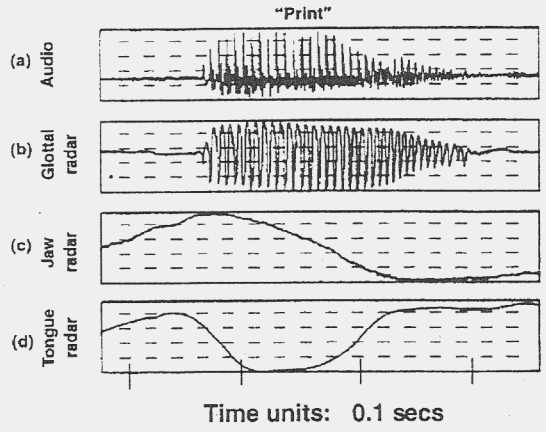

JFH:11/12/98:pt.8tlb

Why Radar and Acoustics?

- Probe structural motions under unusual conditions
  - Micron to centimeter amplitudes
  - At a distance - centimeters to kilometers (i.e., non-contact)
  - Extended area responses
  - High data rates
- New EM sensors may make possible new applications: e.g., speech recognition, speaker verification, object identification, etc.
  - Low cost (in principle)
  - Multiple modalities — impulse radar, field disturbance, homodyne, etc.
  - Human safe

JFH:11/12/98:pt.9tlb

MIR Measurements of Human Glottal Activity and An Estimation of a Voiced Speech Excitation Function

Gregory C. Burnett
Lawrence Livermore National Laboratory

Special purpose, homodyne-mode, micro-power EM sensors, called GEMS, enable the measurement of tissue motions associated with the opening and closing of the human glottis (i.e., the vocal fold opening). These are directly linked to the modulation of the vocal tract air flow as the vocal folds open and close. We show that the "ballooning" of subglottal tracheal tissue, as pressure increases and decreases, is the predominant contributor to the GEMS signal. These relatively simple measurements lead to accurate speech pitch determination, quality of vocal fold contact, individual specific tissue motion patterns, and a voiced speech excitation function.

Defining an Excitation Function of the Human Vocal Tract Using Glottal Electromagnetic Micropower Sensors (GEMS)

CASIS Signal and Imaging Sciences Workshop
November 12, 1998

Gregory C. Burnett

UC Davis/ LLNL DSED

What is the GEMS?

- Emits pulses of very low power (less that one-thousandth that of a cell phone) and short duration
- Center frequency is around 2 GHz, prf 2 MHz
- Uses homodyne detection method to sense the reflectivity of objects around it
- The change in that reflectivity is amplified to produce a signal approximating the velocity of the objects
- In essence an excellent motion and vibration detector

We want to determine what the GEMS is sensing and how that relates to the excitation function

Questions to answer:

- How does the GEMS sense motion?
- What is the physiological basis of the GEMS return?
- How can we relate the GEMS return to subglottal pressure?

Raw GEMS signal coming from neck

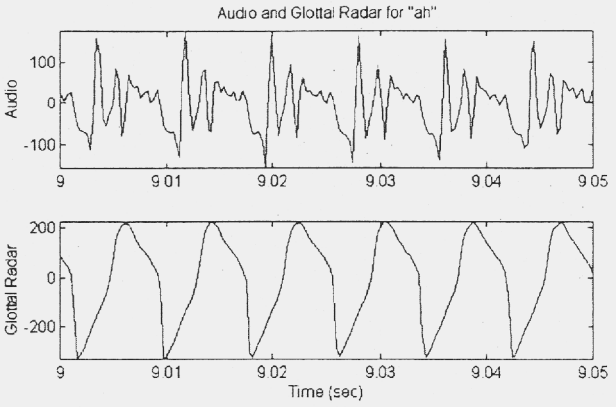

The GEMS has built-in analog filters in order to detect the frequencies of interest (70 - 7000 Hz)

- The filter response was measured by injecting sinusoidal signals into the receive antenna of the radar
- An anticasual filter in conjunction with allpass filters was used to compensate for the phase and magnitude distortion
- As the GEMS measures velocity, position may be derived by approximating the integral with a cumulative sum

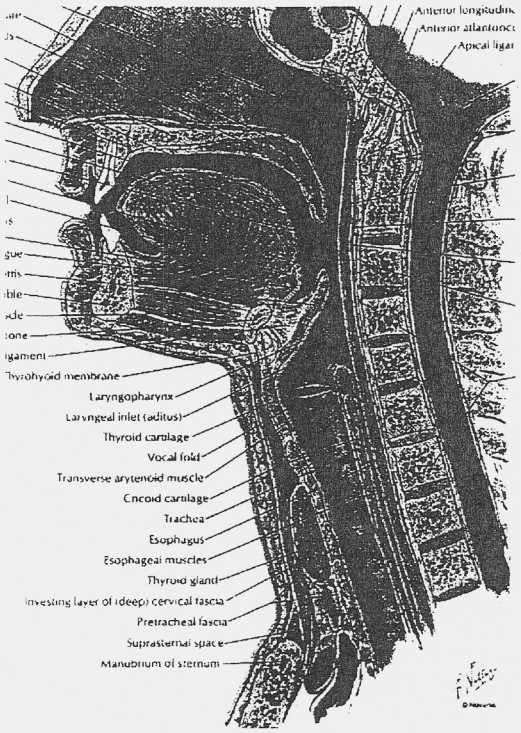

To derive the physiological basis, we must understand the anatomy of the glottal area

Copyright 1989. Novartis. Reprinted with permission from the *Atlas of Human Anatomy*, illustrated by Frank H. Netter, M.D. All rights reserved

A cross-sectional view of the trachea suggests the posterior wall would be a better reflector

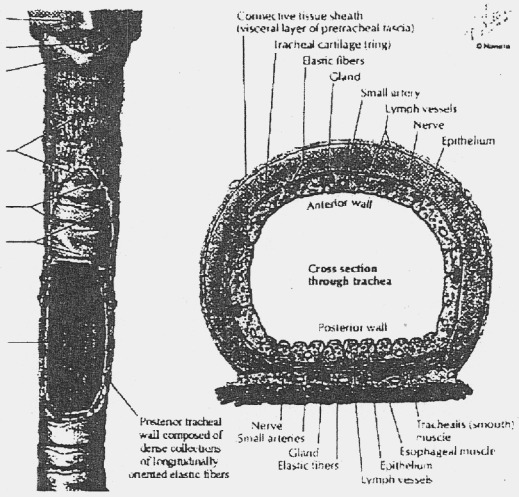

Copyright 1989. Novartis. Reprinted with permission from the *Atlas of Human Anatomy*, illustrated by Frank H. Netter, M.D. All rights reserved

Electromagnetic simulations using Jeff Kallman's TSARLITE indicate the trachea reflects far more energy than the max-open folds

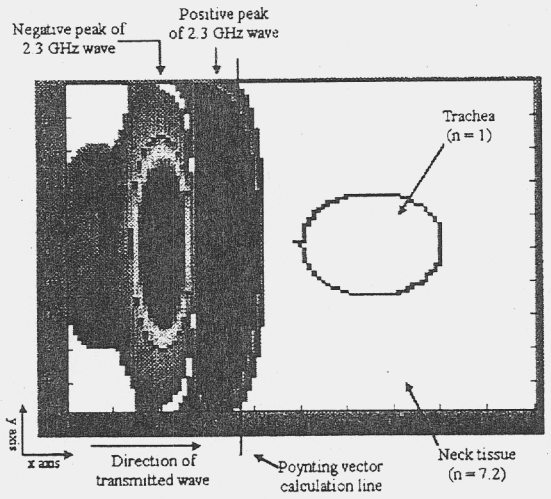

Trachea had a reflectivity of 15.2%, more than 18x the max-open fold reflectivity of 0.8% (close to the noise level of the simulation)

High speed (1000 - 3000 fps) video experiments indicated fold motion did not correlate well with GEMS signal

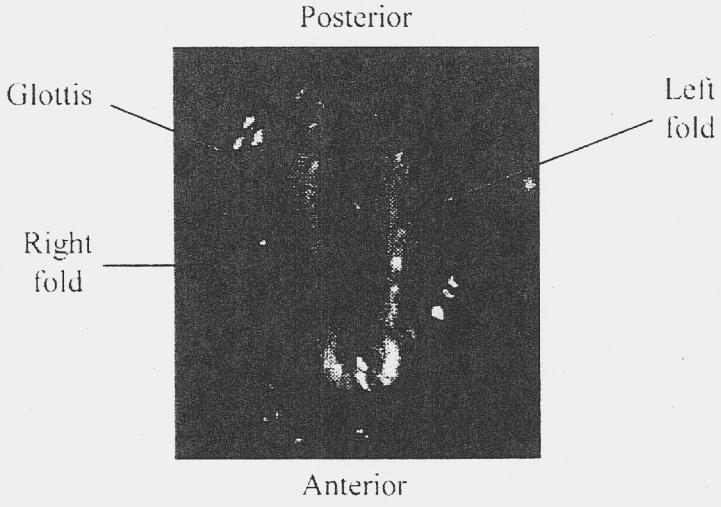

Quantifying the response of the GEMS to physical motion of a signal reflector

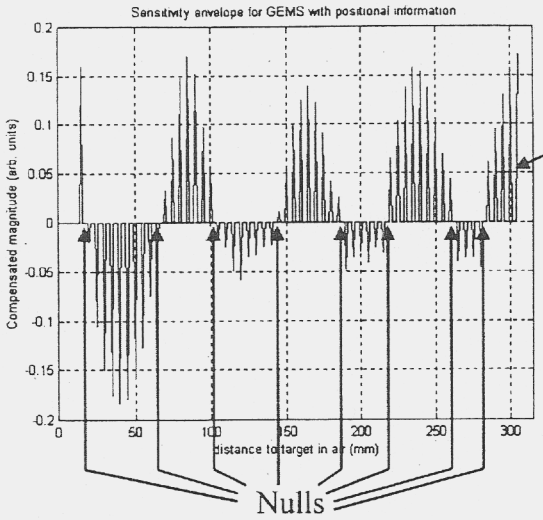

Sensitivity envelope calculated by comparing the inverse filtered and integrated radar signal to an accelerometer-derived position signal

Minimum amplitude detected @ 40 mm and 16 dB SNR was +-4.2 µm.

Nulls in GEM signal strength observed as GEMS is moved away from the glottis indicate the posterior wall is the basis for the reflection

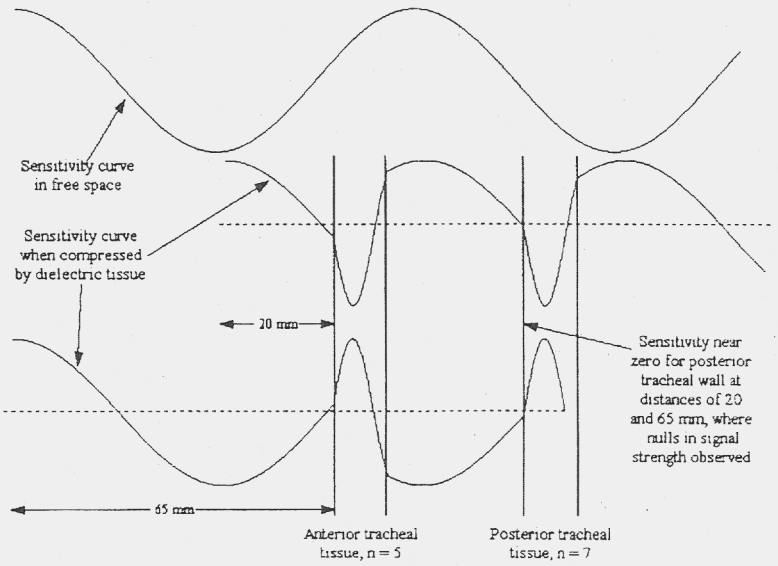

Conclusions about physiological basis of the GEMS return

- The object responsible for the detected vibration is the posterior tracheal wall
- Furthermore, we are detecting subglottal vibrations of the wall, as a phase change is observed when the GEMS is moved from its usual position to an area above the glottis
- Now, we must relate this tracheal motion to the driving subglottal pressure

A lumped-element circuit model is used to quantify the trachea's response to changing air pressure

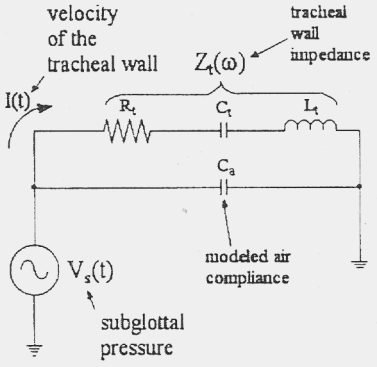

$$V_s(t) = I(t) \cdot Z(\omega)$$

Thus, the inverse filtered, integrated radar signal gives us an approximation to the subglottal pressure (and thus the excitation function) of the vocal tract

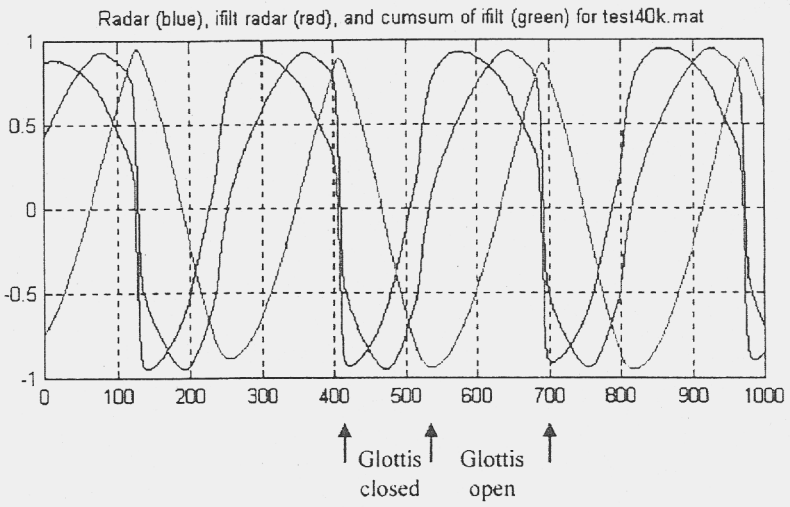

Many thanks to . . .

- John Holzrichter, Larry Ng and Todd Gable
- Roger Perry, Randy Roberts and Tom Woehrle
- Jeff Kallman and Melinda Bass
- Rebecca Leonard and Kathy Krandall of the UC Davis Medical Center
- Jong An

Accurate EM/Acoustic Pitch Estimation

Lawrence C. Ng
Lawrence Livermore National Laboratory

This talk will discuss a new time domain approach in real-time estimation of pitch information for human speech using the small Glottal Electromagnetic Micropower Sensors (GEMS) – a Micropower Impulse Radar (MIR) developed at LLNL specifically for speech applications. GEMS operate in the microwave regime of the EM spectrum at a radiated average power of less than 1 mW, and it uses a field-disturbance mode of reception in which signals are obtained only from moving tissue/air interfaces. The GEMS algorithm and its performance will be discussed in comparison to conventional pitch estimation algorithms. In particular, this talk will show that GEMS algorithm outperforms existing algorithms by a factor of 100 in computational speed and a factor of 20 in accuracy. This paper will also show the inherent advantage that accurate pitch estimation leads to a new improved method of pitch synchronized speech processing.

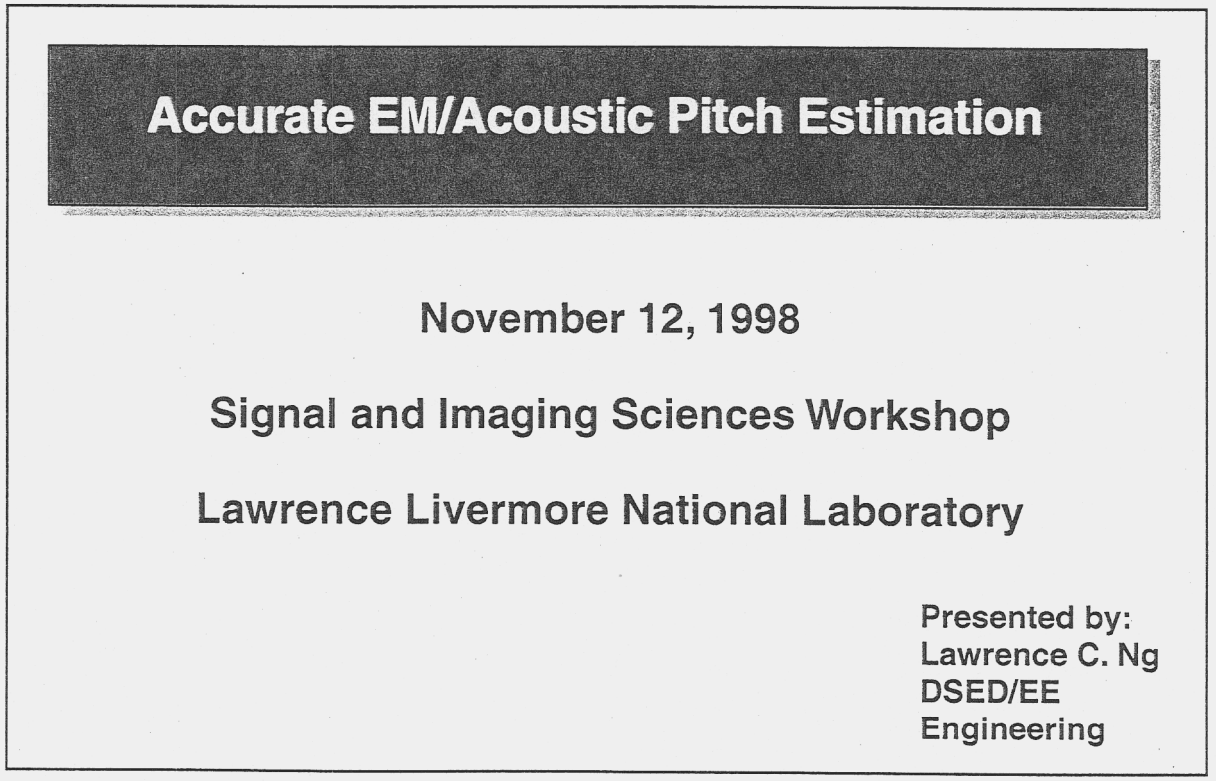

Glottal EM Sensors (GEMS) Tissue Measurements Show Strong Correlation with Vocal-Fold Electroglottalgraphy (EGG) Signal

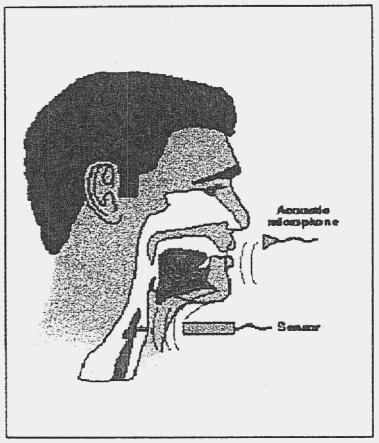

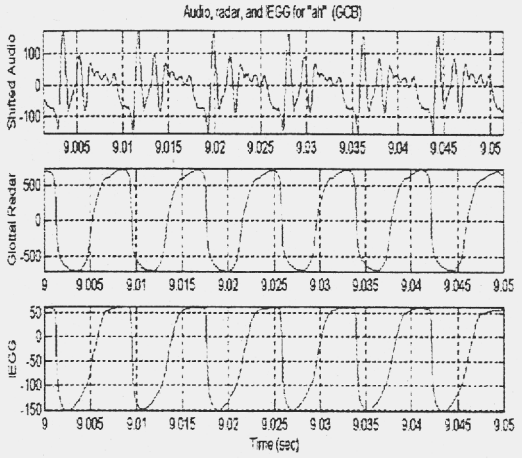

Traditional Pitch Estimation Approaches Using Acoustic Signal

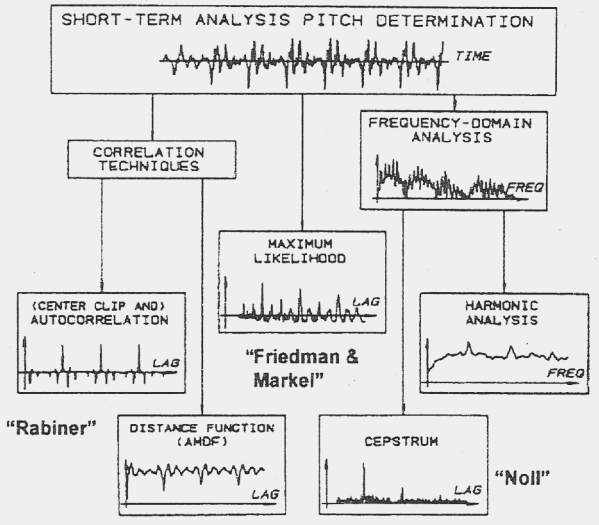

Traditional Error Rate of Pitch Estimation is 1% (for the Best Case) and Degrades Rapidly in Noise

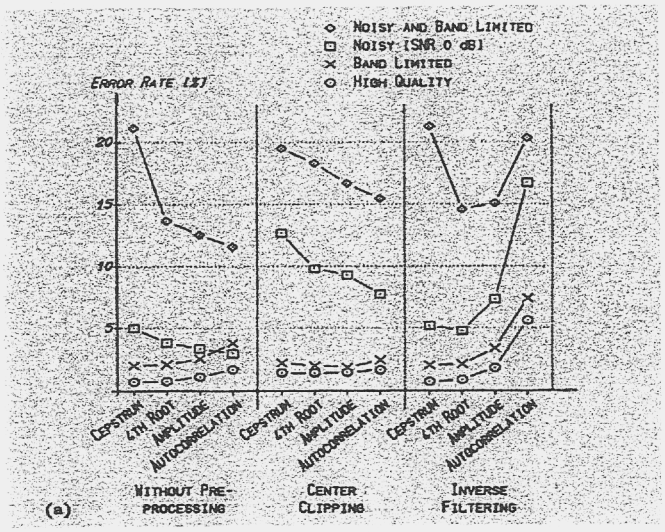

Taken from "Advances in Speech Processing," Furui and Sondhi, Merkker 92

The Em Sensor Yield and Accurate, Robust, Single Glottal Period Pitch Estimate and Speech Onset

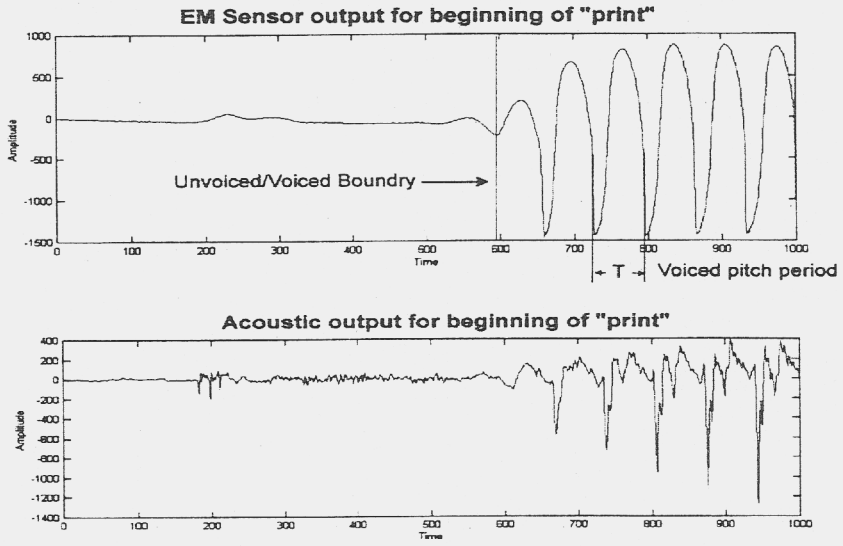

The Zero-Crossing Pitch Algorithm is a Simple, Fast, and Accurate Time Domain Calculation

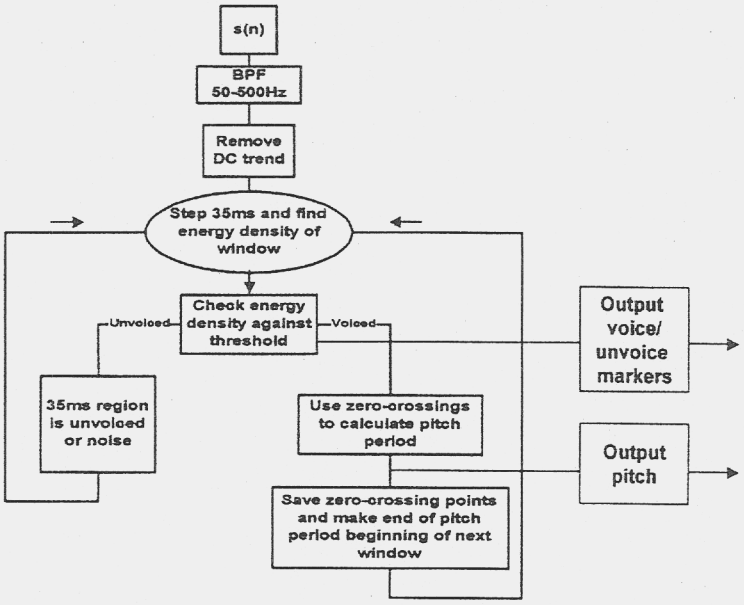

Traditional Cepstral and Autocorrelation Techniques were Used as a Basis for Comparison

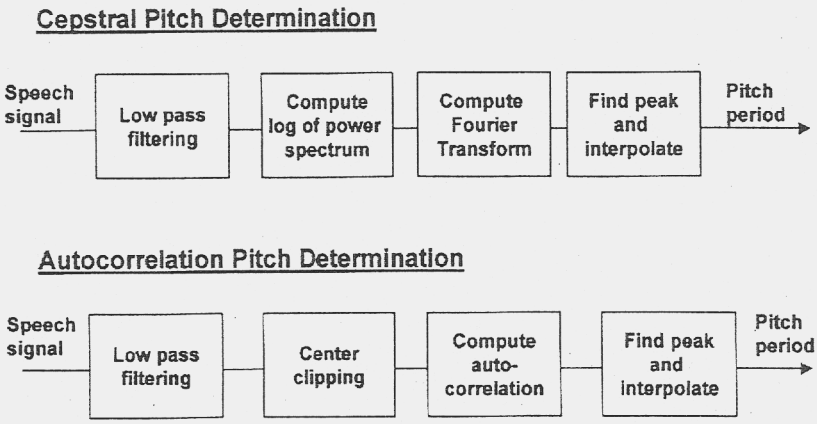

Example of Pitch Estimation Using Correlation and Cepstral Techniques

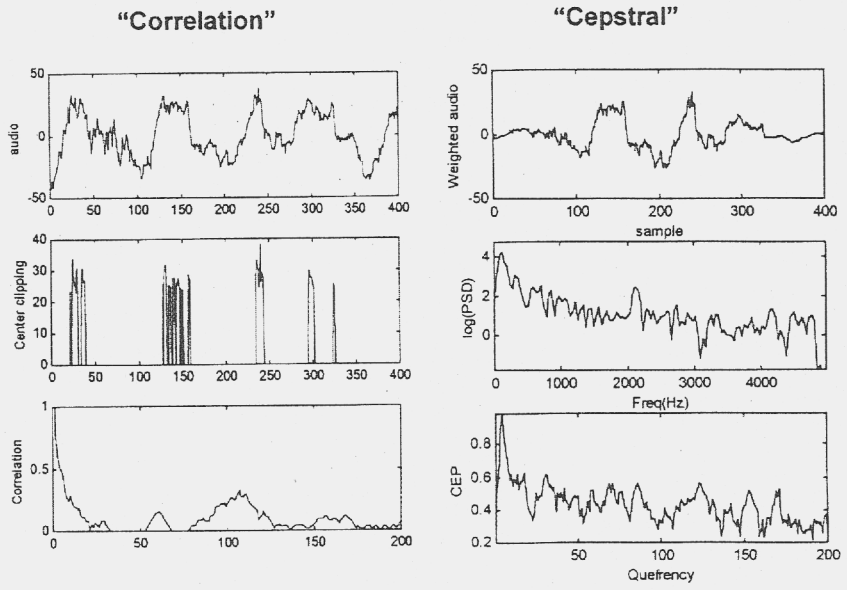

The EM Sensor Gives Better Pitch Estimates Than the Traditional Cepstral Method

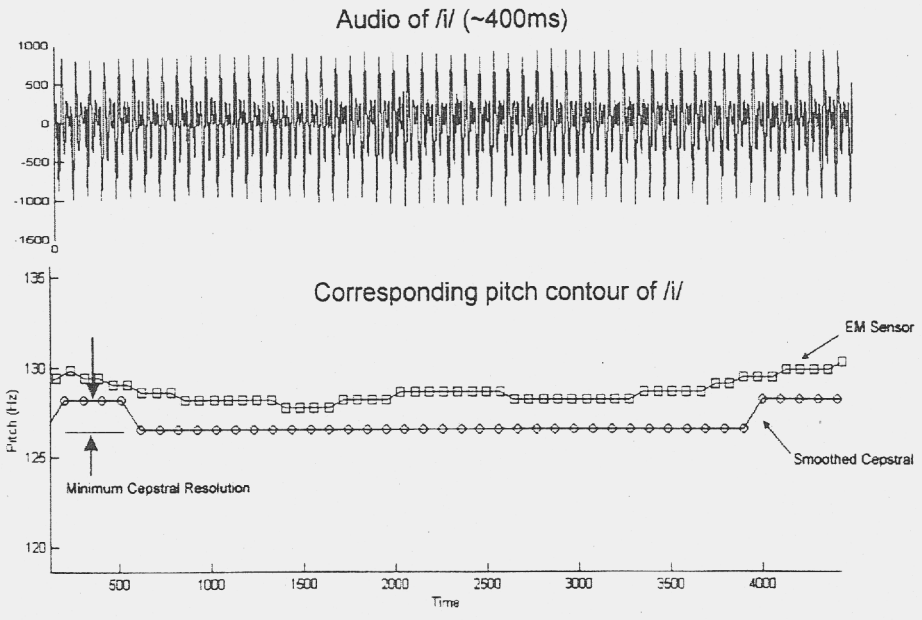

The EM Sensor Yields Smoother, More Accurate Pitch Contours Relative to Traditional Methods

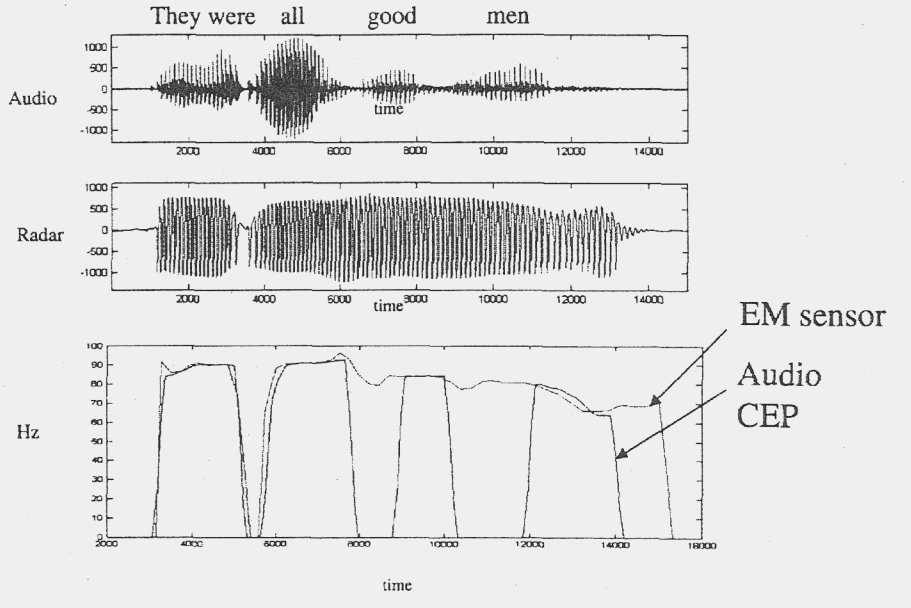

Simulations With Synthetic Signals Confirm the Accuracy of Our Zero-Crossing Pitch Algorithm

Pick f_k at random to four decimal places

Synthetic signal $s(t) = \sum_{N=1}^{20} \frac{1}{N} \sin(2\pi N f_k t)$

Relative Pitch Error

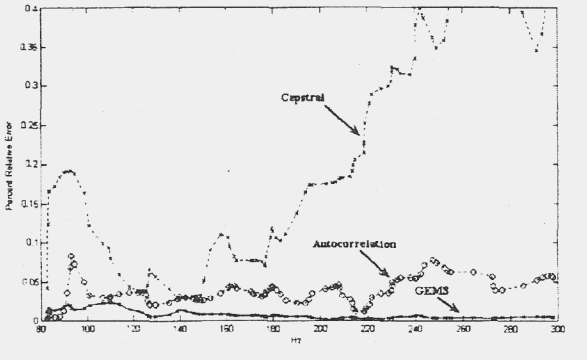

From Tuning Fork Experiments We Determine Pitch Estimate Performance of GEMS

- Generate known signals from tuning fork experiments
  - Compute pitch estimate using cepstral, autocorr, and GEMS zero-crossing
- Results indicated that GEMS pitch estimate is:
  - 100 times faster in computational efficiency
  - 5 to 20 times smaller in error rates
- Conclusions
  - GEMS is insensitive to acoustic noise
  - Fast computation of pitch can provide real-time pitch synchronous speech processing
  - Performance improve with higher sampling rate

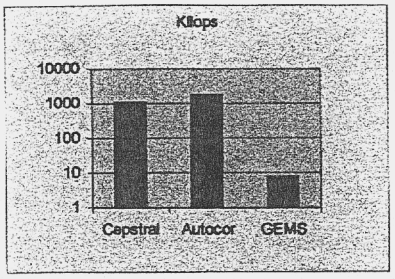

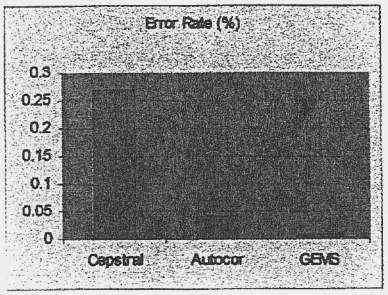

Using a Synthetic Transfer Function We Validated the Improved Accuracy of ARMA Modeling

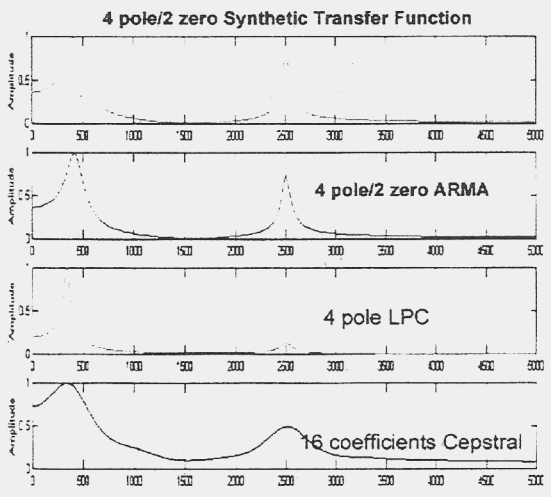

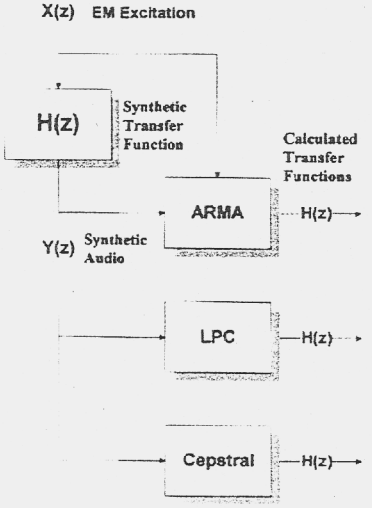

The ARMA Model Yields Accurate and Robust Transfer Functions Which Compare Well to Traditional Models

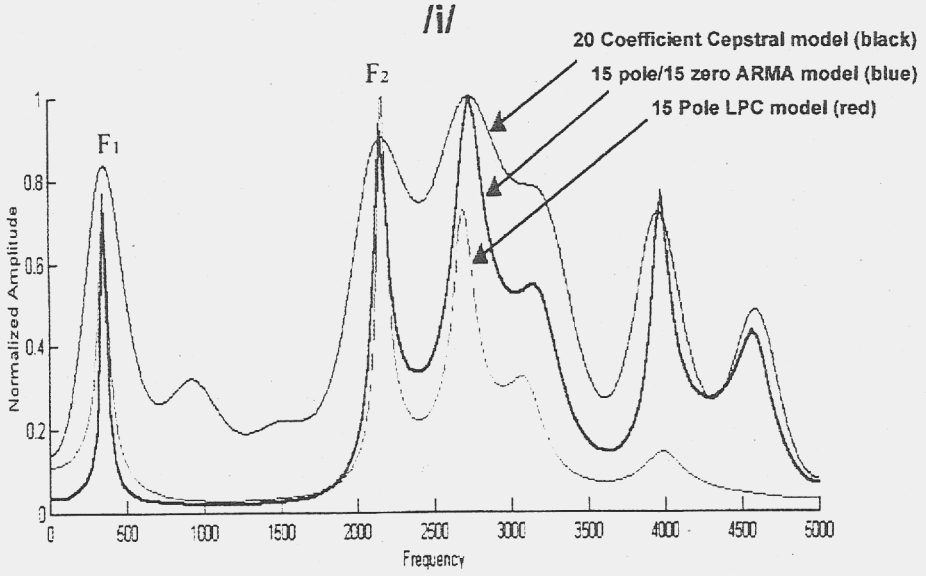

Access to the Voiced Excitation Signal Gives Pitch Synchronous Windows Used by the ARMA Model

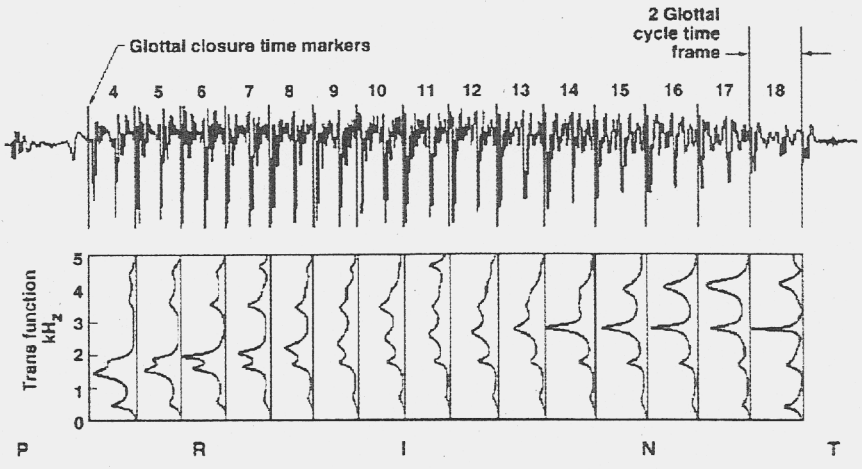

Example of Showing That GEMS' Pitch Estimate is Unaffected by Acoustic Noise

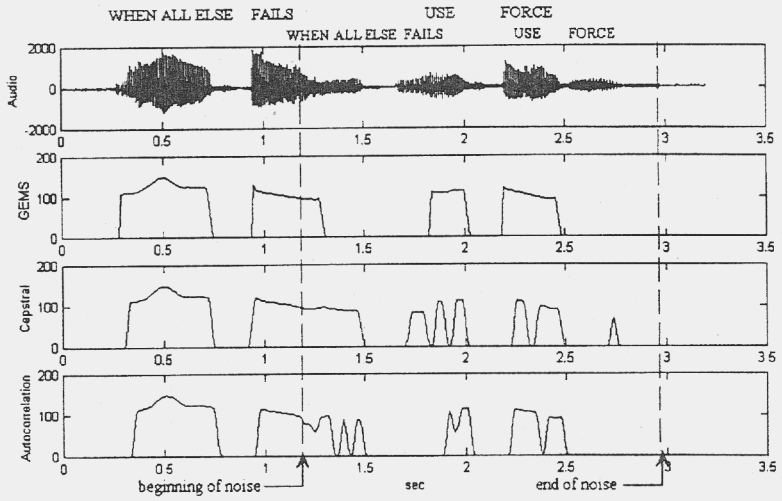

Summary and Conclusions

- **Results indicated that GEMS pitch estimate is:**
  - **100 times faster in computational efficiency**
  - **5 to 20 times smaller in error rates**
  - **GEMS is insensitive to acoustic noise**
  - **Fast computation of pitch can provide real-time pitch synchronous speech processing**
  - **Performance improves with higher sampling rate**

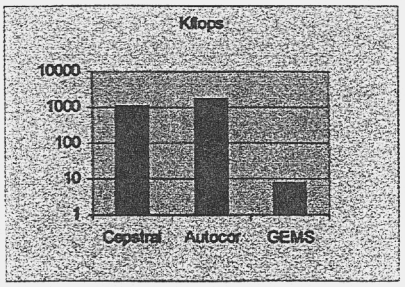

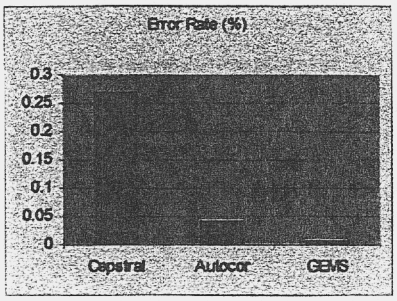

EM-Microphone — A Potentially New Machine Interface for the 21st Century

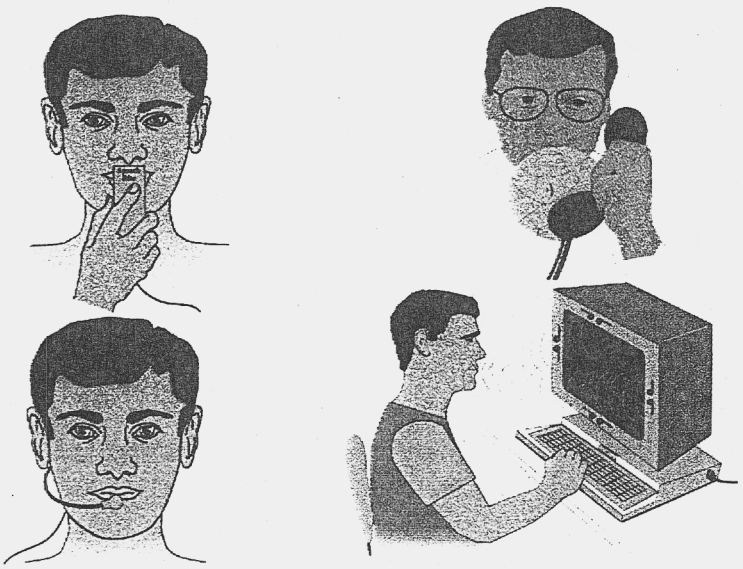

Speaker Verification Using Acoustic and Glottal EM Sensors (GEMS)

CASIS: Signal and Imaging Sciences Workshop

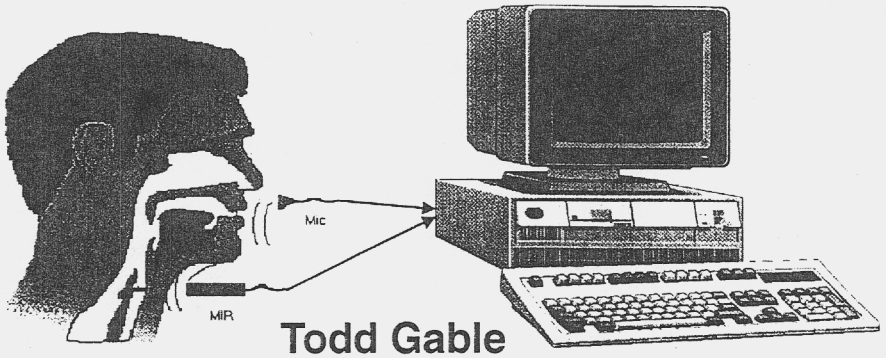

Todd Gable
UCD/LLNL

Overview — Why verification?

- The verification experiment is the first large scale test of the GEM Sensor applied to speech
- Verification involves many of the same types of problems found in other speech applications like speech recognition and speaker identification
- Speaker Verification can compete with or augment biometric security systems like retina scans and fingerprints

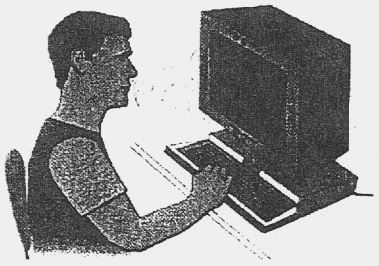

Speaker verification is the process of accepting or rejecting a persons identity claim based on parameters extracted from a test utterance

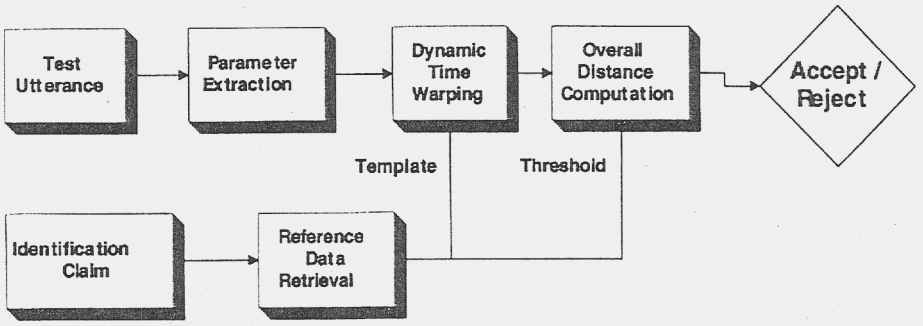

GEMS provide enhanced parameters for verification

Traditional Acoustic Parameters

- Pitch
- Spectral coefficients and their derivatives
- Energy

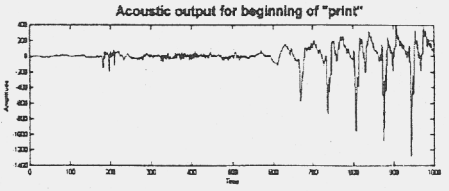

GEMS Enhanced Parameters

- GEMS extracted pitch
- Pitch synchronous spectral coefficients
- Energy
- Pitch synchronous ARMA coefficients
- GEMS signal parameters

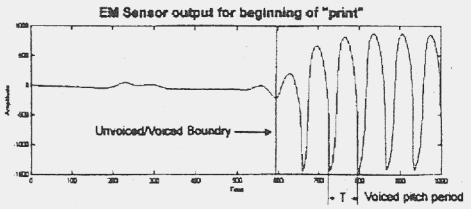

The GEMS signal shows distinct differences among different speakers — suitable for a glottal "fingerprint"

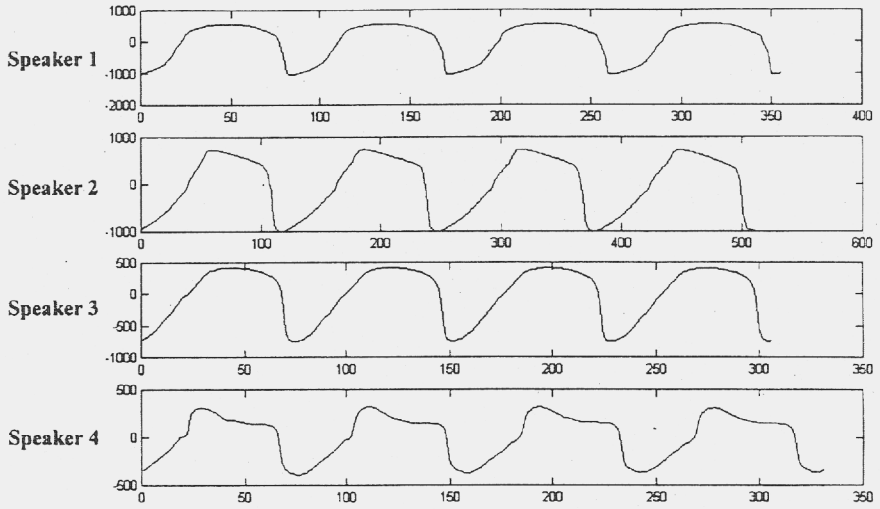

The vocal tract is modeled as an LTI system so we may use ARMA modeling

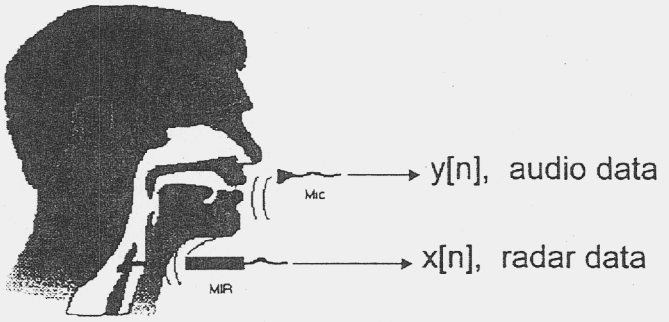

Transfer function $H(z) = Y(z)/X(z)$

Dynamic Time Warping (DTW) is the process of warping two vectors to the same length which yields a distance measure that mathematically tells us how similar they are

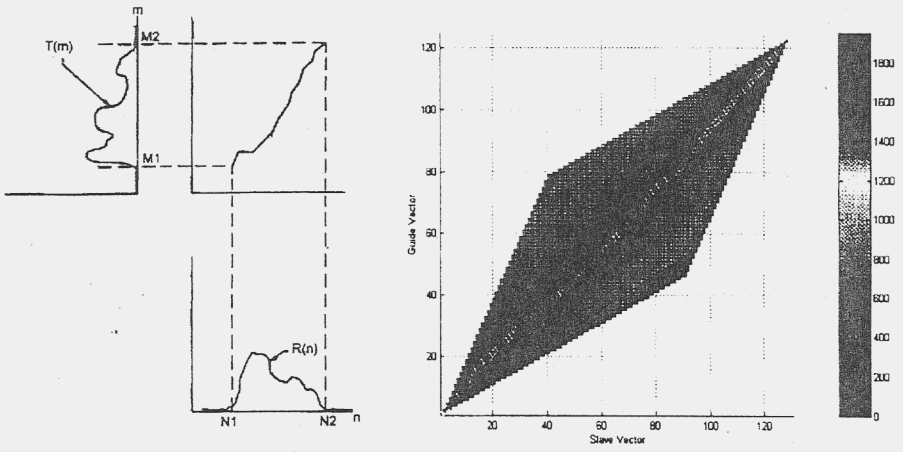

Example Warping

Pitch Contours before time warping

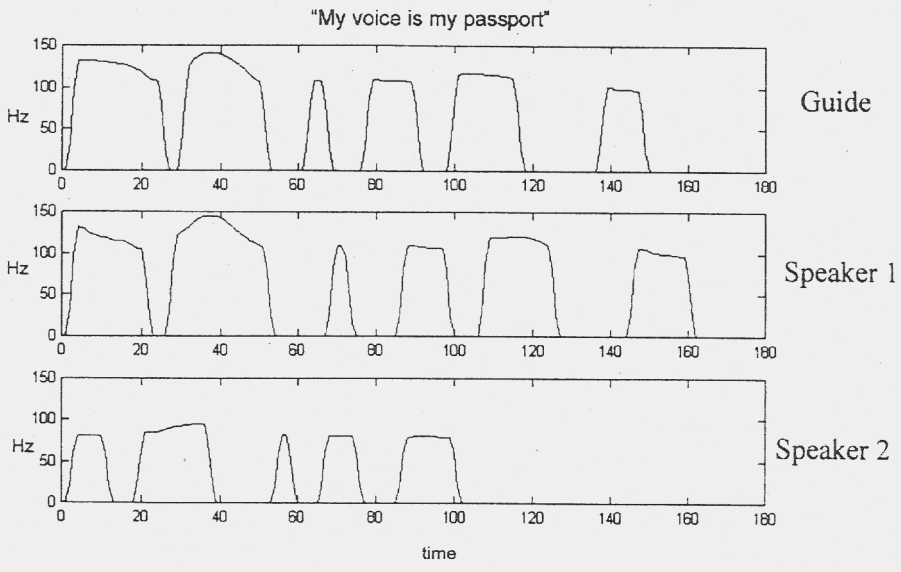

Pitch Contours after time warping

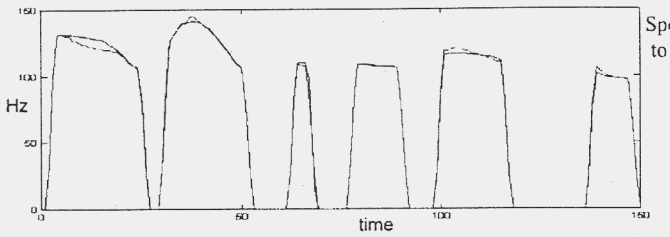

Speaker 1(red) warped to Guide (black)

Warping Distance = 1,112 Same speaker - ***low*** distance

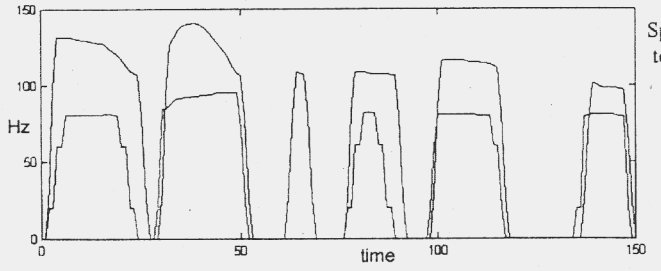

Speaker 2 (blue) warped to Guide (black)

Warping Distance = 234,959 Different speaker - ***high*** distance

Where we are now and what's in the future

- We have audio and GEMS data for fifteen male speakers using standard sentences
- We have algorithms for extracting some verification parameters
- A Dynamic Time Warping algorithm is in place for time-registration and a distance measure
- We still need to finish the parameter extraction software and fine-tune the system
- With the software in place we can run the system for all fifteen subjects and generate statistics
- Eventually port the system to C++ for demonstration purposes

Thank you

Object Identification Using Low Power Radars

Randy Roberts

Signal/Image Processing for Non-Destructive Measurement

Explosive Detection and Discriminant Research for Civil Aviation Security†

Harry E. Martz, Derrill Rikard, Earl Updike, Clint Logan, and Sailes Sengupta
Lawrence Livermore National Laboratory

X- and gamma-ray imaging techniques in nondestructive evaluation (NDE) and assay (NDA) have seen increasing use in an array of industrial, environmental, military, and medical applications. Much of this growth in recent years is attributed to the rapid development of computed tomography (CT). A new application area for CT is civil aviation security explosives detection. The only Federal Aviation Administration (FAA) certified explosives detection system is a linear-array based x-ray CT scanner developed by InVision, Inc. Unfortunately the system's airport false-alarm rate performance is higher than the certification rate. We are working with the FAA William J. Hughes Technical Center to help them advance their explosives detection and discriminant research efforts. We have applied three x-ray CT scanners in four different data acquisition configurations to characterize explosives, distinguish between explosives and x-ray machine false-alarm items; and validate inert, non-hazardous materials that simulate the x-ray properties of explosives. I will describe the x-ray CT scanner configurations, their results and our preliminary analysis of the data.

† This work is funded by the FAA William J. Hughes Technical Center and is performed under the auspices of the U.S. Department of Energy by the LLNL under contract W-7405-ENG-48.

Nondestructive Evaluation Center

presented by

Harry E. Martz, Acting Director NDE Center
Nondestructive and Materials Evaluation Section
Lawrence Livermore National Laboratory

at
Signal and Imaging Sciences Workshop
Lawrence Livermore National Laboratory
Livermore, CA
November 12-13, 1998

The NDE Center's role is to R&D core technologies and competencies required to fulfill LLNL's mission

- Vision
  - To be the World's leader in the research, development, and application of the nondestructive measurement technologies that enable successful LLNL and DOE programs
- Mission
  - To provide LLNL and DOE programs with superior nondestructive measurement capabilities
- FY99 mission objectives are to advance nondestructive measurement core competencies and technologies needed for the following compelling problems
  - Extraordinary laser systems, this includes advanced diagnostics, e.g., for fusion targets, and automated insitu optics damage inspection
  - Weapon system performance, this includes three-dimensional measurements over 15 cm to better than 25 µm, advanced diagnostics, e.g., AHF, and ceramic properties measurements
  - Science-based stockpile stewardship, specifically durability and life prediction
  - Arms control, nonproliferation, and international security related to reducing the threat from weapons of mass destruction

The NDE Center's current strategic focus includes five objectives required to meet LLNL program needs

Objectives:

Quantitative NDE—The objective of quantitative multi dimensional NDE is to obtain measurements to evaluate physical properties: geometry, density, elemental & molecular composition, thermal, structural, mechanical, radioactive assay, etc., in all three dimensions an as a function of time for the materials/objects we characterize. We set a goal of 0.1% accuracy for each of these properties at video frame rates. This includes integration of inspection, evaluation and characterization methods to predict material response and life times, and whe necessary, reduce data to a quantitative decision.

Fast Nanoscale Imaging—The fast Nanoscale imaging objective is to provide multiple programs with quantitative multidimensional (>3D) imaging down to nanoscale lengths. Most techniques that provide such a capability to date are surface and near surface methods. G goal is to do this on a specimen in bulk(3D, i.e., beyond near surface. We want to develop NDE techniques that can obtain spatial resolut of 100 nm (resolve two objects separated by 100 nm) over 1 mm field of view at video frame rates. We need to determine if "super resolution" is possible and useful to obtain spatial resolutions to better than the diffraction limit of the NDE imaging systems.

Embedded in Design—NDE should be the driver that unites currently very diverse and somewhat noncoupled technologies such as design and modeling, materials development, characterization and testing, prototyping, process monitoring and control, reverse engineeri and reuse and waste management into a global package of integration and iteration. The objective of 'embedded in design' is to couple her into the programs to such an extent that we are an integral element in each of these areas. For example, NDE should be integrated into the design and specification of systems. This could enable new concepts such as "smart structures."

Multispectral—The multispectral objective is to expand the spectral range of current NDE imaging technologies and to increase the synergism between different NDE methodologies. This will include methods to register/fuse different NDE data sets in multiple dimensio to facilitate prediction of material behavior and life times.

Portability—The objective of portability is to reduce current and new NDE systems to a size that is on the order of a small suitcase (2×10^5 cm^3 or ~8ft^3) with individual modules weighing no more than 50 lbs. for field use. This requires source, detector, and power research and development. We also need to research and develop remote/passive NDE methods for confined/hard to access spaces.

Focus areas	D&NT†	Lasers†	NAI†	Energy/Env†	Bioscience†	Other†
Quantitative NDE	H-Landram/ Dolan/Kallman/		M	H	H	H
Fast Nanoscale Imaging	H	H-Huber	M	M	H	H
Embedded in Design		H	M	H	M	H
Multispectral	M	H	H-Epperson	H	H	M
Portability	M	M	H	H	M	M

Compelling NDE Center problems

- Measurement Systems
  - See inside objects beyond what NDE has seen before
    - > Improve spatial resolution down to nm scale
    - > Increased penetration/contrast to see inside materials not accessible before
    - > Temporal (fast) volumetric imaging
- Analysis and Interpretation
  - Multi-dimensional (>3D) signal and image processing
    - > Speed, accuracy and noise reduction in processing
    - > Data interpretation—We see more and more things; what does this mean to the customer
    - > Fusion of different NDE measurement systems data

Measurement systems, and analysis and interpretation must be developed jointly to get optimal synergy

Nanometer scale is the world of the future

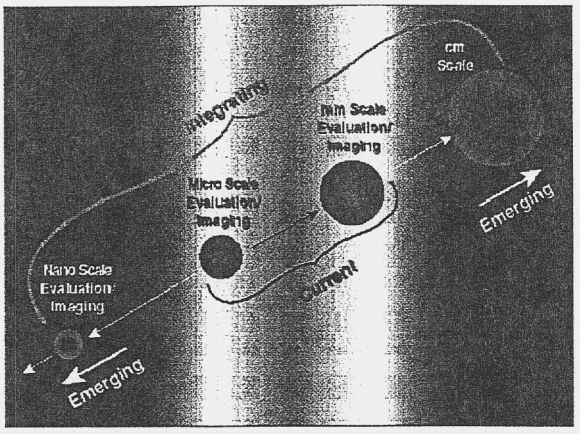

It is clear that one NDE challenge is to head in the nano-scale direction in addition to improving current scale capability

Automated multi-dimensional data acquisition, processing and interpretation is the world of the future

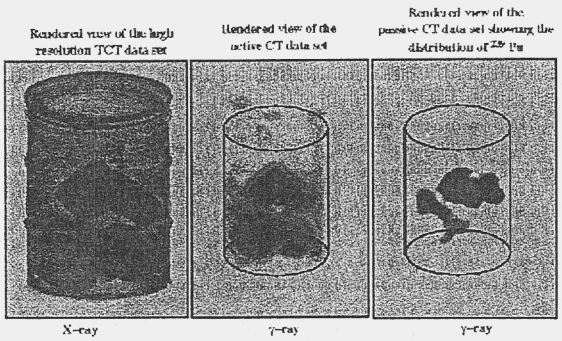

Data Reduction:
3 grams
Weapons grade
Plutonium

Decision:
Transuranic (not low-level) waste disposal required

Typically multi-dimensional data are required to produce a single number to make a crucial decision

"GBytes to a Bit"

"GBytes to a Bit"

Ultrasonic Compound B-scan Imaging

Co-authors: T. J. Gomm, J. A. Mauseth
Idaho National Engineering and Environmental Laboratory
Lockheed Martin Idaho Technologies Company

The imaging of the internal contents of thin-wall tubes has led to the implementation of a little-used ultrasonic imaging technique that allows compounded images to be created from a series of simple B-scan images. These compound B-scans have distinct imaging advantages over standard ultrasound A-scan, B-scan, and C-scan modes, as well as some tomographic imaging methods.

Although this method is finding use in the medical world, there are issues pertaining to couplant homogeneity, reflection, and diffraction that must be addressed for application in the testing and imaging of metallic targets.

This presentation clearly defines the implementation of the Compound B-scan. The steps needed to convert each standard B-scan image to a dimensional image are discussed. The issue of non-homogeneity in the couplant is addressed. Because the time-to-spatial dimension conversion requires knowledge of the couplant velocity, use of non-homogenous couplant dictates that a different conversion algorithm be developed. Artifacts resultant in the compounded images are presented and discussed.

Test results are presented that show the ability of the Compound B-scan to image both concave and convex surfaces as well as tightly-packed clusters and phantoms in thin-wall tubes.

Keywords: Ultrasound, Compound B-scan, Tomography

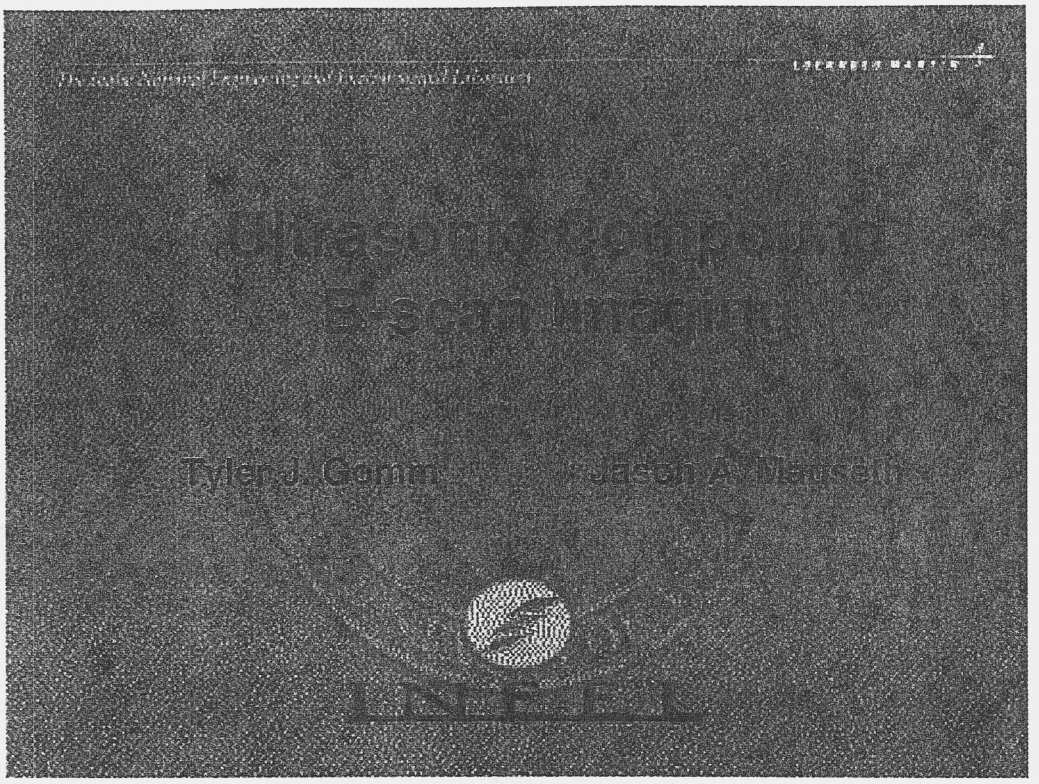
Ultrasonic Composite
B-scan Imaging
Tyler J. Gomm
Jason A. Hansen

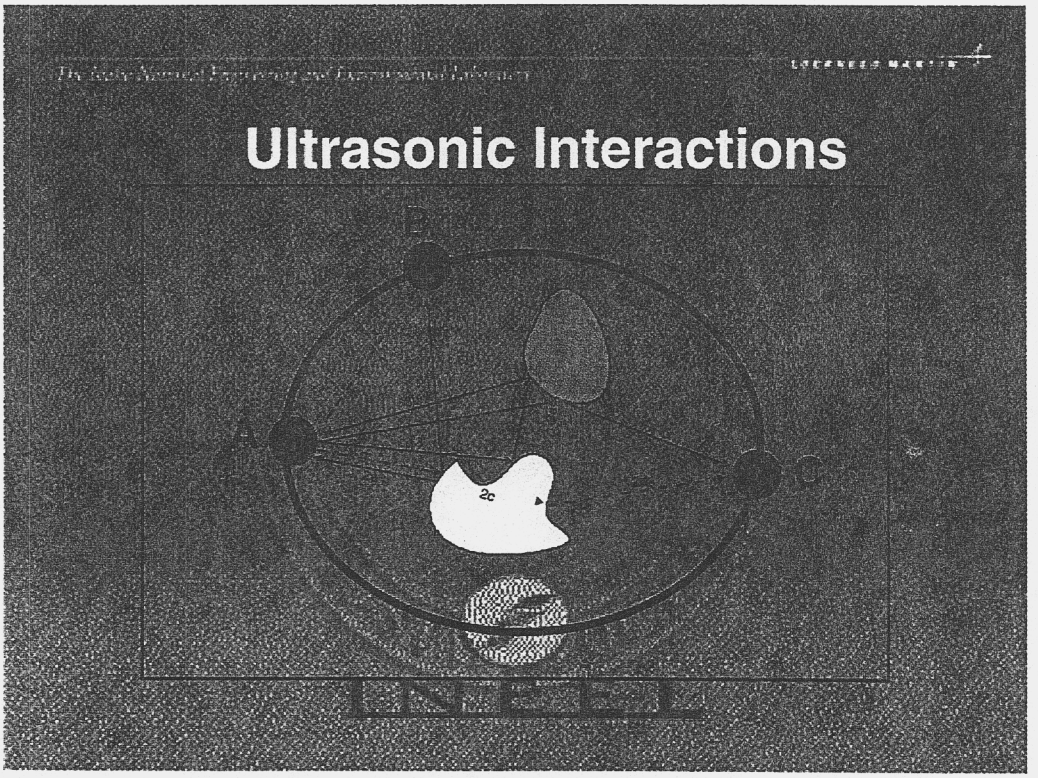
Ultrasonic Interactions
B
A
C
2c

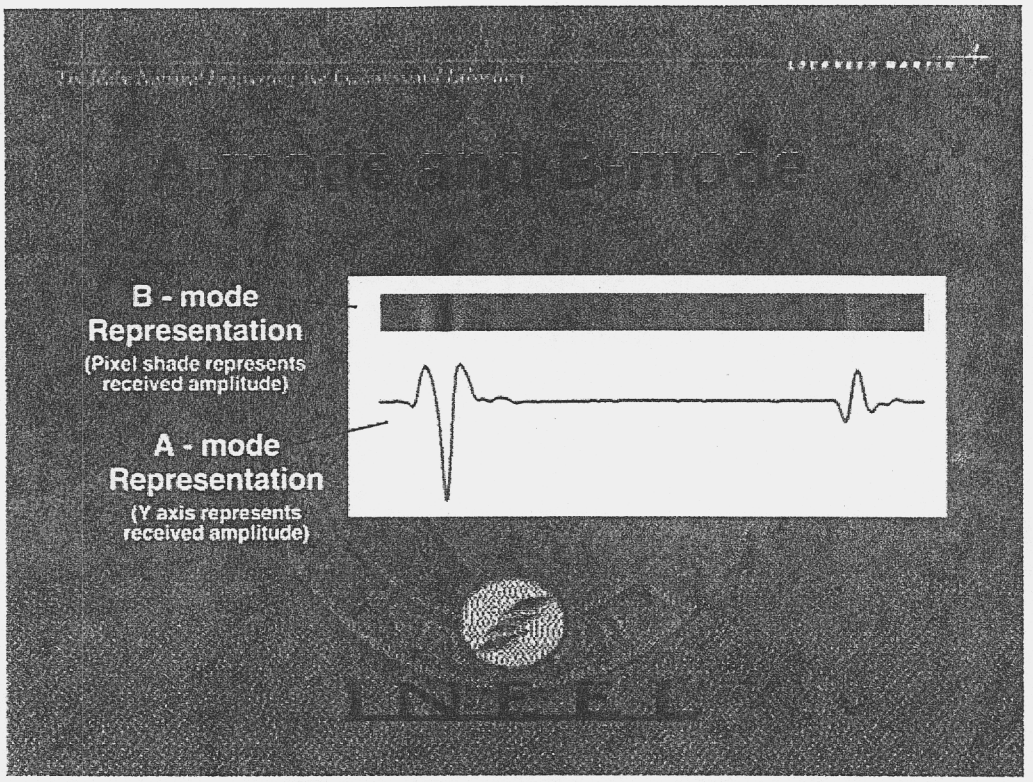
B - mode
Representation
(Pixel shade represents
received amplitude)
A - mode
Representation
(Y axis represents
received amplitude)

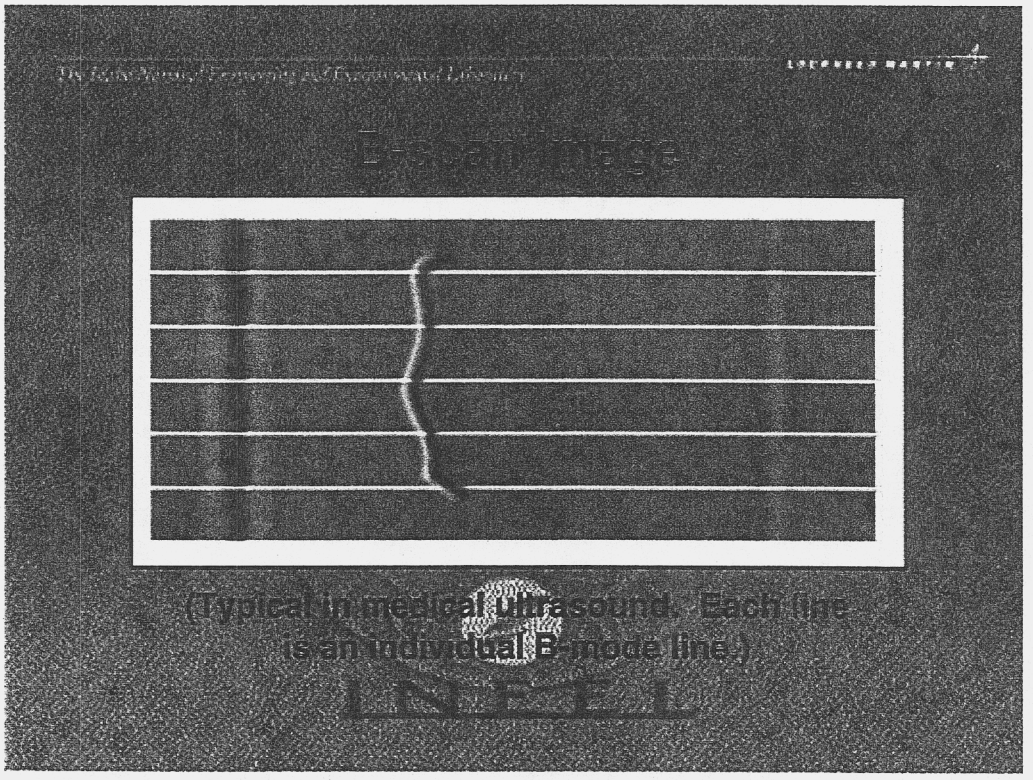
(Typical in medical ultrasound. Each line
is an individual B-mode line.)

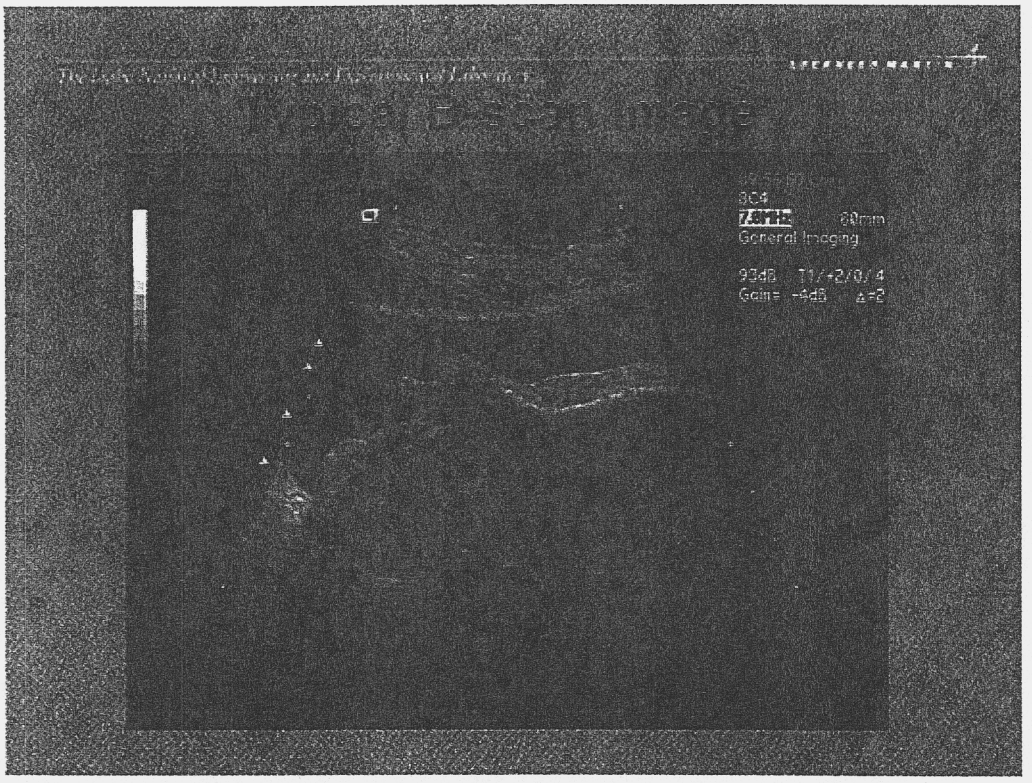
General Imaging

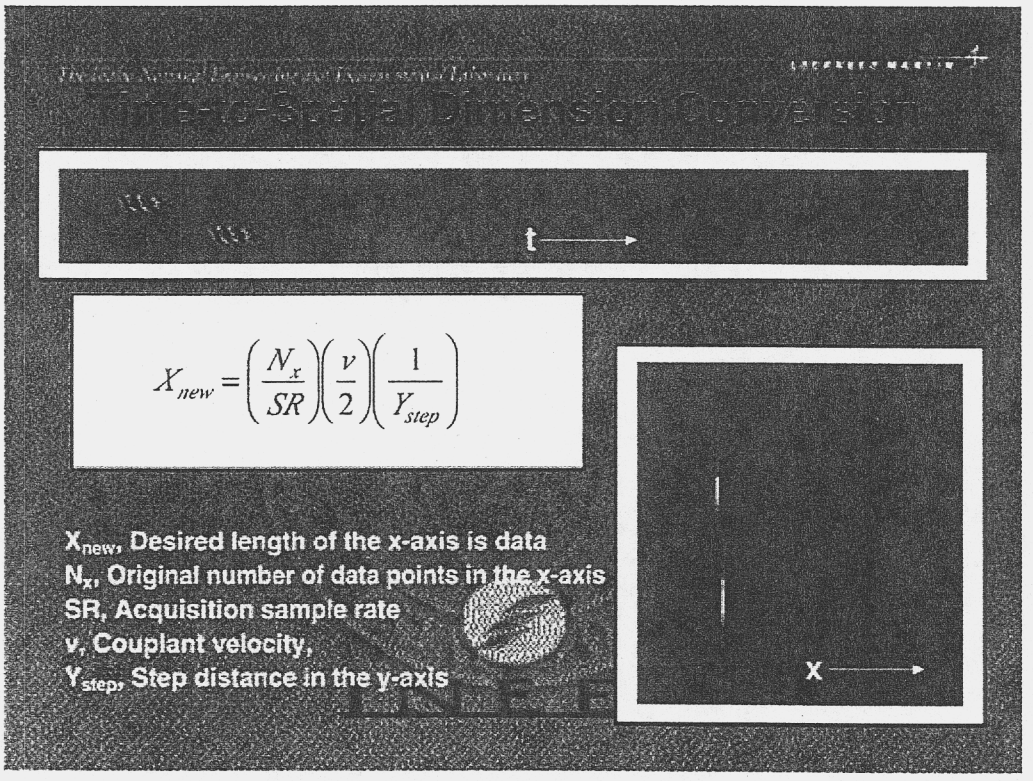
t
$X_{new} = \left(\frac{N_x}{SR}\right)\left(\frac{v}{2}\right)\left(\frac{1}{Y_{step}}\right)$
X_{new}, Desired length of the x-axis is data
N_x, Original number of data points in the x-axis
SR, Acquisition sample rate
v, Couplant velocity,
Y_{step}, Step distance in the y-axis
X

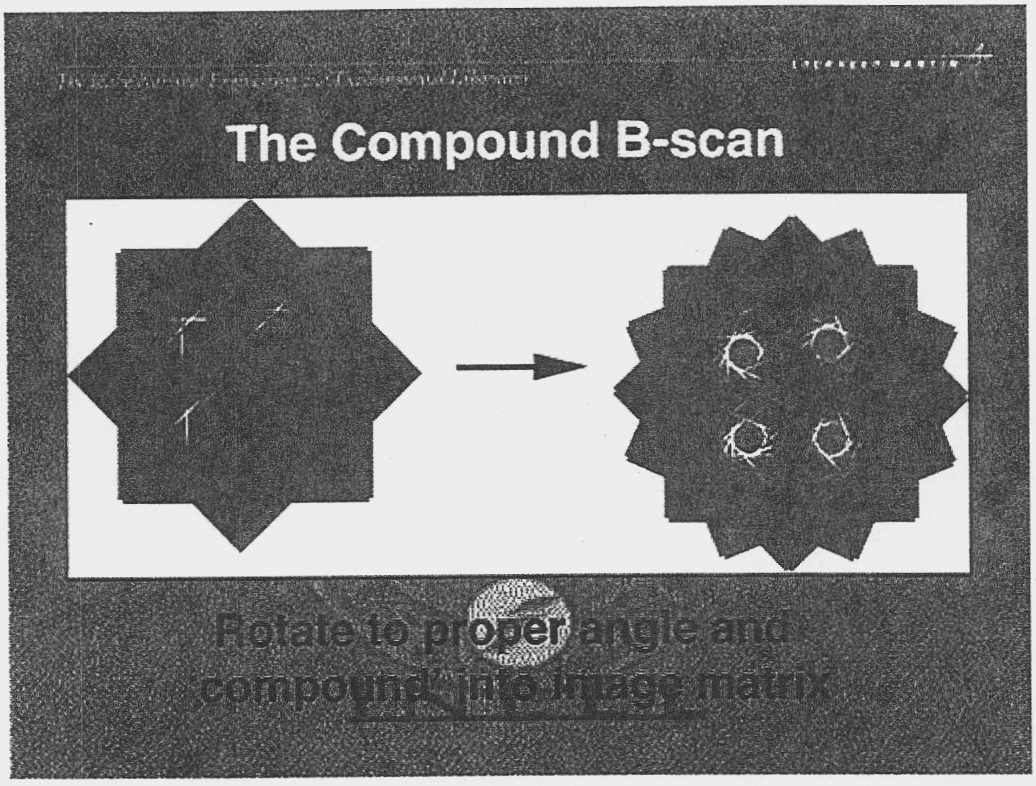
The Compound B-scan
Rotate to proper angle and
compound into image matrix

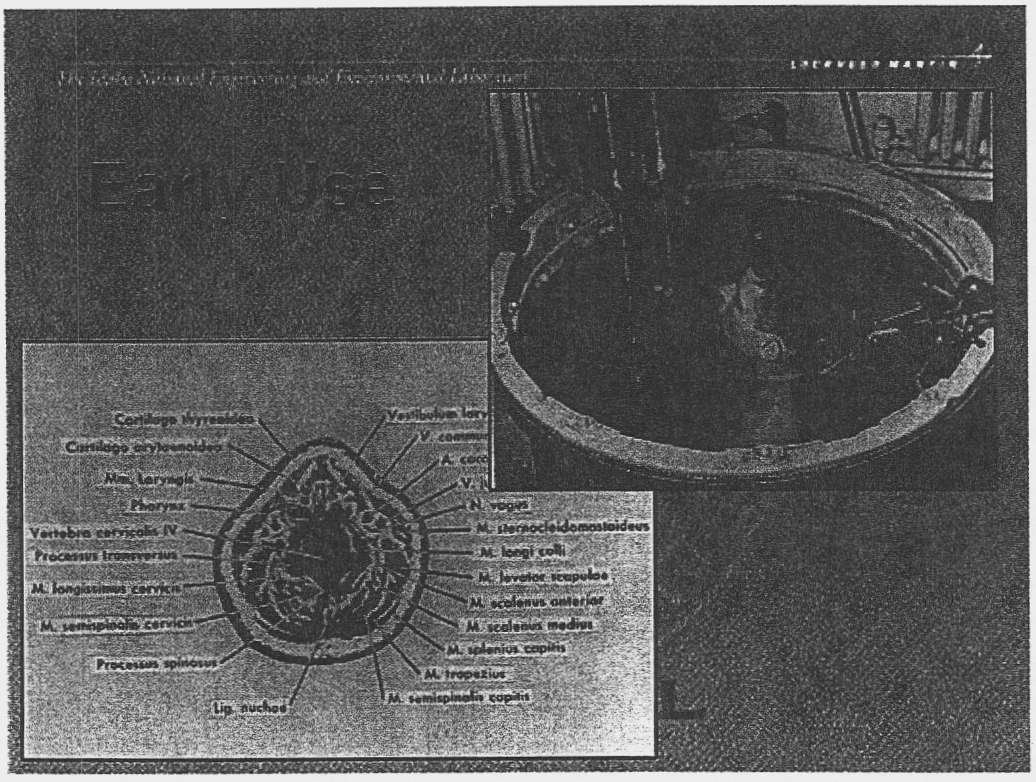
Cartilago thyreoidea
Cartilago arytaenoidea
M. laryngis
Pharynx
Vertebra cervicalis IV
Processus transversus
M. longissimus cervicis
M. semispinalis cervicis
Processus spinosus
Lig. nuchae
M. sternocleidomastoideus
M. longi colli
M. levator scapulae
M. scalenus anterior
M. scalenus medius
M. splenius capitis
M. trapezius
M. semispinalis capitis

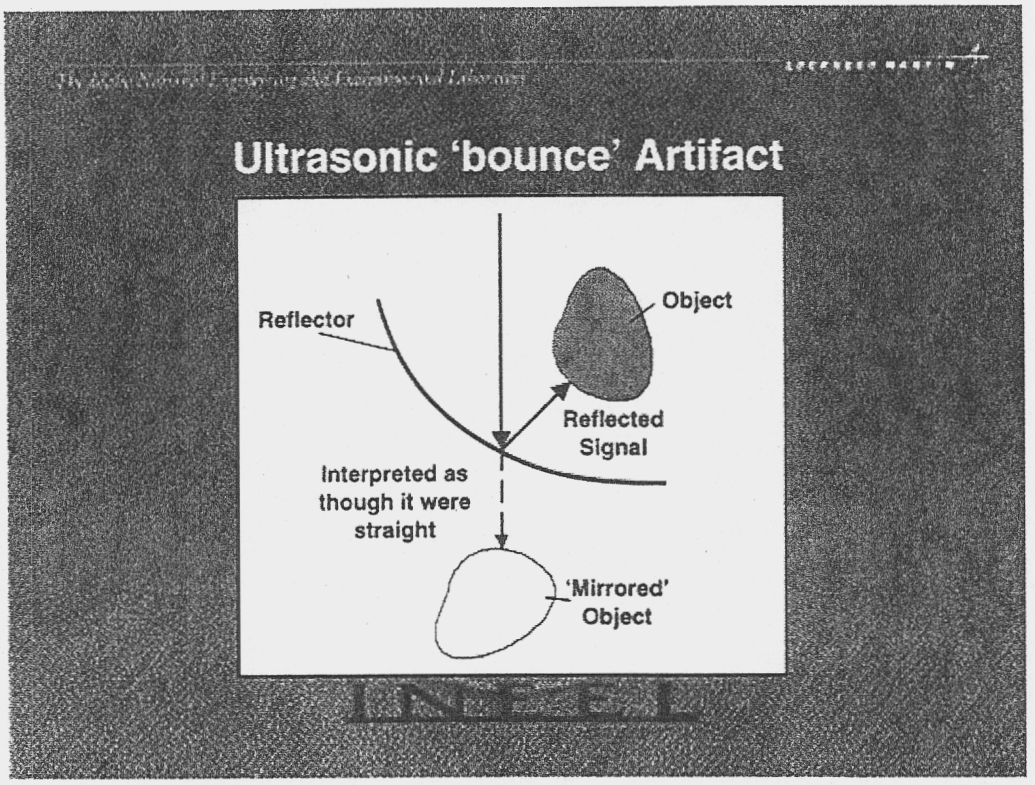
Ultrasonic 'bounce' Artifact
Reflector
Object
Reflected Signal
Interpreted as though it were straight
'Mirrored' Object

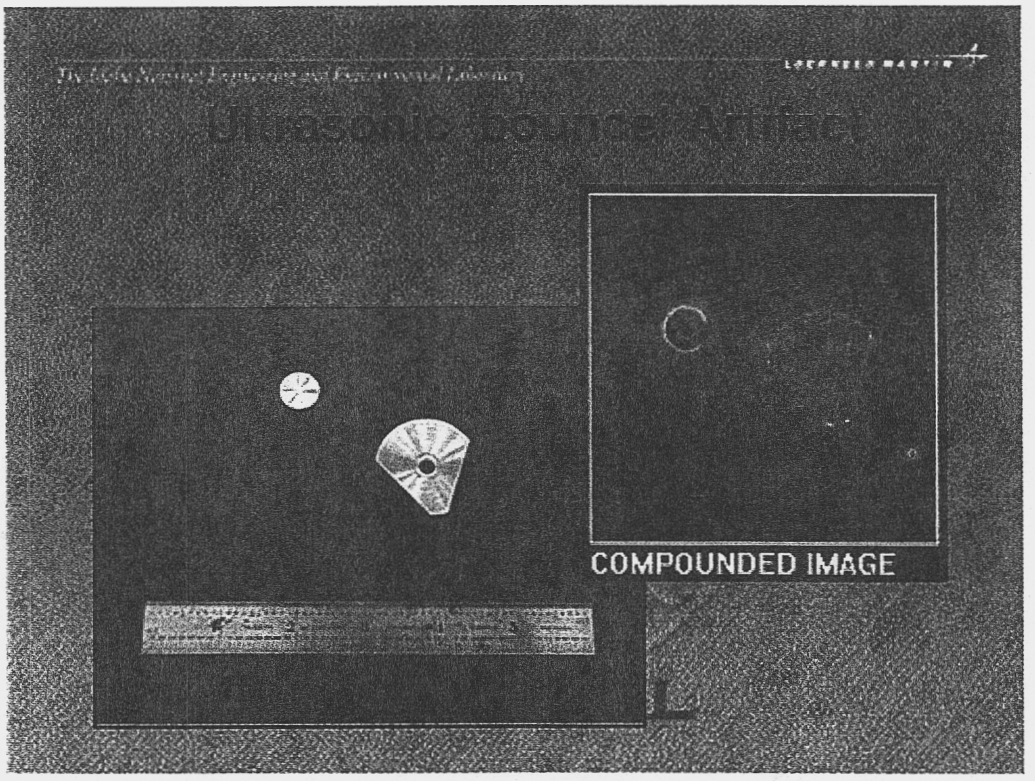
COMPOUNDED IMAGE

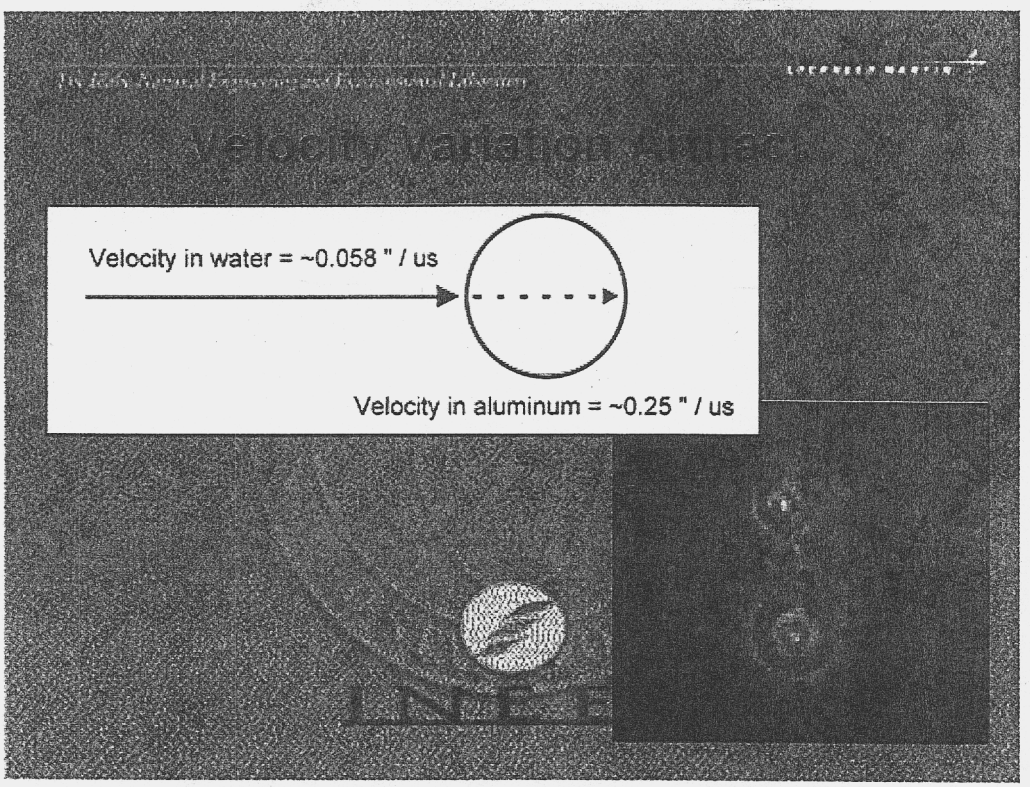
Velocity in water = ~0.058 " / us
Velocity in aluminum = ~0.25 " / us

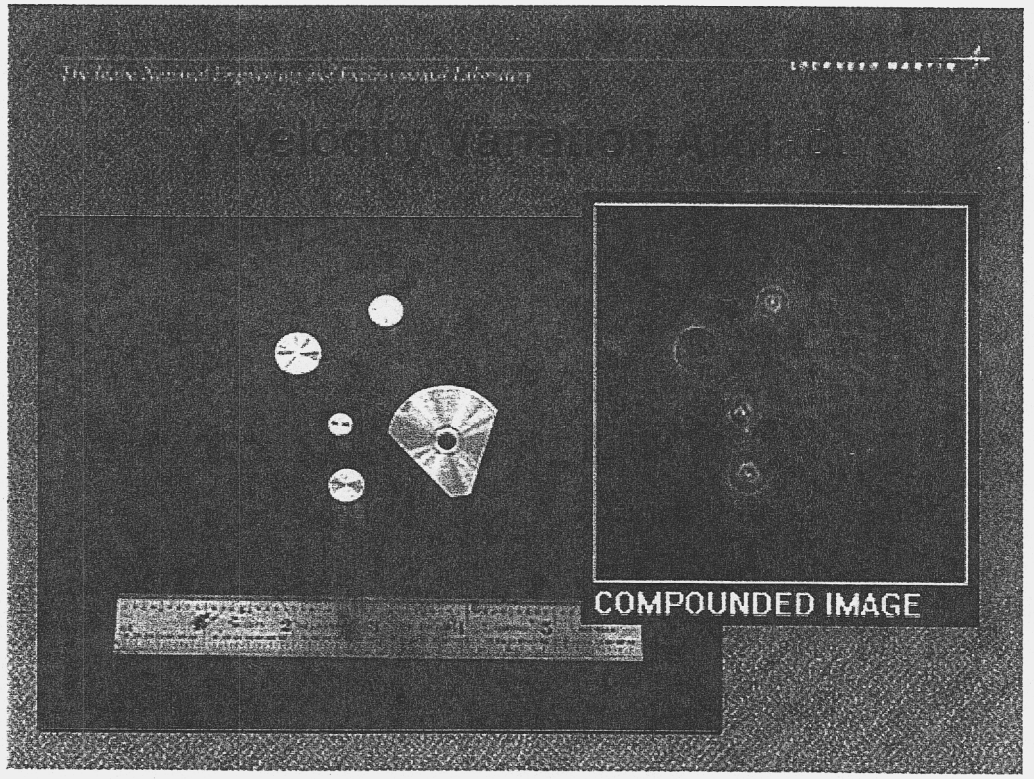
COMPOUNDED IMAGE

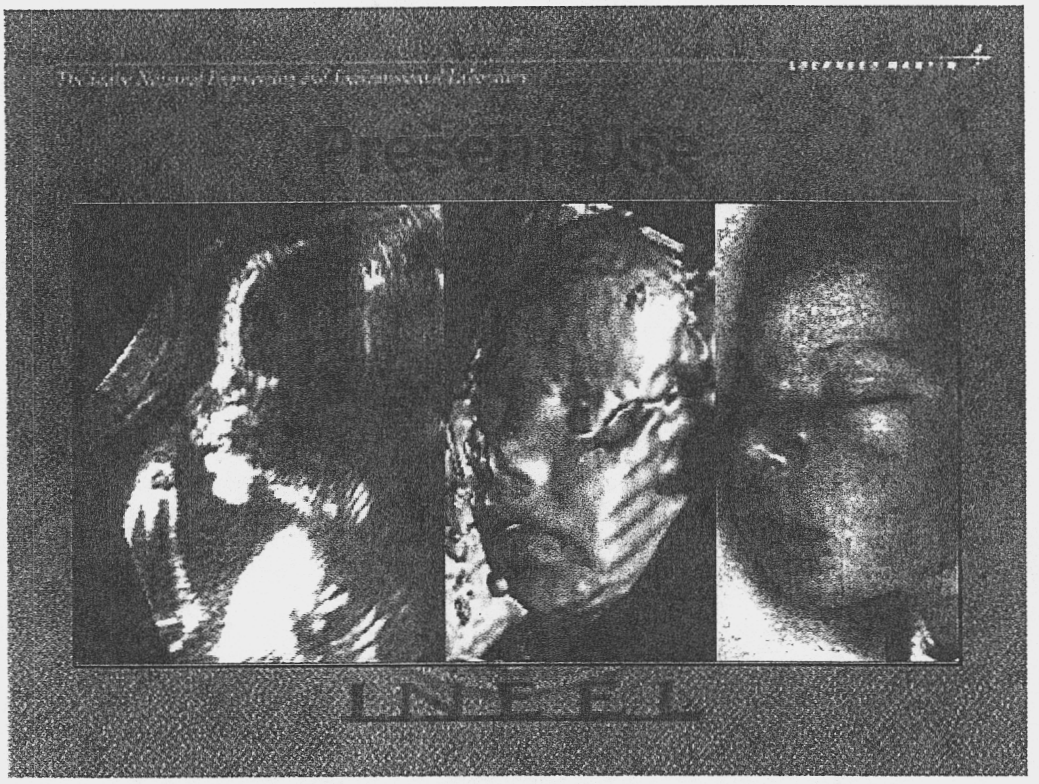

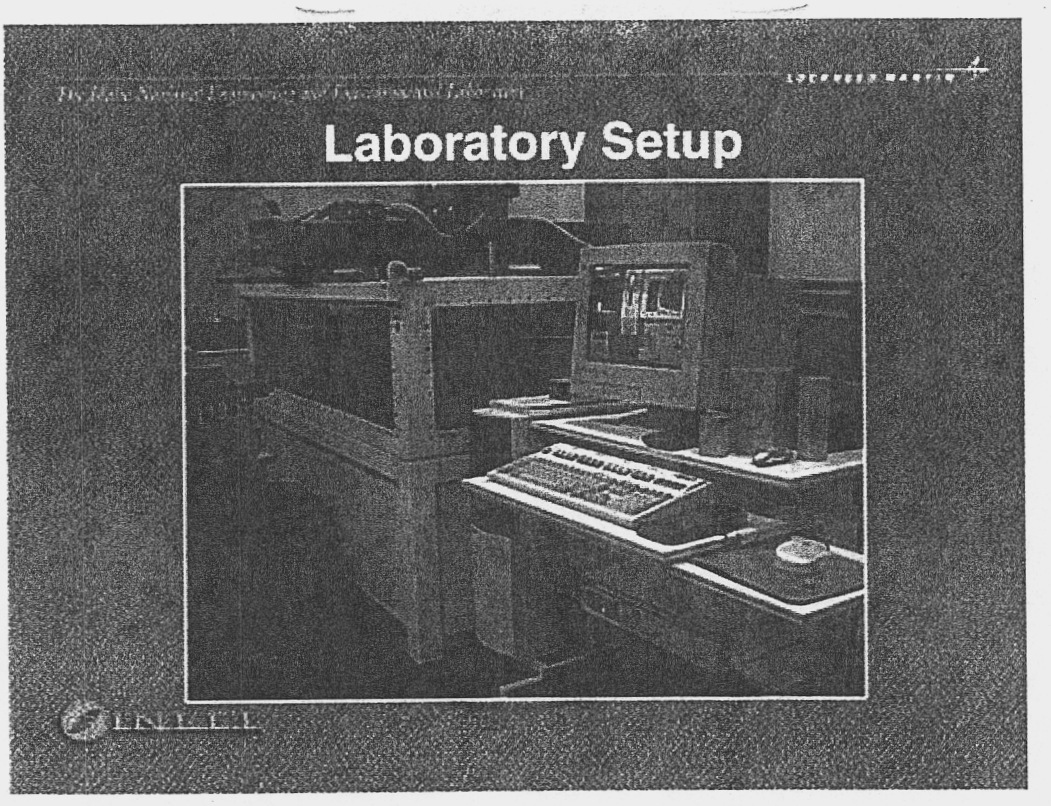
Laboratory Setup

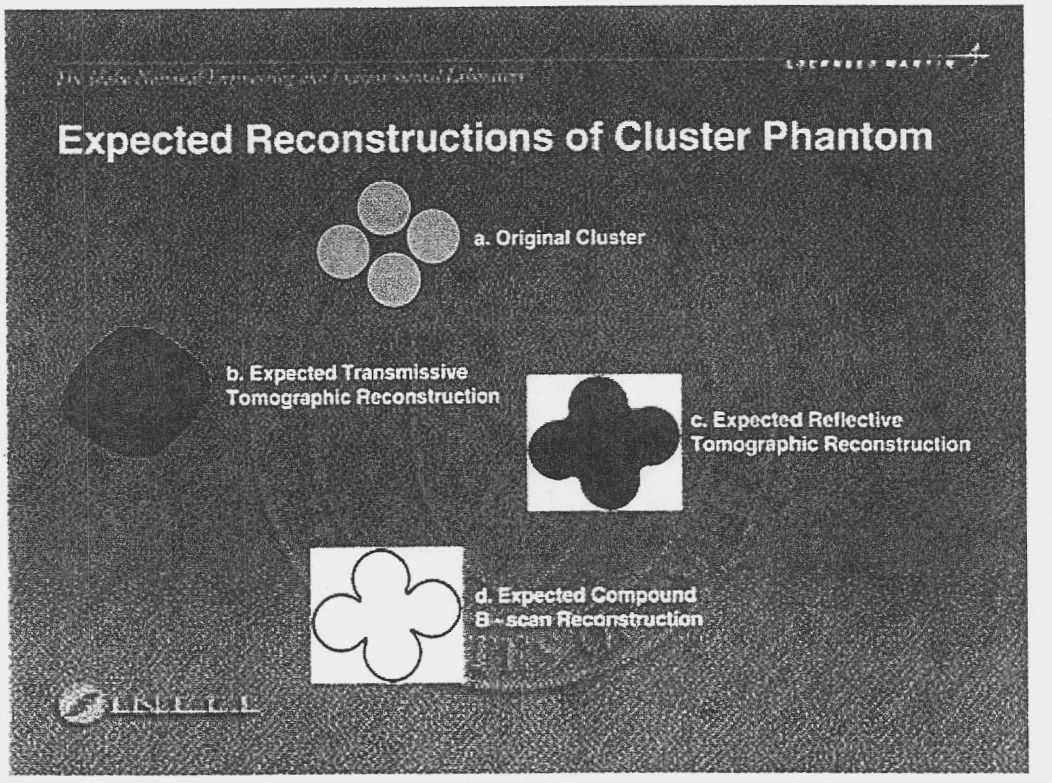
Expected Reconstructions of Cluster Phantom
a. Original Cluster
b. Expected Transmissive Tomographic Reconstruction
c. Expected Reflective Tomographic Reconstruction
d. Expected Compound B - scan Reconstruction

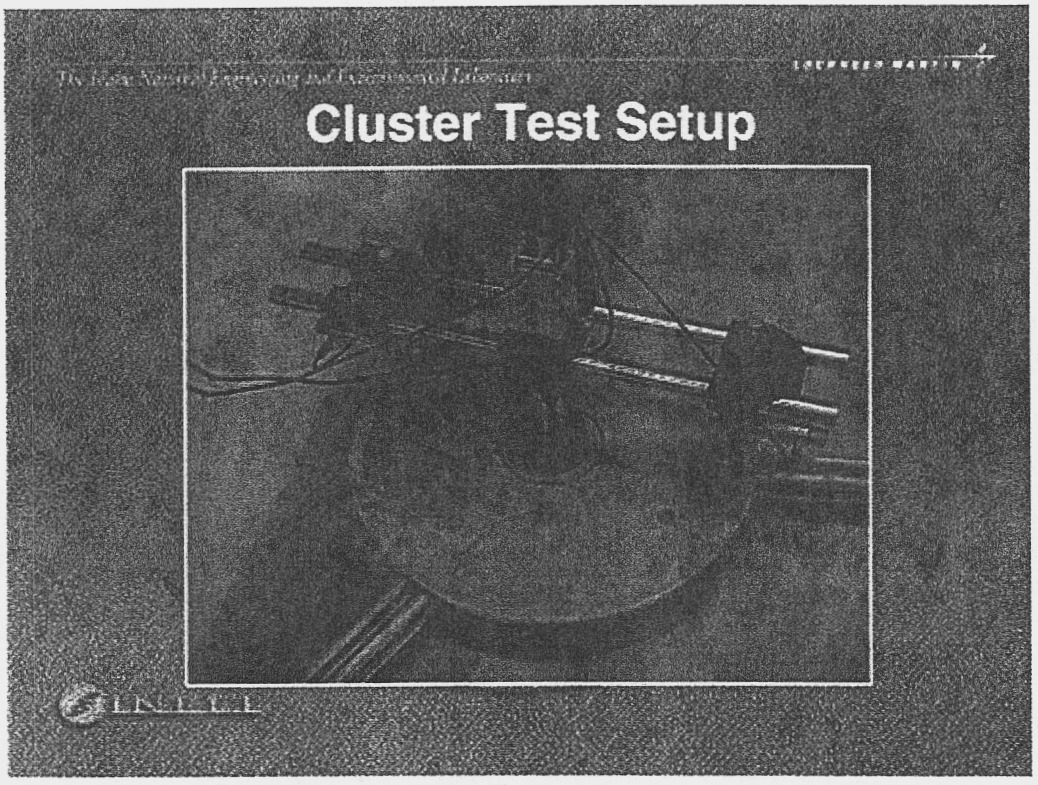
Cluster Test Setup

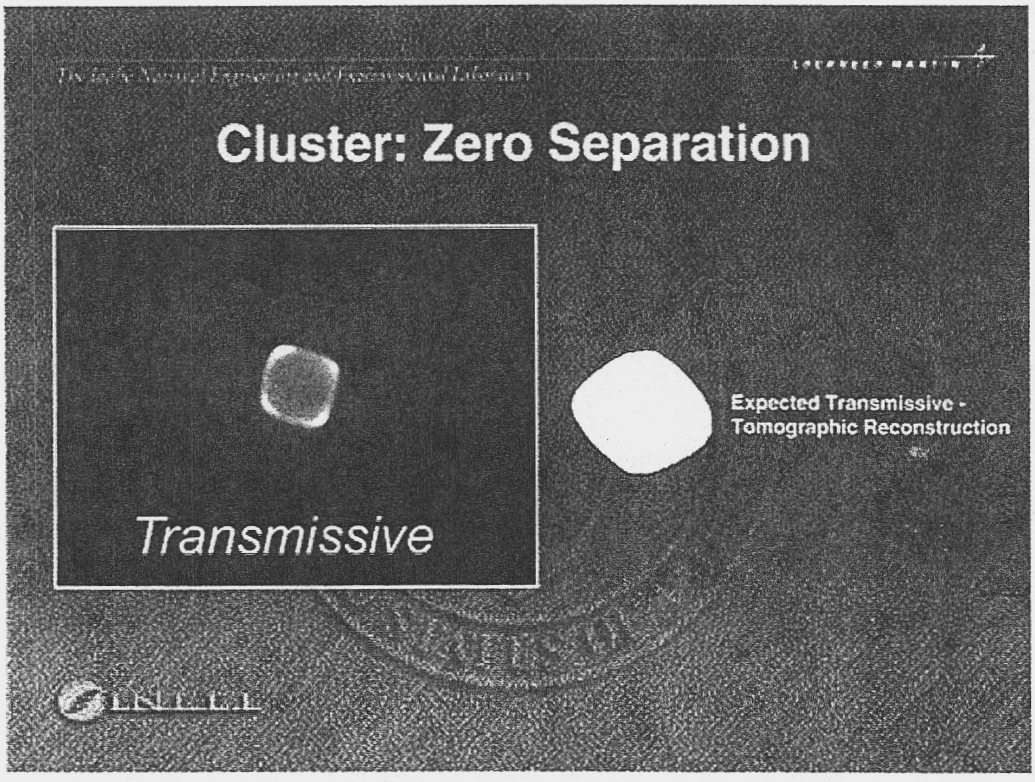
Cluster: Zero Separation
Transmissive
Expected Transmissive -
Tomographic Reconstruction

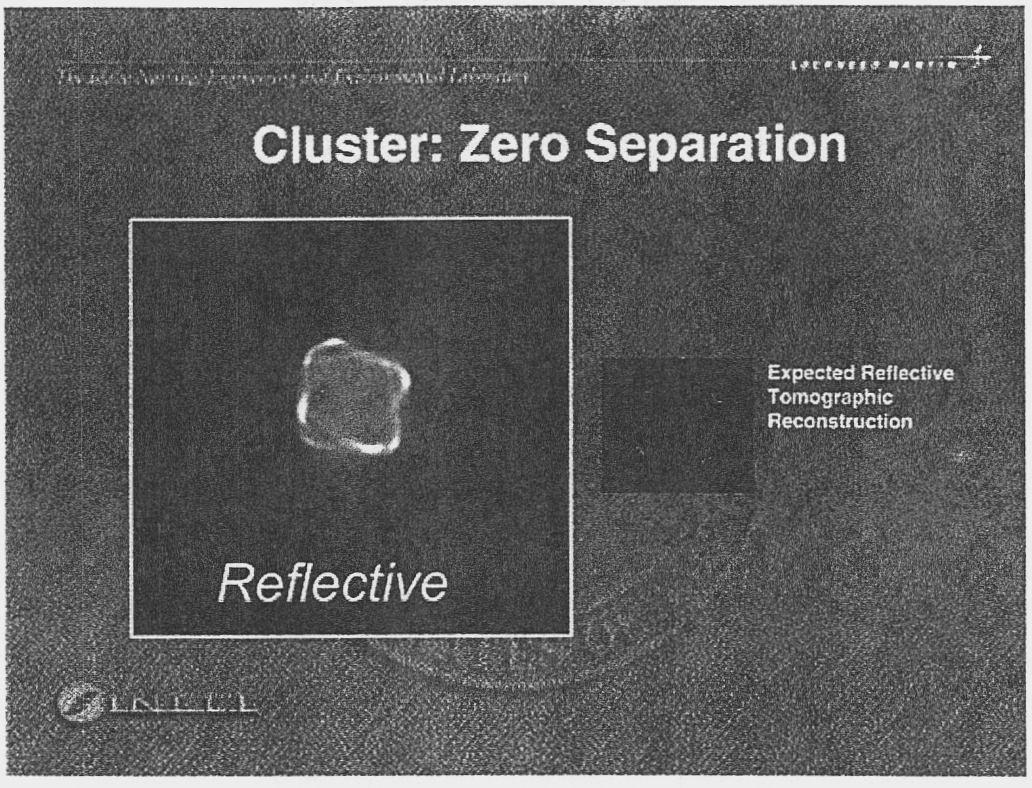
Cluster: Zero Separation
Reflective
Expected Reflective
Tomographic
Reconstruction

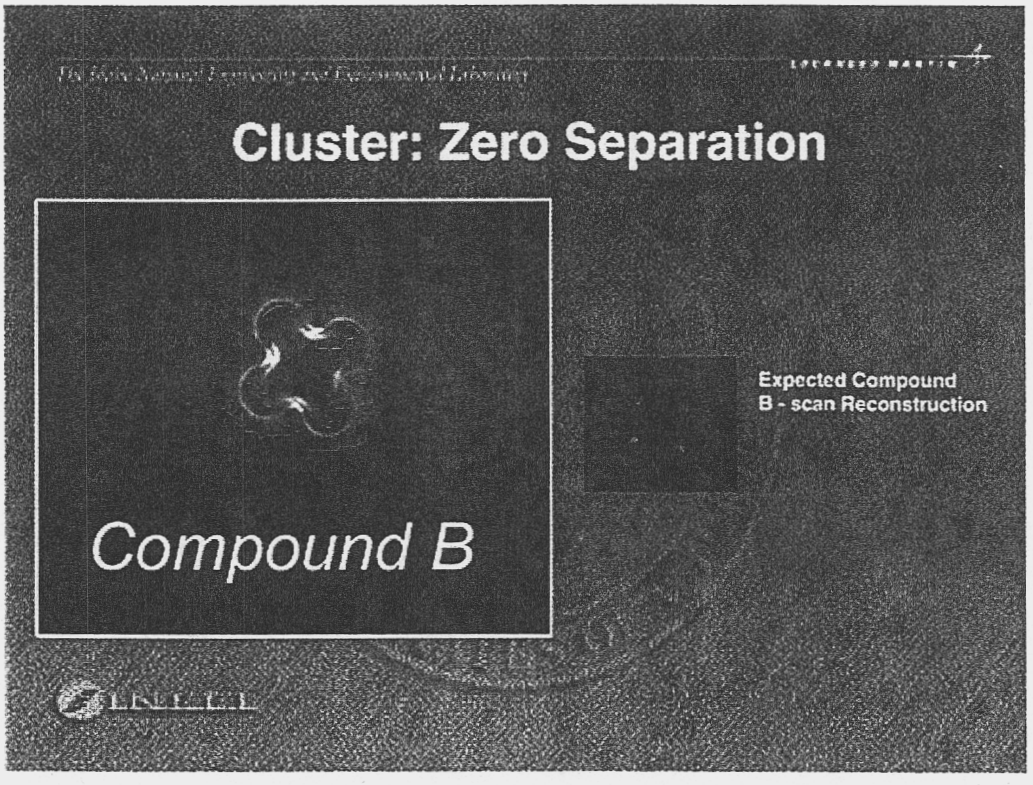
Cluster: Zero Separation
Compound B
Expected Compound
B - scan Reconstruction

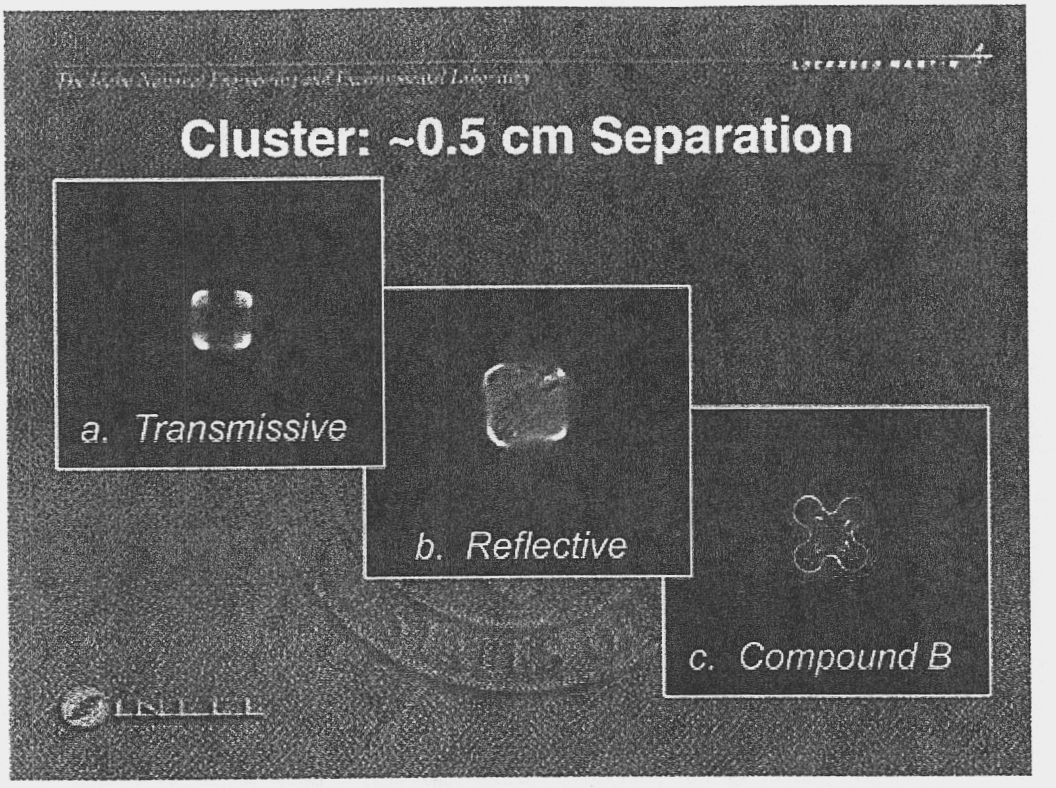
Cluster: ~0.5 cm Separation
a. Transmissive
b. Reflective
c. Compound B

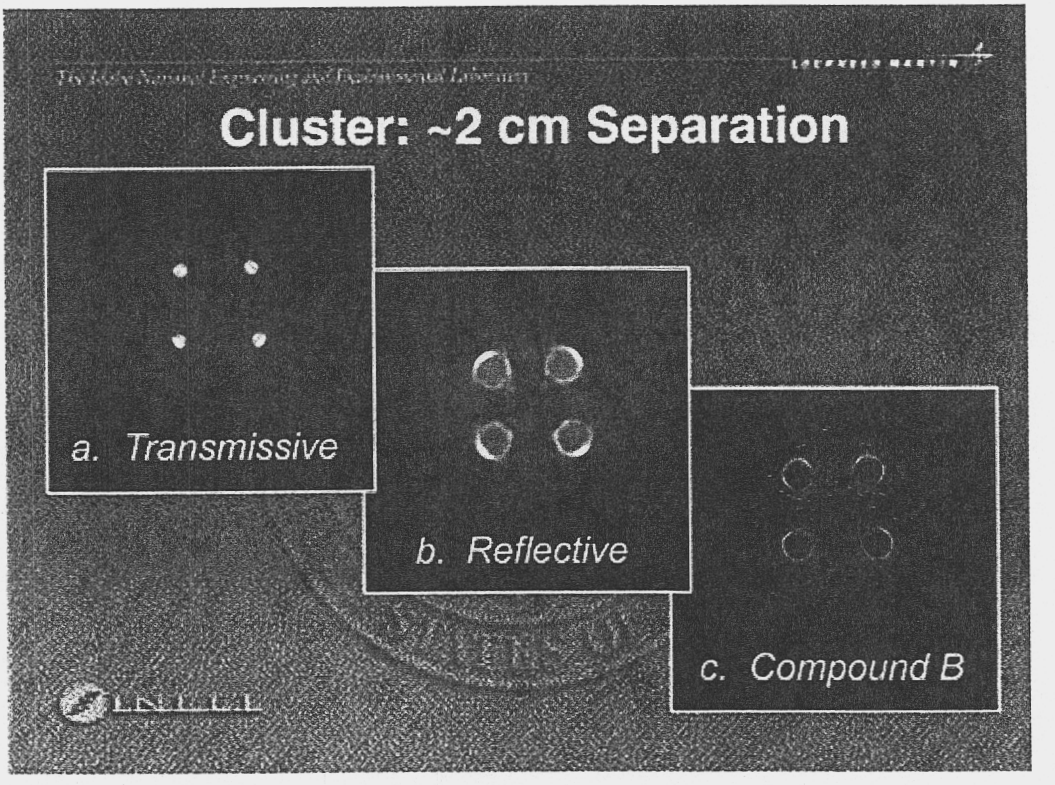
Cluster: ~2 cm Separation
a. Transmissive
b. Reflective
c. Compound B

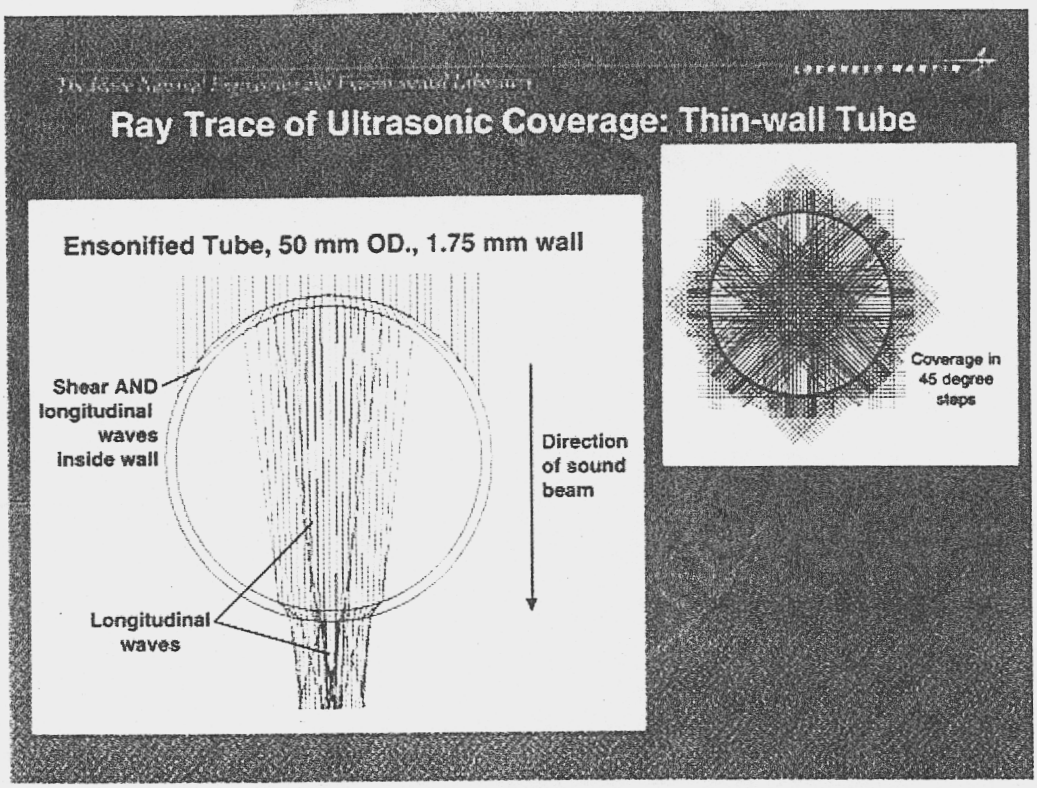
Ray Trace of Ultrasonic Coverage: Thin-wall Tube
Ensonified Tube, 50 mm OD., 1.75 mm wall
Shear AND longitudinal waves inside wall
Direction of sound beam
Longitudinal waves
Coverage in 45 degree steps

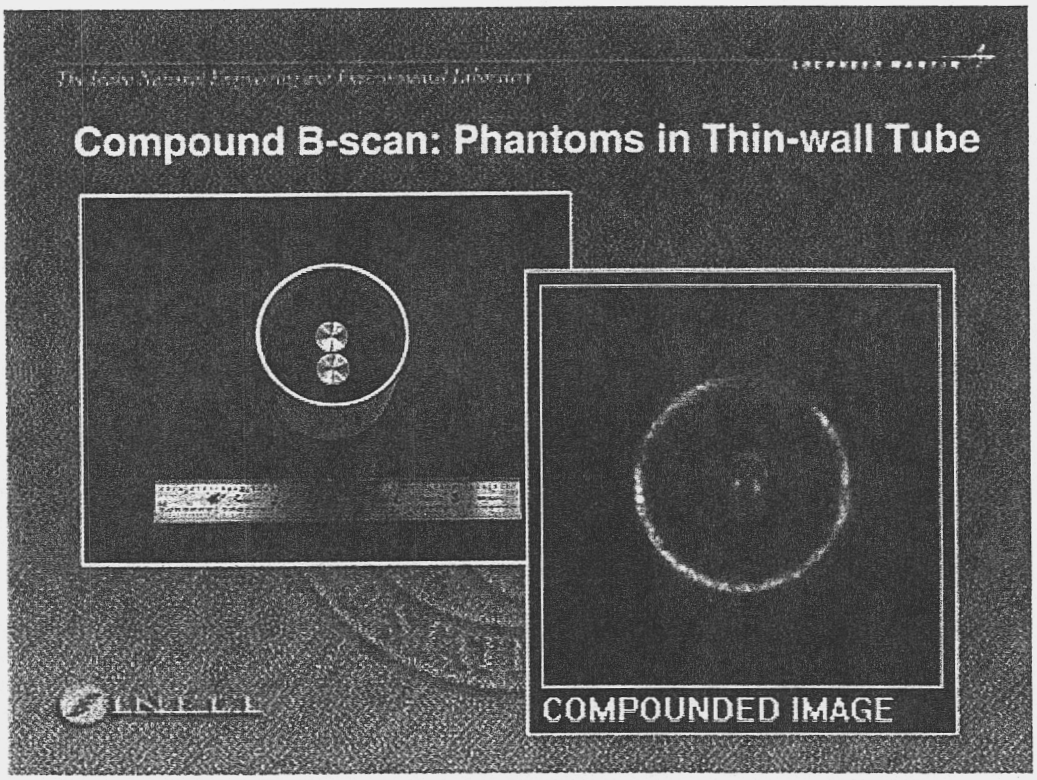
Compound B-scan: Phantoms in Thin-wall Tube
COMPOUNDED IMAGE

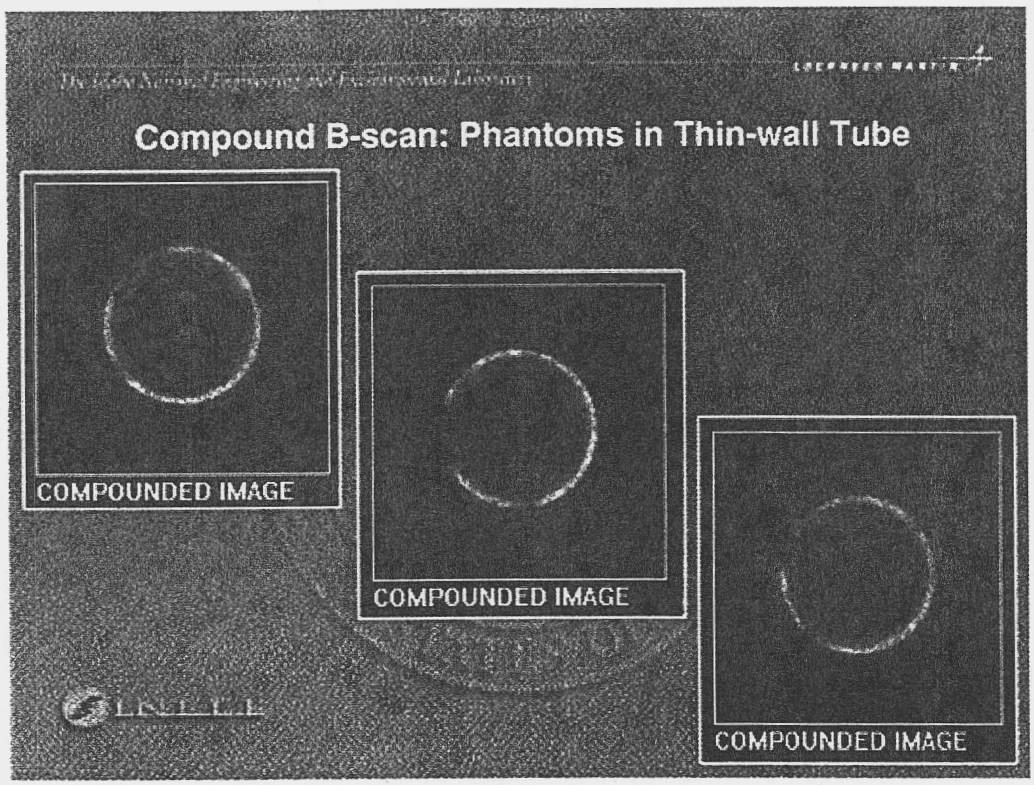
Compound B-scan: Phantoms in Thin-wall Tube
COMPOUNDED IMAGE
COMPOUNDED IMAGE
COMPOUNDED IMAGE

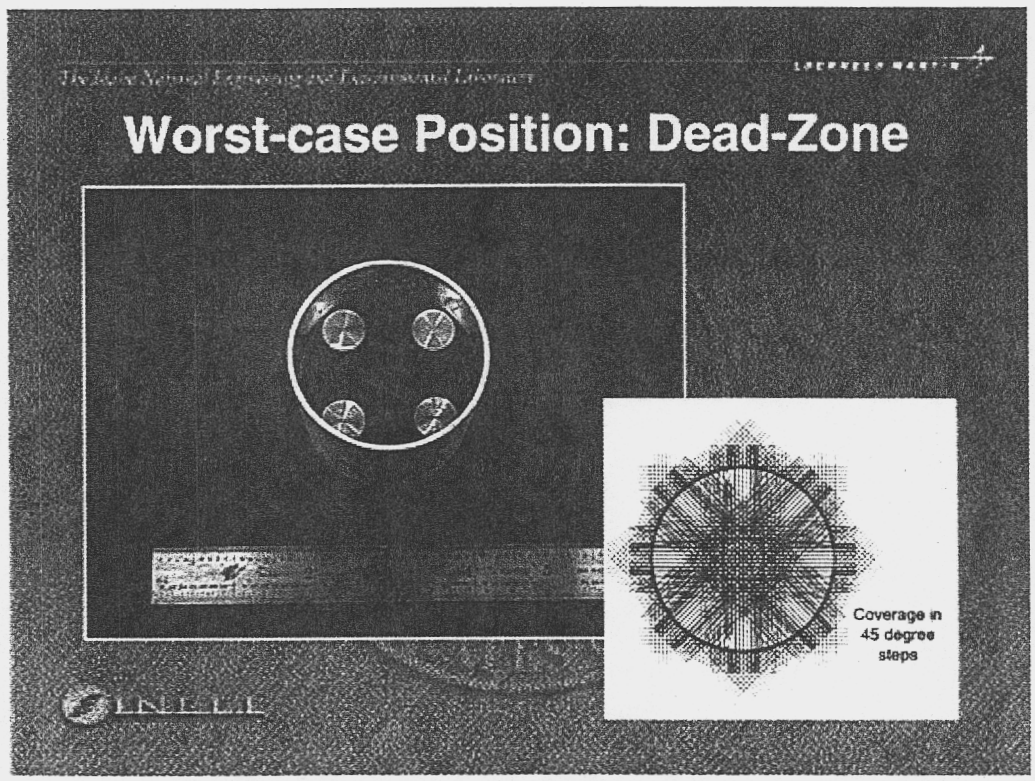
Worst-case Position: Dead-Zone
Coverage in 45 degree steps

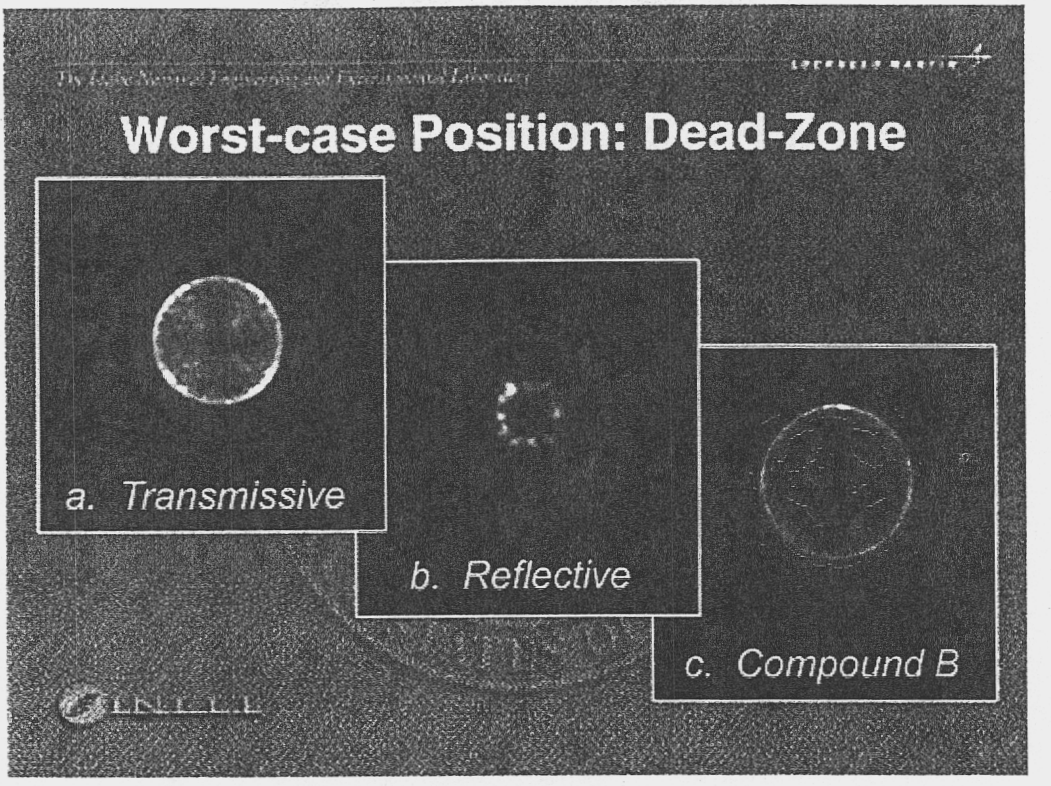
Worst-case Position: Dead-Zone
a. Transmissive
b. Reflective
c. Compound B

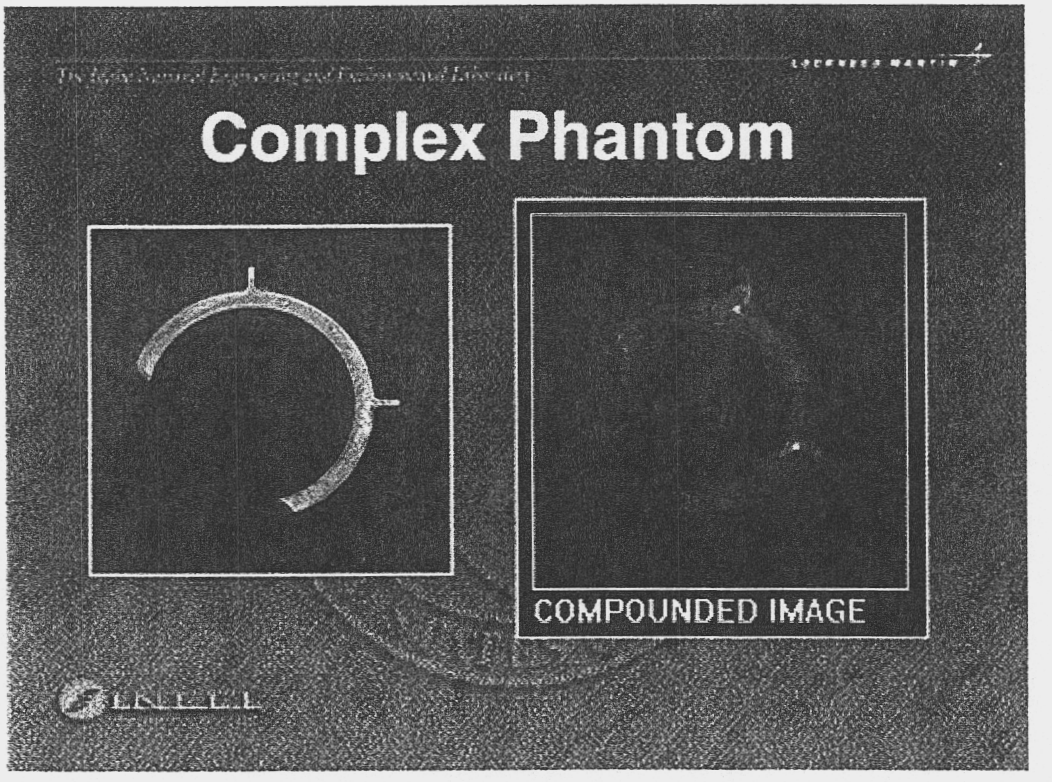
Complex Phantom
COMPOUNDED IMAGE

Gigahertz Photodetectors: *Faster, Smaller, Cheaper*

KE & JS Froeschner

Martin, Froeschner & Associates
14300 Mines Road
Livermore, California 94550 USA

tel: 520 409 1121
fax: 925 449 4647

Presented at the
Signal and Imaging Sciences Workshop
Sponsored by the Center for Advanced Signal and Imaging Sciences
at Lawrence Livermore National Laboratory
12 November 1998

Martin, Froeschner & Associates • 14300 Mines Road • Livermore, California • 94550 USA • tel: 520 409 1121 • fax: 925 449 4647

Lawrence Livermore National Laboratory

Adhesion assessed using shock-wave exfoliation

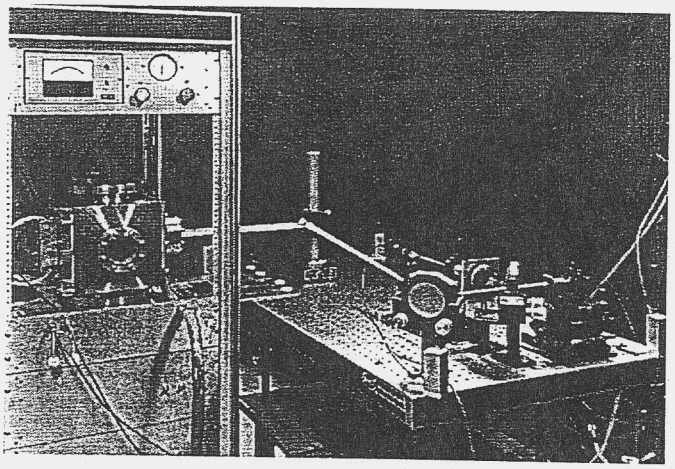

Martin, Froeschner & Associates • 14300 Mines Road • Livermore, California • 94550 USA • tel: 520 409 1121 • fax: 925 449 4647

Sub-nanosecond Velocimetry with a New Kind of VISAR

K.E. & J.S. Froeschner, A.G. Youssos, T. Timke and M. Kiriakopoulos

Commission of the European Communities Joint Research Centre Institute for Advanced Materials
Postbus 2, 1755 ZG Petten, The Netherlands

(KEF & JSF, Martin, Froeschner & Associates, 14300 Mines Road, Livermore, California 94550 USA)

Abstract

A fresh approach to the principles of the delay leg interferometer which was ultimately developed by Barker, Hemsing and others as the "VISAR" [Velocity Interferometer System for Any Reflector] has resulted in an implementation which is simple, reliable, cost effective and capable of velocity measurements with sub-nanosecond time resolution.

Results from laser induced shock exfoliation experiments which measure the adhesion strength of thin films on ceramic substrates are reported. These experiments require resolution of the shock structure produced by a 0.3 or 8 nanosecond Nd:YAG laser pulse interacting with a 0.5 to 1 micrometer thick energy absorbing layer deposited on the rear surface of the substrate/thin-film specimen, representative of an advanced turbine blade structure. Measurement of the velocity details of the film free surface during exfoliation, by Doppler shift of reflected laser light allows direct determination of the adhesion strength of the film/substrate interface at high strain rates and in ideal one-dimensional plane strain conditions.

The extremely small scale of the experiment requires very high time resolution. The Doppler Velocity Interferometer developed for these studies will be described in detail. Significant features include replacing the usual glass etalon with a zero-cost air delay leg, an extremely short optical path length, compact, rack-mounted configuration, all solid-state components including illumination by semiconductor diode laser and signal detection with sub-nanosecond PIN photodiodes.

in *22nd International Congress on High-Speed Photography and Photonics*, Dennis L. Paisley, Alan M. Frank, Editors, Proc. SPIE 2869, pages 1058-1064

Martin, Froeschner & Associates • 14300 Mines Road • Livermore, California • 94550 USA • tel:[+1] 510 909 1121 • fax:[+1] 925 449 1647

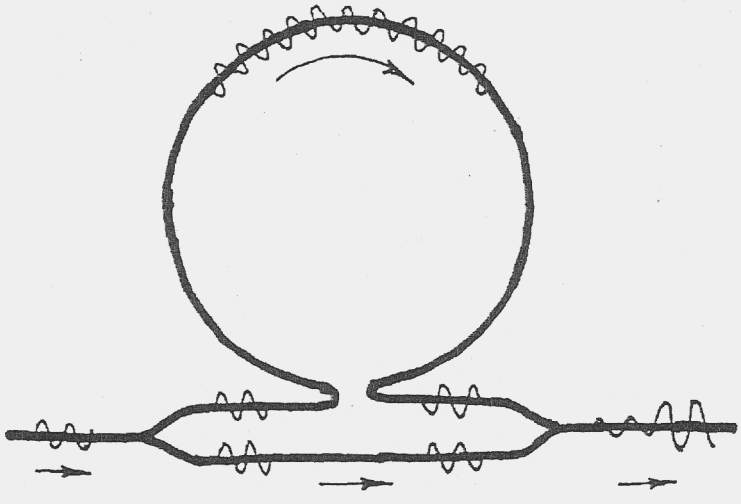

The Basic Delay Leg Interferometer

Martin, Froeschner & Associates • 14300 Mines Road • Livermore, California • 94550 USA • tel:[+1] 510 909 1121 • fax:[+1] 925 449 1647

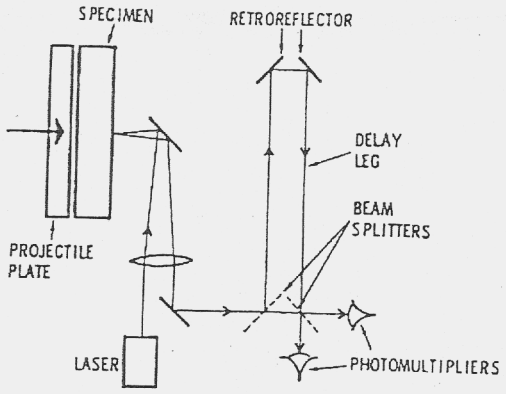

The Original Sandia Velocity Interferometer

Marion Froeschner & Associates • 11800 Vineyard Road • Livermore, California • 94550 USA • tel +1 510 449 1121 • fax +1 925 449 4647

COHERENT AND INCOHERENT LIGHT FROM SPIKE FILTER

$I_c(t) + I_I(t)$

The Barker-Hemsing Velocity Interferometer System for Any Reflector, "VISAR," in Full-Quadrature, Push-Pull Configuration

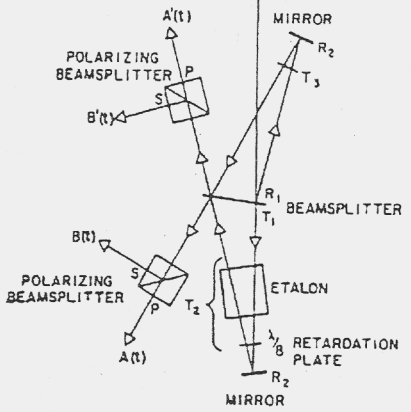

Marion Froeschner & Associates • 11800 Vineyard Road • Livermore, California • 94550 USA • tel +1 510 449 1121 • fax +1 925 449 4647

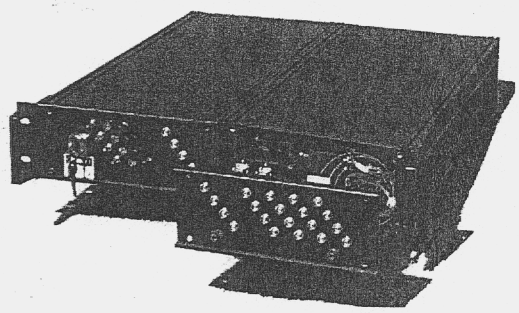

The MF&A Doppler Velocity Interferometer and Laser System

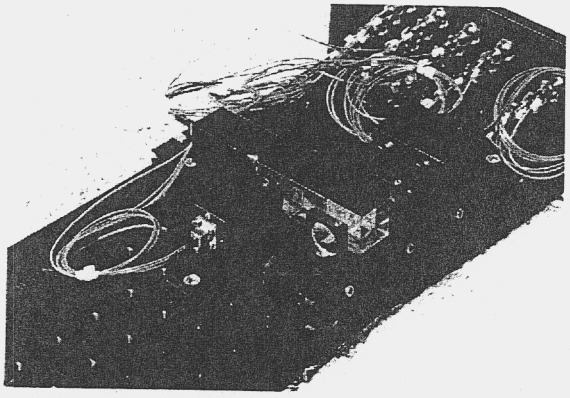

Inside the MF&A Doppler Velocity Interferometer

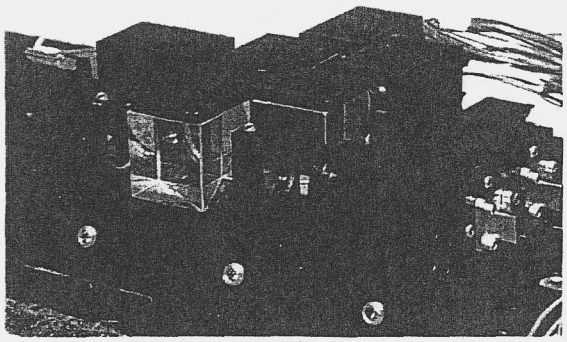

The Heart of the Interferometer:
A Cemented Prism Assembly That Never Needs Adjustment or Alignment

Wave Precision & Associates • 1400 Stea Road • Livermore, California • 94550 USA • tel [1] 510 606 1121 • fax [1] 925 449 [illegible]

Figure 4. Same experiment as above but with the time scale expanded. Note the shifting phase relationship between the fundamental and the first harmonic.

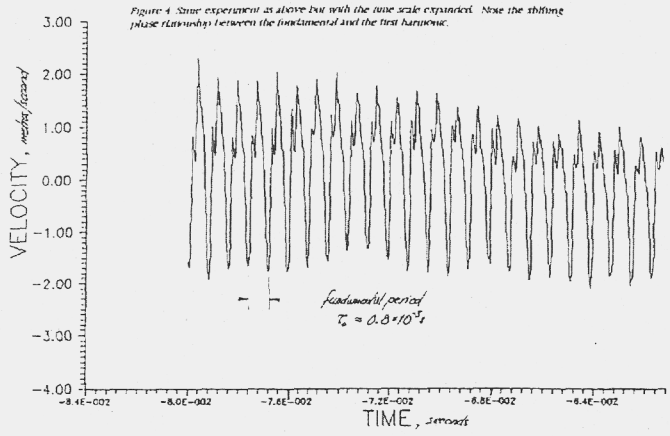

Vibration of Bond Paper Acoustically Driven at 1200 Hz

Wave Precision & Associates • 1400 Stea Road • Livermore, California • 94550 USA • tel [1] 510 606 1121 • fax [1] 925 449 [illegible]

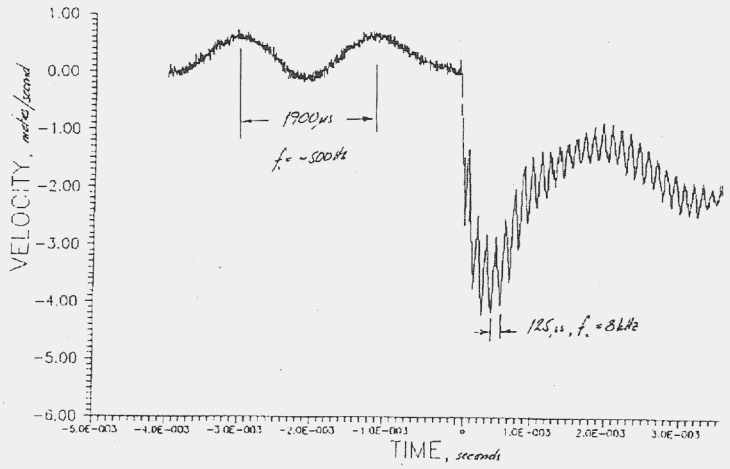

Response of a Thin Ti Diaphragm to a Nd:YAG Laser Pulse

Marvin Friedrichs & Associates • 1180 Shaw Road • Livermore California • 94550 USA • tel +1 510 490 1121 • fax +1 925 449 4647

Biased Detectors

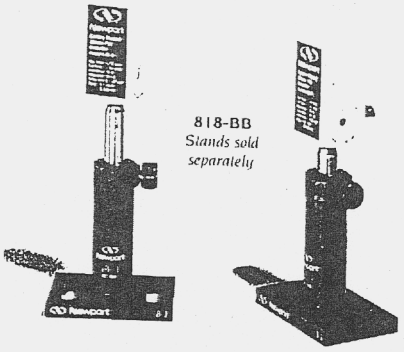

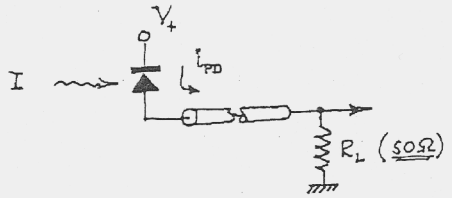

$$E = i_{PD} \cdot R_L$$
$$= I \cdot \text{Responsivity} \cdot R_L$$
$$\tau = R_L C$$
$$BW\,(-3dB) = 0.16\,\frac{1}{R_L C}$$

Biased Photodiode Circuit

Marin Broechart & Associates • 1430 Vista Road • Livermore, California • 94550 USA • tel (1) 510 400 1121 • fax (1) 925 449 4647

Fermionics *Opto-Technology*

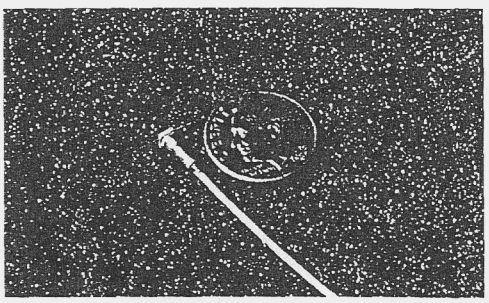

InGaAs Photodiode Bonded Directly To Optical Fibre End

Marin Broechart & Associates • 1430 Vista Road • Livermore, California • 94550 USA • tel (1) 510 400 1121 • fax (1) 925 449 4647

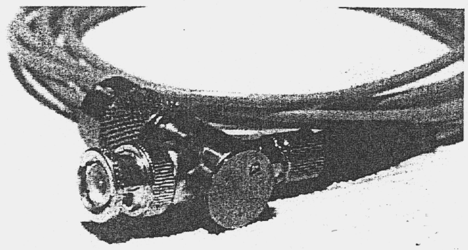

MF&A Series 99 Biased Photodiode Module

[illegible]

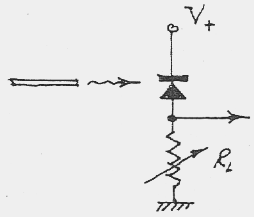

Optical Fibre to Scope
No co-ax!

Series 99 Photodetector Module with Variable Load Resistance

[illegible]

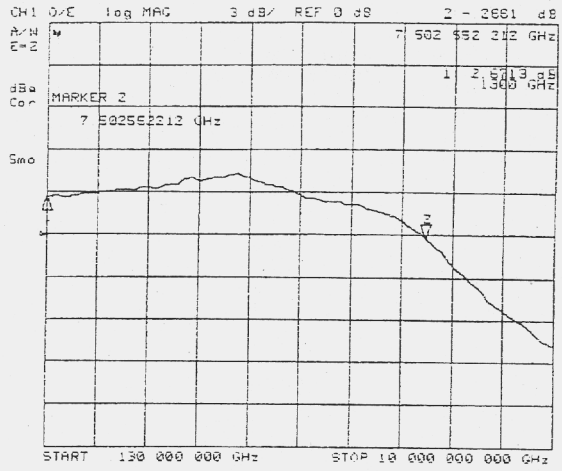

Frequency Response for Series 99 InGaAs-2 Biased Photodiode

Varna Enterprises • 14300 Vanes Road • Livermore, California • 94550 USA • tel 510 909 1121 • fax 510 925 449 4647

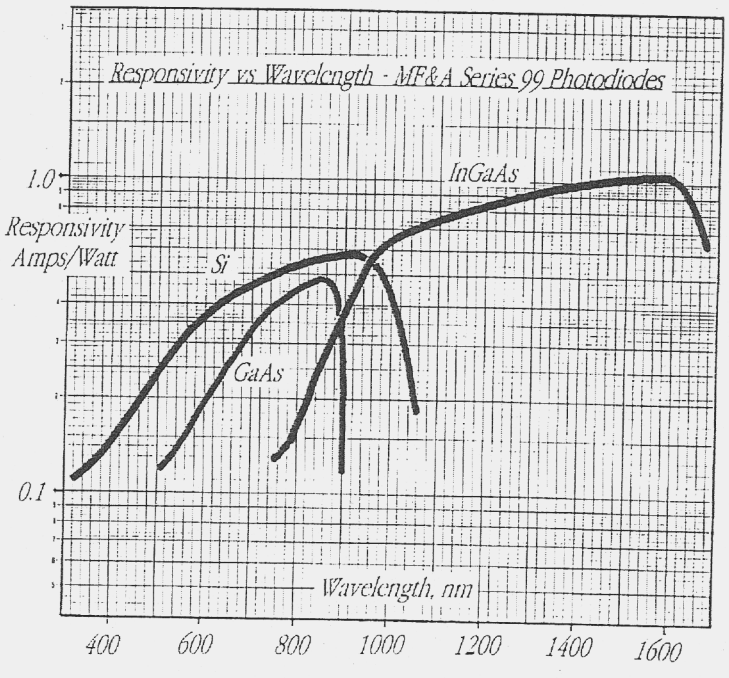

Varna Enterprises • 14300 Vanes Road • Livermore, California • 94550 USA • tel 510 909 1121 • fax 510 925 449 4647

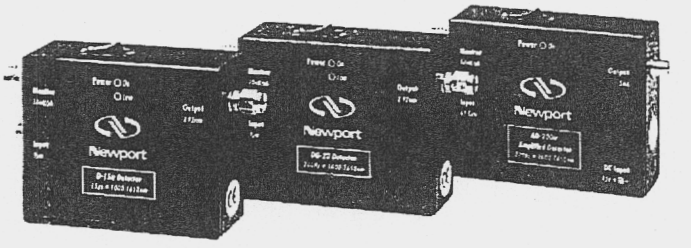

D Series Broadband Detectors (400-1700 nm)

Optical Conversion Gain vs. Bandwidth

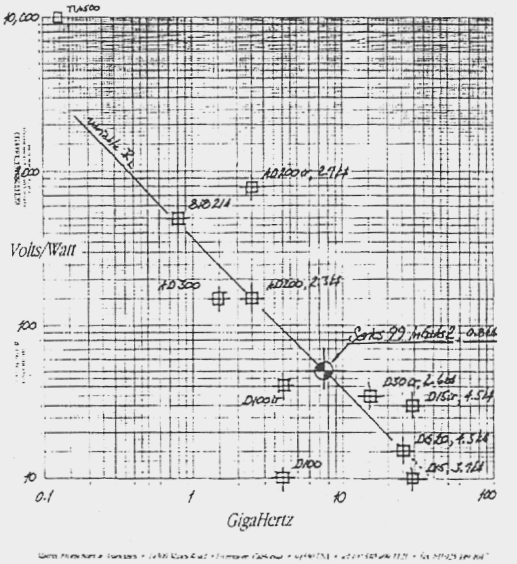

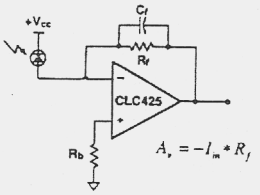

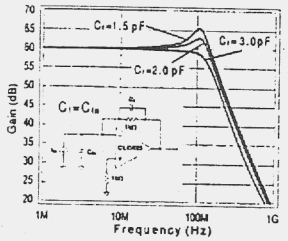

Classical Op Amp Transimpedance Amplifier

Maxim Freschner & Associates • 1400 Myers Road • Livermore, California • 91550 USA • tel (+1) 510 400 1121 • fax (+1) 925 449 4647

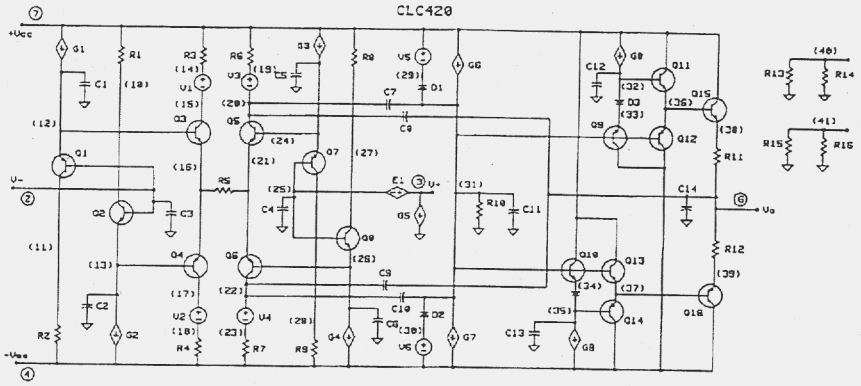

Typical Op Amp Internal Circuit Schematic

Maxim Freschner & Associates • 1400 Myers Road • Livermore, California • 91550 USA • tel (+1) 510 400 1121 • fax (+1) 925 449 4647

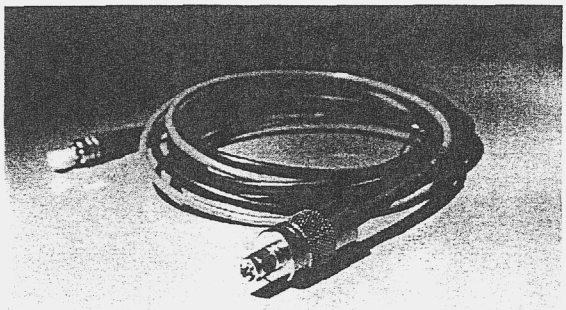

MF&A Series 99 Amplified Photodetector Module

Martin Fraschner & Associates • 11900 Mora Road • Livermore, California • 94550 USA • tel +1 510 606 1121 • fax +1 925 449 4647

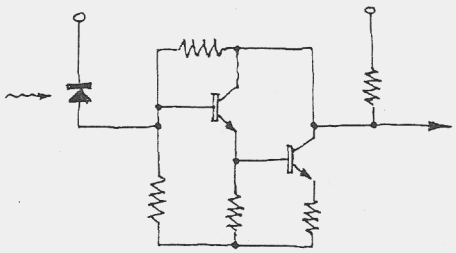

Heterojunction Bipolar Darlington Configuration used in MF&A Series 99 Amplified Photodetector Modules

Martin Fraschner & Associates • 11900 Mora Road • Livermore, California • 94550 USA • tel +1 510 606 1121 • fax +1 925 449 4647

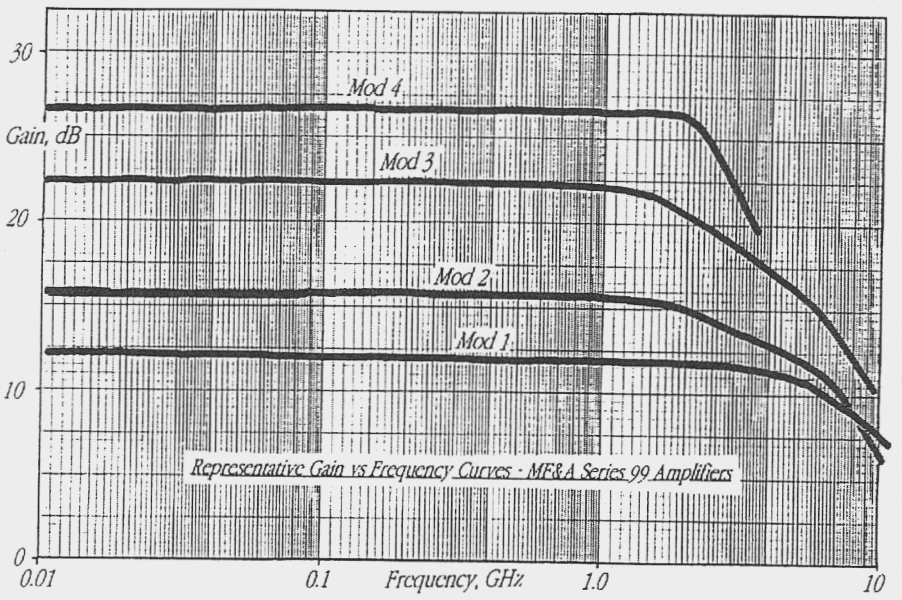

Marin Frenchner & Associates • 14300 Mines Road • Livermore, California • 94550 USA • tel 1-1 510 459 1121 • fax 1-1 925 449 4647

Optical Conversion Gain vs. Bandwidth

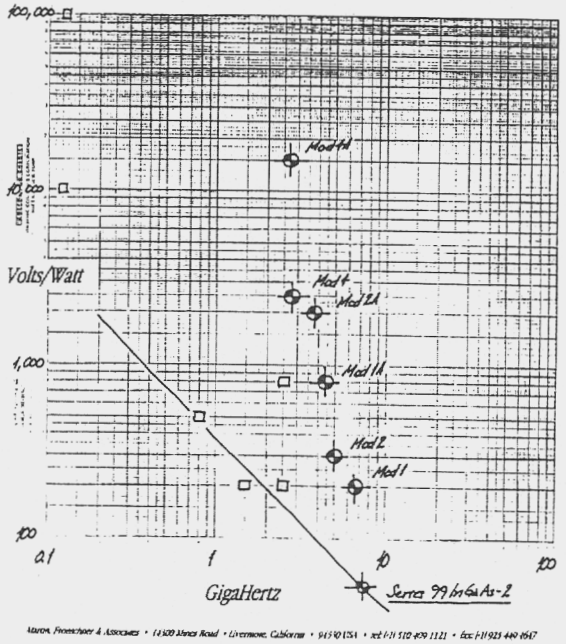

Marin Frenchner & Associates • 14300 Mines Road • Livermore, California • 94550 USA • tel 1-1 510 459 1121 • fax 1-1 925 449 4647

	Si-1	Si-2	GaAs	InGaAs-1	InGaAs-2
Spectral Range	400-1000 nm	320-1000 nm	450-870 nm	850-1700 nm	850-1700 nm
Responsivity	0.6 A/W@850	0.52 A/W@760	0.3 A/W@850	0.9 A/W@1550	0.9 A/W@1550
Bandwidth (-3db)	350 MHz	1.5 GHz	10 GHz	3.5 GHz	≥7.5 GHz
Rise/Fall Time	≤1 ns	230 ps	40 ps	100 ps	≤50 ps
Capacitance	8.5 pF	1.5 pF	0.2 pF	0.8 pF	0.17 pF
Active Area	2.54 mm dia.	400 µm dia.	200 µm sq.	100 µm dia.	60 µm dia.
Dark Current	≤10 nA	≤0.1 nA	≤0.3 nA	≤0.4 nA	≤0.4 nA

Photodiode Specifications

Martin Froeschner & Associates • 11300 Mines Road • Livermore, California • 94550 USA • tel +1 510 409 1121 • fax +1 925 449 4647

	Mod1	Mod2	Mod1A	Mod2A	Mod4	Mod4A
Bandwidth (-3dB)	DC to 10 Ghz	DC to 7 GHz	7 GHz	5 GHz	DC to 2.8 GHz	2.8 GHz
Rise/Fall Time	35 ps	50 ps	50 ps	70 ps	125 ps	125ps
Transimpedance	200 Ω	300 Ω	800 Ω	2,000 Ω	2,500 Ω	15,000 Ω
Noise Figure	5.3 dB @ 2GHz	4.7 dB @ 2GHz	10.6 dB @ αGHz	9.4 dB @ 2GHz	2.6 dB @ 1.5GHz	7.3 dB @ 1.5GHz
Coupling	DC or AC	DC or AC	AC only	AC only	DC or AC	AC only
Output Power (P_{1dB})	11.3 dBm	12.4 dBm	11.3 dBm	12.4 dBm	-2 dBm	12.4 dBm

Transimpedance Amplifier Specifications

Martin Froeschner & Associates • 11300 Mines Road • Livermore, California • 94550 USA • tel +1 510 409 1121 • fax +1 925 449 4647

Martin, Froeschner & Associates Series 99 Photodetector Modules

Comparison of Measured Risetimes to Specifications

	Serial No.	t_{meas}	t_{pd}	t_{amp1}	t_{amp2}	t_{calc}
InGaAs2 Mod1	135	55ps	≤50	35	–	61ps
Si2 Mod4 Mod 4	136	280ps	230	125	125	290ps
InGaAs1 Mod 3	091	100ps	100	120	–	156ps
InGaAs2 Mod2	105	62ps	≤50	50	–	71ps
InGaAs2 Mod1A	148	80ps	≤50	35	35	70ps

Risetimes are from 10% to 90% measured by independent laboratories.

$$t^2_{calc} + t^2_{pd} + t^2_{amp1} + t^2_{amp2}$$

Martin, Froeschner & Associates • 14300 Mines Road • Livermore, California • 94550 USA • tel:[+1] 510 409 1121 • fax:[+1] 925 449 4647

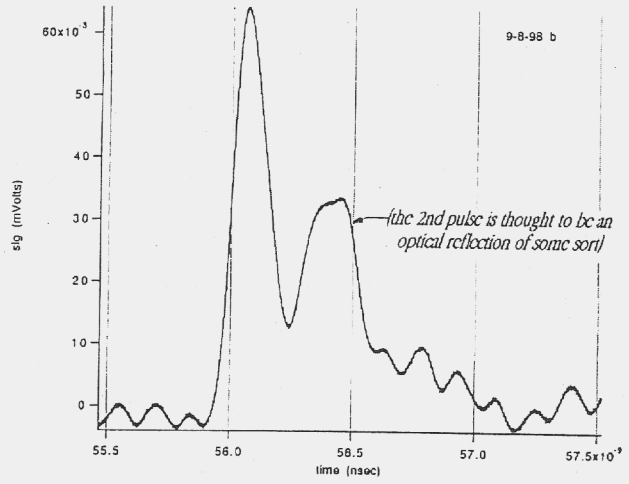

Response of Series 99 InGaAs-2 Mod 1A Photodetector to 90 femtosecond 820nm Pulse

Martin, Froeschner & Associates • 14300 Mines Road • Livermore, California • 94550 USA • tel:[+1] 510 409 1121 • fax:[+1] 925 449 4647

Noise Recorded by Independent Lab (CIENA Corporation)

$$N_{Series\ 99} = \sqrt{1.98^2 + 1.24^2} = 1.5mV\ rms$$

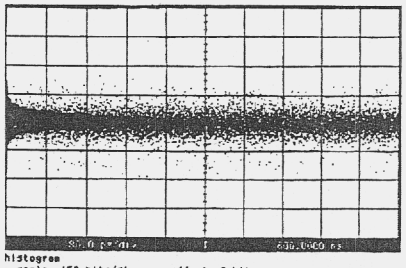

histogram
scale 150 hits/div offset 0 hits
mean 96.4076 µV median 156.8625 µV µ±1σ 78.6%
std dev 1.24213 mV hits 10.98 khits µ±2σ 95.6%
p-p 16.3137 mV peak 751 hits µ±3σ 98.7%

Baseline

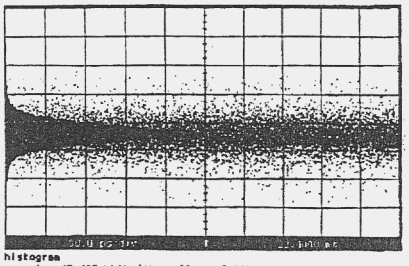

histogram
scale 47.485 khits/div offset 0 hits
mean 111.0424 mV median 111.0607 mV µ±1σ 75.6%
std dev 1.98305 mV hits 5.632 Mhits µ±2σ 95.5%
p-p 33.7255 mV peak 237.4 khits µ±3σ 98.8%

Series 99 InGaAs-2 Mod 1 with DC Offset Null

Alarm, Incochran & Associates • 1400 Vines Road • Livermore, California • 94550 USA • tel:[+1] 510 409 1121 • fax:[+1] 925 449 4547

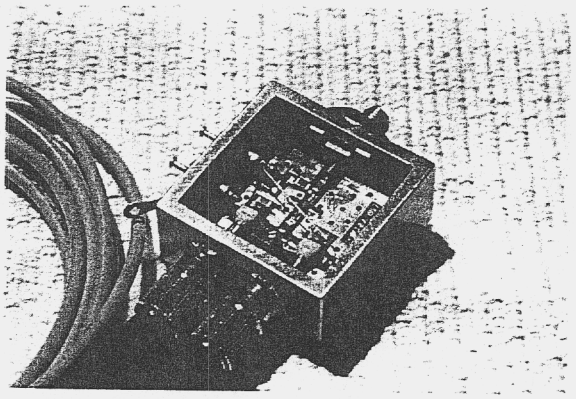

MF&A 2.5 Gb/scc Differential Optical Receiver

Alarm, Incochran & Associates • 1400 Vines Road • Livermore, California • 94550 USA • tel:[+1] 510 409 1121 • fax:[+1] 925 449 4547

Martin, Froeschner & Associates

Series 99 Fast Compact Photodetector Modules

A new line of inexpensive and compact fiber-coupled photodiode modules simplify capturing fast [...] light signals for analysis. These devices are intended to approximate as closely as possible, a length of fiber optic cable that can be connected directly into the input jacks of your oscilloscope or other electronic data acquisition device. Conversion of the optical signal to electronic current and voltage occurs at the last possible moment, within a mm or so of the input jacks of your scope. Coax cable and the problems of reflections, termination loads, phase distortion and so forth are totally eliminated. The devices are extremely compact and rugged, taking up about as much room as a typical BNC terminator. They come in unamplified versions for use when sufficient light is available, and amplified versions for low light levels.

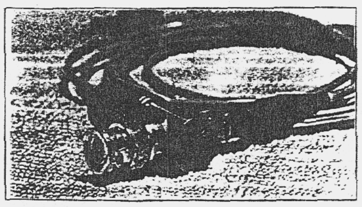

Dimensions: 0.55" (16mm) diameter by 1" to 1.75" (25 to 40 mm), excluding connectors and optical fiber
Construction: machined from solid brass, plated, internal components potted in resin
Power: internally contained, easily replaceable alkaline battery or optional cable to External Power Supply
Controls: On/Off switch incorporated in battery housing. Variable Load and other Options use a multi-turn cermet pot

Optical Fiber and Connector

We will build your modules with whatever optical fiber, cable and connectors you specify. We normally stock single mode 9/125µm and both 50/125µm and 62.5/125µm multimode fiber with 0.9mm polymer buffer and 3mm kevlar jacket. Other types such as 100/140 µm are available. The fiber to photodiode connection is angle polished for low (-45dB) back reflection.

The input end of the optical fibre will be fitted with whatever type of optical fibre connector you desire. The range of normal options include: none, i.e. a bare fibre pigtail, 2mm ceramic ferrule only, NTT-FC, SC, ST and SMA. The fibre end itself will be polished to any of the standard specifications flat, PC, SPC or APC(8°). If you need something else, just specify so on the Order Form.

Optional Light-Collecting Optics

If the signal you want to analyze is in the form of a beam in free-space we can provide light collecting optics instead of or in addition to the optical fibre connectors described above. The simplest is a 2mm diameter GRIN lens and ferrule assembly permanently fixed on the end of the fibre. For larger beams a 6mm diameter fixed focus aspheric lens assembly is available. We also offer a micro-alignable fixture with 18mm aperture focusable achromatic lens. Precision fine thread adjustments allow you to maximize the coupling of the incoming beam into the fibre. The unit is also directly compatible with "micro-rail" optical component systems made by Newport, Melles Griot, Thorlabs and others and is "C" threaded for compatibility with Edmund Scientific's modular component line. Finally, large aperture catadioptic systems for collecting light from weak, extended or distant sources can be provided. Details available upon inquiry.

Photodiode Selection

The two major considerations in selecting the photodiode for your application are spectral response and speed. Photodiodes based on different semiconductor materials have, in general, different ranges of light wavelength to which they are most sensitive. For example, Silicon based diodes are most sensitive in the 400nm (nearly UV) to 1000nm (near IR) spectral range and cover the visible well. InGaAs is relatively insensitive to visible light but responds well to the IR used in information systems.

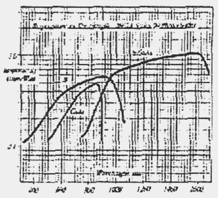

The intrinsic speed of the photodiode is also determined by the semiconductor material. The higher electron mobility in InGaAs allows response times which are simply not attainable with Si. Our latest GaAs model offers unprecedented speed in the visible range. Other factors which might be important to your needs, such as Dark Current and Capacitance are also listed in the table on the next page.

The photodiode in all our modules is reverse biased to minimize intrinsic capacitance for maximally fast response.

Estimation of Signal Level

You can estimate the signal level (voltage) that you can expect to see, for your light intensity, directly from the Responsivity as shown in the graph above and in the table below, from

dV[volts] = dI[watts] • Responsivity [amps/watt] • R[ohms]

where dV is the change in output signal corresponding to a change of dI in the light power input and R is the load resistance, normally 50Ω. Since the Responsivity is near unity, in general you will need on the order of 10mW in the optical input fibre in order to get output signals in the 100mV range.

Photodiode Specifications (others available, call or write for details)

	Si-1	Si-2	GaAs	InGaAs 1	InGaAs 2
Spectral Range	400-1000 nm	320-1000 nm	450-870 nm	850-1700 nm	850-1700 nm
Responsivity	0.6 A/W@900	0.52 A/W@850	0.3 A/W@850	0.9 A/W@1550	0.7 A/W@1550
Bandwidth (-3db)	350 MHz	1.5 GHz	10 GHz	3.5 GHz	≥7.5 GHz
Rise/Fall Time	≤1 ns	250 ps	40 ps	100 ps	≤50 ps
Capacitance	85 pF	1.5 pF	0.2 pF	0.8 pF	0.17 pF
Active Area	2.54 mm dia.	400 µm dia.	30 µm sq.	100 µm dia.	60 µm dia.
Dark Current	≤10 nA	≤0.1 nA	≤0.3 nA	≤0.4 nA	≤1.0 nA
Detachable Optical Fiber	yes	yes	no	no	no

Transimpedance Amplifier Option

When the light level gets below the mW regime, the expected signal is uncomfortably near the noise floor of most systems. In order to get acceptable signal levels from very low light levels the current from the photodiode must be amplified. In the Series 99 we use hybrid bipolar technology in Darlington configurations. Expected signal levels can be estimated using the previous equation, but substituting the Transimpedance Gain from the table below in place of the load resistance. It should be noted that the gain figures in the specification below are approximate and that actual performance may differ by up to a factor of two depending on amplifier product variations, output loading and so on.

Measurements of the noise spectrum have been made by independent labs on several of our systems. An InGaAs-2 Mod1 with DC Offset Null contributed about 1.5mV rms over 20GHz with power on to both amplifiers and the photodiode and no light input. (The scope by itself had an intrinsic noise floor of about 1.2mV rms.) Calculations show this to be consistent with the Noise Figure specified below. The equivalent optical noise density at the input is about 50pW Hz$^{-1/2}$. An AC coupled InGaAs-2 Mod2 system tested at one of the National Laboratories showed a 0.5mV rms noise floor, also consistent with the Noise Figure. The equivalent optical input noise density is about 90pW Hz$^{-1/2}$. This system reliably receives differential digital data at 2.5Gb/s with light levels as low as a few µW peak.

Transimpedance Amplifier Specifications (others available, call or write for details)

	Mod1	Mod2	Mod1A	Mod2A	Mod4	Mod4A
Bandwidth (-3dB)	DC to 3.0GHz	DC to 7 GHz	7 GHz	5 GHz	DC to 2.6 GHz	3.0 GHz
Rise/Fall Time	55 ps	50 ps	50 ps	70 ps	125 ps	125ps
Transimpedance	200 Ω	300 Ω	900 Ω	2100 Ω	2500 Ω	15,000 Ω
Noise Figure	5.5 dB @ 5GHz	4.2 dB @ 5GHz	3.86 dB @ 3GHz	6.4 dB @ 3GHz	2.6 dB @ 1.5GHz	7.3 dB @ 1.5GHz
Coupling	DC or AC	DC or AC	AC only	AC only	DC or AC	AC only
Output Power (P_{1dB})	11.5 dBm	12.4 dBm	11.5 dBm	12.4 dBm	[illegible] dBm	12.4 dBm

Keep in mind that the transimpedance amplifier is an option. If your light levels are adequate, use the basic configuration (unamplified but biased photodiode) without the added current drain, cost and noise of an amplifier.

Output Electrical Connector

Electronic output connector choices include BNC, TNC, Type N, SMA and SMC in either gender. Wiltron K, 7/16 and others are available at some extra cost. If you need something really unusual, specify on the Order Form or call to discuss your needs.

Output Coupling and Offset Null Option

The output signal can be connected directly to the output connector, DC coupling, or through a capacitor, AC output coupling.

Amplified versions which are DC coupled will have an output offset bias of several volts when the photodiode is dark, due to transistor biasing. This offset is eliminated with the DC Offset Null option which uses a second matched reference amplifier to drive the ground side of the output connector. A multi-turn precision pot controls the input to this second amplifier so that any residual offset due to amplifier mismatch, photodiode dark current or background light can be trimmed out.

Amplified versions are also available with AC output coupling through a capacitor. The higher gain versions use two stages of amplification and are currently available only as AC coupled units.

Termination, Variable Load and Gain Options

These modules are designed to be mounted directly onto the input jack of your scope. When used this way there is no coax cable to cause reflections so terminating with exactly 50Ω is not necessary. With unamplified modules the terminal or load resistance directly affects both the signal level and bandwidth. A unique optional feature available on unamplified Series 99 modules is a Variable Load resistance, a multi-turn precision potentiometer which can be adjusted to high values for maximum sensitivity during alignment, for instance. Once you have found the beam you can reduce the sensitivity and maximize the bandwidth. You can fine tune the gain-bandwidth tradeoff to meet your systems particular needs.

The output impedance of the amplified modules is already low so you should set the input impedance of your scope to 1MΩ. The amplifiers will drive a 50Ω load but there may be a reduction in signal level. If you need to drive a 50Ω load with an amplified DC coupled module you will need the DC Offset Null option and should have external power.

Output signal level in the amplified versions can be controlled over about a 6dB range by varying the supply voltage. The MF & A External Power Supply has a precision multi-turn potentiometer on the front panel for this purpose.

Power Considerations

The unamplified modules have very low current drain and the small internal batteries should last for a year or so of normal use.

In the amplified modules, internal replaceable battery life is short. Use of the power cord configuration and an external power supply is recommended. Any power supply is a potential source of noise. The MF & A External Power Supply provides noise free power to the photodiode and amplifiers from gel-cell batteries which are charged when the photodetector module is not in use. When the photodetector module is active, the system is completely disconnected from the external AC source, and power is provided through a shielded cable. A larger rack mount version will power up to sixteen Series 99 Photodetector Modules with individual control over each.

You can have a Series 99 PHOTODETECTOR MODULE built to your specifications.

LASERS & OPTRONICS TECHNOLOGY AWARD WINNER '97

Input Optical Connector & Polish:
☐ none ☐ flat
☐ 2mm ferrule ☐ PC
☐ NTT-FC ☐ SPC
☐ SC ☐ APC (8°)
☐ ST ☐ other _____
☐ SMA
☐ other ___

Light-Collection Optics:
☐ none
☐ 2mm GRIN *($125)*
☐ 9mm fixed aspheric *($225)*
☐ Alignable Micro-Rail & "C" thread compatible *($395)*
☐ large aperture (inquire)

Photodiode:
☐ Si-1, 400-1000nm, 350 MHz *($595)*
☐ Si-2, 320-1000nm, 1.5 GHz *($795)*
☐ GaAs, 450-870nm, 10 GHz *($895)*
☐ InGaAs-1, 850-1700nm, 3.5 GHz *($695)*
☐ InGaAs-2, 850-1700nm, ≥7.5 GHz *($795)*
Variable Load Option: ☐ continuous 10-10kΩ *($95)*

Optical Cable:
☐ 9/125 µm single mode
☐ 50/125 µm multimode
☐ 62.5/125 µm multimode
☐ other _____

Jacket:
☐ 0.9mm buffer only
☐ 3mm Kevlar and Polymer over 0.9mm buffer
☐ other _____

Length:
☐ 1 meter (standard)
☐ other _____

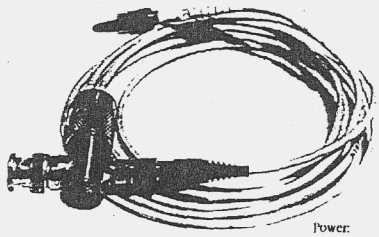

Amplifier: ☐ none ☐ yes
Amplifier Options:
☐ Mod1, 10GHz *($175)*
☐ Mod2, 7GHz *($175)*
☐ Mod1A, 7GHz *($350)*
☐ Mod2A, 5GHz *($350)*
☐ Mod4, 2.8GHz, High Gain *($175)*
☐ Mod4A, 2.8GHz, Very High Gain *($350)*

Power:
☐ internal batteries ☐ external power cable, 2 meter shielded

External Power Supply:
☐ 12volt rechargeable gel-cell with EMI/RFI shielding *($125)*
☐ Multiple Output Rack Mount version, powers up to 16 modules *($425)*

Output Electronic Connector & Gender:
☐ BNC ☐ male plug (as shown)
☐ TNC ☐ female jack
☐ N, 50 Ohm
☐ N, 75 Ohm ☐ SMA
☐ SMC
☐ other _____

Output Coupling:
☐ AC (user-frequency ___ ___
☐ DC
☐ DC with Offset Null Option *($105)*

If your needs are not covered by the range of possibilities listed above, don't give up or throw this away. Phone us or fax us to discuss your particular requirements in detail.

Hamm Precision & Associates • 14300 Doolittle Road • Livermore, California • 94550 USA • tel (1) 510 870 1221 • fax (1) 925 449 4647

InGaAs Linescan Camera System for Paper Web Moisture Measurements

By Jose E. Hernandez

The latest results in applying InGaAs sensor technology for measuring moisture on paper will be presented. Traditionally lead sulfide sensors have been used for measuring moisture on paper at 1.9 microns. The lead sulfide detector is a photo resistive element, and requires complex electronics and temperature stabilization to work properly. InGaAs on the other hand operates in a photo voltaic mode, which is quite stable, however, standard InGaAs only operates to about 1.7 microns. We will present preliminary results of a system that has been tested on a paper web using a less optimum absorption band at 1.4 microns, but which benefits from using an InGaAs based linescan camera system. This system also has the main benefit of providing a continuos moisture measurement across the entire web, compared to current scanning systems which only sample a small percentage of the web.

Evaluation of an Amorphous Selenium Array for Industrial X-Ray Imaging

Clint Logan, Lawrence Livermore National Laboratory

The large market for digital x-ray imaging in medicine has driven the development of flat panel imaging devices. We evaluated one such device using the higher energy x-rays typical of industrial applications. This imager is a 360 x 430-mm array employing amorphous selenium (amSe). It was developed and manufactured by Sterling Diagnostic Imaging. Liberty Technologies is developing a product for the NDE market. We obtained this array from Liberty Technologies.

The defining characteristic of this technology is that electrons produced by radiation interaction in the Se are directly collected and processed. There is no intermediate scintillation or other conversion process. We compare performance to existing LLNL technology. We found:

- Modulation transfer function remains high as spatial frequencies approach the limit imposed by the 139 μm pixel size.
- Increasing x-ray energy degrades spatial resolution performance somewhat, but the amSe imager performs well in spectra as energetic as 450-kV applied potential.
- The low-frequency response, <0.1 mm-1, of this amSe imager is poor at energies of interest to NDE. Secondary radiation transport in material behind the Se is a significant contributor to this attribute.
- Required exposure for the spectra tested ranges from 10 to 100 mRoentgen. This is 15 to 100 times less than LLNL's home-built system employing scintillating glass and a CCD camera. Cycle time for CT applications will be dominated by read and refresh time of nearly 1 minute. This will allow for great flexibility in utilizing microfocus (low power) sources or large souce-to-detector distances.
- Except for issues of peripheral electronics, which we did not address, Monte Carlo simulations suggest that this amSe imager could offer attractive performance at x-ray energies of 3 MeV or more.

This amSe imager shows great promise for digital radiography and CT. We encountered no problems in operating it in x-ray spectra up to 450 kV applied voltage.

UCRL-JC-132315 Abs

Evaluation of an Amorphous Selenium Array for Industrial X-Ray Imaging

Clint Logan,
Jerry Haskins, Kenn Morales and Earl Updike, Jim Fugina, Tony Lavietes,
Dan Schneberk, Greg Schmid and Keo Springer

Peter Soltani
Liberty Technologies, Inc
Conshohocken PA

Ken Swartz
Sterling Diagnostic Imaging
Newark, Delaware

Signal and Imaging Sciences Workshop
November 12, 1998

amSe imager directly collects electrons with no intermediate conversion to light

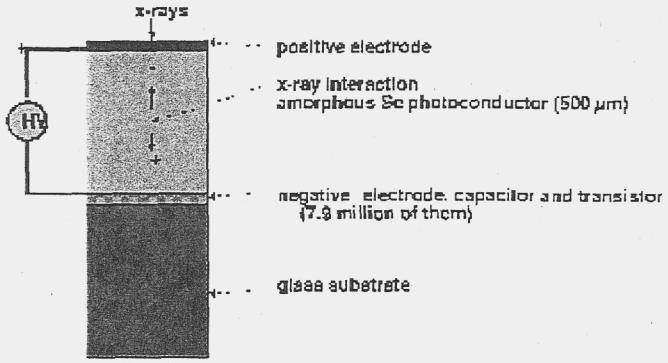

pixel pitch	139 μm (Nyquist of 3.6 lp/mm)
fill factor	86%
digitizing	14 bits
active area	14 inch x 17 inch (2,560 x 3,072 pixels)

We evaluated performance with three heavily-filtered spectra

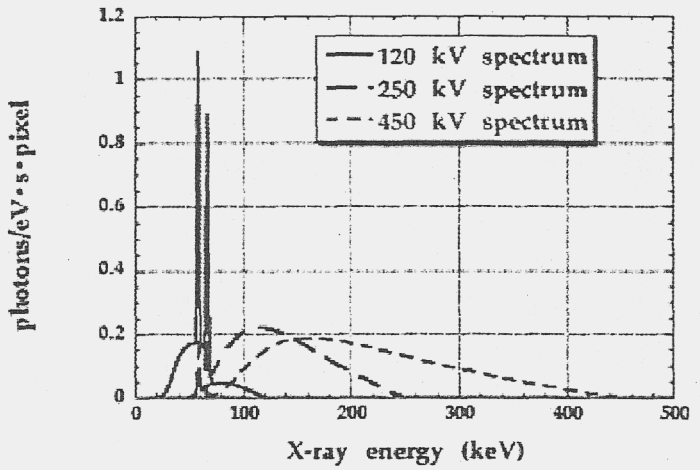

Monte Carlo results indicate degraded MTF as energy increases

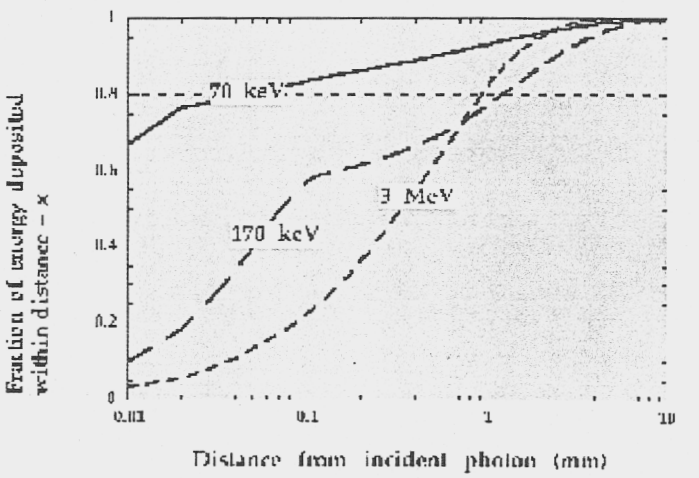

We used a 450-kV Philips source at 3 m

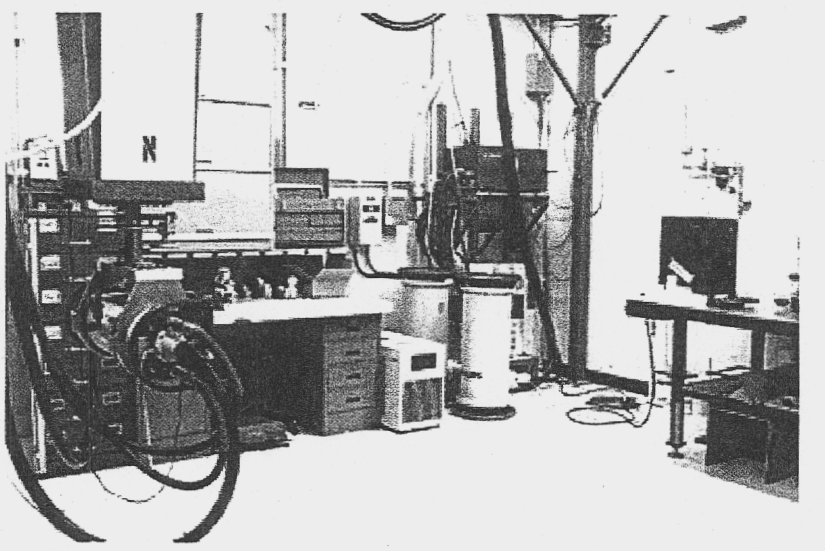

Test objects are:
an edge, a slug, and a line-pair gage

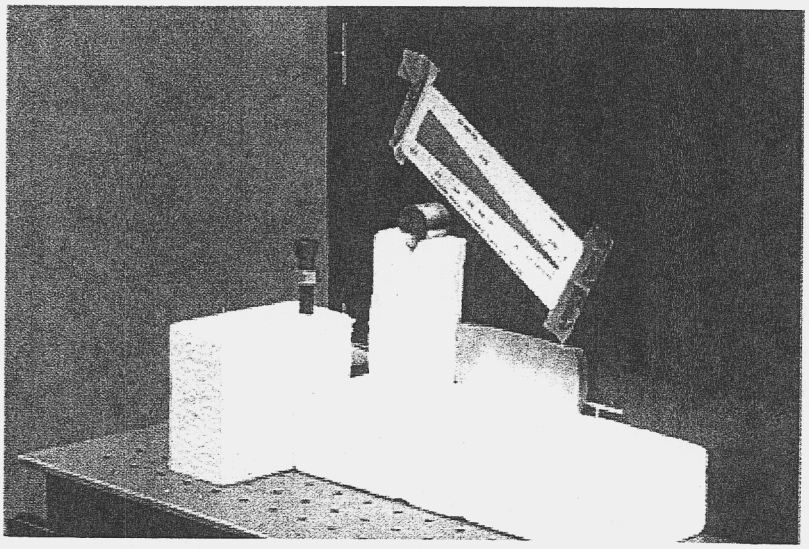

The amSe imager requires fewer x-rays than a lens-coupled CCD system

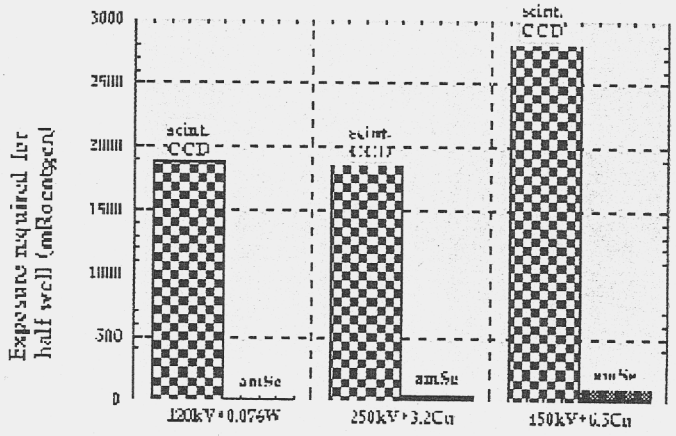

MTFs for amSe in three x-ray spectra

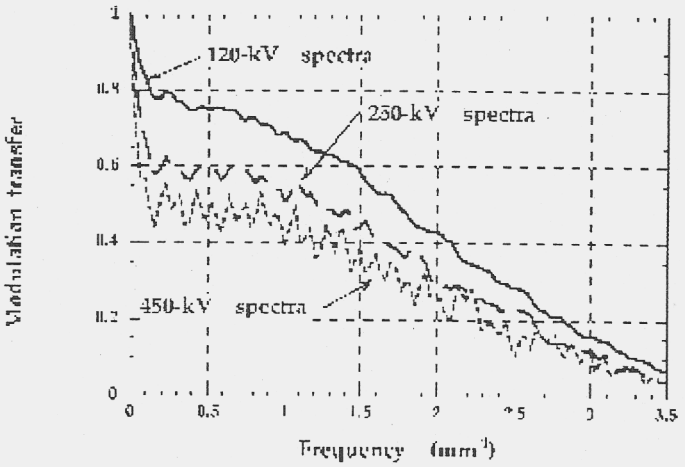

amSe is superior to glass/CCD at all but the lowest spatial frequencies

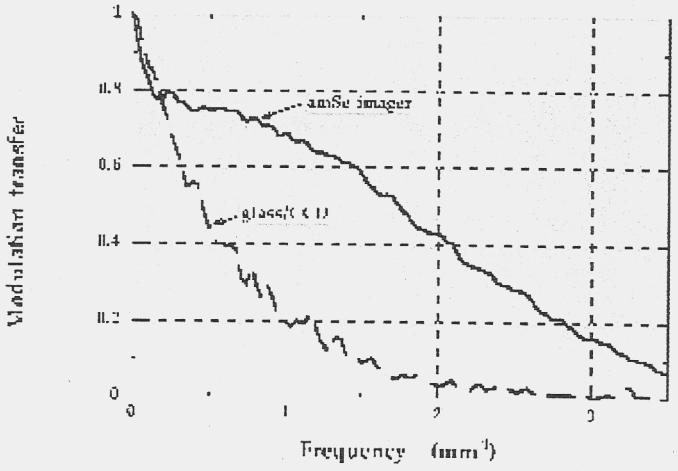

poor low frequency MTF for amSe imager is evident in image of a slug

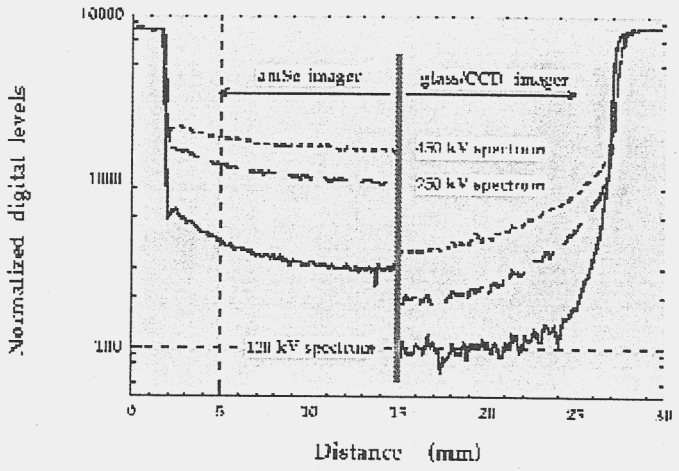

Let the images speak

The object is a Pb line pair gage 0.1 mm thick.
The x-ray spectrum is the 450-kV spectrum, so the object is very low contrast.
Images are raw with no corrections.

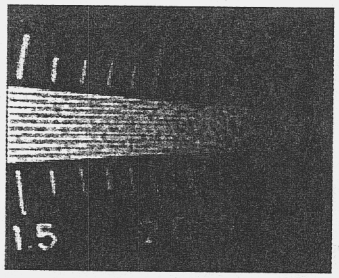

glass/CCD

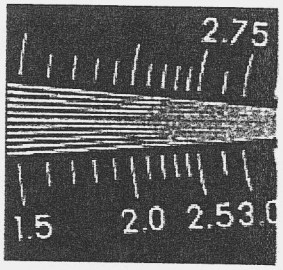

amSe

The amSe imager has extremely interesting attributes.

Matched Field Imaging of Laser-Based Ultrasound Data

Robert Huber, James Candy
Lawrence Livermore National Laboratory

Laser-based ultrasonic nondestructive evaluation is a non-contact testing and characterization technique that extends the application of ultrasonic testing to a wider variety of testing situations. This includes materials at elevated temperature, parts with curved surfaces, components with highly polished surfaces, which would be damaged by contact or immersion techniques, and hazardous materials. Although, laser-based ultrasound offers several advantages over traditional piezoelectric transducer ultrasound, its lower sensitivity restricts its use. Signal processing offers a way of increasing the sensitivity of laser-based ultrasound. Matched field imaging has been applied to data obtained from laser-based ultrasound tests. This signal processing technique uses a novel correlation canceling approach to locate flaws in parts. This technique compares data obtained from a real part to data obtained from a flawless reference. Through this processing, information that correlates between the two data sets is eliminated, leaving information about any flaws present in the part. Data will be presented on tests run on an aluminum part before and after a drill hole was placed in the part. Images obtained using the matched-field technique will be shown.

This work was performed under the auspices of the Department of Energy by the Lawrence Livermore National Laboratory under contract W-7405-Eng-48.

Matched Field Imaging of Laser-Based Ultrasound Data

Robert Huber

James Candy

Talk Organization

- Introduction
- LU Problem (Defect detection and imaging)
- Signal Pre-processing
- Matched Field Imaging
- Summary

PZT or LBU

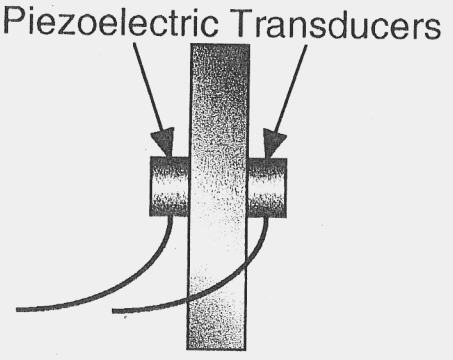

Great SNR
Eye Safe

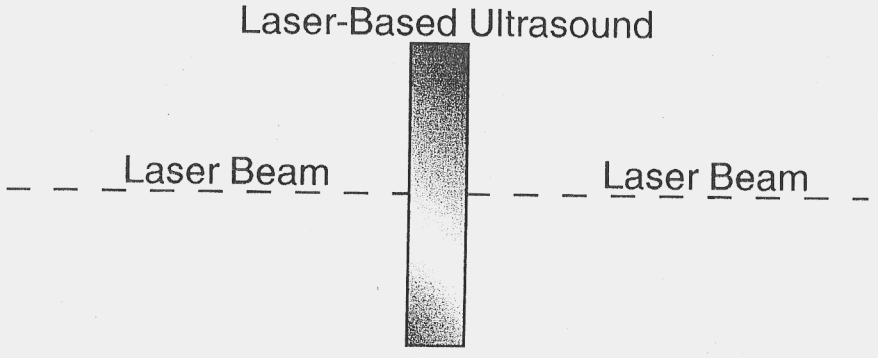

Non-contact
Remote
Small Footprint
Does not load or
damage surface

Signal Variation

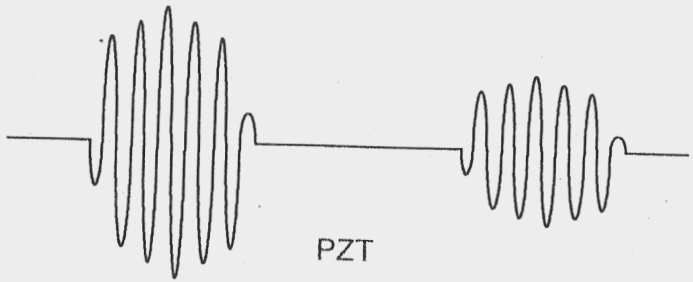

PZT

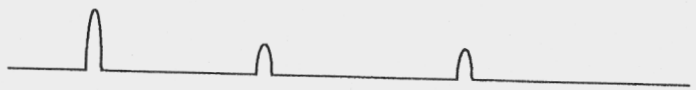

LBU Ablative

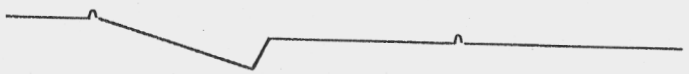

LBU Thermoelastic

Test Configuration

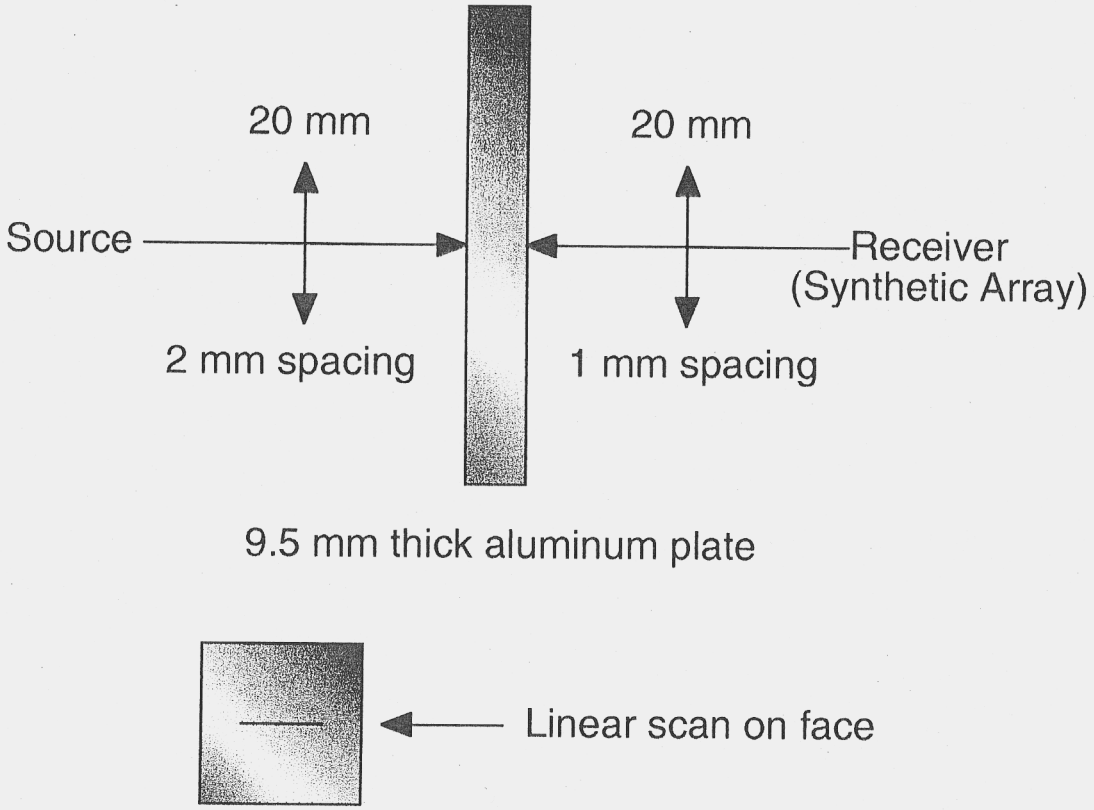

Two Problems That Interest Us:

- Defect Detection (Epicenter Only)
- Localization/Imaging (Synthetic Array)

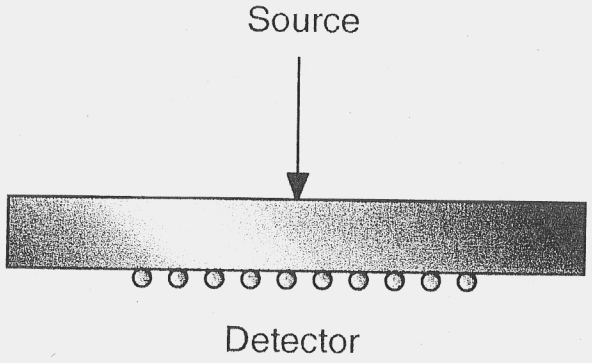

Synthetic array data set for one source location.

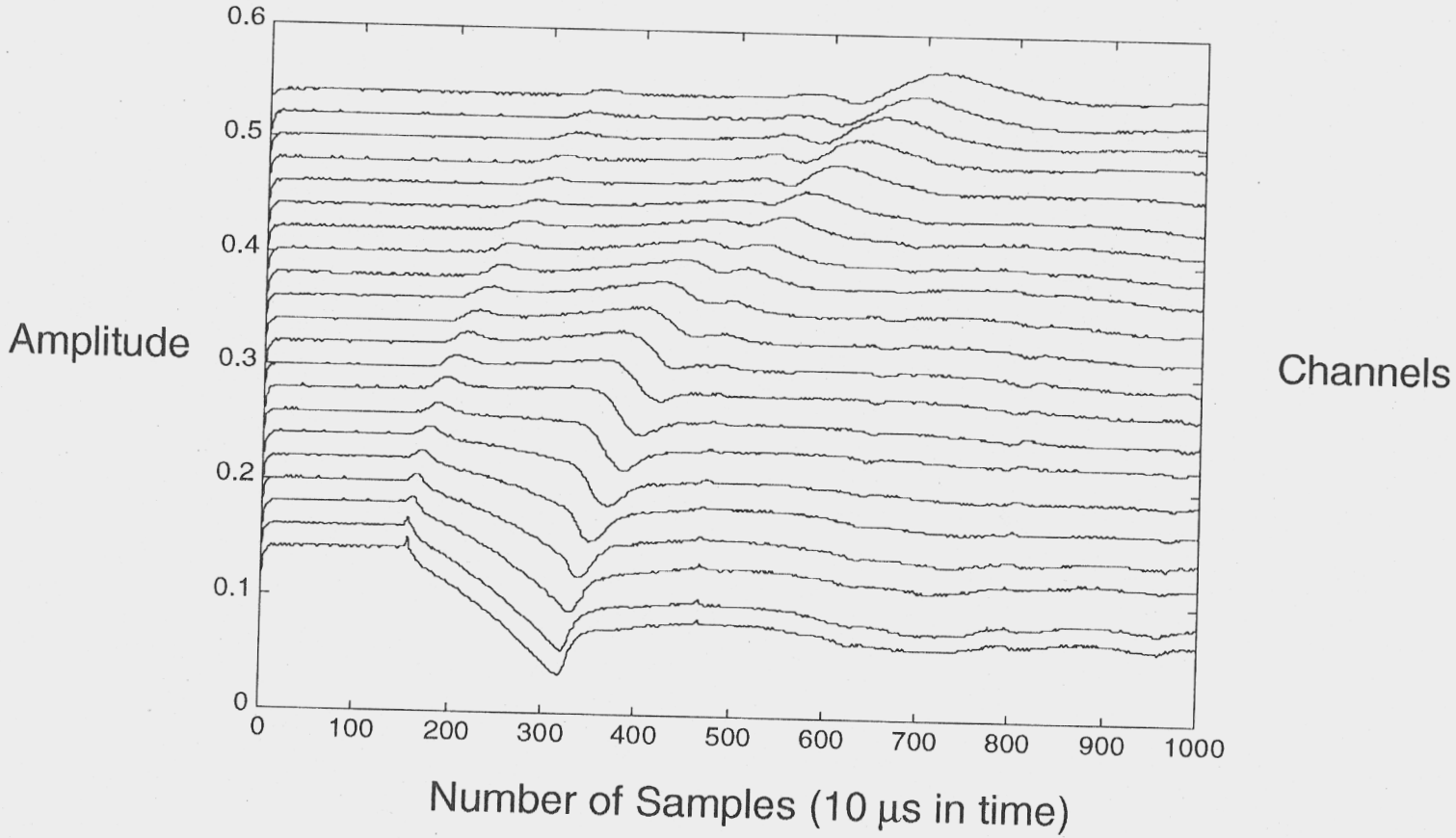

Pre-Processing

- De-mean/ de-trend
- Correlation Canceling

CORRELATION/NOISE CANCELLING PROBLEM

GIVEN a set of noisy measurement data AND a reference signal (correlated to noise or disturbance).

FIND the "best" (mean-squared error) estimate of the noise/disturbance to cancel its effect.

APPLICATIONS: signal processing, fetal heartbeat, cockpit communications, body function monitoring etc.

CORRELATION/NOISE CANCELLER STRUCTURE

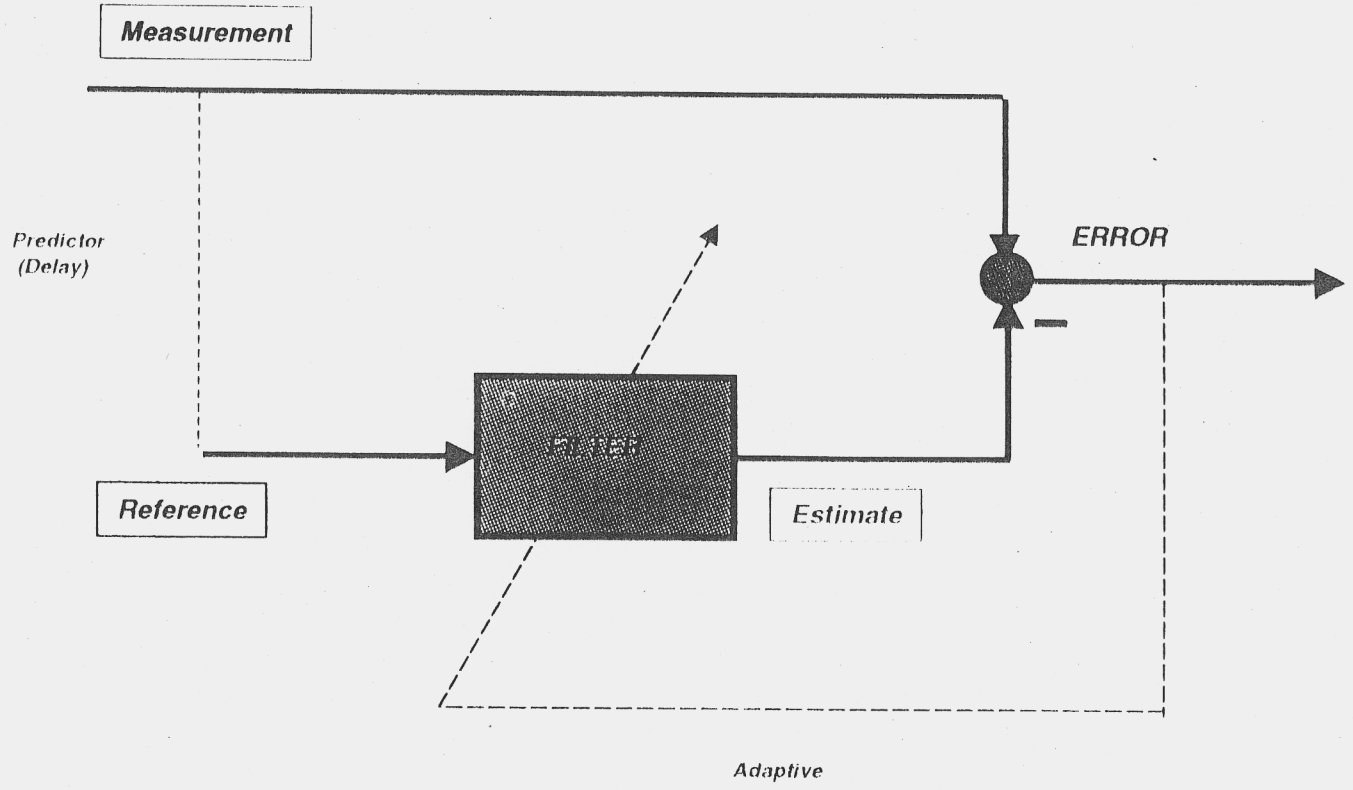

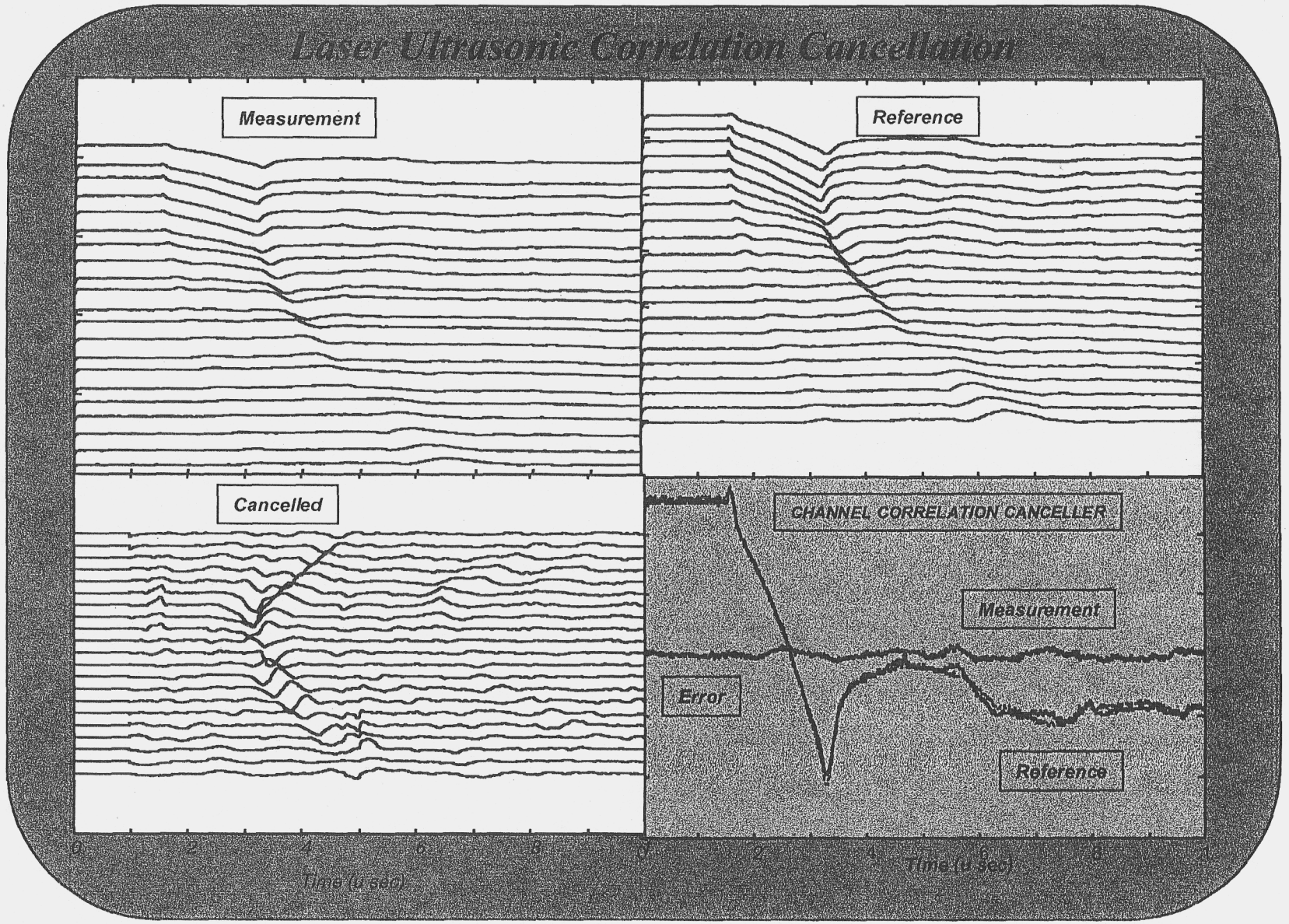
Laser Ultrasonic Correlation Cancellation
Measurement
Reference
Cancelled
CHANNEL CORRELATION CANCELLER
Measurement
Error
Reference
0
2
4
6
8
Time (u sec)
0
2
4
6
8
Time (u sec)

We use a simple homogeneous model of the test specimen (medium) characterized by the Green's function:

In the *spatio-temporal* domain

$$\boxed{g(r_m, r_n; t) = \frac{1}{|r_m - r_n|}\delta(t - \tau_{mn})}$$

or in the temporal *Fourier* domain as:

$$\boxed{G(r_m, r_n; \omega) = \frac{1}{|r_m - r_n|}e^{-j\omega(t-\tau_{mn})}}$$

where the time delay is given by:

$$\tau_{mn} = \frac{|r_m - r_n|}{v}$$

which is an outgoing spherical wavefront emanating from a point source

With our broadband source, we have that:

- the displacement field measured by the array is simply the source convolved with the Green's function of the medium:

$$f(r_m, r_n; t) = g(r_m, r_n; t) * s(r_m, r_n; t)$$

or for the homogenous medium

$$f(r_m, r_n; t) = \frac{1}{|r_m - r_n|} s(t - \tau_{mn})$$

- simply a delayed and attenuated replica of the source

LAWRENCE LIVERMORE NATIONAL LABORATORY

Therefore, our approach to "imaging"using this model is to:

- assume a scatterer (source) location (r_i, r_j) on the specimen or equivalently pixel position (i, j)
- using the homogenous medium model *calculate* the attenuation and required time delays

$$\left\{ \frac{1}{|r_i - r_j|}, \tau_{ij} \right\}$$

- perform the required "beamforming" (shift and sum)

$$bf(t) = \sum_{\ell=1}^{L-1} \alpha_{ij} f(t - \tau_{ij})$$

- extract the significant features from the resulting signal (beamformer output): peaks, power, etc.

Epicenter Source Location

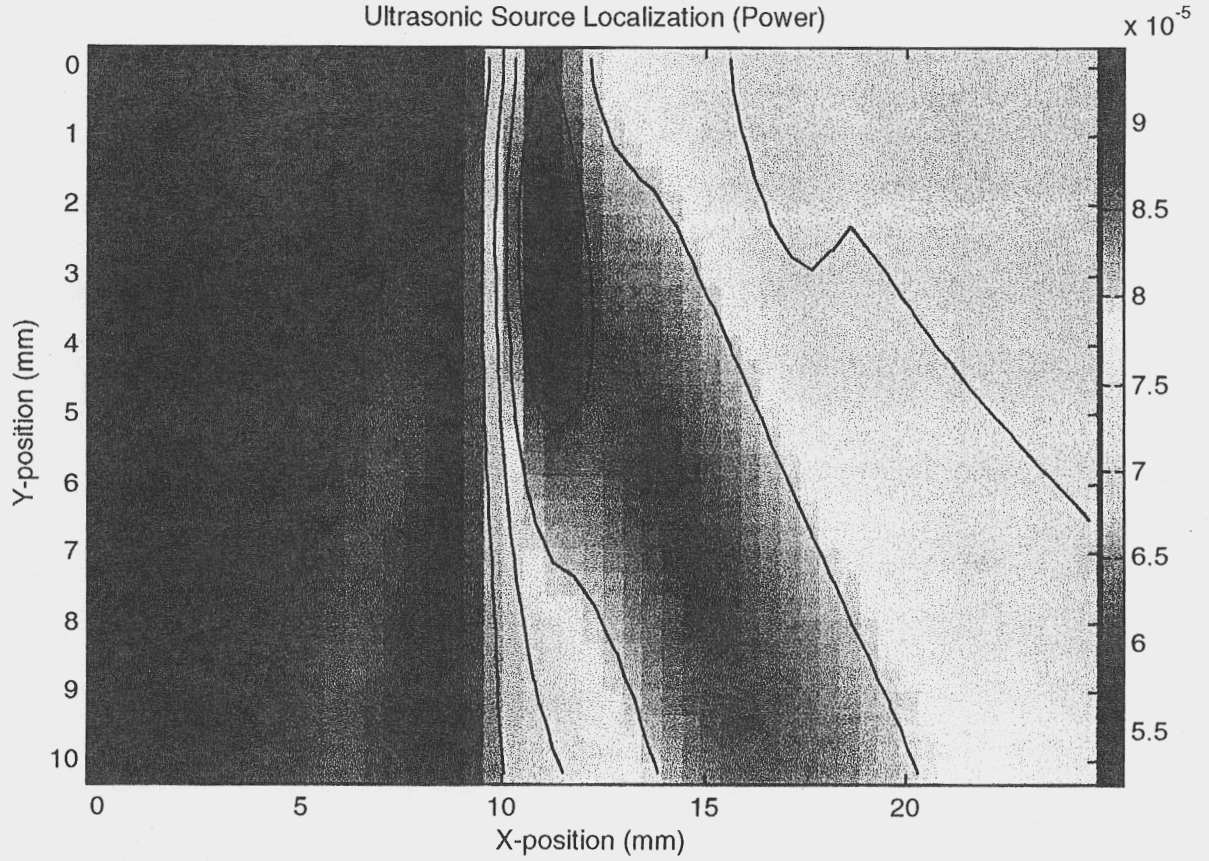

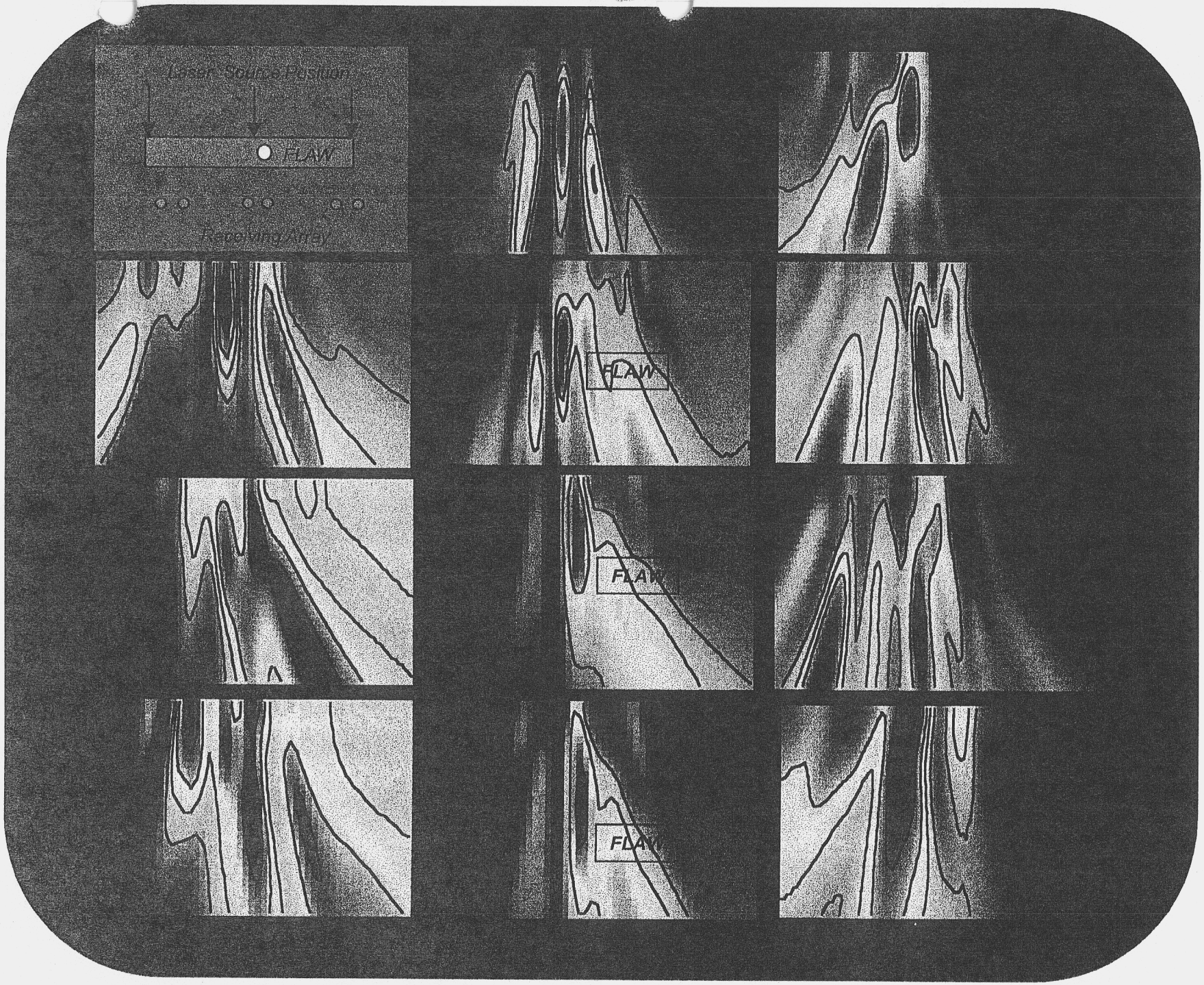
Laser Source Position
FLAW
Receiving Array
FLAW
FLAW
FLAW

We have applied this novel correlation canceling scheme to laser-based ultrasound signals to obtain images of a defect.

R.N. Bracewell

NASA and the European Space Agency are planning to obtain images of nonsolar planetary systems, understanding that success would rally public support for continued space exploration.

The NASA Terrestrial Planet Finder, with a possible launch date of 2010, will go beyond simple detection of a massive planet, constructing an image of where the planets are and analyzing their atmospheres. In the event of success, imaging individual planets would follow (2020?).

Suppressing the blinding radiation of the central star, a main technical challenge, is to be met by an infrared interferometer in orbit near Jupiter. The technique will be explained and ground-based tests, both completed and planned, will be described.

STANDARD SYSTEM

SUN AND JUPITER SEEN FROM 10 PC (3×10^{17} m)

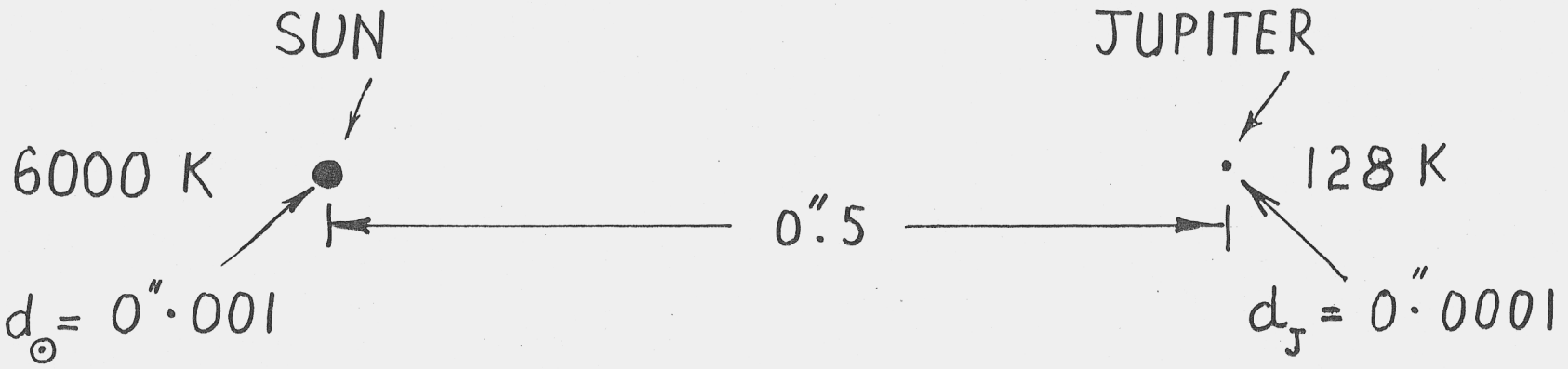

THE INFRARED ADVANTAGE: 50 db

See *Nature* **274**, 780, 1978

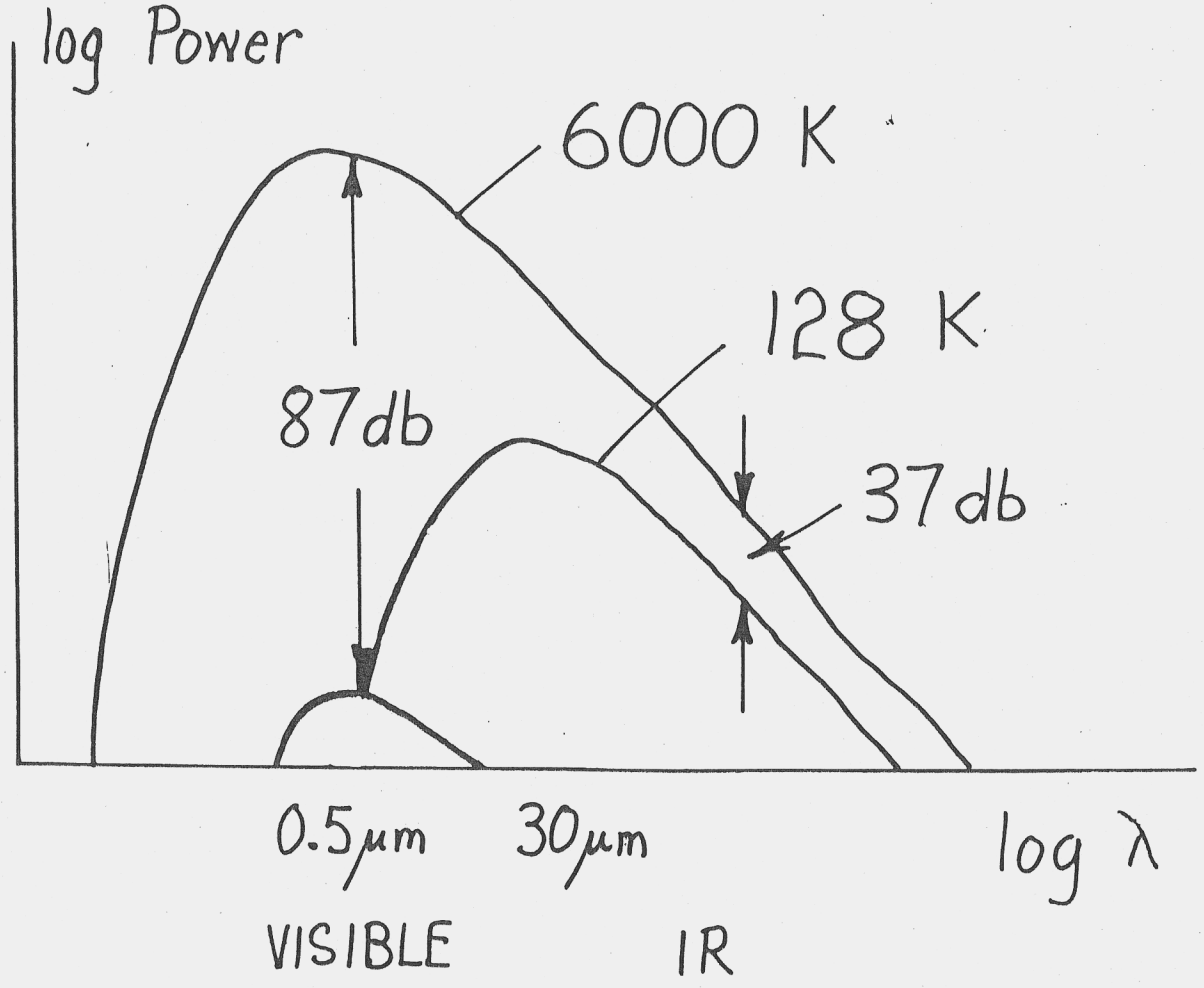

Icarus, 38, 136, 1979

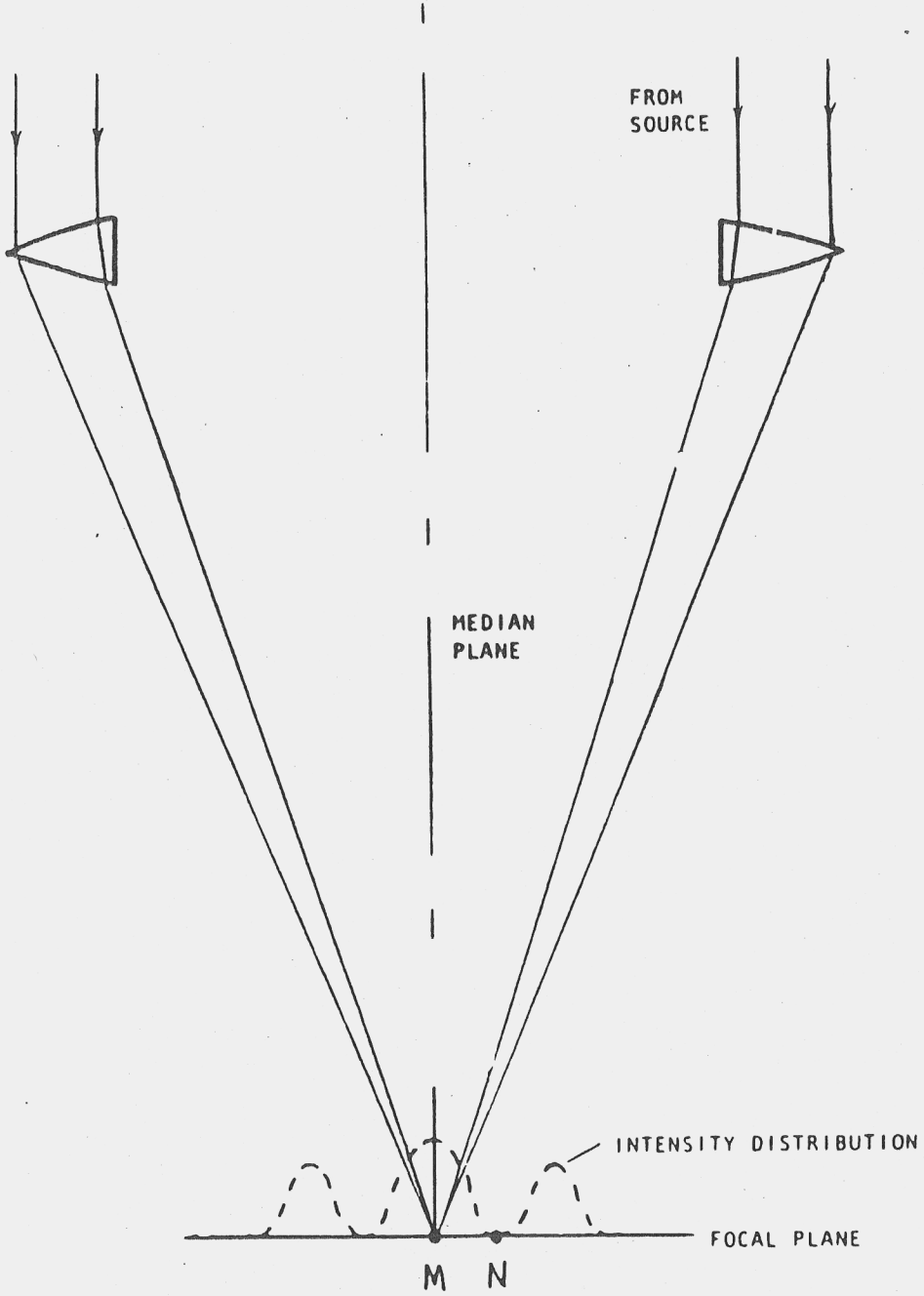

FIG. 4. Simple stellar interferometer.

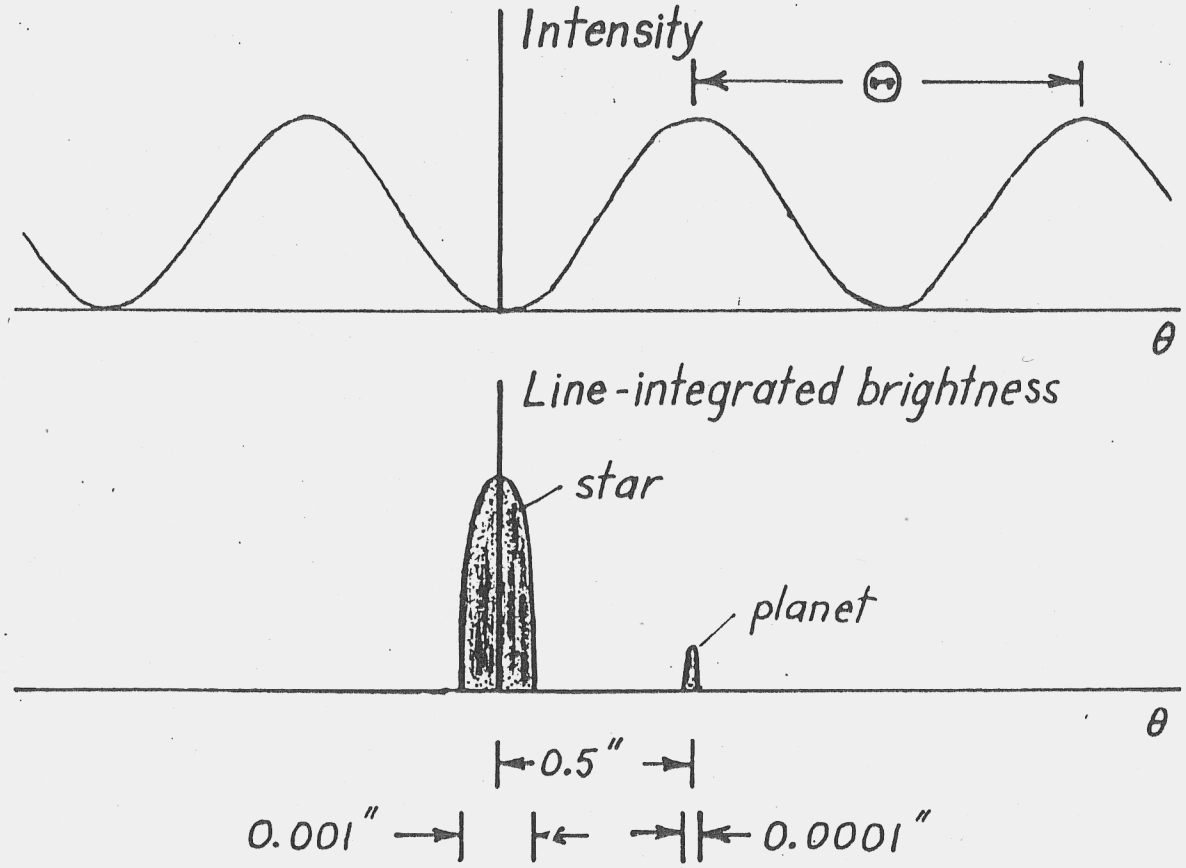

Fig. 2. Intensity of interference fringes and line-integrated brightness ($W\,m^{-2}\,Hz^{-1}\,rad^{-1}$) of star and planet (not to scale).

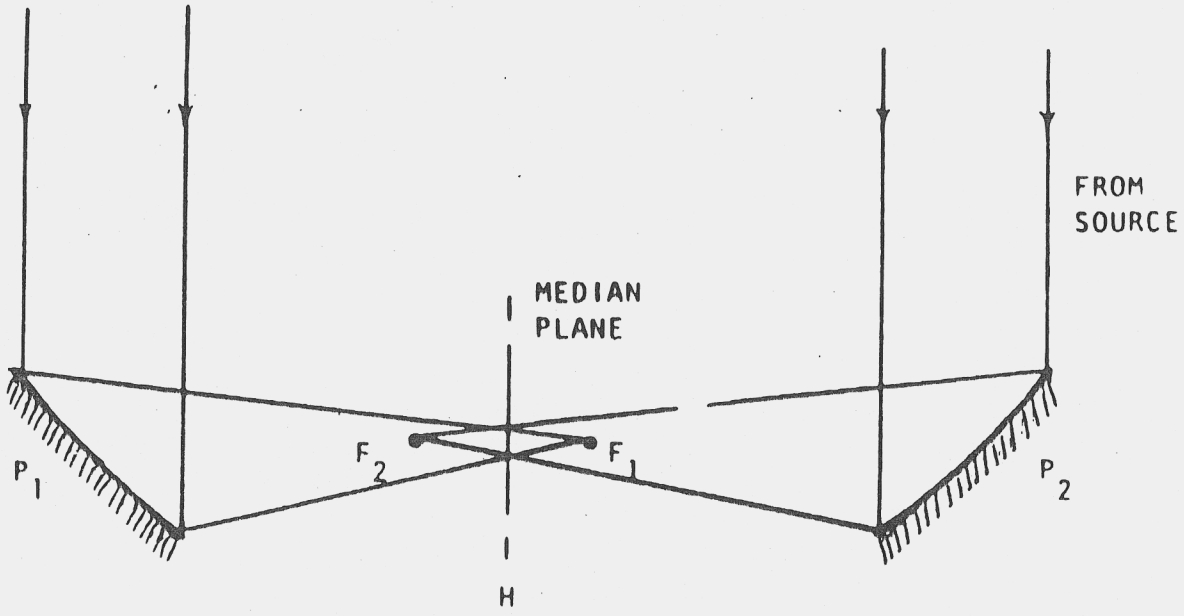

FIG. 5. Interferometer using reflection optics exhibits wideband null.

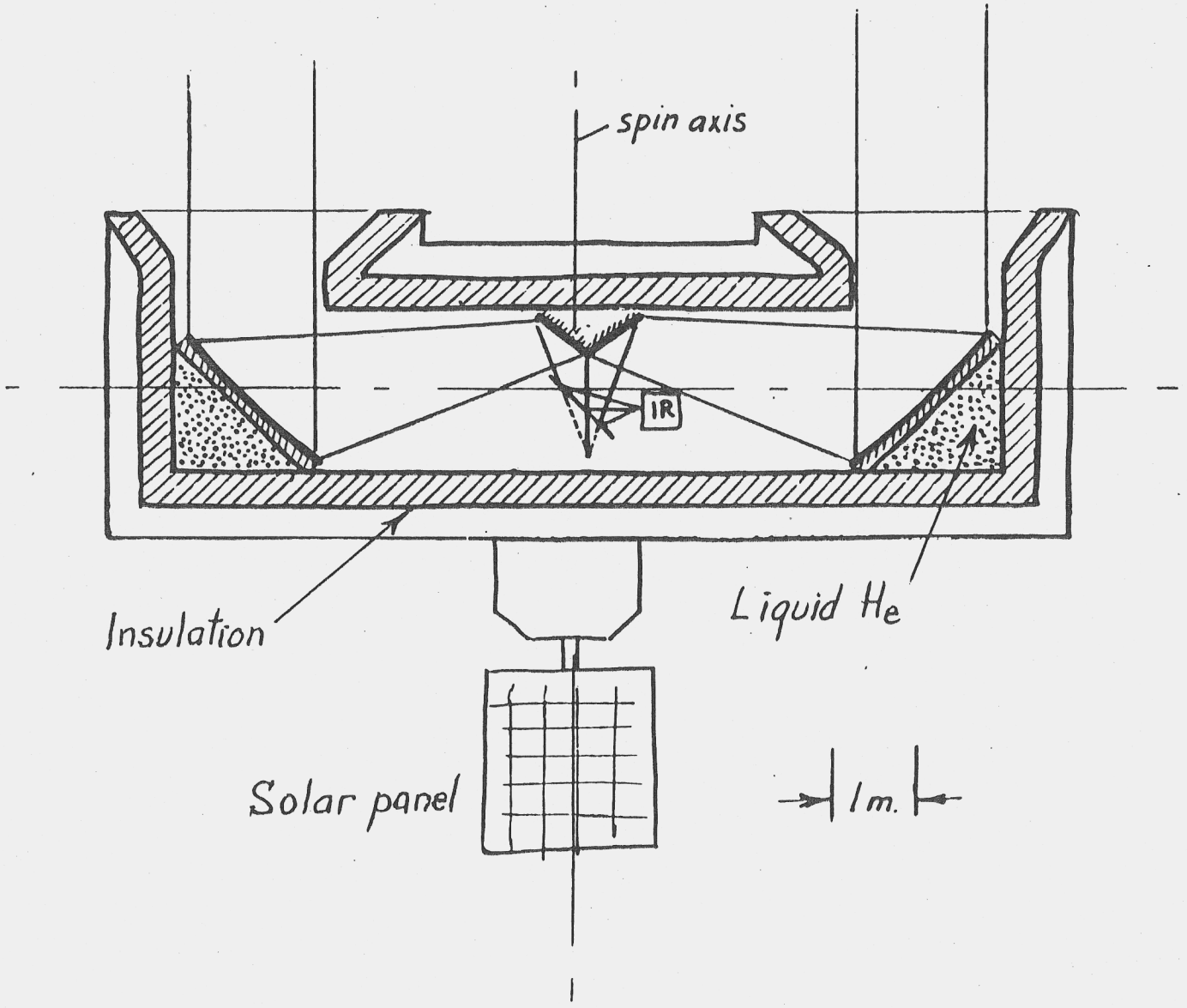
spin axis
IR
Insulation
Liquid He
Solar panel
1m.

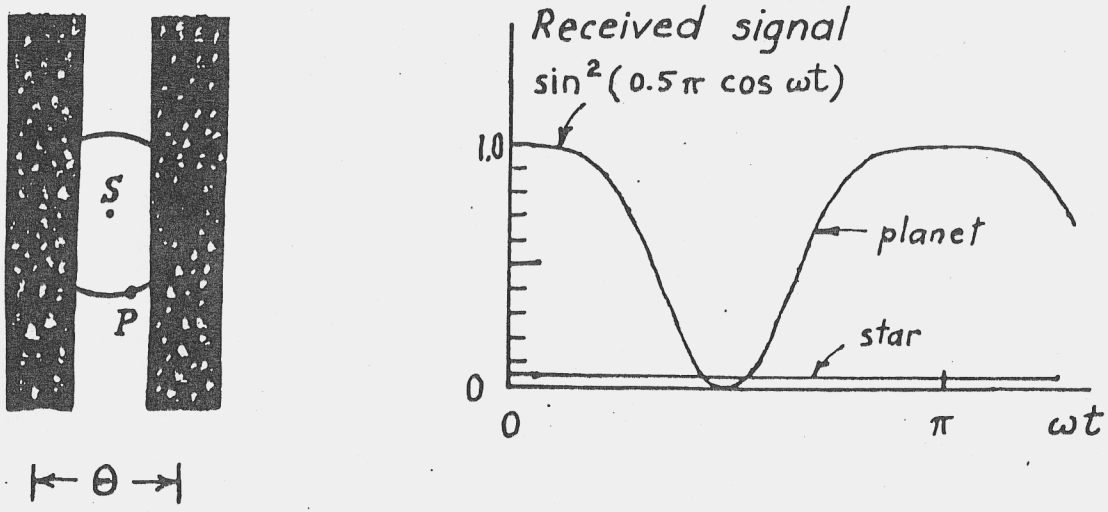

Fig. 3. As planet P traces locus through fringes of spacing Θ, flat topped signal rich in 4ω is received. Precisely centered star S produces small constant signal

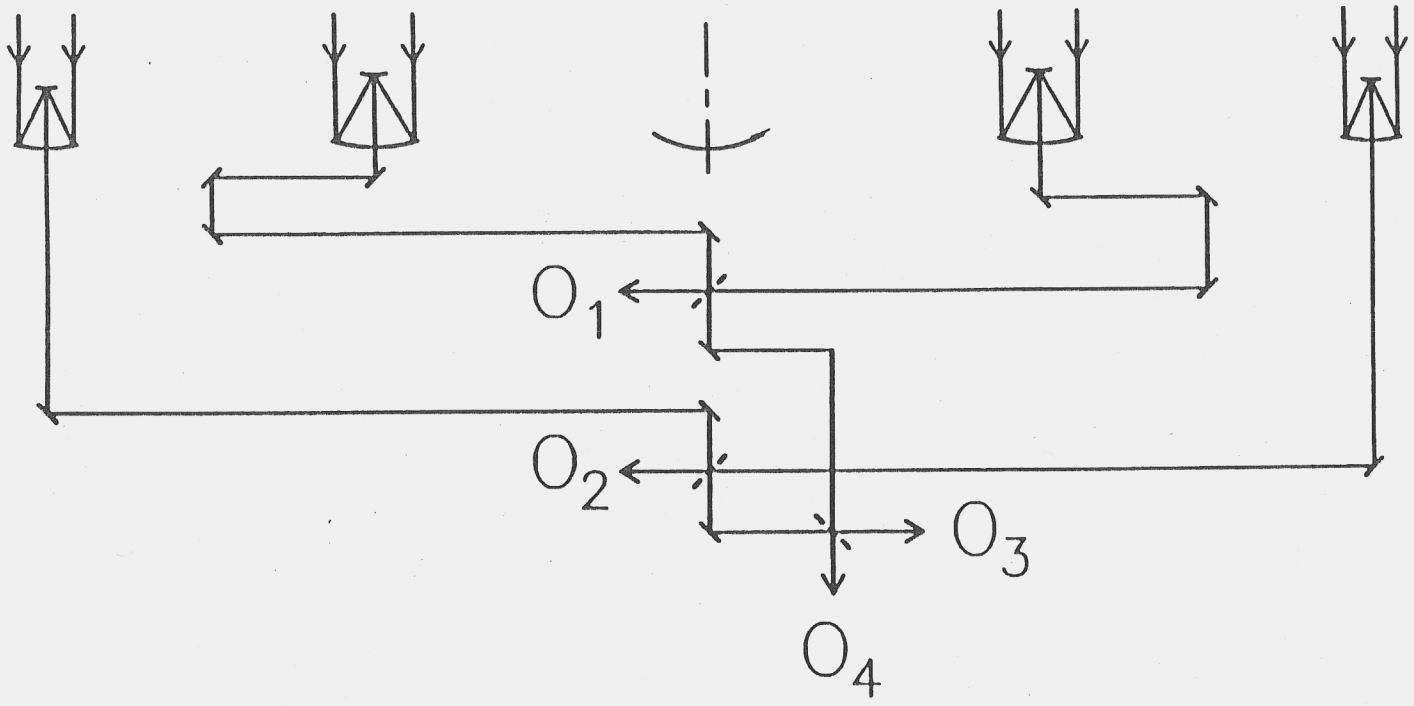

Figure 1. Schematic diagram of the 4-element linear nulling interferometer. The beam combiners feeding O_1 and O_2 have equal transmitted and reflected intensities. The final combiner is chosen to yield amplitudes in the ratio (inner pair/outer pair) = 0.504.

*Figs. 1–7 from Angel & Woolf, Astrophys. J., **475**, 373-379, Jan 1997*

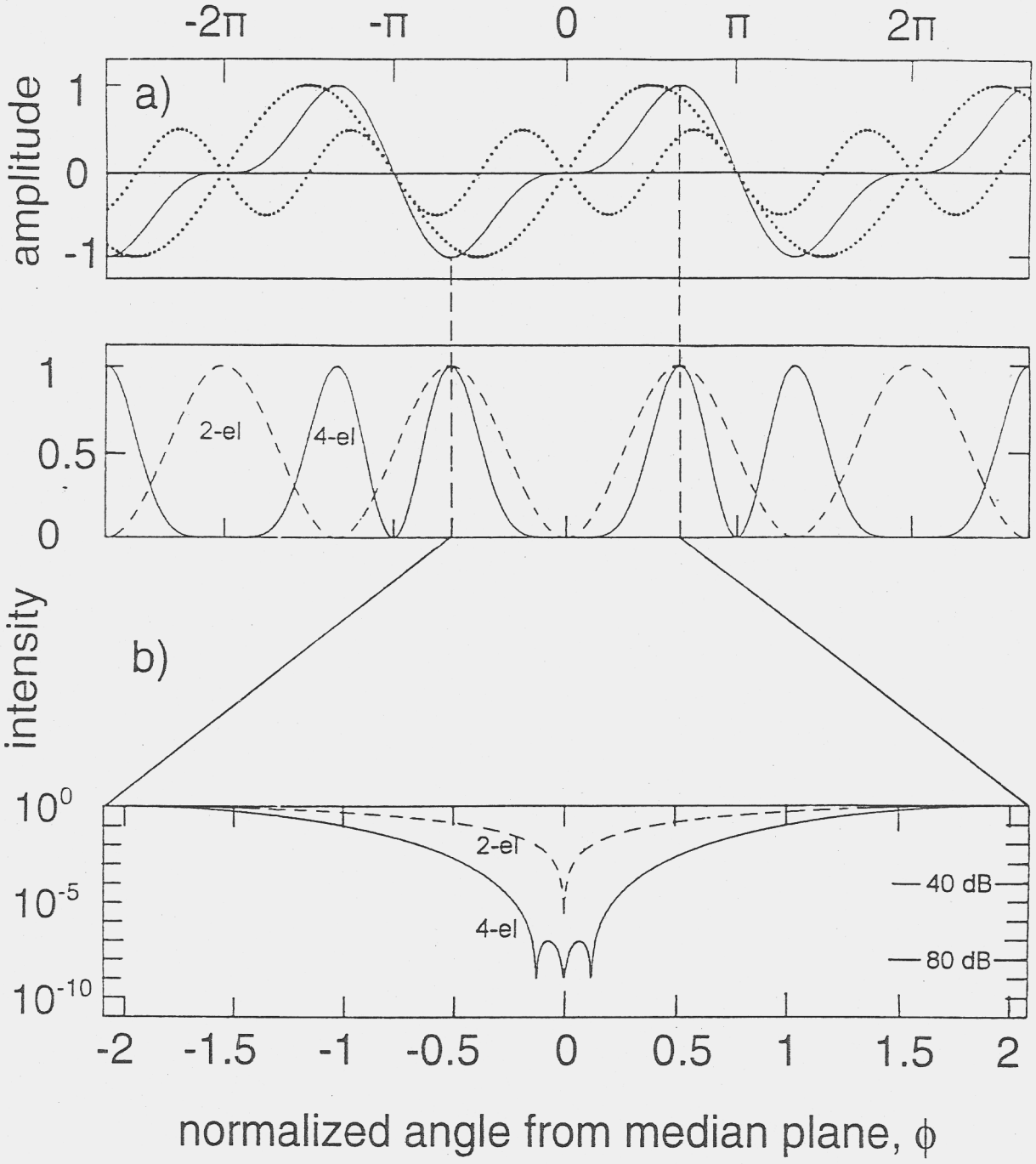

Figure 2. a) Dotted curves show separately the fringe amplitudes for the inner and outer Bracewell pairs of the 4 element interferometer (the two terms of Eq.3). For a source at the meridian plane, both amplitudes are zero, and the slopes are equal and opposite, leading to a summed amplitude with the zeroth, first and second order terms all zero (unbroken curve). b) The transmitted intensities of the 4 element interferometer and of a single Bracewell pair 3/8 as long, chosen to have its first maxima at the same absolute angle from the meridian plane (broken line). The normalized angle (which depends on length) is appropriate for the 4 element interferometer. The central nulls are shown expanded and in logarithmic scale, to illustrate the much greater depth and width achieved by the 4 element configuration.

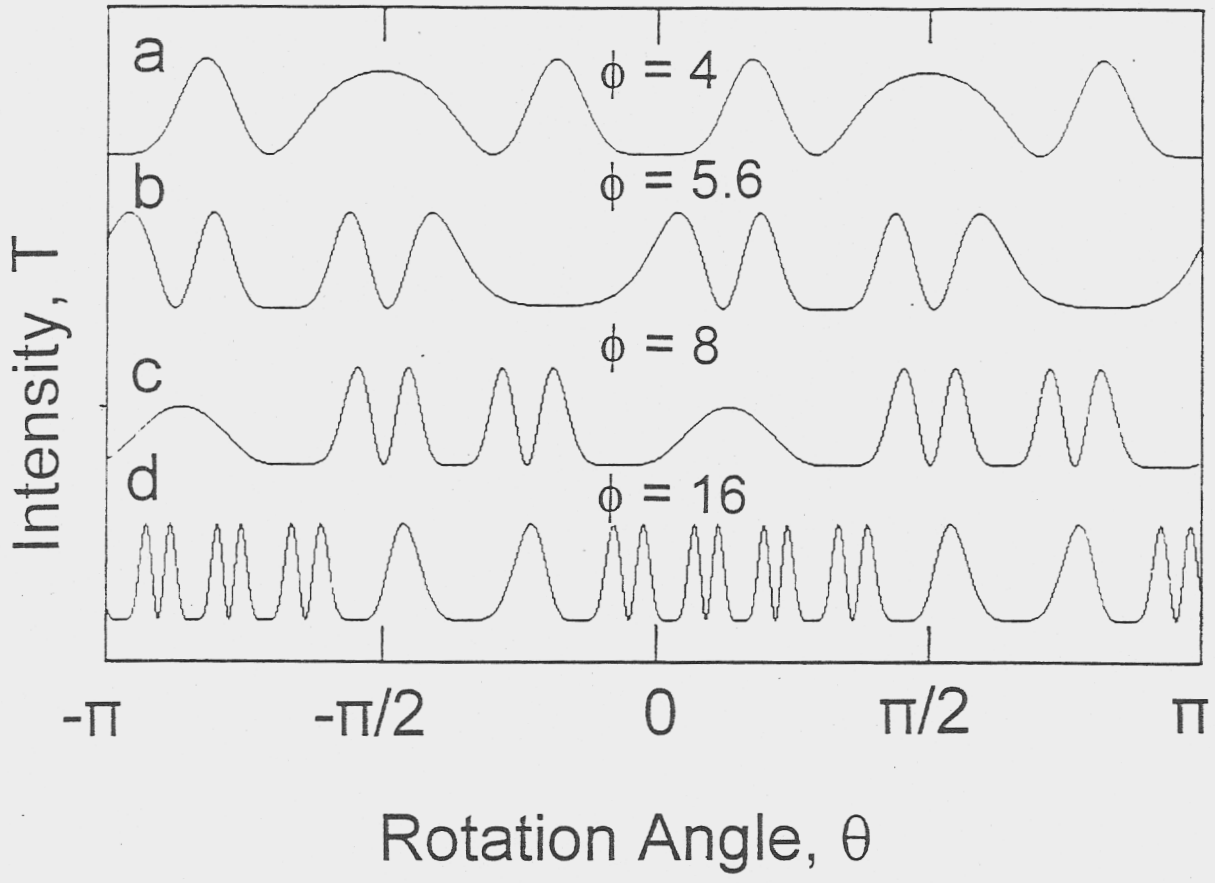

Figure 3. Transmitted intensities as a function of rotation angle θ for different maximum values of ϕ and position angle β.

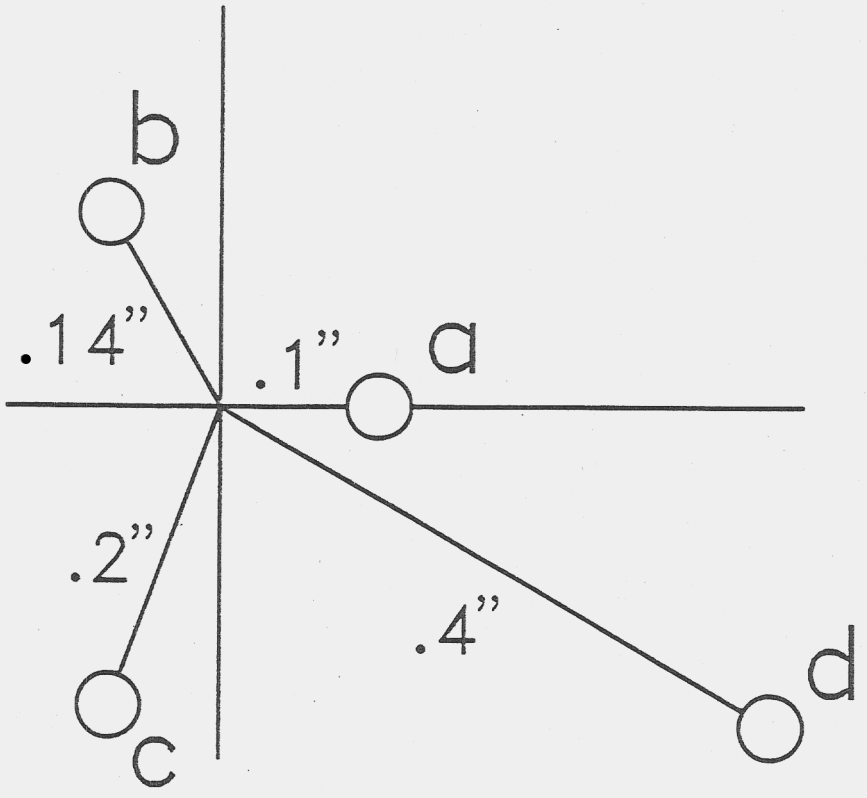

Figure 4. Locations of planets used to model interferometer response. Separations are given in arcseconds, and correspond to projected separations 1 - 4 AU from a star seen from 10 pc.

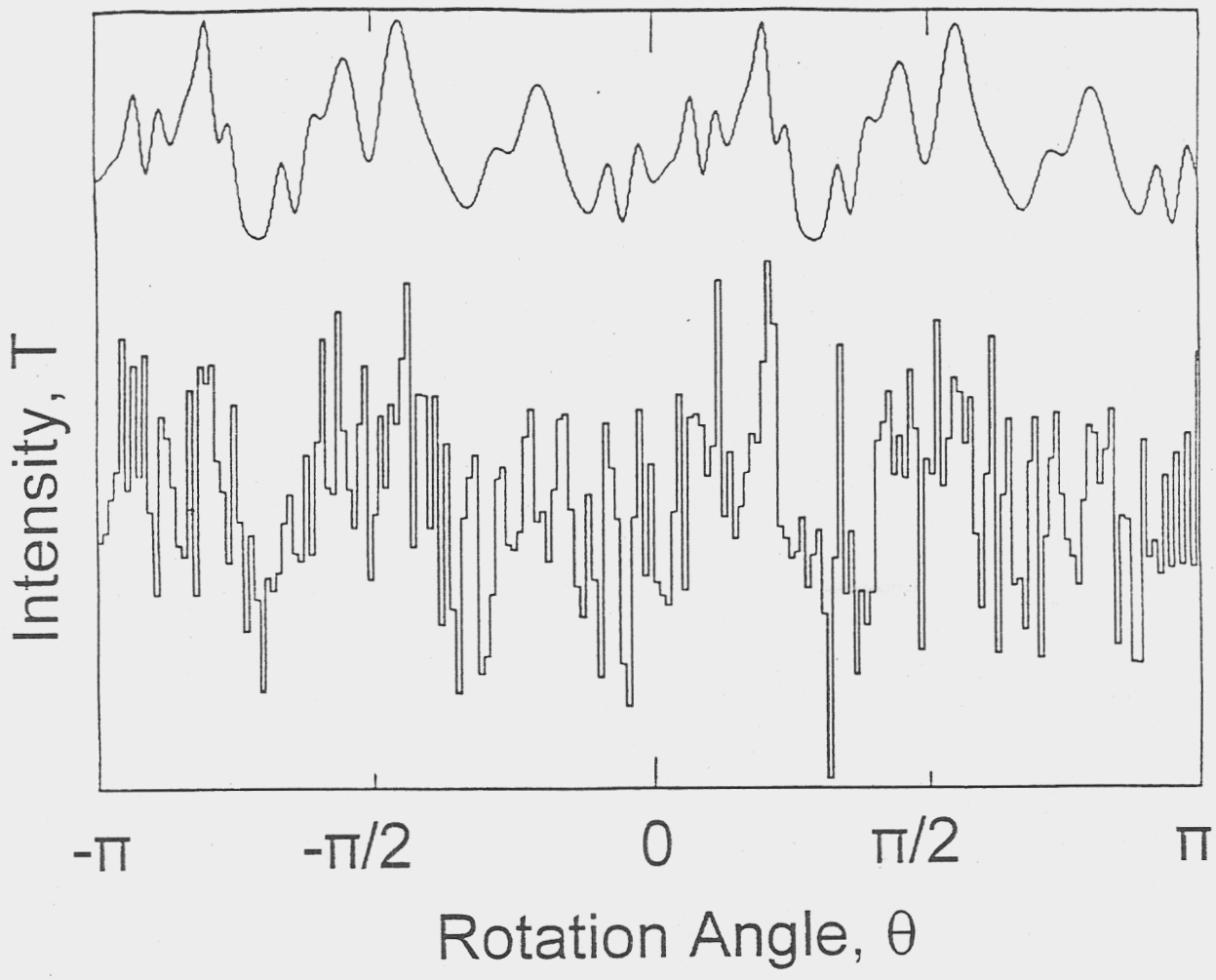

Figure 5. a) is the combined 10 μm signal for all 4 planets in figure 4 (b) shows the same signal as with the addition photon noise, as projected for a 10-hour integration and 1 μm bandwidth. Each planet is projected to be as bright as the Earth seen from 10 pc. The photon noise level is appropriate for a stellar zodiacal cloud having the same luminosity as the sun's.

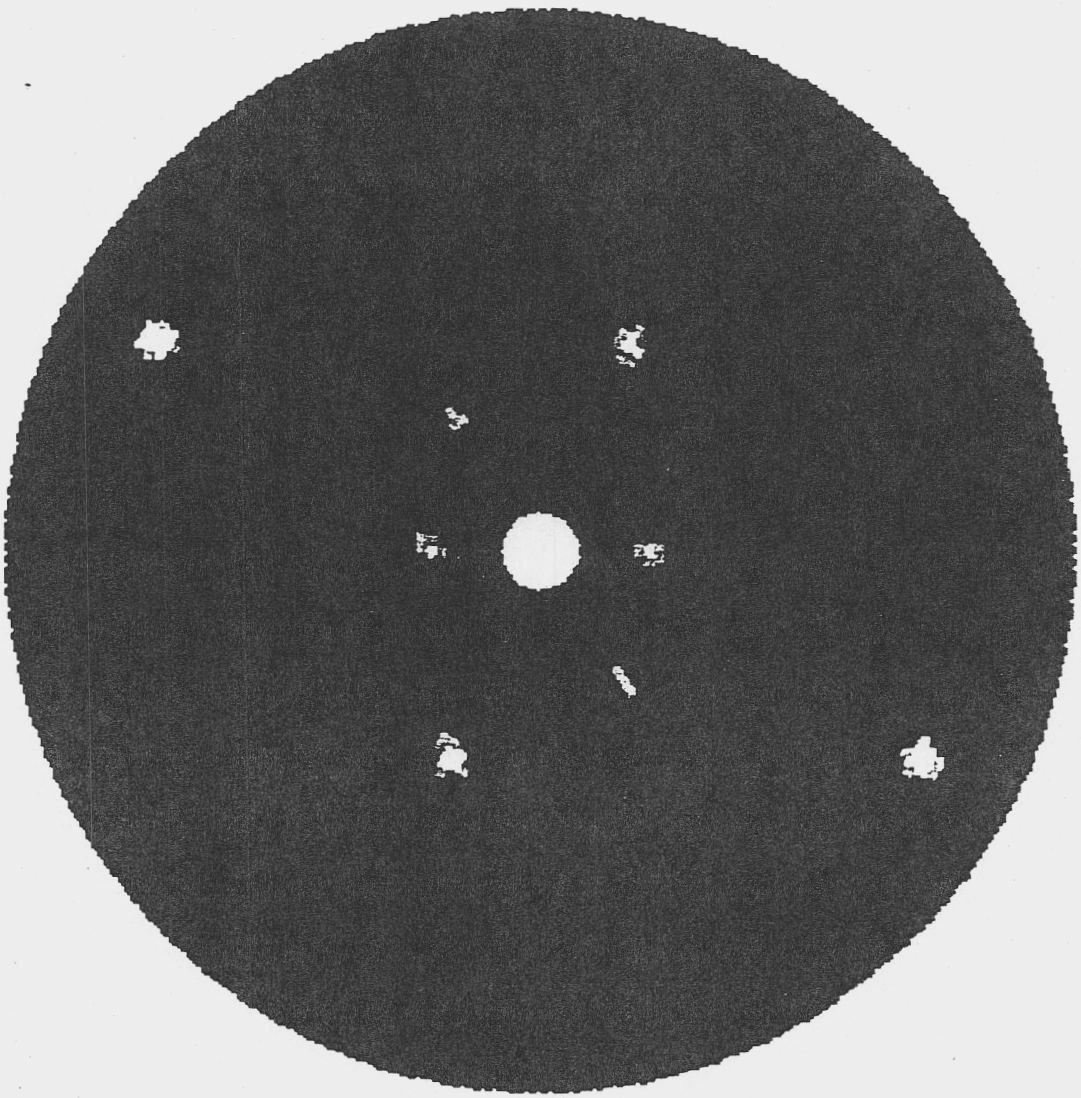

Figure 6. Image of 4 planets recovered by cross correlation from synthesized noisy interferometer data like fig 5b, over 10 wavelength bands from 7 - 17 μm. The image doubling could be removed by extended observations.

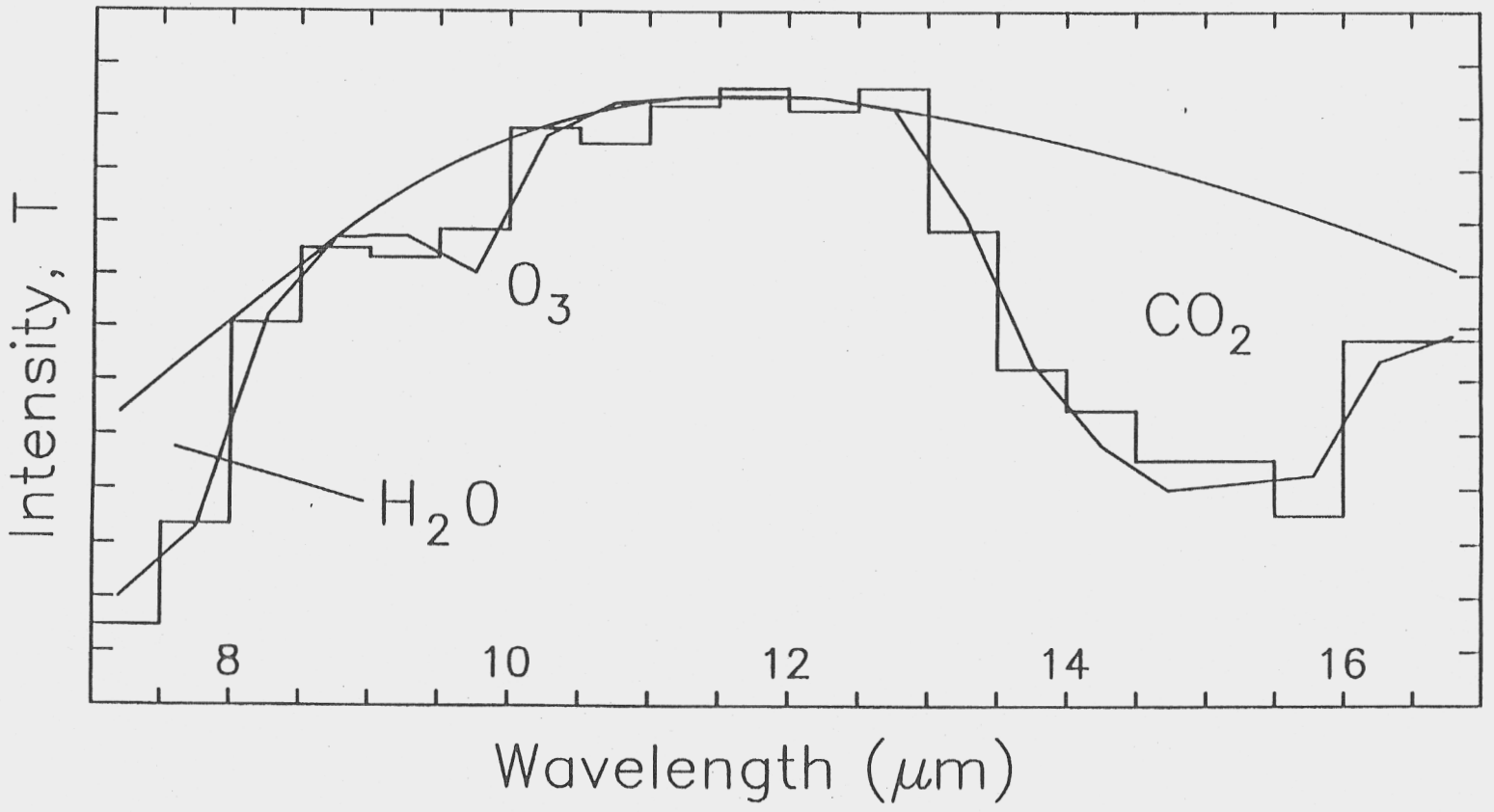

Figure 7. A spectrum of the Earth at a resolution of 0.5μ and a signal/noise ratio of 20:1, as would be obtained from 80 days of observation of a solar system-like set of planets at 10pc. The circles give the true spectrum. The smooth line shows a black-body curve.

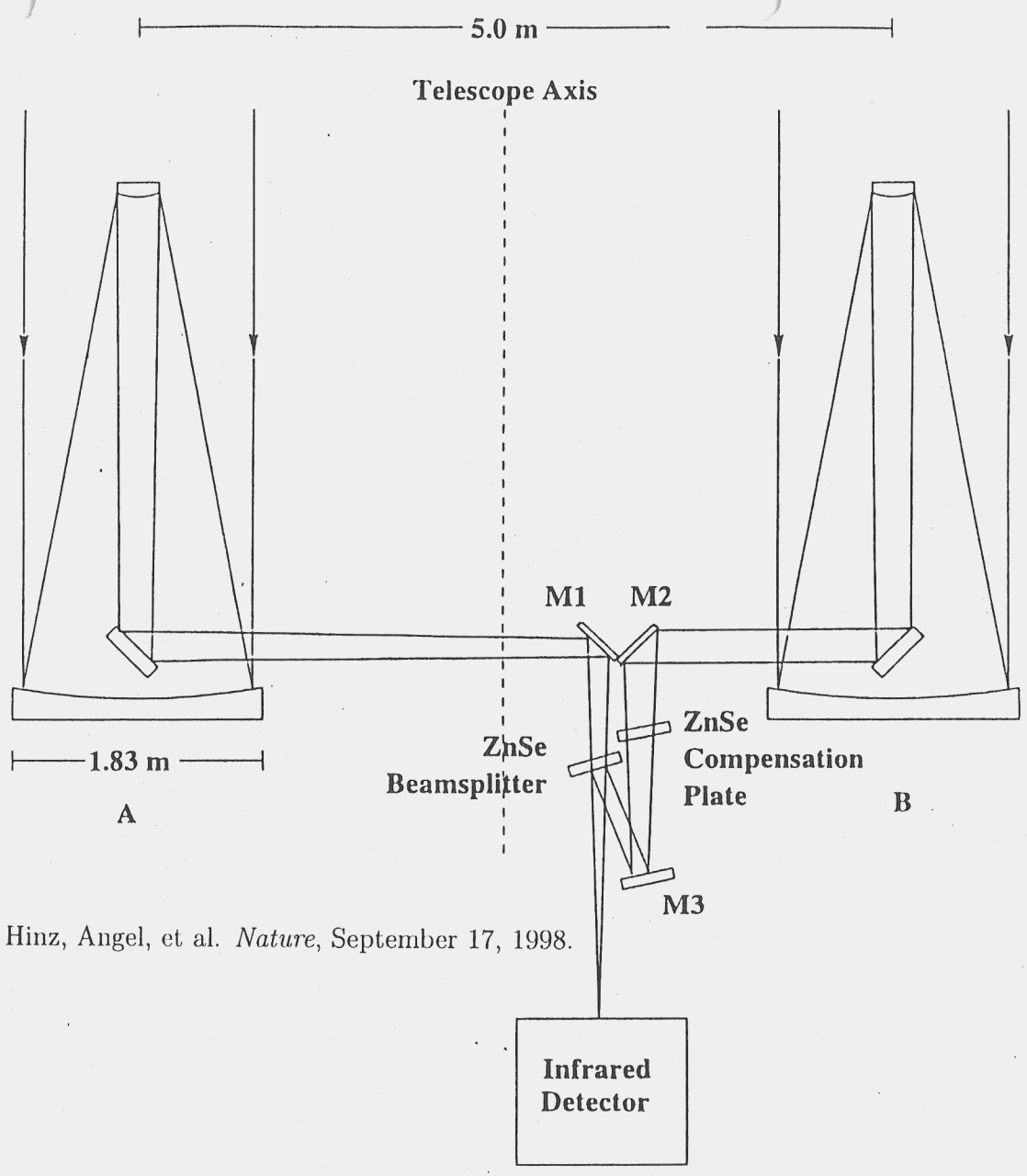

Hinz, Angel, et al. *Nature*, September 17, 1998.

Fig. 1.— Schematic of our nulling interferometer at the MMT. The beam path-lengths are equalized by translating the beamsplittter vertically.

UCRL-JC-132278 abs

Novel Interferometer-Spectrometer for Sensitive Doppler Planet Detection

David Erskine, Jian Ge
Lawrence Livermore National Lab

A saturn-like planet at saturn-like distances creates a wobble in the velocity of a star of about 3 m/s, and Earth-like planets even less, about 0.1 m/s. Current spectrometers have velocity resolution of 3-10 m/s, which is insufficient to detect Saturn-like or smaller planets. Secondly, these spectrometers are not light efficient, allowing only bright stars to be measured. Thirdly, these instruments are not portable or space-launchable, and their highly individual character makes comparison of data during 10-30 year orbits problematic. We have built a novel instrument (called a fringing spectrometer) which is a hybrid of an interferometer and spectrometer, which is particularly well suited for accurately measuring small Doppler shifts in a light efficient manner, is portable and space-launchable, and was constructed from off-the-shelf components on hand. Other advantages include a 200x larger field of view compared to the Lick Observatory spectrometer, stability, and independence from slit vignetting vagaries. We are testing it on sunlight by seeking the 12 m/s @ 27 day effect of the moon tugging the Earth. (Jupiter on the sun is 12 m/s). We have built an algorithm to unwrap the phase of the interferogram to 1/10000 wave (corresponding to ~ 1 m/s Doppler velocity). This is a 20x improvement in the art over monochromatic interferograms and may lead to other applications in high precision metrology.

Keywords: Spectrometer, Doppler shift, Interferometer

This work was performed under the auspices of the Department of Energy by the Lawrence Livermore National Laboratory under contract W-7405-Eng-48.

Deconvolution of images from the Lick Observatory adaptive optics system

J. M. Brase

J. Kolman

B. A. Macintosh

CASIS 1998

Deconvolution of images from adaptive optics systems

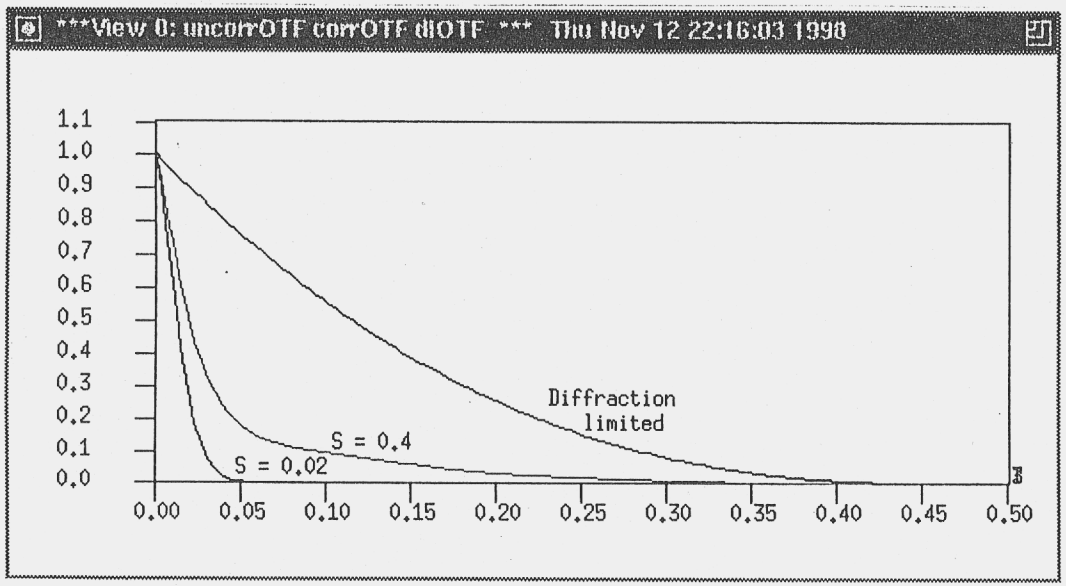

- Current AO systems provide partial correction of images in the near infrared (1-2.2 μm)

- Because adaptive optics corrected images contain frequency components out to the diffraction limit (at Strehl > 0.1), deconvolution should work significantly better than for uncorrected images

Stochastic deconvolution algorithms for AO applications are based on Poisson image models

The image measurement g(j) is a Poisson distributed random variable with mean

$$\overline{g(j)} = h(j) * f(j)$$

where j is the spatial index
h is the point spread function
f is the object

The MAP estimate of the object f is given by

$$\arg\max_f p(f|g) = \arg\max_f \frac{p(g|f)p(f)}{p(g)}$$

If we assume a uniform prior probability p(f), the MAP estimate reduces to the maximum likelihood estimate

$$\arg\max_f p(g|f)$$

Formulation for Poisson measurement and prior probability

Assuming Poisson statistics for p(f) and p(g|f) and the above measurement model, the MAP estimate is given by

$$f(j)=\overline{f(j)}\exp\left\{\left[\frac{g(j)}{h(j)*f(j)}-1\right]*h(j)\right\}$$

Where $\overline{f(j)}$ is the expected value of the object f.

The maximum likelihood estimate is given by

$$\left[\frac{g(j)}{h(j)*f(j)}\right]*h(j)=1$$

Both estimates are nonlinear sets of equations that must be solved iteratively.

Reference: Hunt, SPIE 1567, 600, 1991

Iterative solutions of the MAP and ML equations

MAP:

$$f_{n+1}(j) = f_n(j) \exp\left\{\left[\frac{g(j)}{h(j) * f(j)} - 1\right] * h(j)\right\}$$

ML:

$$f_{n+1}(j) = f_n(j) \left\{\left[\frac{g(j)}{h(j) * f(j)}\right] * h(j)\right\}$$

Note that the ML algorithm is generally referred to as Lucy-Richardson deconvolution.

The algorithm is initialized with $f_0(j) = g(j)$. The iteration is stopped when

$$\frac{1}{N}\sum_j \left|\left(f_n(j) * h(j)\right) - g(j)\right|^2 < \text{var}\, g$$

Comparison between ML and MAP restorations_

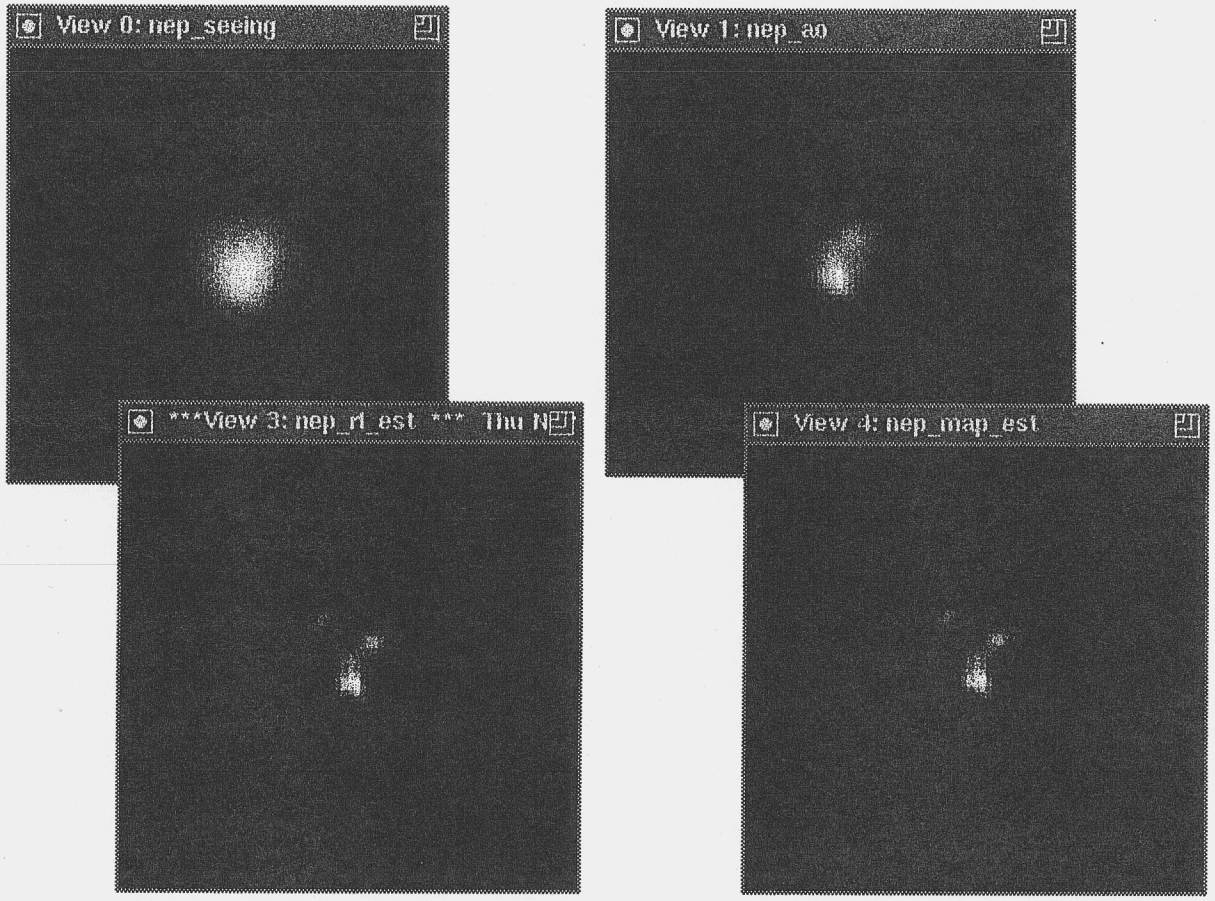

Restoration with and without adaptive optics correction

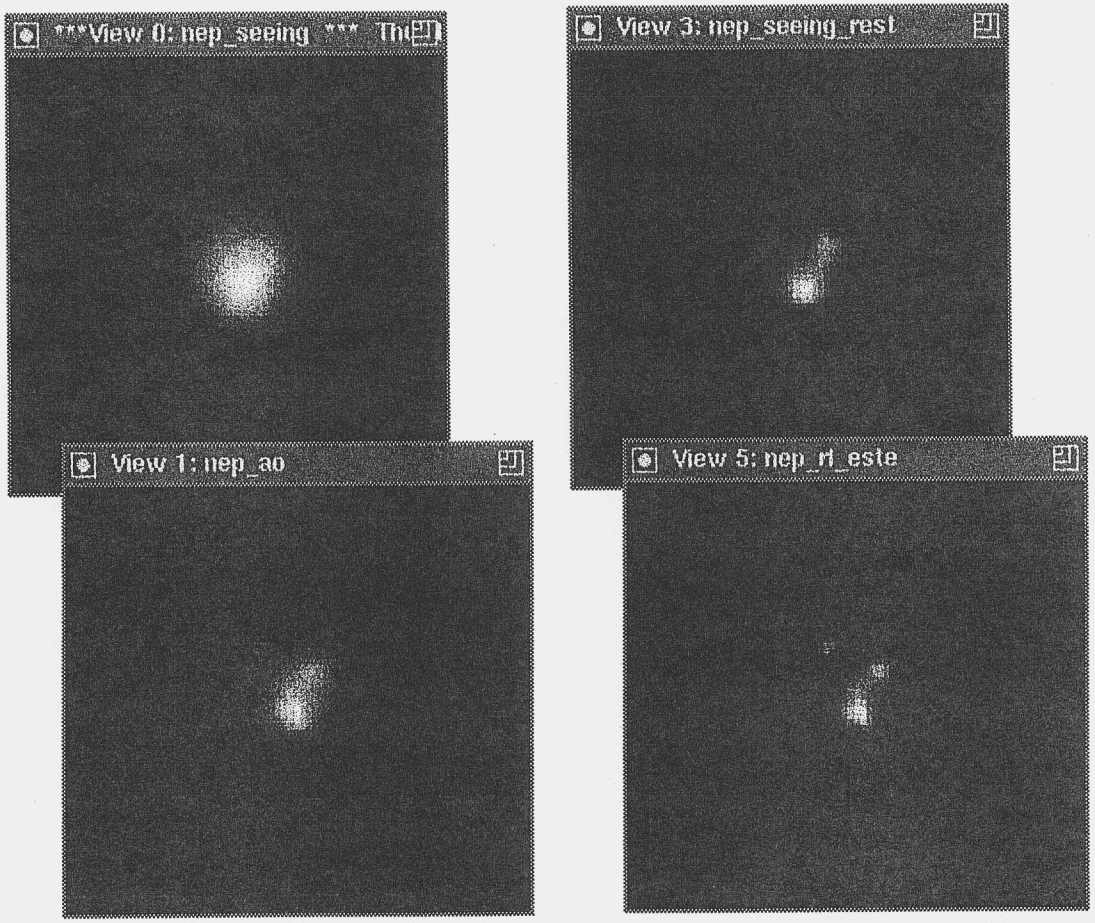

Much remains to be done on restoration of AO images

Point-spread-function estimation is the most serious problem. The psf varies in time as the atmosphere changes which makes the use of calibrator stars very difficult.

Two approaches are being investigated:

- estimation of the psf from AO system real-time diagnostic data
- joint estimation of the object and psf (blind or myopic deconvolution)

The psf also varies with angle from the AO guidestar. This will require spatially variant deconvolution techniques. Not a big problem right now because IR array FOV is within the isoplanatic angle (to first order).

LBNL/Lick Observatory Fully-Depleted CCD Image Sensor Development

S. Holland, D. Groom, A. Karcher, M. Levi, N. Palaio, S. Perlmutter

Lawrence Berkeley National Laboratory

R. Stover, W. Brown, K. Gilmore, and M. Wei

University of California Observatories, Lick Observatory

We are developing CCD image sensors for astronomy and astrophysics applications. The devices are derived from high-energy physics detector technology. The back-illuminated CCD's are fabricated on ultra-pure, high-resistivity silicon substrates [1-2]. A bias voltage applied to the back-side contact results in full depletion of the 300μm thick substrate. The depletion voltage is relatively low due to the high resistivity of the starting silicon, about 10,000 Ω-cm, which corresponds to a purity level of about 1 part in 10^{11}.

This device has several advantages over conventional thinned, back-illuminated CCD's. Because of the large absorption depth of near-infrared photons in silicon, thinned CCD's typically have poor response in the λ = 800nm – 1μm region. In addition, fringing results from multiply-reflected waves when narrow-band, long-wavelength light is imaged. The much thicker device described here has greatly improved near-infrared response and negligible fringing. In addition, we have demonstrated good quantum efficiency in the short-wavelength range for back-illuminated devices. This is accomplished with a simple back-side window consisting of a thin layer of in-situ doped polycrystalline silicon with an antireflection coating of indium tin oxide.

[1] S.E. Holland et al, "A 200 x 200 CCD image sensor fabricated on high-resistivity silicon," IEDM Technical Digest, pp. 911-914, 1996.

[2] R.J. Stover et al, "Characterization of a fully depleted CCD on high resistivity silicon," Solid State Sensor Arrays: Development and Applications, Proceedings of SPIE, vol. 3019, pp. 183-188, 1997.

Keywords: Charge coupled device, back illuminated, fully depleted

Author contact: Steve Holland
Lawrence Berkeley National Laboratory
Mail Stop 50B-6208B
Berkeley, CA 94720
510-486-5069 (5401 FAX)
seholland@lbl.gov

Extrasolar Planet Search with an Adaptive Optics Spectrometer with R = 200,000

Jian Ge
Lawrence Livermore National Lab

Roger Angel, Nick Woolf, Mike Lloyd-Hart
Steward Observatory, The University of Arizona

Robert Fugate
Starfire Optical Range, Air Force Phillips Lab

A breakthrough in extrasolar planet searches has been made in recent years using precision Doppler techniques. About 10 extrasolar planets have been detected at typical precision of 15 m/s. However, these previous techniques have not had the sensitivity to detect solar system analogs, which should represent most planet populations.

The new adaptive optics spectrometer, being developed by us at Steward Observatory, is capable of providing much improved sensitivity to routinely detect Jupiter and Saturn-like planets. The spectrometer takes full advantage of adaptive optics corrected images in the wavelength range between 0.4 to 1.0 microns from the Starfire Optical Range 3.5 m telescope to provide spectral resolution of R = 200,000, a factor of four times higher than previous spectrometers used in planet searches.

It will well resolve absorption line profiles from late-type stars, which are the main targets for present planet searches. With a large format back-illuminated 2kx4k CCD detector, a wavelength of 400 nm is covered in a single exposure. This permits the selection of a large number of stellar absorption lines for simultaneous study of line profiles from different stellar atmospheric layers. Precise measurements of the variations in the shapes of different line profiles would help distinguish small Doppler perturbations with amplitude of around 1 m/s caused by sub-Jupiter mass planet companions from that caused by stellar activities.

This work was performed under the auspices of the Department of Energy by the Lawrence Livermore National Laboratory under contract W-7405-Eng-48.

Extrasolar Planet Search with Adaptive Optics Spectrometer with R = 200,000

Jian Ge
Lawrence Livermore National Lab

Roger Angel, Nick Woolf, Mike Lloyd-Hart
Steward Observatory, Univ. of Arizona

Robert Fugate
Starfire Optical Range, Air Force Phillips Lab

Outline

- Overview
- Novel Adaptive Optics Spectrometer
- Sub-Jupiter Mass Planet Searches

Overview

1995-Present

- **A dozen of extra-solar planets discovered with precision Doppler technique**

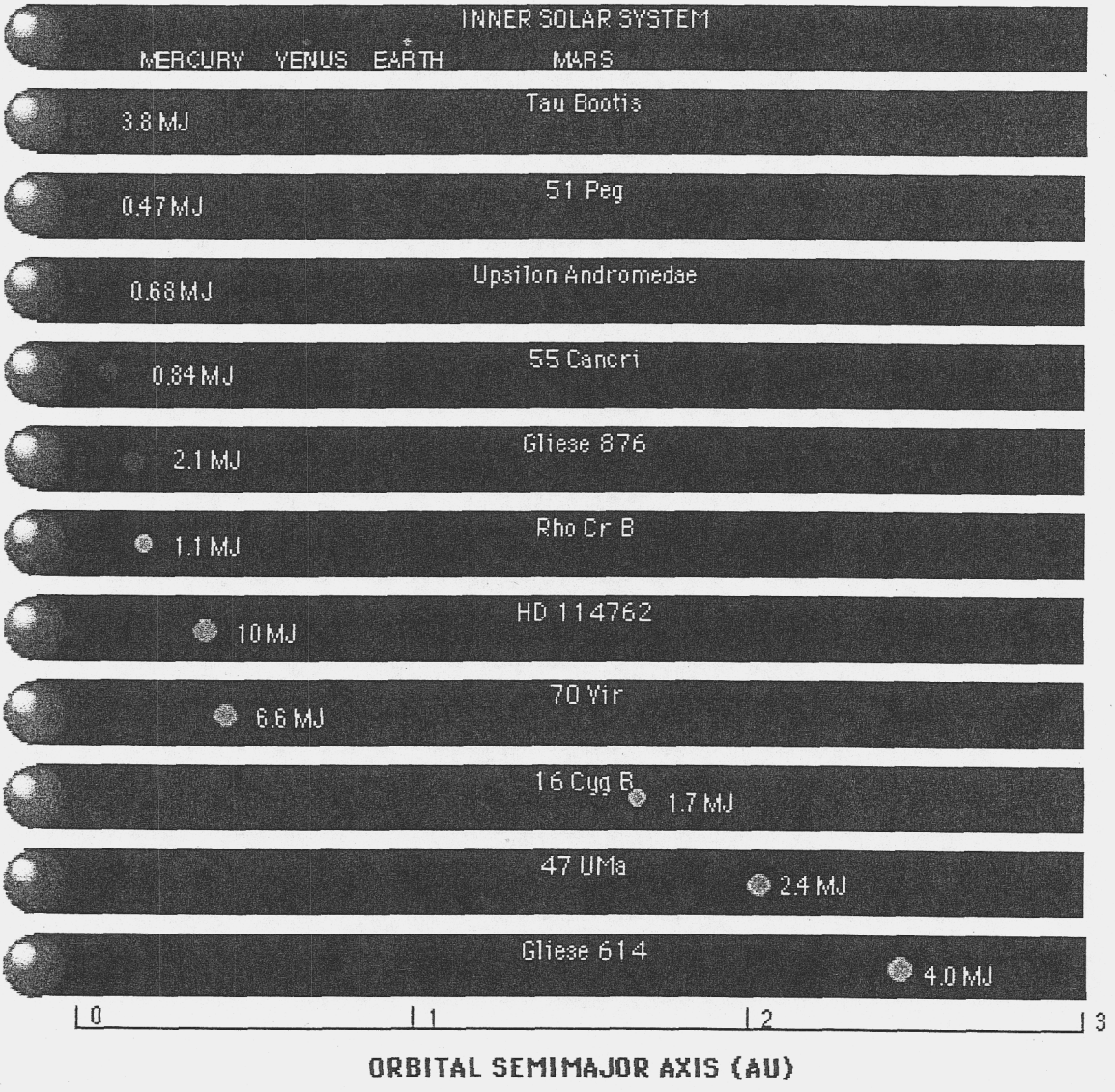

From http://cannon.sfsu.edu/~gmarcy/planetsearch

Extrasolar Planets Properties

- **Radius < 3 Astronomical Unit vs. 5 AU for Jupiter**
- **Mass ~ 1 – 10 $M_{Jupiter}$**
- **Period ~ 3.3 – 1092 days**
- **Eccentricity ~ 0.0 – 0.7**

Current Technology Limits

- **Doppler precision** $\geq$ 3 m/s $\Rightarrow$ 4σ **detection limit, Jupiter-like planets (12.5 m/s variation on the Sun)**
- **Spectral resolution R ~ 50,000, limited by** ATMOSPHERIC SEEING, **no line profile information**
- **Stellar activity including** photospheric granulation, turbulence, magnetic cycling, stellar oscillation etc **could mimic small Doppler perturbation,** ~ 3 m/s, **caused by smaller planets**

What is Next for Doppler Planet Search?

- **Improve precision to 1 m/s or less for sub-Jupiter mass planet search**

- **Saturn-like planet, 3 m/s over 30 years**

- **Earth-like planet, 0.1 m/s over 1 year**

Solutions to New Challenges

- **Higher spectral resolution with adaptive optics (Ge et al.):**

  - Resolve line profiles
  - Simultaneously trace stellar activity & planet perturbation
  - Reduce wavelength calibration errors

- **Combination of spectrometer and interferometer (Erskine & Ge):**

  - very stable point spread function (PSF) over broad wavelength coverage

Jian Ge, LLNL, 11/10/98

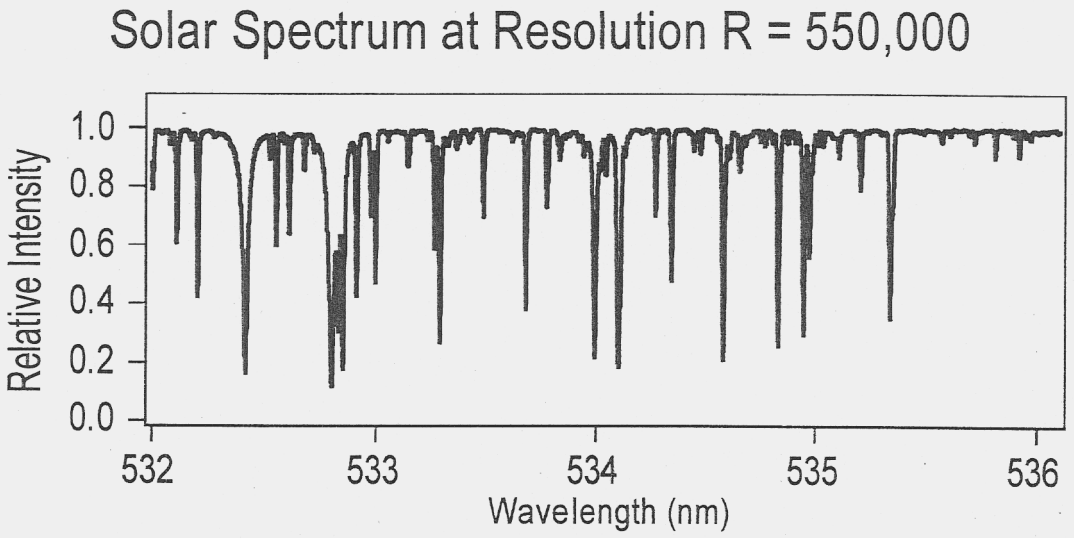

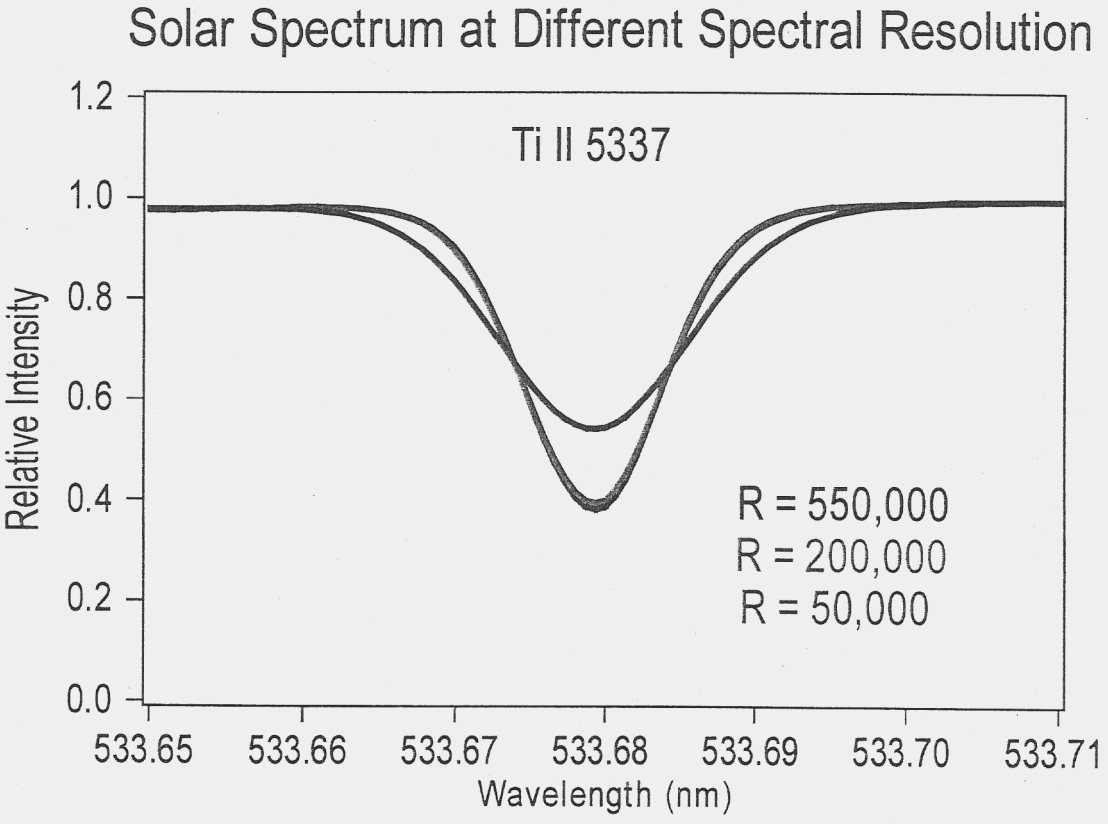

Jian Ge, LLNL, 11/10/98

Bisector of Solar Spectral Line, Ti II 5337, with R = 550,000

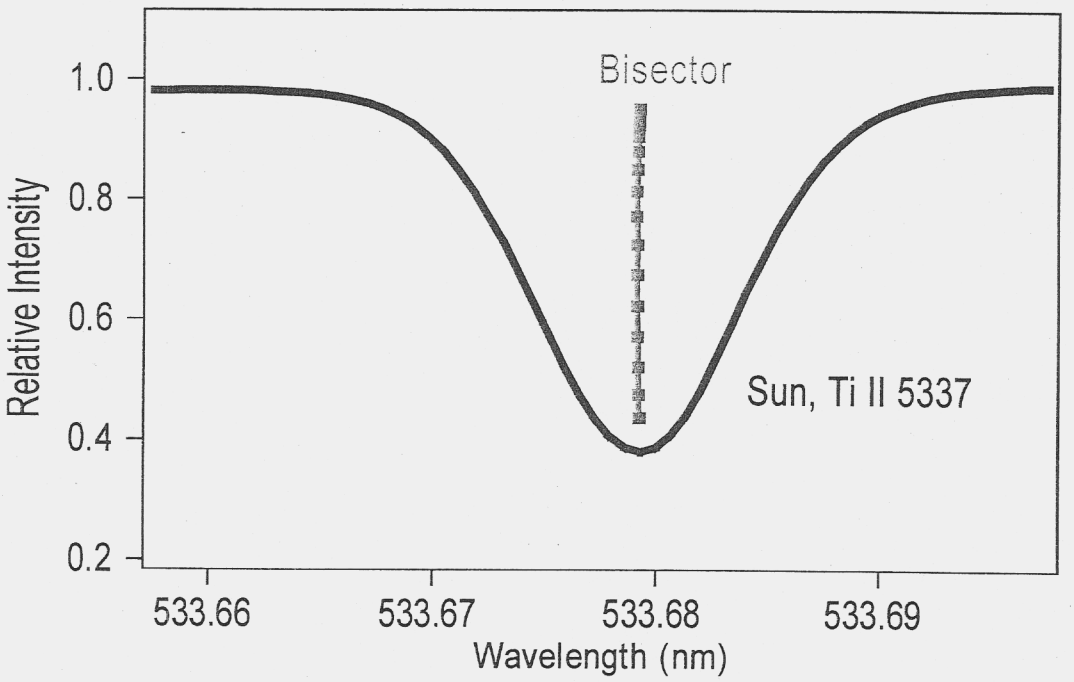

Expanded Part of Bisector: Distorted "C" Shape

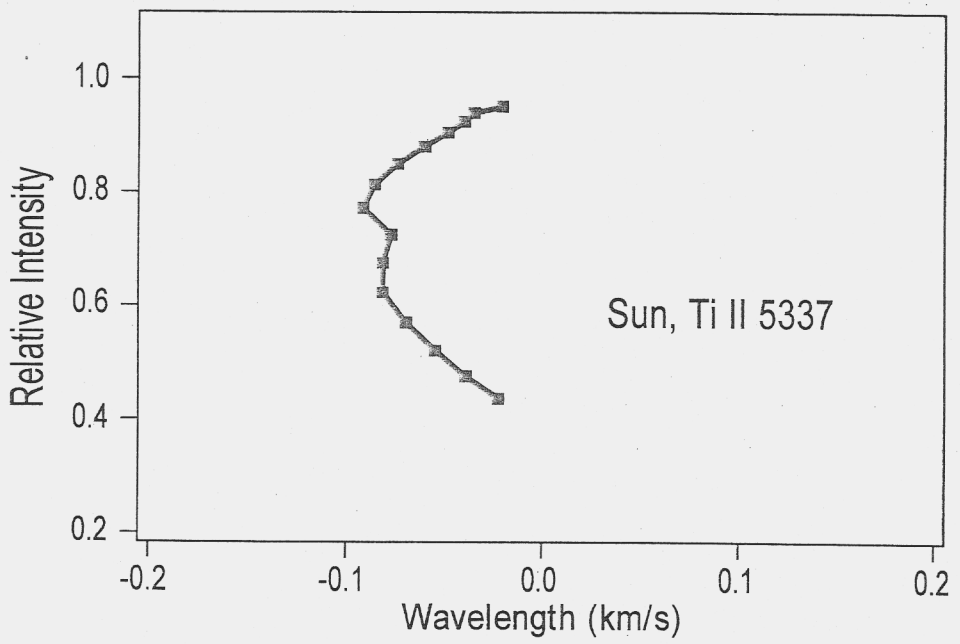

Jian Ge, LLNL, 11/10/98

Comparison of Bisectors from Different Resolution

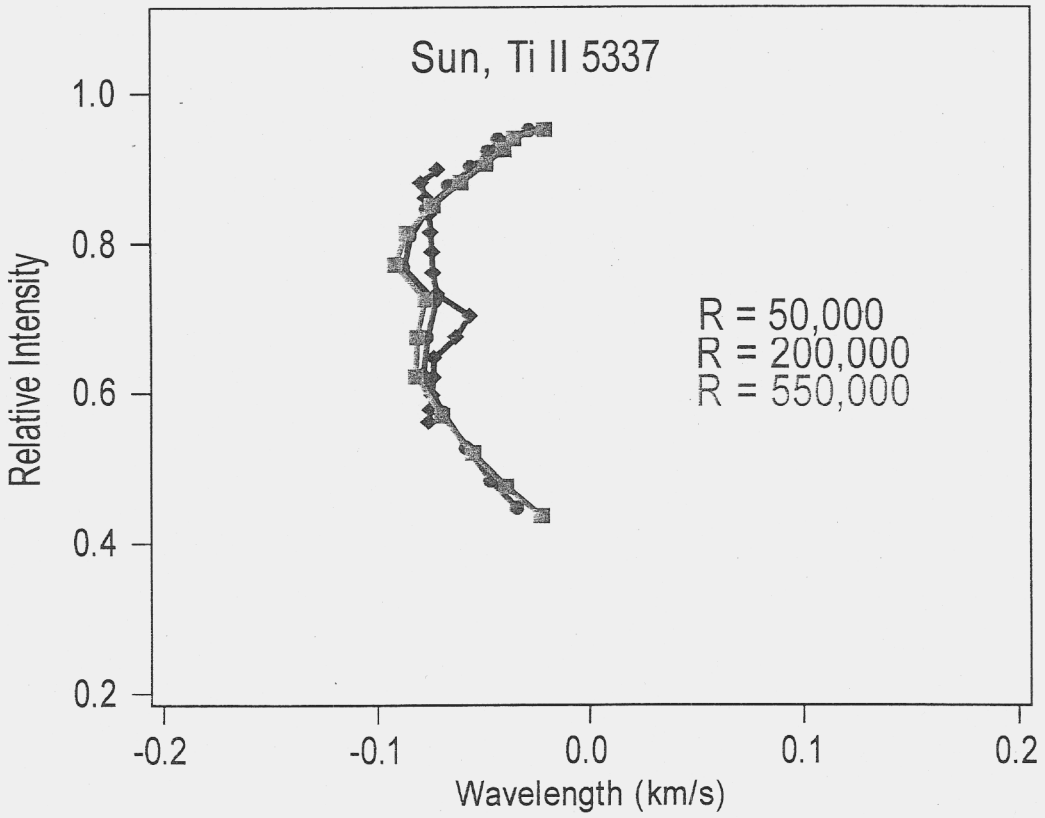

R = 50,000 cannot preserve line profile information
R = 200,000 required for line profile measurements

Novel Adaptive Optics Spectrometer

I-band (0.9 μm) Image at Mt. Wilson 100 inch

Seeing-limited image, 1 arcsec

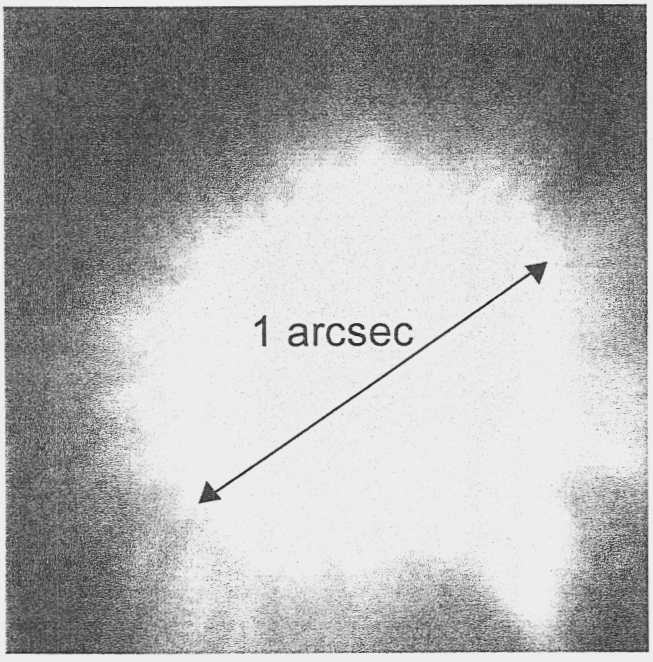

Adaptive Optics corrected image: 0.071”

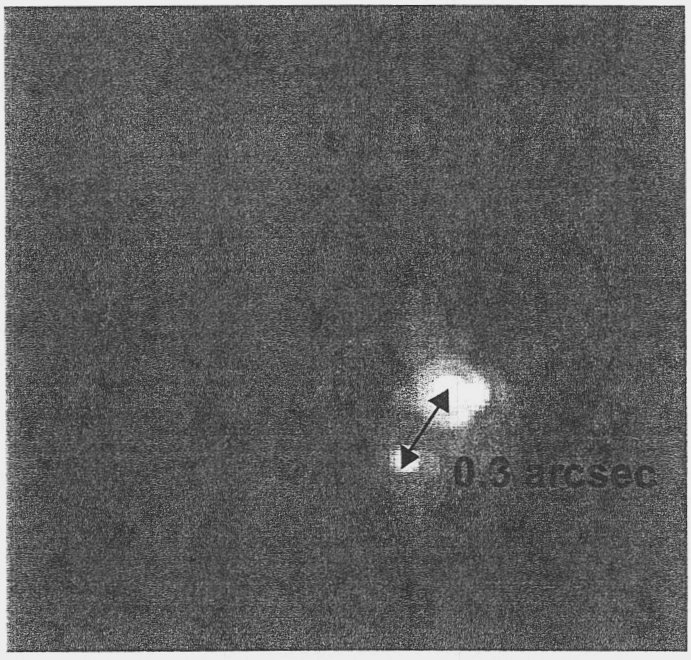

Advantages of adaptive optics spectroscopy:

- **Smaller slit width without large photon loss** $\Rightarrow$ higher resolution, high efficiency

- **Smaller image size in the spatial direction** $\Rightarrow$ **packing more cross-dispersed orders on a detector** $\Rightarrow$ large wavelength coverage

- **Smaller image size** $\Rightarrow$ higher spatial information

- **Optics small and slow** $\Rightarrow$ low cost

New era of ultra-high resolution AO spectroscopy

R ~ 200,000 – 500,000 with AO vs. R ~ 50,000 w/o AO

Test of a novel prototype AO spectrometer at Starfire Optical Range 1.5m telescope, Air Force Phillips Lab and at Mt. Wilson 100inch telescope

Setup of AO spectrometer at Mt. Wilson 100 inch telescope, Nov. 1997

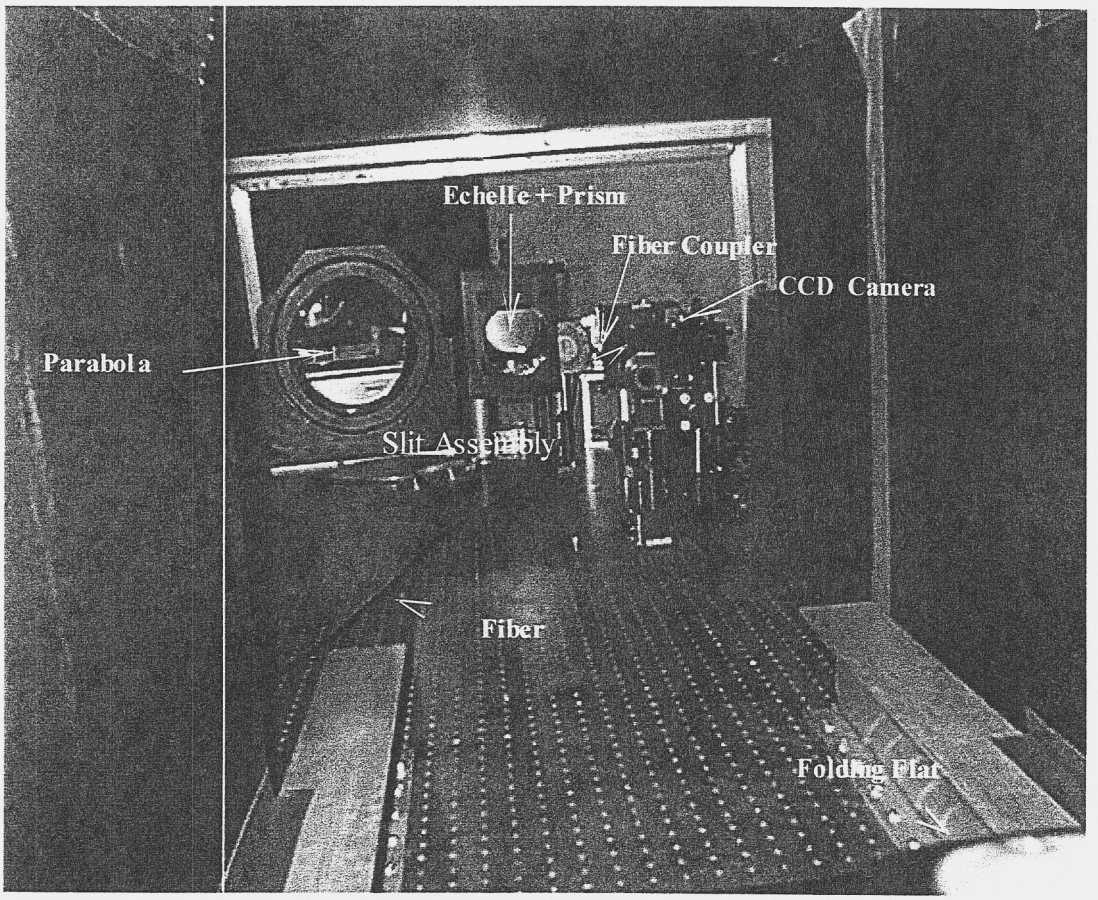

- Off-axis parabola focal length = 6 m
- F/# = 55
- Grating: 250x125 mm^2 R2 echelle
- Cross-disperser: 160x160 mm^2 8 deg wedge prism
- Beam diameter: 125 mm
- Working wavelength: 0.4-1.0 μm

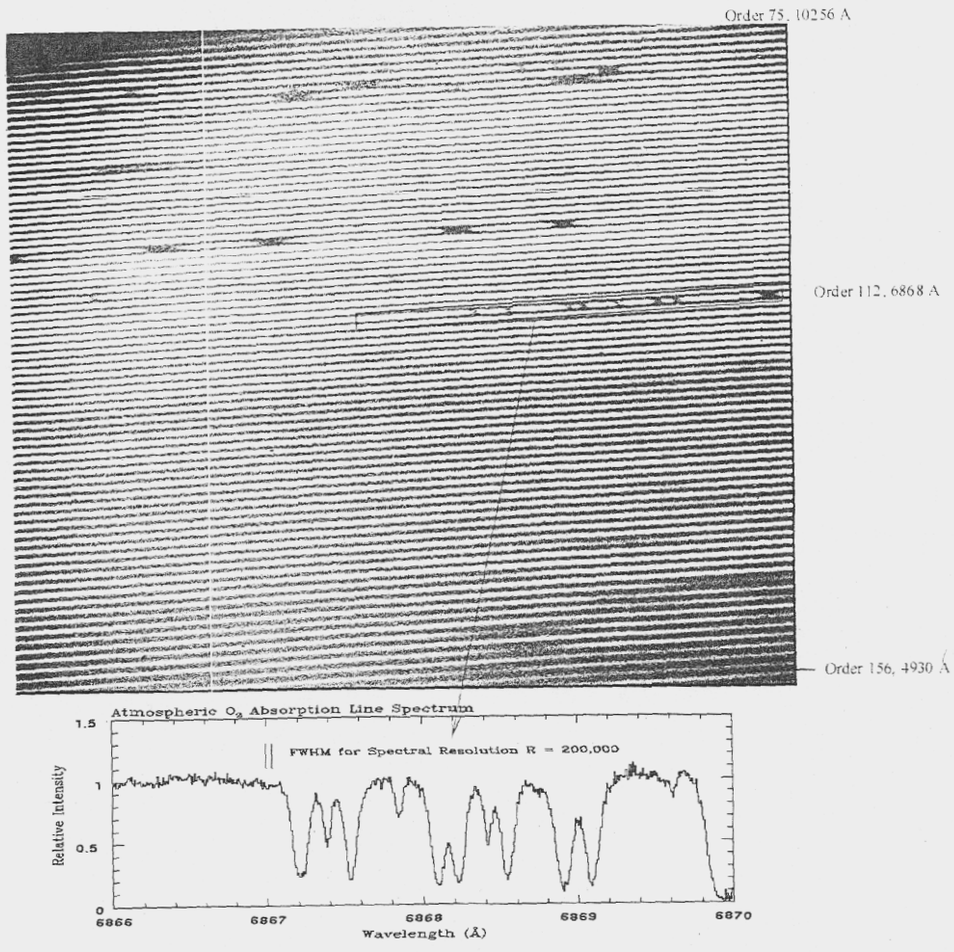

Fiber-fed spectrum of α Ori at Mt Wilson 100 inch telescope, Nov. 1997. A near single mode fiber with only 10 μm core size

- **Spectral Resolution, R ~ 200,000, 0.5 – 1.0 μm**
- **~ 80 cross-dispersed orders covered by a 25x25 mm^2 CCD detector**
- **~ 650 Å wavelength coverage**

Adaptive optics spectroscopy of interstellar pottasium absorption line at R = 250,000, at Starfire Optical Range 1.5 m telescope, Nov. 1995

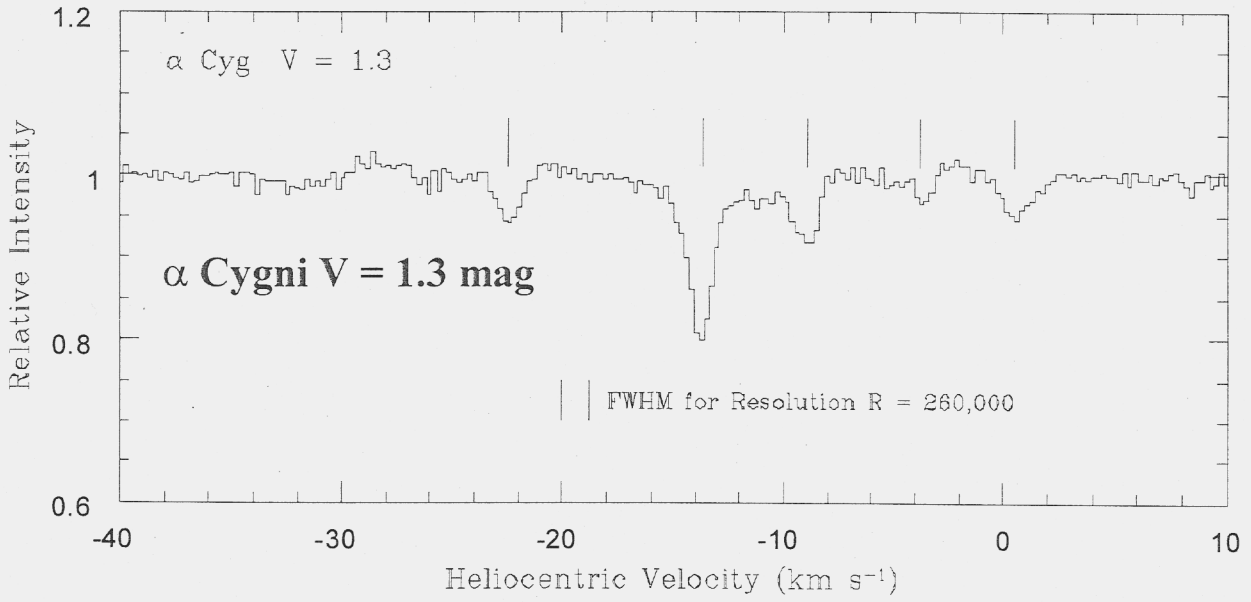

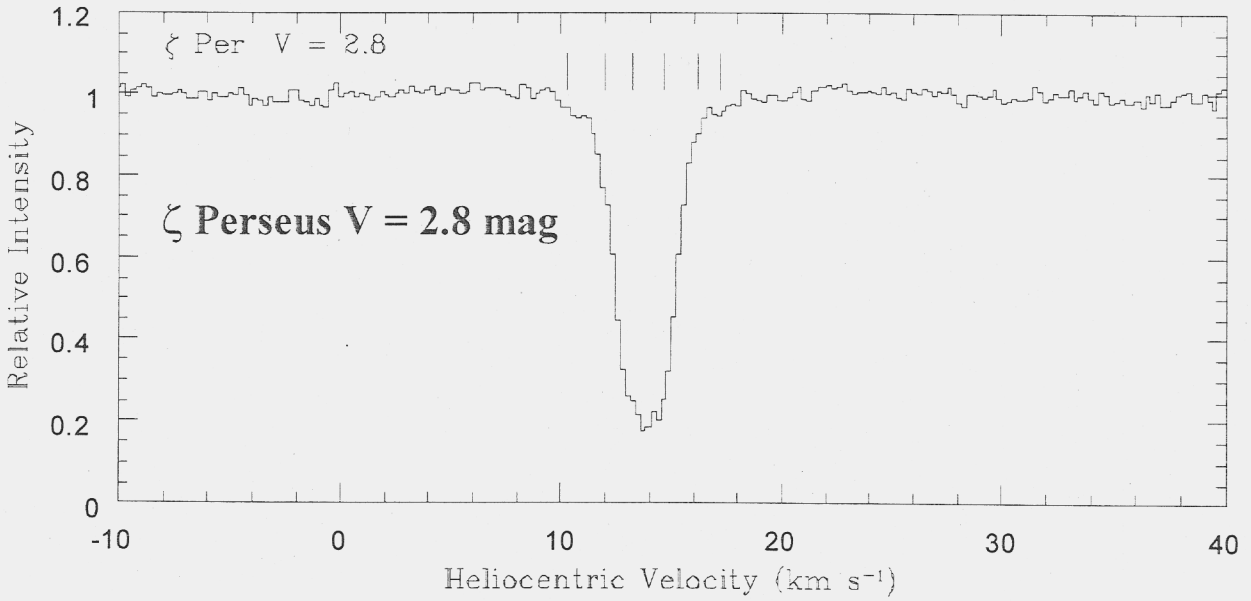

New Optimized AO Spectrometer Design

Maksutov-type design, all spheres

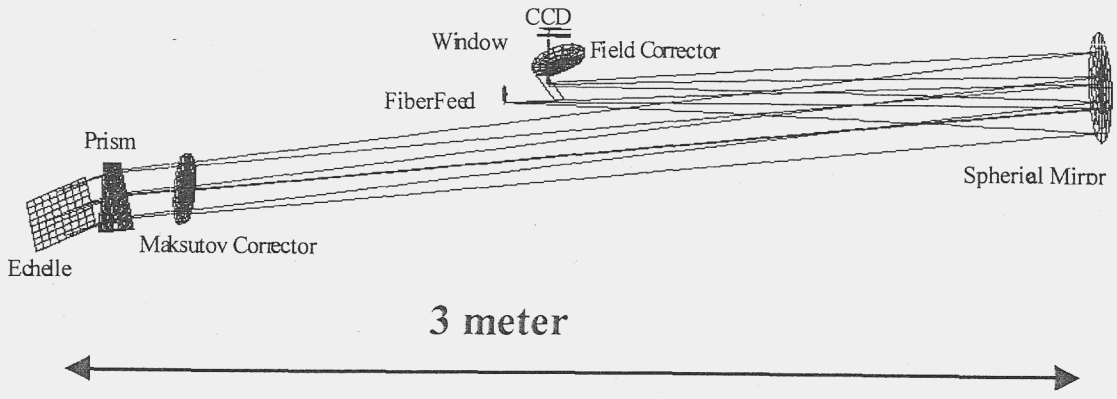

Near single mode fiber-fed optical cross-dispersed echelle spectrometer

- **Focal length: 1900 mm**
- **Focal ration: F/# = 16**
- **~ 10 μm core size fused silica fiber, preserve AO system etendue**
- **Separated from telescope, more stable**
- **Portable, easily matched with different optical telescopes with AO system**
- **Much less scattering light**

Spectral format on a 2kx4k CCD detector with 30x60 mm^2

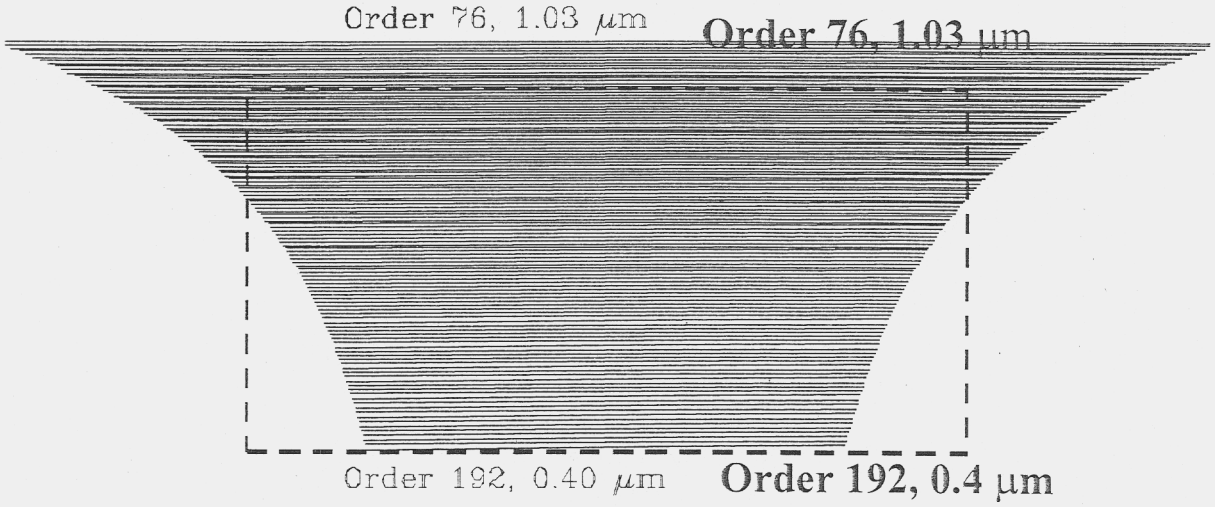

- Spectral resolution: R = 200,000
- Total detection efficiency: 4% (including telescope, AO, spectrometer and CCD detector)
- Wavelength coverage per exposure: 4000 Å

Sub-Jupiter Mass Planet Searches

- **Signal-to-noise ratio per CCD pixel: S/N ~ 1000**
  At SOR 3.5 m telescope, R = 200,000, 0.5 hour exposure, V = 5 mag.

- **Doppler shift error per pixel: σ_V ~ 18 m/s (photon statistics)**

- **Doppler shift error per absorption line: σ_V ~ 4 m/s for ~ 20 pixel to sample typical lines**

- **For ~ 700 strong stellar absorption lines covered by iodine absorption (0.5 – 0.6 μm), mean error: σ_V ~ 0.2 m/s — ultimate precision!**

Saturn Signal Observed with a Precision of 1 and 3 m/s

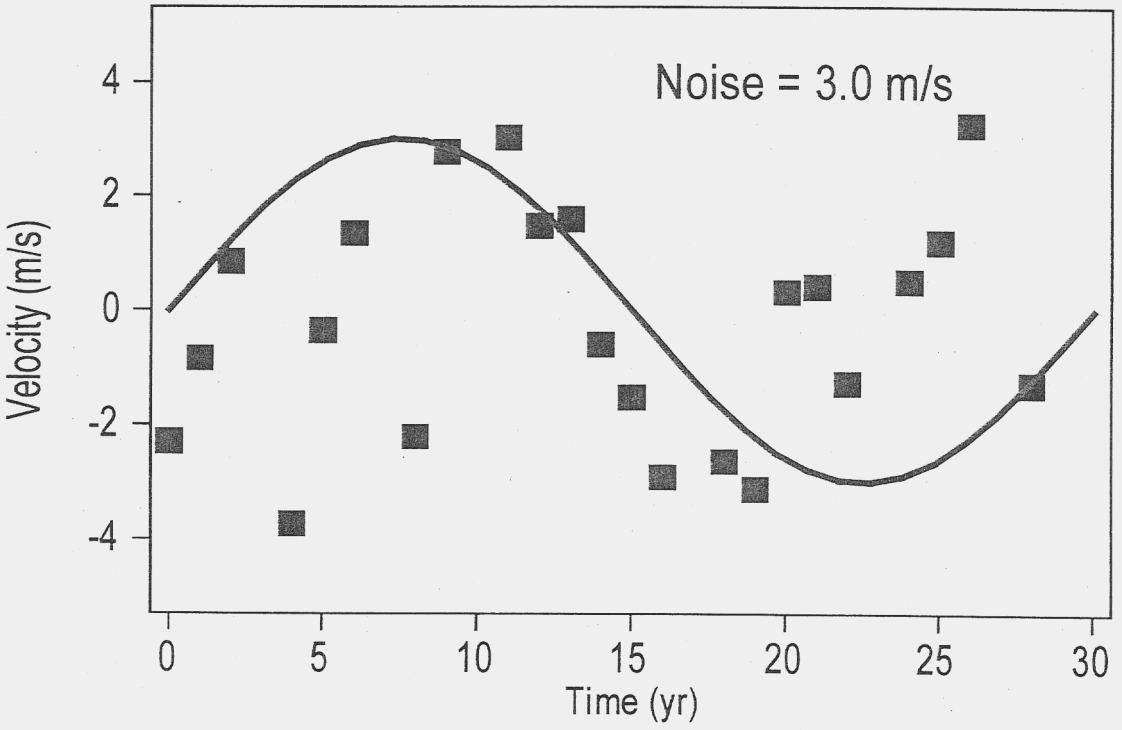

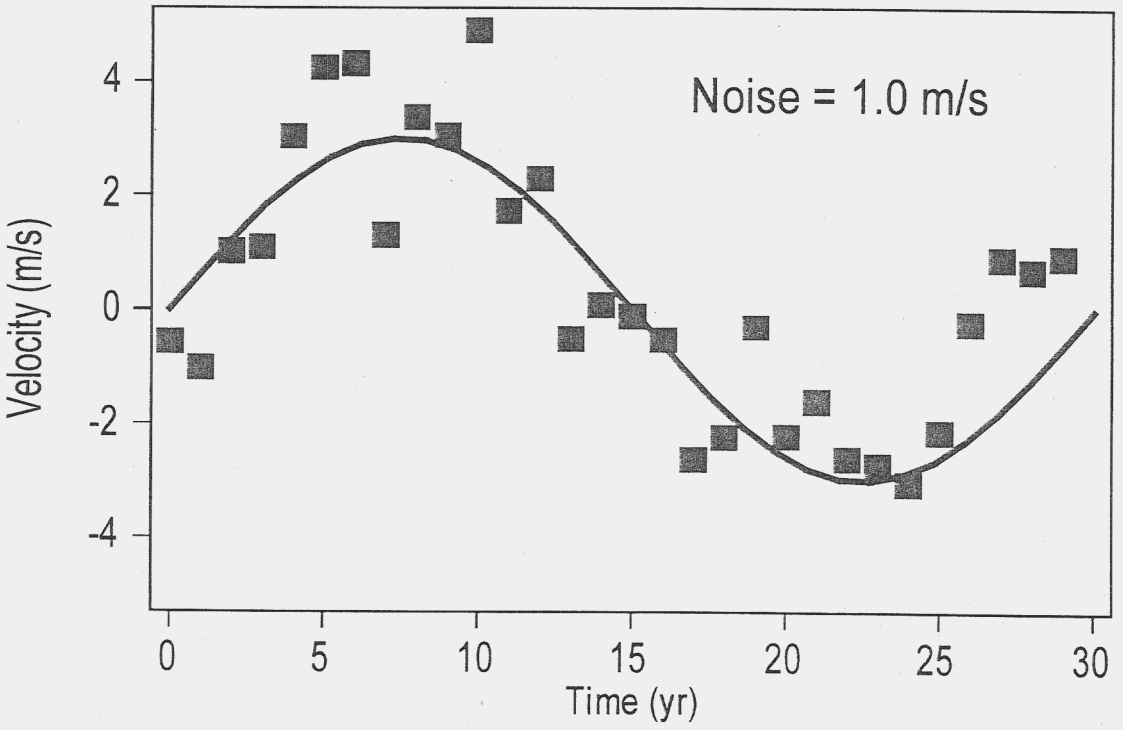

Simultaneous study of stellar activity

- First time of large wavelength coverage, ~ 4000 Å, with R = 200,000

- Simultaneously monitor different stellar absorption lines of different ionization and excitation, which respond differently to different atmospheric heights, and to hotter and cooler patches of surface

- Simultaneously monitor perturbations from small extra-solar planets and stellar activity, initiate the study with ~ 1 m/s accuracy

Micro-Satellite Technology for the 21st Century

Lawrence C. Ng
Ng6@llnl.gov

This paper will examine the development of micro-satellite technology for use in space. It is envisioned that potential missions for the micro-satellites may include: rendezvous with a satellite, conduct proximity inspection, land on a satellite, and perform rescue or other logistic mission. The critical enabling technology for this capability is the development of an agile micro-satellite or MicroSat. A MicroSat is a small satellite weighing only a few tens of kilograms but carrying onboard a host of lightweight sensors and actuators, inertial navigation instruments and avionics. When equipped with a propulsion system and smart guidance, navigation and control software, the MicroSat has the ability to maneuver precisely in space in both orientation and translation. When further equipped with smart vision based image analysis software and repair tools, the MicroSat can autonomously perform many of the functions mentioned above. Ground command and control support can therefore be minimized and used only to augment and enhance performance by providing ground truth knowledge, such as emphemeris data. The MicroSat can also function in a tele-robotic mode, with a man-in-the-loop, to more effectively execute complex (less predictable) maneuvers and to provide a manned presence (in surrogate form) when and where one is required. This technology will help define the critical pathfinder capability for future operations in near Earth space.

UCRL-ID-129880

Date: 29 Oct 1998 14:12:05 -0700

Detecting Massed Troops with the French SPOT Satellites

By Vipin Gupta and George Harris

This study is a technical assessment on the utility of the French SPOT satellites for detecting troop concentrations in a desert environment. The capabilities of the SPOT satellites for this specific application were tested empirically using two archived SPOT images of the Saudi-Iraqi border acquired shortly before and during the 1991 Gulf War. Change detection analysis was done to detect, locate, and identify troop deployments. The results were then extrapolated to forecast the feasibility of using medium resolution, broad swath imagery to detect and track future offensive attack preparations. The presentation concludes with a discussion on the security implications associated with the future deployment of SPOT-type systems as well as an appendix on the impact of using SPOT-type imagery to support conventional and unconventional weapons strikes on imaged troop concentrations.

Detecting Troop Concentrations using the French SPOT satellite

A Case Study from the 1991 Gulf War

Vipin Gupta
Systems Research Dept.
Sandia National Labs
Livermore, CA

George Harris
NAI Directorate
Lawrence Livermore Lab
Livermore, CA

Initiated by SNL/CA and LLNL
Sponsored by Sandia Cooperative Monitoring Center (NN-40)

What's the question and why answer it

Q: Can one use fuzzy (~10 m resolution) satellite images to detect the massing of troops?

Q: Can one use such imagery for early warning and targeting?

A: Yes and Yes

How we did it...

1. Selected a real war situation (1991 Gulf War)
2. Selected a division to observe (the US 24th Mech)
3. Obtained "before" and "after" images
4. Conducted change detection analysis
5. Compared results with ground truth

Implications

- Moderate resolution, broad swath imagery is widely available to all countries
- Countries can utilize this technology to monitor borders and DMZs
- Technology can be used for long-range targeting

Deployed and planned commercial satellites with SPOT-type sensors

Satellite	Country	Resolution of SPOT-type Sensor	Swath Width	Launch Date
SPOT 1-4	France	10 meter panchromatic	120 km*	1986, 1990, 1993, 1998
COSMOS series TK-350	Russia	10 meter panchromatic	300 km	1987-1998
IRS-1C, IRS-1D	India	6 meter panchromatic	141 km*	1995, 1997
Priroda	Russia	6 meter panchromatic	40, 80 km	1996
ADEOS	Japan	8 meter panchromatic	80 km	1996
OrbView 3	USA	8 meter hyperspectral	5 km	1999
KOMPSAT	S. Korea	10 meter multispectral	40 km	1999
RESOURCE21	USA	10 meter panchromatic	205 km	2000
ALOS	Japan	10 meter multispectral	70 km	2000

* – wide swath obtained by using multiple side-by-side sensors simultaneously

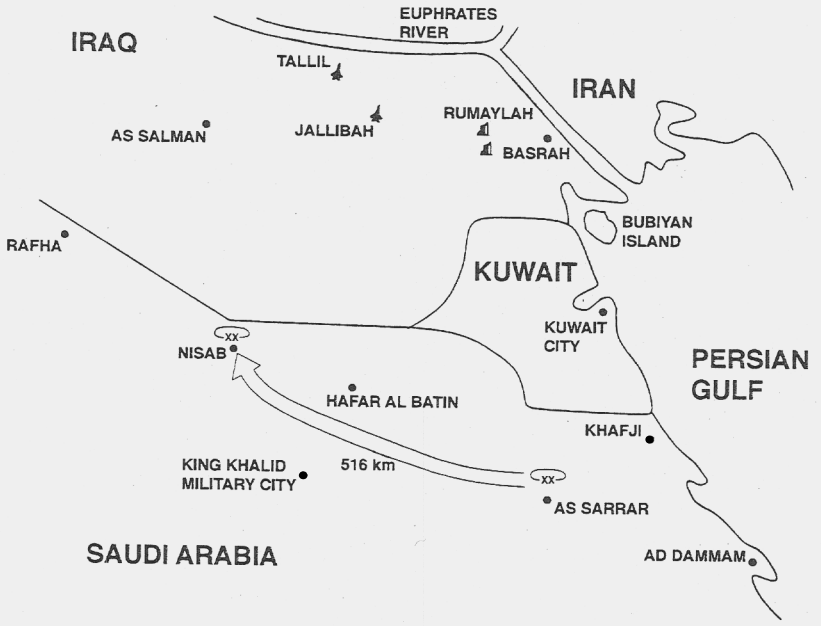
IRAQ
EUPHRATES RIVER
TALLIL
IRAN
AS SALMAN
JALLIBAH
RUMAYLAH
BASRAH
BUBIYAN ISLAND
RAFHA
KUWAIT
KUWAIT CITY
PERSIAN GULF
NISAB
HAFAR AL BATIN
KHAFJI
KING KHALID MILITARY CITY
516 km
AS SARRAR
SAUDI ARABIA
AD DAMMAM

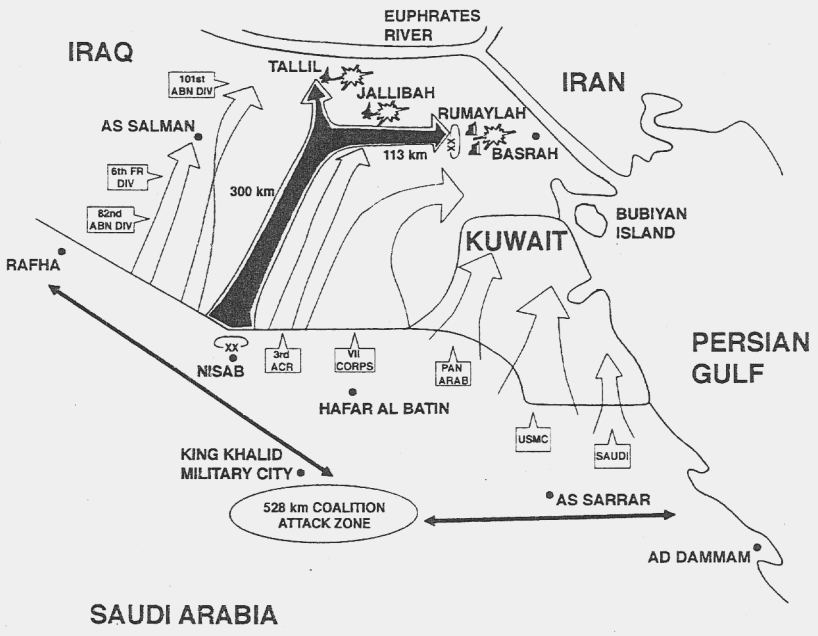
EUPHRATES
RIVER
IRAQ
IRAN
TALLIL
JALLIBAH
RUMAYLAH
BASRAH
101st
ABN DIV
AS SALMAN
6th FR
DIV
82nd
ABN DIV
300 km
113 km
XVIII
KUWAIT
BUBIYAN
ISLAND
RAFHA
XX
NISAB
3rd
ACR
VII
CORPS
PAN
ARAB
HAFAR AL BATIN
PERSIAN
GULF
USMC
SAUDI
KING KHALID
MILITARY CITY
528 km COALITION
ATTACK ZONE
AS SARRAR
AD DAMMAM
SAUDI ARABIA

Figure 1

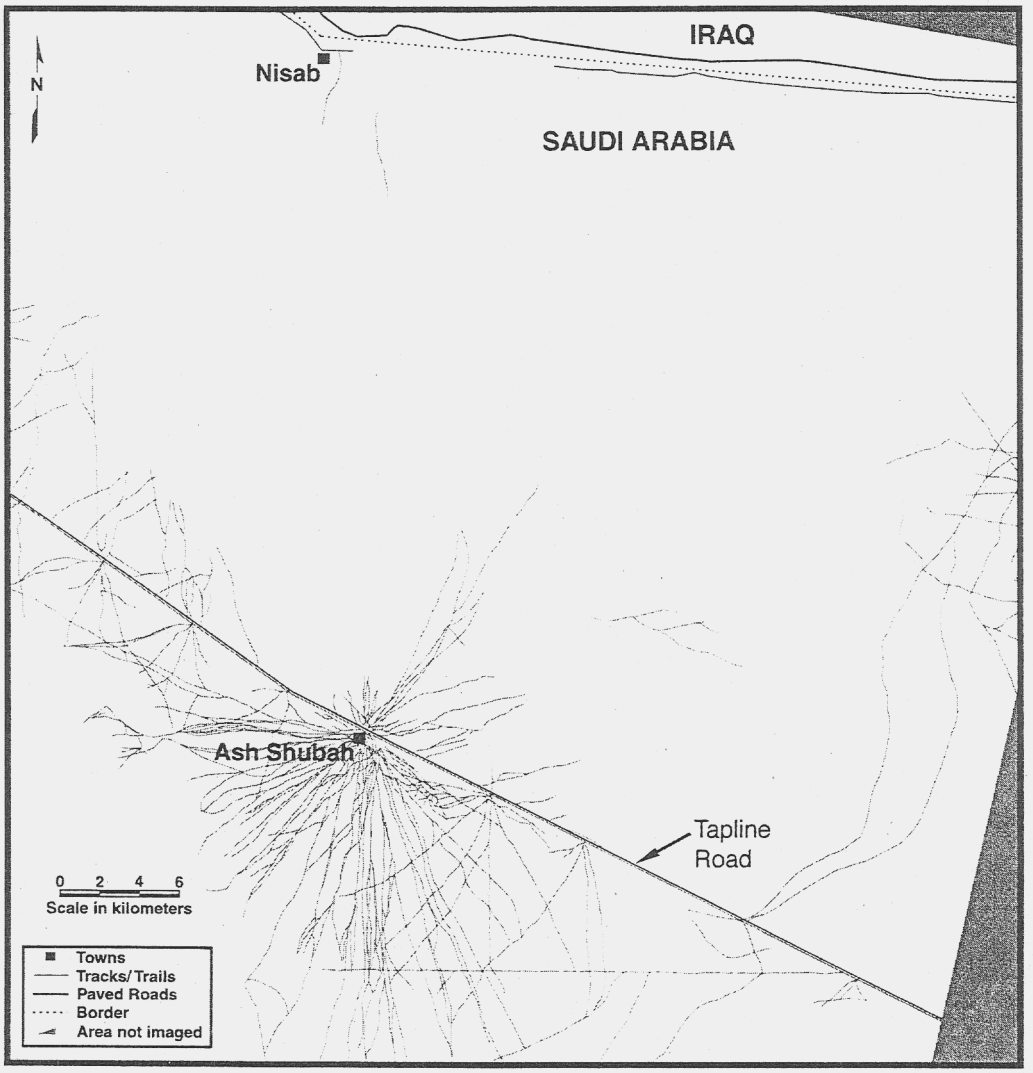
IRAQ
Nisab
N
SAUDI ARABIA
Ash Shubah
Tapline
Road
0 2 4 6
Scale in kilometers
Towns
Tracks/Trails
Paved Roads
Border
Area not imaged

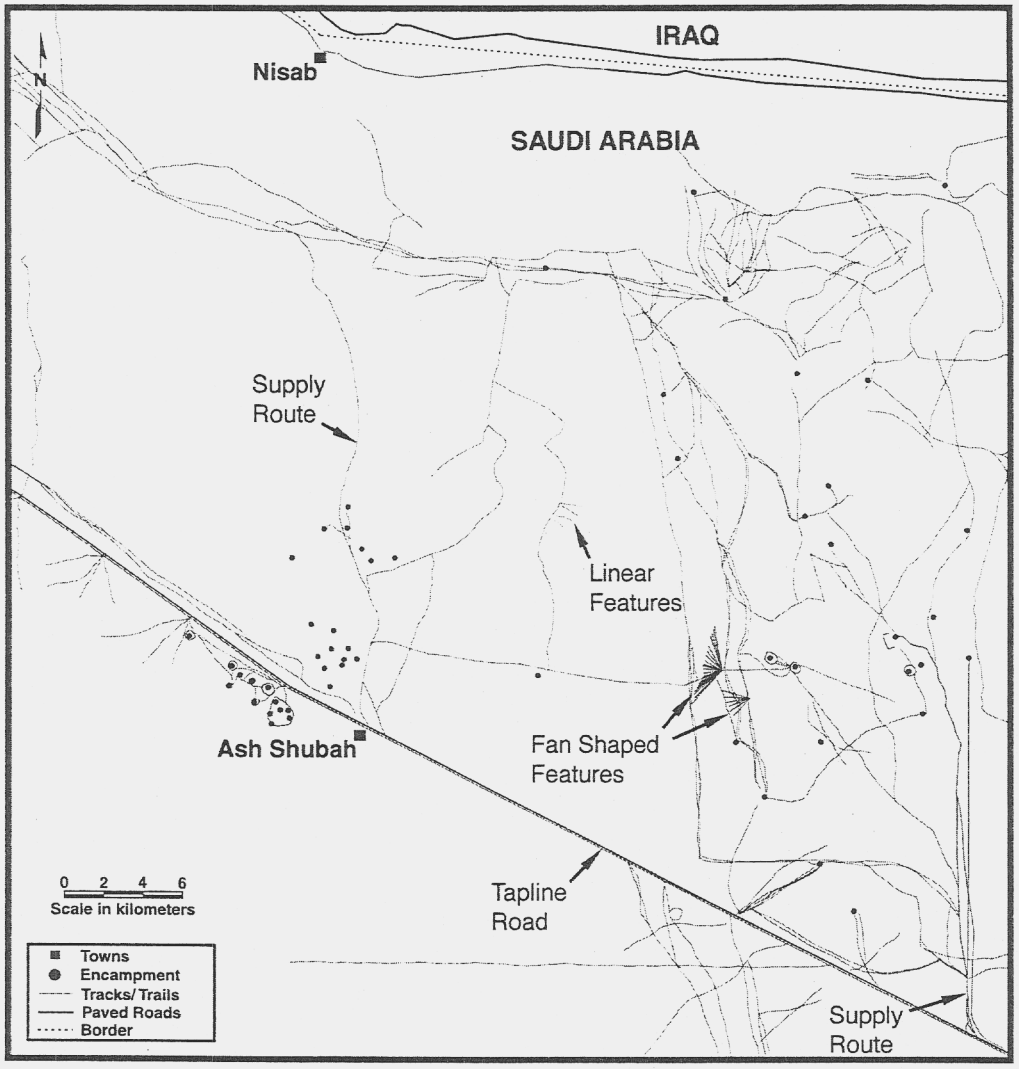
IRAQ
Nisab
N
SAUDI ARABIA
Supply
Route
Linear
Features
Fan Shaped
Features
Ash Shubah
Tapline
Road
Supply
Route
0 2 4 6
Scale in kilometers
Towns
Encampment
Tracks/ Trails
Paved Roads
Border

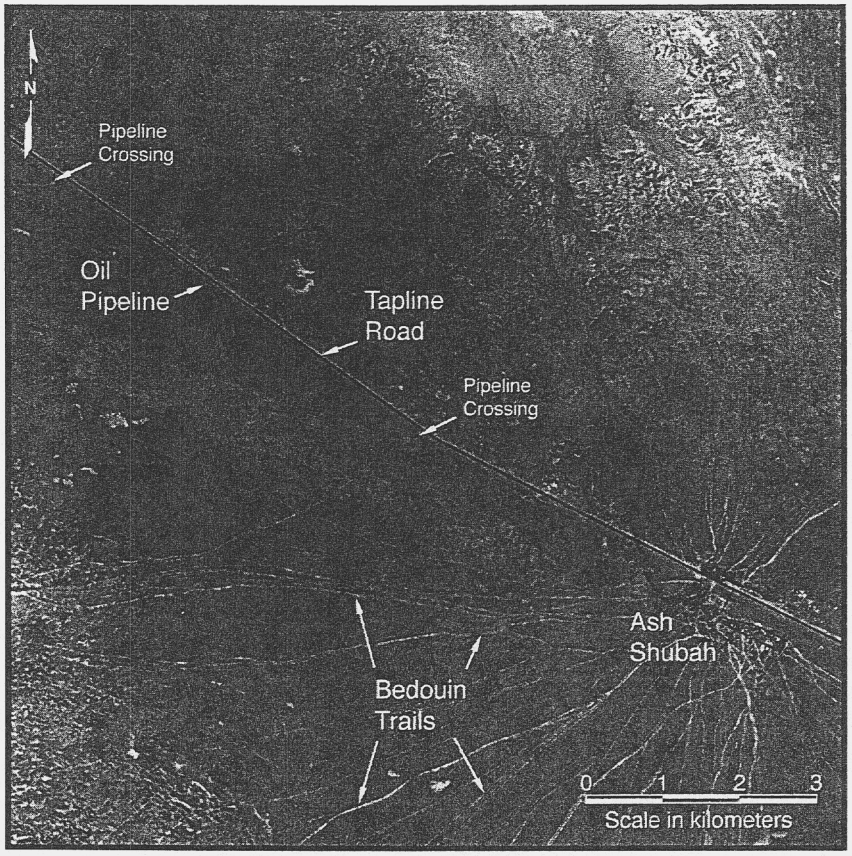
N
Pipeline
Crossing
Oil
Pipeline
Tapline
Road
Pipeline
Crossing
Ash
Shubah
Bedouin
Trails
0
1
2
3
Scale in kilometers

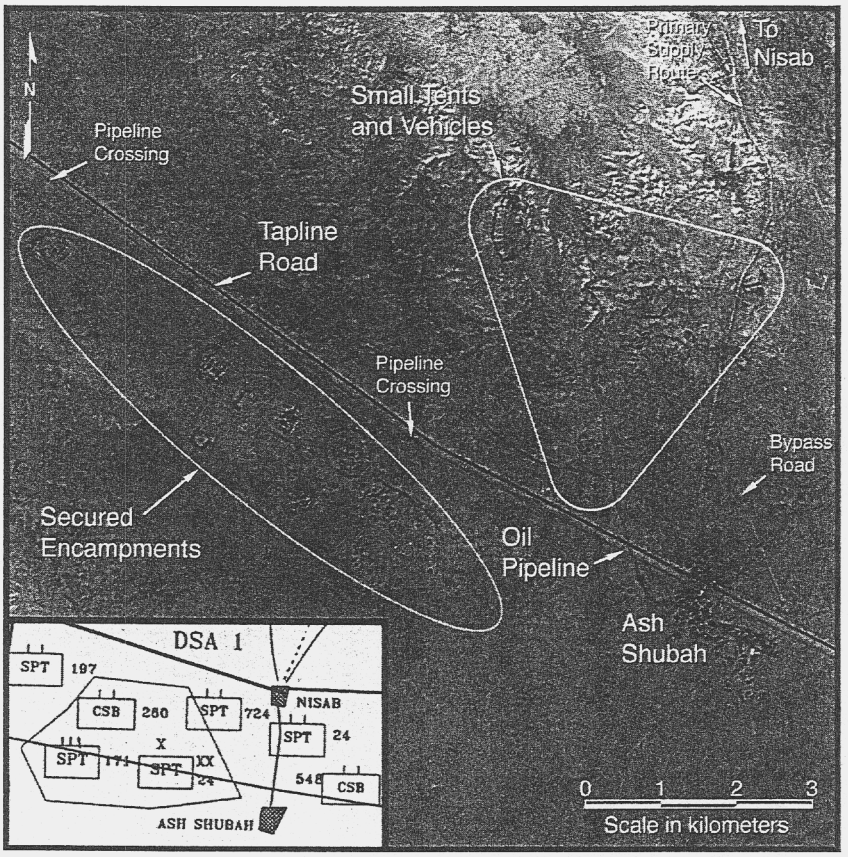
N
Primary Supply Route
To Nisab
Small Tents and Vehicles
Pipeline Crossing
Tapline Road
Pipeline Crossing
Bypass Road
Secured Encampments
Oil Pipeline
Ash Shubah
DSA 1
SPT 197
CSB 260
SPT 724
NISAB
SPT 24
SPT 171
SPT XX 24
548 CSB
ASH SHUBAH
0 1 2 3
Scale in kilometers

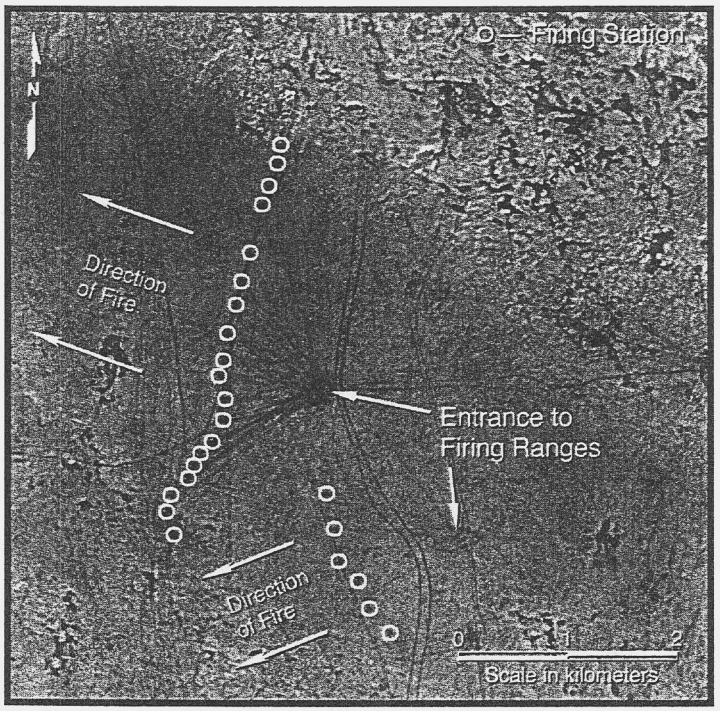
Firing Station
N
Direction of Fire
Entrance to Firing Ranges
Direction of Fire
0
1
2
Scale in kilometers

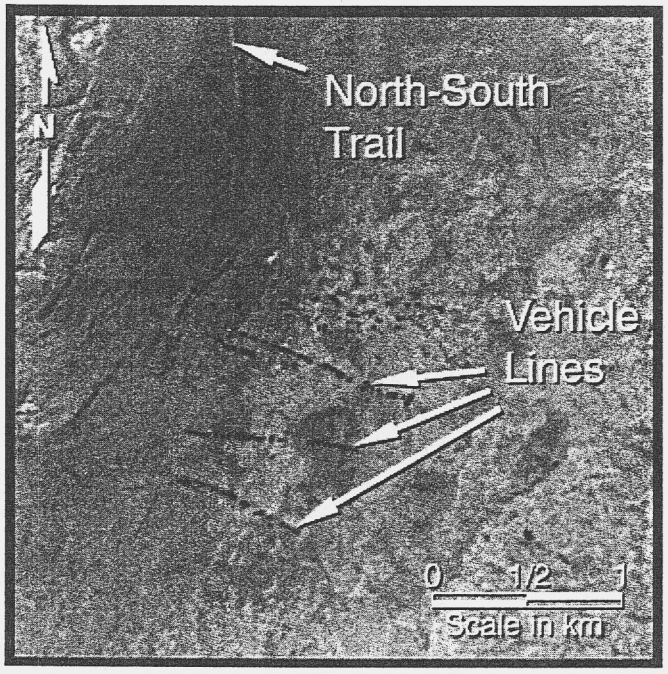
North-South
Trail
N
Vehicle
Lines
0
1/2
1
Scale in km

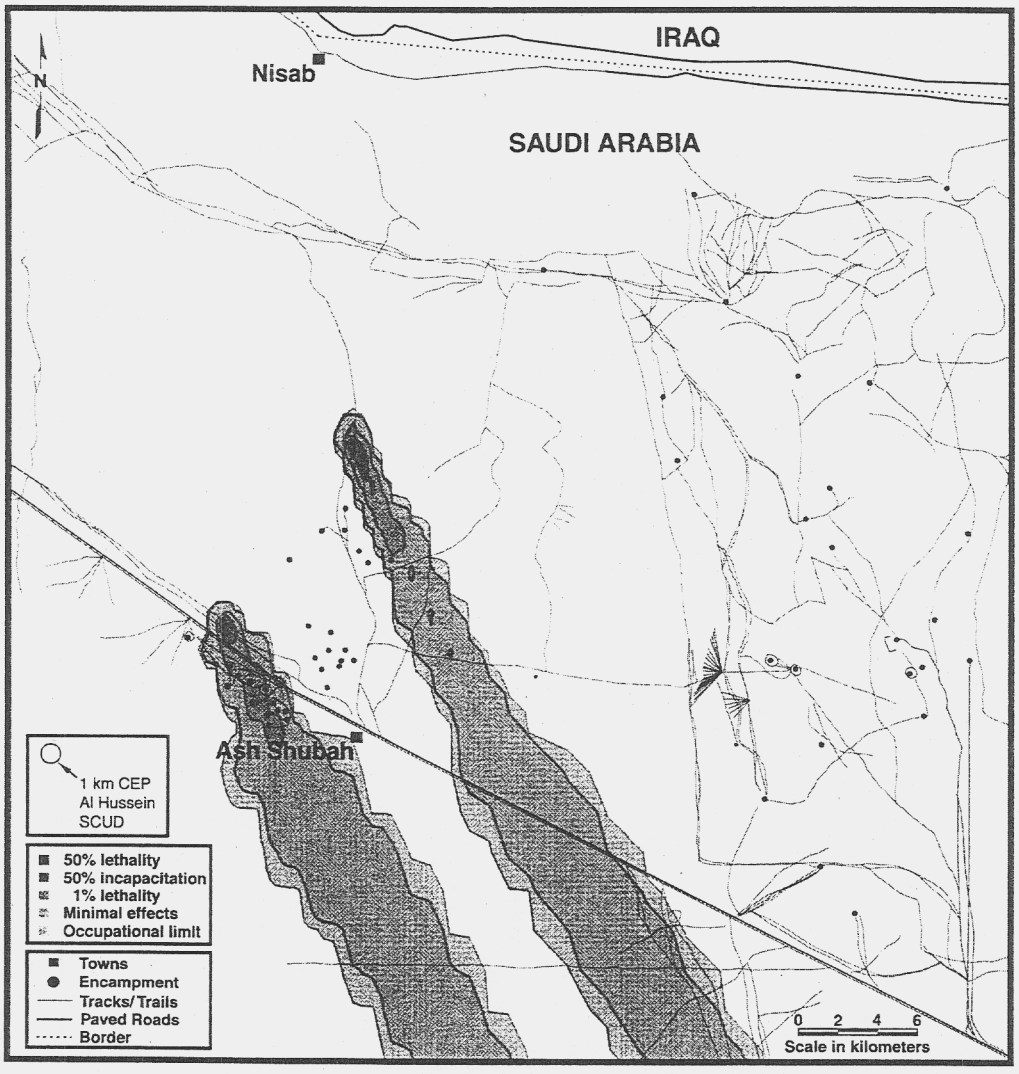
IRAQ
Nisab
N
SAUDI ARABIA
Ash Shubah
1 km CEP
Al Hussein
SCUD
50% lethality
50% incapacitation
1% lethality
Minimal effects
Occupational limit
Towns
Encampment
Tracks/Trails
Paved Roads
Border
0 2 4 6
Scale in kilometers

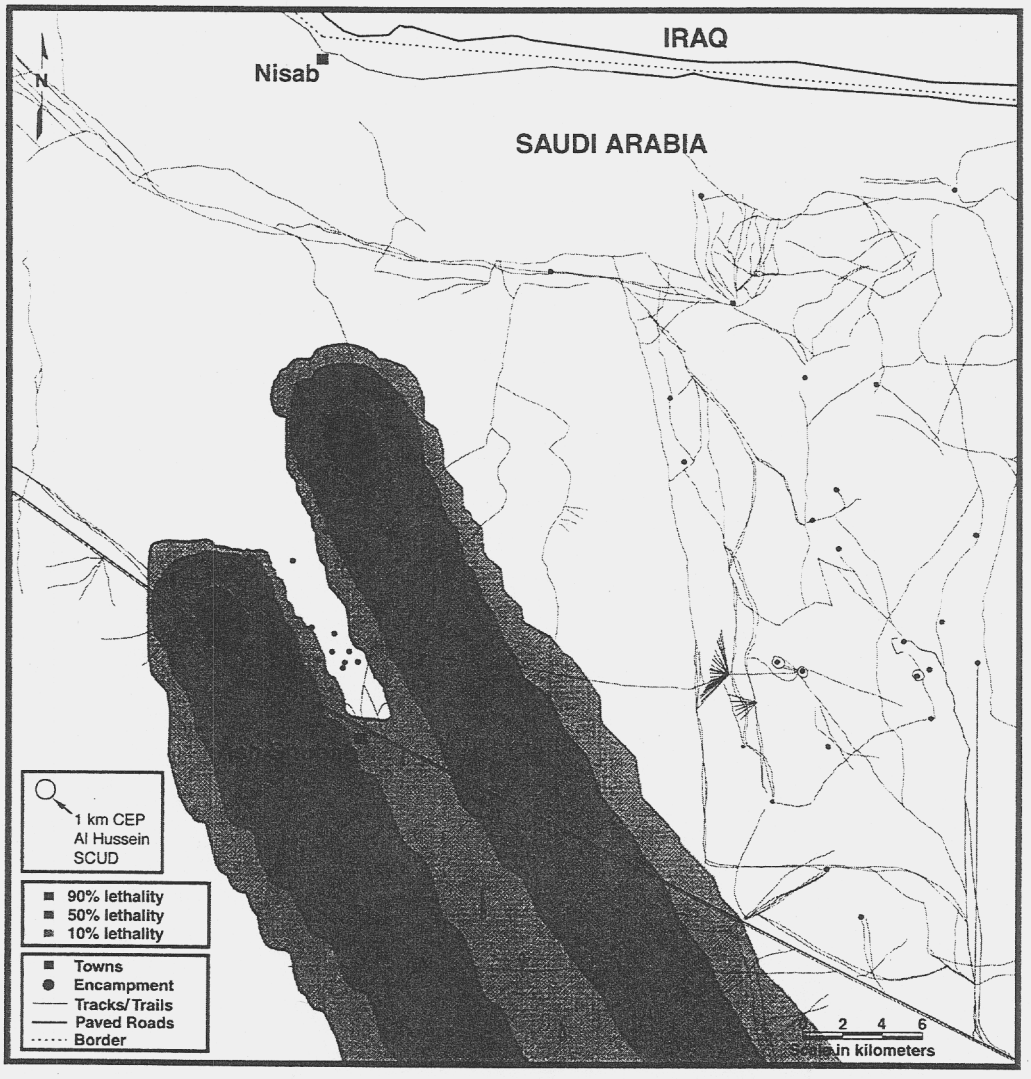
IRAQ
Nisab
N
SAUDI ARABIA
1 km CEP
Al Hussein
SCUD
90% lethality
50% lethality
10% lethality
Towns
Encampment
Tracks/ Trails
Paved Roads
Border
2 4 6
Scale in kilometers

Combined Sensing and Simulation for Enhanced Evaluation of Large Structures

David McCallen
Structural and Applied Mechanics Group
Lawrence Livermore National Laboratory

Abstract

With the proliferation and advancement of sophisticated numerical simulation software tools over the past twenty years, computational simulation of large structural systems has been a subject area experiencing rapid growth. Large-scale computer simulation is an essential tool in the design and analysis of modern structures and engineers are now highly reliant on large-scale structural simulations to design and evaluate the performance of critical new structures, and to establish the performance of expensive retrofits on existing structures. With the enormous cost and construction effort associated with many large structures, it is imperative that computer simulations provide an accurate picture of structural performance spanning a multiplicity of loading environments - for example bomb blast, earthquakes and ambient vibrations. Despite the advances in computational methods, there remains a significant degree of uncertainty in predicting the field performance of many large-scale structural systems. These uncertainties are rooted in our inability to precisely quantify the phenomenological behavior of certain aspects of structural excitation and structural response - e.g. uncertainties in the precise deformation characteristics of complex structural element interconnections or uncertainties in estimation of the actual loads a structure will be subjected to. In order to advance our ability to accurately and confidently simulate the response of structures, use must be made of measured structural response characteristics and measured excitation functions.

In the current study, techniques are being investigated which allow evaluation of simulation model accuracy with the possibility for subsequent enhancement of the simulation model. The multidisciplinary LLNL tools being employed include finite element based structural simulation, model based signal processing, and remote sensing and data communication. The overall objective of this research is to symbiotically couple numerical simulation with field measurement of structural behavior through model based signal processing. The essential links between simulation and measurement are indicated in the Figure. As indicated in the Figure, information from a numerical structural model and data from field measurements of structural response are fed into a model-based signal proces-

sor. The signal processing toolbox is used to evaluate whether the model and as-built structure are in agreement, or if there is a discrepancy between the dynamical behavior of the model and the actual structure. In addition, research on the signal processing toolbox will attempt to discriminate the source of existing discrepancies between the simulation model and the as-built structure. Once discrepancies can be identified, the basis for damage detection in a structural system has been established. Experimental measurements before and after an event can be employed to identify changes in the structural system and identification of the source of the differences with a damage detector can be performed in order to investigate where damage has occurred in a large distributed structure. The result

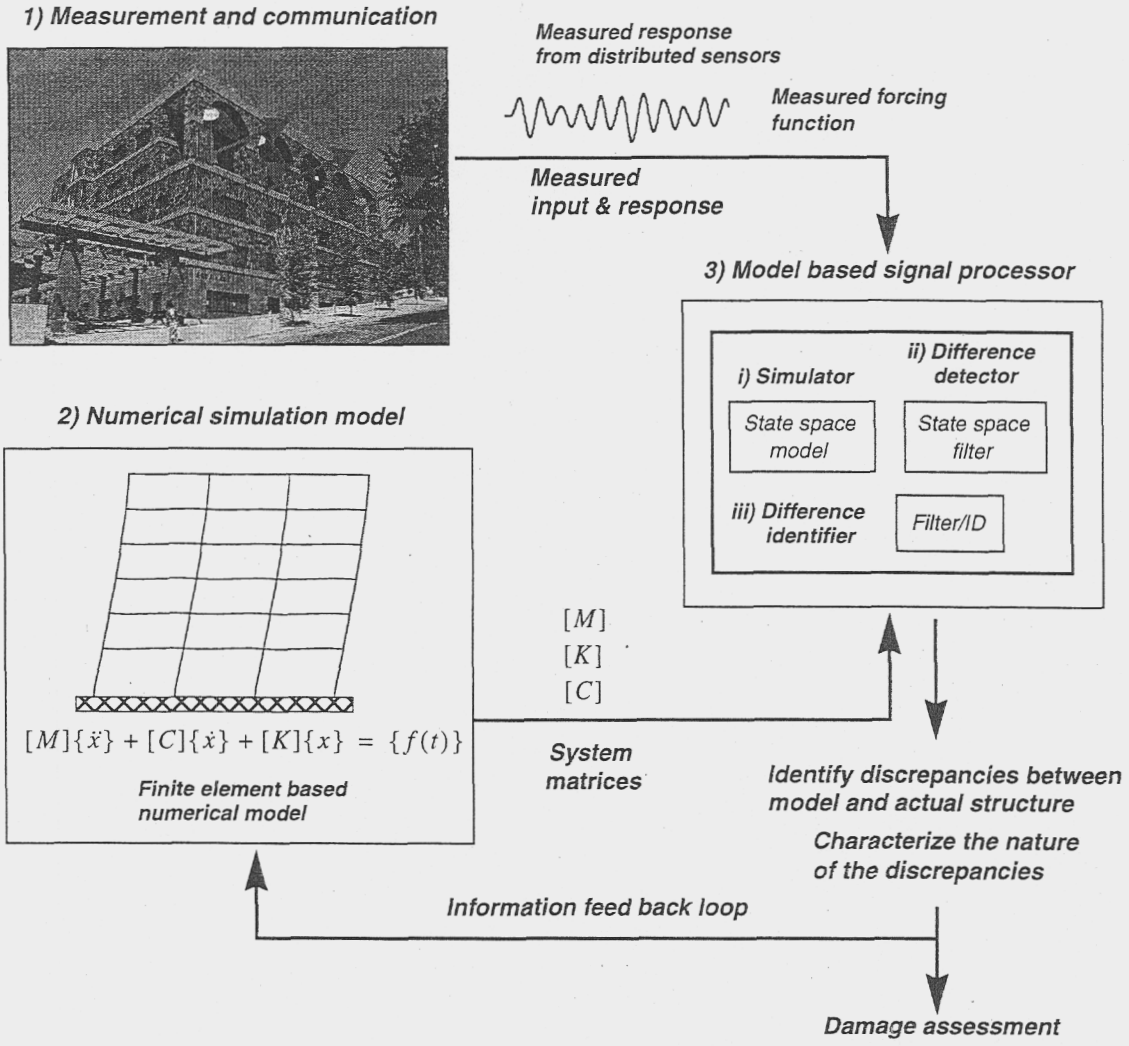

will be enhanced accuracy and reliability of numerical simulation of structural response, and the ability to monitor fundamental changes in complex structural systems, a prerequisite to health monitoring and damage detection.

Failure Detection for Mechanical Structures: A State-Space Model-Based Approach

Gregory A. Clark
Lawrence Livermore National Laboratory

This paper describes early applied research to develop signal processing algorithms for detecting failures (flaws) in mechanical structures using vibrational measurements and a state-space model-based detection approach. Throughout this study, an example 5-story building model is used to simulate the structure and demonstrate the signal processing/detection algorithms. Future project plans involve applying these algorithms to stressed monumental structures in California, including the Oakland-San Francisco Bay Bridge, the Bixby Creek Bridge and the National Ignition Facility (NIF) structure at LLNL.

The first step is the development of dynamic equations of motion used to model linear mechanical structures of the commonly-used "M-C-K" form. Once the state-space model is formulated, its dynamic behavior is validated with the M-C-K model developed by our mechanical engineering colleagues. A Gauss-Markov model of the linear system with noise is developed and used as the basis for a Kalman filter for estimating the system states and measurements. Finally, a detector consisting of a statistical whiteness test on the innovations (estimation errors) is used to detect any structural failures.

The work herein focuses on simulated linear structures and the detection of structural failures. The problems of real data from controlled experiments with actual structures, failure identification, failure location, nonlinear systems, large-scale structures will be addressed in future work.

This paper describes results from the LLNL Joint ME/EE LDRD Tech Base Project, known as "Combined Sensing and Modeling for Enhanced Evaluation and Safety of the Built Environment." and "Determining the Vulnerabilities of Stressed Monumental Structures."

This work was performed under the auspices of the Department of Energy by the Lawrence Livermore National Laboratory under contract W-7405-Eng-48.

Date: Tue, 20 Oct 1998 15:45:21 -0700

Parametric Time-Frequency Estimation of Prosthetic Heart Valve Sounds.

By Perkins D. E., Thomas G. H., and Clark G.

Prosthetic heart valves have been responsible for extending and improving the quality of life of many people with serious heart conditions. Even though the heart valves are extremely reliable they are susceptible to the long-term fatigue and structural defects expected for mechanical devices operating over long periods. In this paper we describe the application of parametric time-frequency estimation techniques to acoustic measurements of prosthetic heart valve sounds under test in an anechoic tank. The analysis reveals interesting results when comparing fractured to normal valve sounds. The emphasis of this work is the application of recursive parametric techniques to "track" changes in propagation sounds as it is captured by a sensitive omnidirectional hydrophone.

Near Field / Far Field Transition Distance for Broad Band Acoustic Pulses

David H. Chambers and D. Kent Lewis
Lawrence Livermore National Laboratory

Acoustic pulses emitted from a planar array can be designed to produce a very narrow beam of energy in the near field of the array. In the far field the array behaves like a point source and the energy spreads accordingly. For single frequency pulses the near field / far field transition distance is predicted by the familiar formula for the Rayleigh range. However, this formula has no meaning when the band width of the pulse is very wide. In this talk we present alternative formulas which predict the near field / far field transition distance for pulses with arbitrary band width. These reduce to the classical Rayleigh range expression in the narrow band width limit. Comparisons between the predicted transition distance and simulations for broad band acoustic pulses emitted from a ring array are shown.

Key words: diffraction, pulse, radiation

This work was performed under the auspices of the Department of Energy by the Lawrence Livermore National Laboratory under contract W-7405-Eng-48.

Near Field / Far Field Transition Distance for Broad Band Acoustic Pulses

David H. Chambers
Strategic Systems Support Program
Lawrence Livermore National Laboratory

CASIS Workshop, Nov. 12-13, 1998

Radiation of acoustic potential

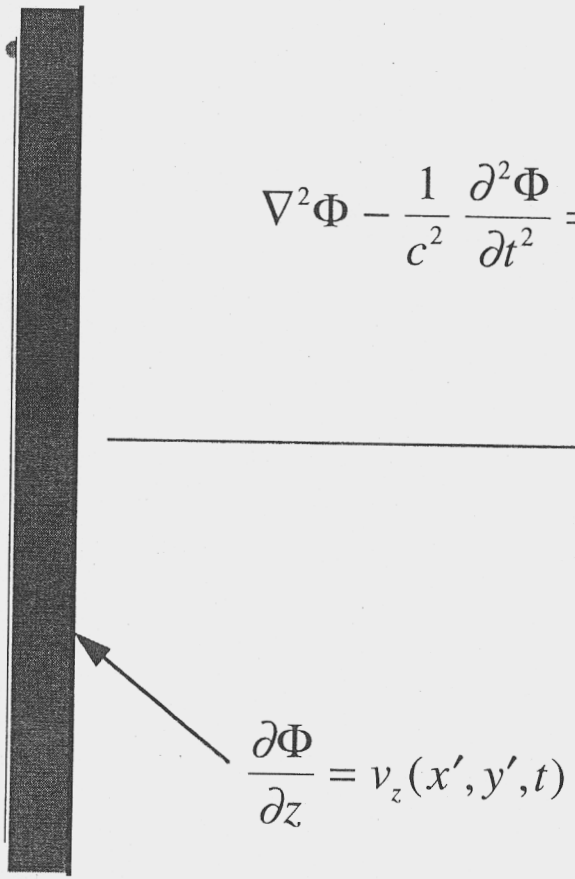

$$\nabla^2\Phi - \frac{1}{c^2}\frac{\partial^2\Phi}{\partial t^2} = 0$$

$$p = -\rho_0 \frac{\partial\Phi}{\partial t} \quad , \quad \tilde{u} = \nabla\Phi$$

z

Solution:

$$\Phi(x,y,z,t) = -\frac{1}{2\pi}\int \frac{v_z(x',y',t-R/c)}{R}\, dA' \quad ,$$

$$\frac{\partial\Phi}{\partial z} = v_z(x',y',t)$$

$$R = \sqrt{(x-x')^2 + (y-y')^2 + z^2}$$

Acoustic radiation from an oscillating piston

- Let normal velocity in a circular region of radius "a" be $\exp(i\,\omega\,t)$
- Potential is given by

$$\Phi(r,\vartheta,t) = -\frac{\exp(i\,\omega\,t)}{2\pi}\int_{-\pi}^{\pi} d\varphi \int_{0}^{a} d\rho\,\frac{\rho}{R}\exp(-i\,k\,R)$$

$$R = \sqrt{r^2+\rho^2-2r\rho\sin\vartheta\cos\varphi}$$

- On axis ($\vartheta = 0, \quad r = z$) we obtain

$$\Phi(z,t) = -\frac{2}{k}\exp\left(i\omega\left(t-\bar{z}/c\right)\right)\sin\left[\frac{1}{2}k\,z\left(\sqrt{1+a^2/z^2}-1\right)\right]$$

$$\bar{z} = \frac{1}{2}z\left(1+\sqrt{1+a^2/z^2}\right)$$

Behavior of amplitude factor

- Plot amplitude factor $\frac{2}{k}\sin\left[\frac{1}{2}kz\left(\sqrt{1+a^2/z^2}-1\right)\right]$ for various ka

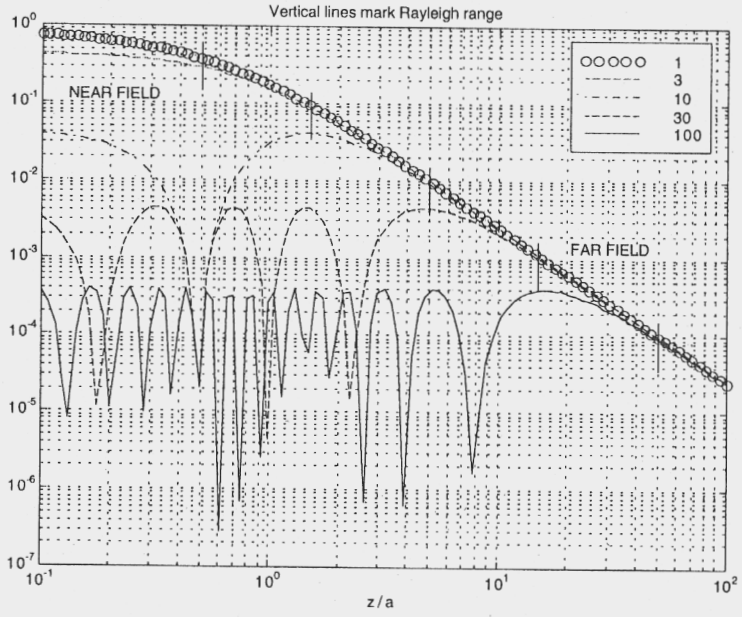

- For z/a > ka/2 (Rayleigh range) amplitude decreases as 1/r

Comparison between near field and far field behavior

- Near field:
  - complicated behavior
  - high degree of control (e.g. focusing)
  - finite size of array is important
  - amplitude variation is arbitrary (can be constant on axis)

- Far field:
  - field behavior depends only on angle from axis and range
  - low degree of control
  - array is equivalent to a point radiator
  - amplitude falls off in all directions as 1/r

Prediction of near field / far field transition

- For single frequency piston radiator, transition distance is well defined by the Rayleigh range
- Rayleigh range is useful for arrays with elements radiating in phase with constant amplitude at a single frequency (narrow band)
- No Rayleigh range is defined for narrow band radiation with phase differences between elements or for broad band radiation
- Expect transition for band-limited radiation to lie between Rayleigh ranges of lowest and highest frequencies

Heuristic estimate for short pulses

- Consider a piston radiator emitting a short pulse (broad band)

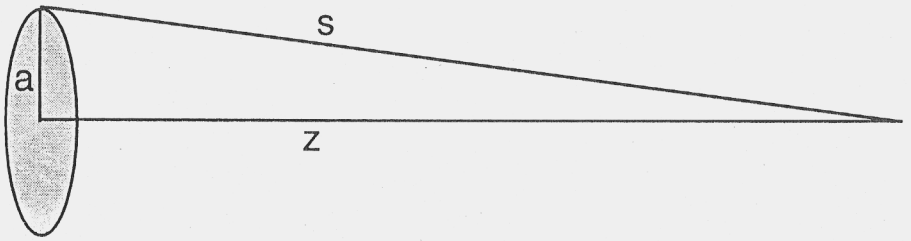

- Let τ be the pulse width, then fractional time delay between paths is

$$\frac{\Delta t}{\tau} = \frac{s - z}{c\,\tau} = \frac{\sqrt{z^2 + a^2}}{c\,\tau}$$

- By setting $\Delta t/\tau = \beta << 1$ at $z = z_R$ we obtain the estimate

$$z_R = \frac{a^2}{2\beta c\,\tau}$$

Transition distance for general axisymmetric source distributions

- Heuristic estimate does not consider amplitude shading or variation of excitation within circular aperture

- Use radiation formula for acoustic potential as basis for estimating transition distance:

$$\Phi(z,t) = -\int_{-\infty}^{\infty} d\omega \exp(i\,\omega\, t) \int_0^a \frac{d\rho\,\rho}{\sqrt{\rho^2 + z^2}} V_{z0}(\rho,\omega) \exp\left(-i \frac{\omega}{c} \sqrt{\rho^2 + z^2} \right)$$

where $V_{z0}(\rho,\omega)$ is the Fourier transform of the normal velocity

- In the far field this becomes

$$\Phi_{FF}(z,t) = -\frac{1}{z} \int_{-\infty}^{\infty} d\omega \exp(i\,\omega\,(t - z/c)) \int_0^a d\rho\,\rho V_{z0}(\rho,\omega)$$

Define transition distance

- Transition distance is the distance where the difference between the actual potential and its far field approximation $\Delta\Phi = \Phi - \Phi_{FF}$ is less than a prescribed value β

- More precisely: $$\frac{\left\|\Delta\Phi(z_R, t)\right\|}{\left\|\Phi_{FF}(z_R, t)\right\|} = \beta$$

  where $$\left\|f(z,t)\right\|^2 \equiv \int_{-\infty}^{\infty} \left|f(z,t)\right|^2 dt = 2\pi \int_{-\infty}^{\infty} \left|F(z,\omega)\right|^2 d\omega$$

- In case of multiple values, choose largest

Approximate integral to calculate distance

- Integral for $\Delta\Phi$ is

$$\Delta\Phi(z_R, t) = \int_{-\infty}^{\infty} d\omega \int_0^a d\rho\, \rho V_{z0}(\rho, \omega) \left[1 - \frac{z_R}{\sqrt{\rho^2 + z_R^2}} \exp\left(-i \frac{\omega}{c} \sqrt{\rho^2 + z_R^2} \right) \right]$$

- Make approximation for large z:

$$1 - \frac{z_R}{\sqrt{\rho^2 + z_R^2}} \exp\left(-i \frac{\omega}{c} \sqrt{\rho^2 + z_R^2} \right) \approx \frac{\rho^2}{2 z_R^2} \left(1 + i\, \omega\, z_R / c \right)$$

- This allows one to solve for z_R

Formula for transition distance

- Transition distance is given by

$$z_R^2 = \frac{1}{8\beta^2 c^2}\frac{M_{22}}{M_{00}}\left[1 + \sqrt{1 + 16\beta^2 c^4 \frac{M_{02}\,M_{00}}{M_{22}^2}}\right]$$

where

$$M_{m\,n} \equiv \int_{-\infty}^{\infty} \omega^m \left| \int_0^a \rho^{1+n} V_{z0}(\rho, \omega)\, d\rho \right|^2 d\omega$$

- Due to approximation of integral, we expect this to be accurate when transition distance is much greater than radius

Special case: single frequency

- Let $V_{z0}(\rho, \omega) = f(\rho)\,\delta^{1/2}(\omega - \omega_0)$, then

$$M_{mn} = \omega_0^m \left|F_n\right|^2 , \qquad F_n \equiv \int_0^a \rho^{1+n} f(\rho)\, d\rho$$

$$z_R^2 = \frac{\omega_0^2}{8\beta^2 c^2} \frac{\left|F_2\right|^2}{\left|F_0\right|^2} \left[1 + \sqrt{1 + \frac{16\beta^2 c^4}{\omega_0^4} \frac{\left|F_0\right|^2}{\left|F_2\right|^2}} \right]$$

- For $f(\rho) = 1$ we have

$$z_R = \frac{k_0 a^2}{4\beta\sqrt{2}} \left[1 + \sqrt{1 + 64\beta^2 / k_0^4 a^4} \right]^{1/2} \approx \frac{1}{2} k a^2 \quad for \quad \beta = \frac{1}{2}$$

Piston pulse case

- Let $V_{z0}(\rho,\omega) = V_0(\omega)$ *for* $\rho \le a$ then

$$M_{m\,n} = \mu_m \frac{a^{2(n+2)}}{(n+2)^2} \quad , \quad \mu_m \equiv \int_{-\infty}^{\infty} \omega^m \left| V_0(\omega) \right|^2 d\omega$$

$$z_R = \frac{a^2}{4\beta}\sqrt{\frac{\mu_2}{2\mu_0}}\left[1 + \sqrt{1 + \frac{64\beta^2 c^4}{a^4}\frac{\mu_0^2}{\mu_2^2}}\right]^{1/2}$$

- Gaussian pulse: $v_{z0}(t) = -\frac{2t}{\tau^2}\exp\left(-t^2/\tau^2\right)$

$$z_R = \frac{1}{4\beta}\sqrt{\frac{3}{2}}\frac{a^2}{c\,\tau}\left[1 + \sqrt{1 + \frac{64\beta^2}{9}\left(\frac{c\,\tau}{a}\right)^4}\right]^{1/2}$$

Compare prediction with transition distance determined by numerical simulation

- Calculate on-axis pressure field for a 24 ring array (equally spaced) driven with a prescribed velocity distribution
- Determine on-axis behavior of $\int_{-\infty}^{\infty} p^2(z,t)\,dt$
- Set transition distance at point where on-axis fall off deviates by 5% from far field rate
- Compare with prediction using $\beta^2 = 1/8$

Comparison with two classes of pulses

- Gaussian piston pulses with varying durations: $0.01 \le c\,\tau / D \le 1.0$
- Ziolkowski's MPS pulses with varying waists

$$v_{z0}(\rho, t) = \left.\frac{\partial \Phi_{MPS}}{\partial z}\right|_{z=0}, \qquad s(\rho, z, t) = \frac{\rho^2}{z_0 + i\,(z - c\,t)} - i\,(z + c\,t)$$

$$\Phi_{MPS}(\rho, z, t) = \mathrm{Re}\left[\frac{2\,R_m z_0}{z_0 + i\,(z - c\,t)} \frac{\exp\left(-z_0 s(\rho, z, t)/w_0^2\right)}{s(\rho, z, t) + 2\,R_m}\right]$$

$$R_m = 1000, \quad z_0 / D = 0.0064, \quad 0.1 \le w_0 / D \le 10$$

Decay curves for Gaussian piston pulses

Decay curves

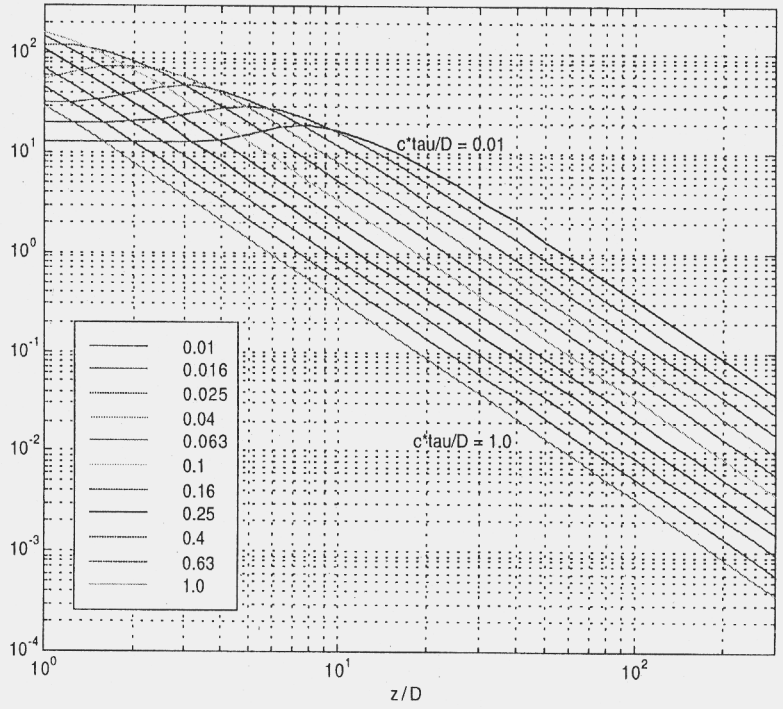

Deviation from far field

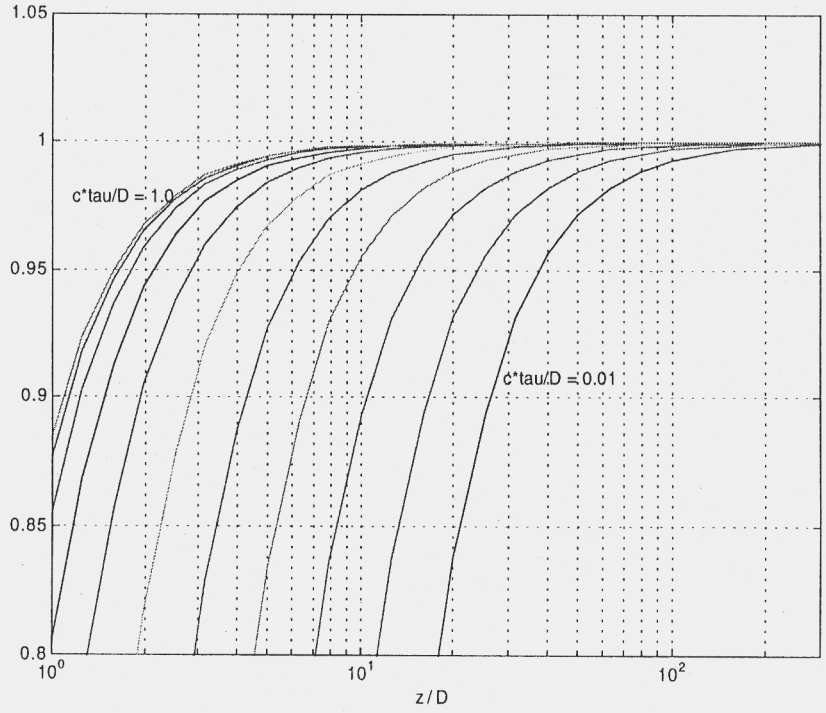

Transition distances for Gaussian pulses

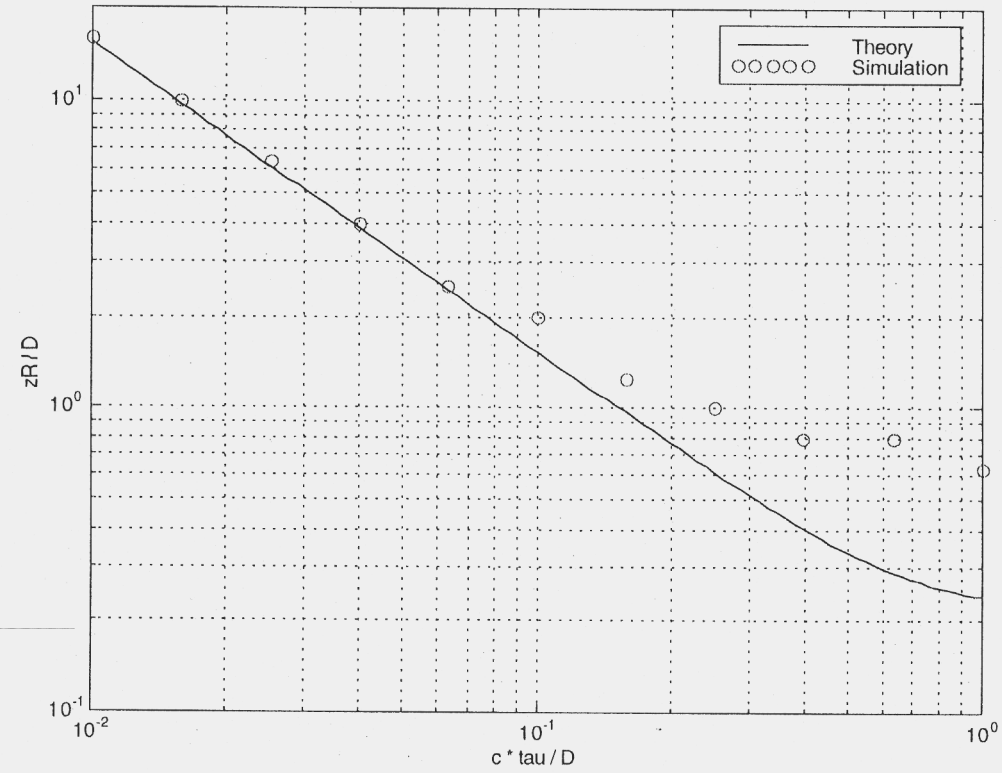

Velocity distributions for MPS pulses

Plotted as functions of c*t/D, largest amplitude is at center of array

$w_0/D = 0.01$

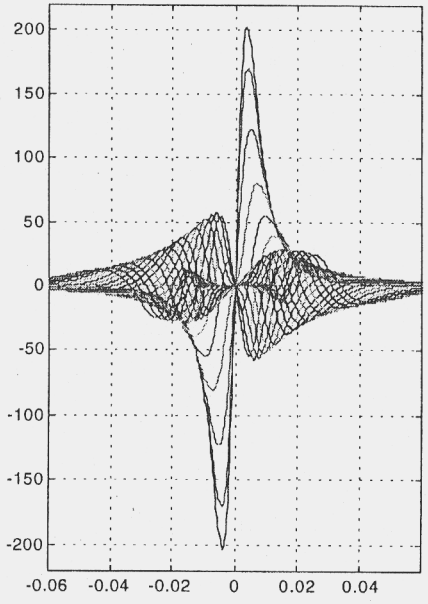

$w_0/D = 1.0$

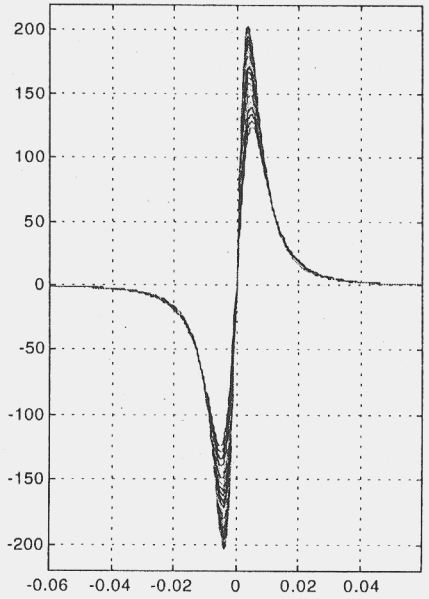

$w_0/D = 10$

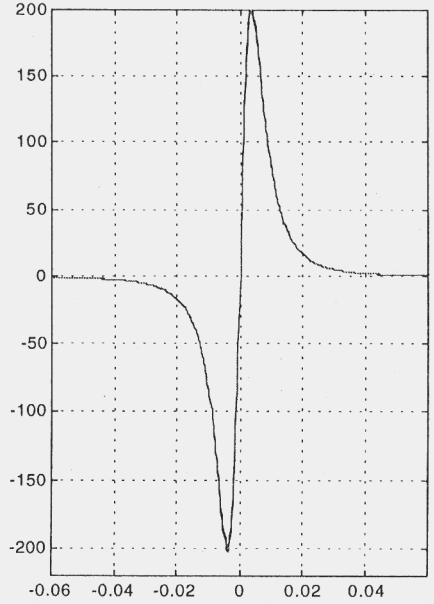

Decay curves and deviation from far field

Decay curves

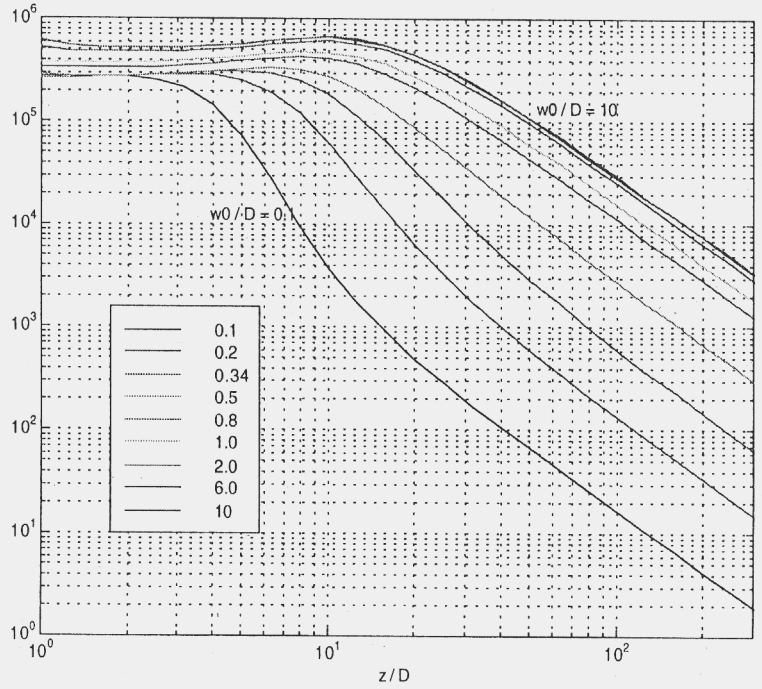

Deviation from far field

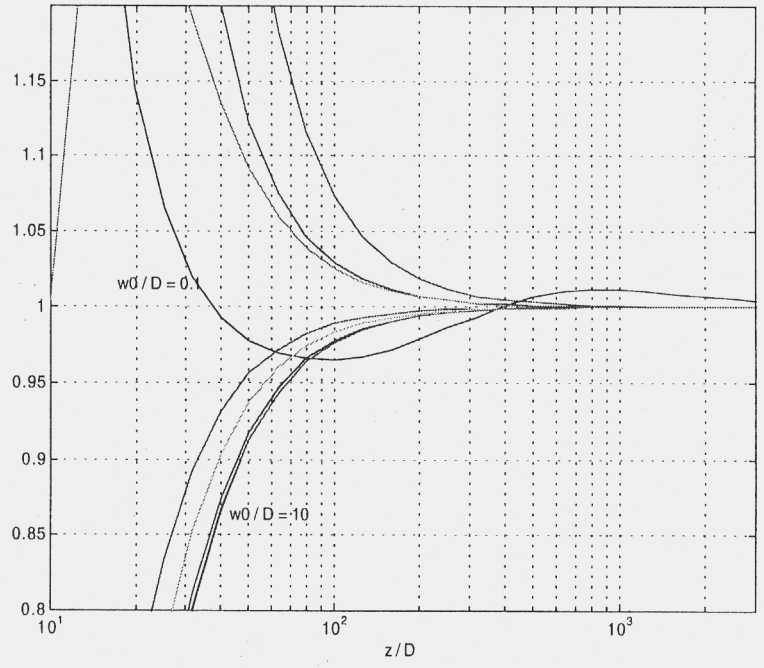

Transition distances for MPS pulses

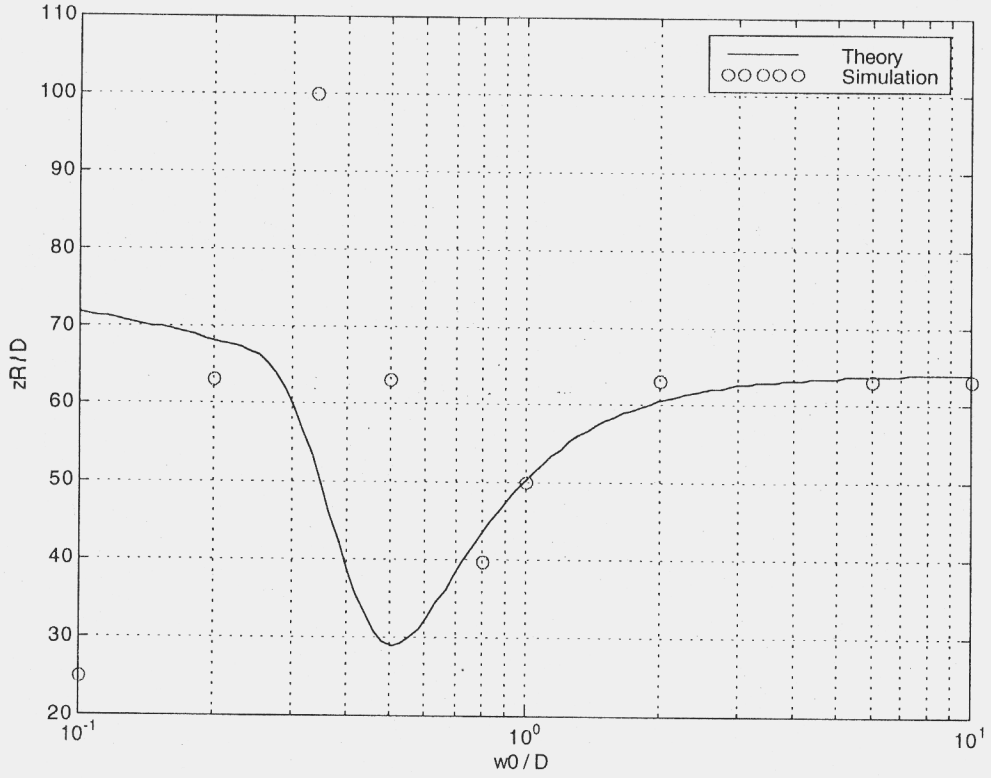

Conclusions

- An estimate of near field / far field transition distance has been formulated for general broad band axisymmetric velocity distributions
- Estimate agrees with Rayleigh range formula for single frequency piston radiation
- Estimates of transition distance from simulation data depend on which field is being calculated
- Transition distance estimate works well for pulses whose initial velocity distributions do not vary greatly within the aperture
- Further analysis is required to determine true range of validity of the estimate

Optimization of Array Generated Fields for Broad Frequency Band Width

Kent Lewis
Lawrence Livermore National Laboratory

Accurate active beam forming methods depend on putting the right signal at the right place at the right time. Modern arrays are increasing dependant on individual source signals for each element or set of elements in a larger array. This capability allows generation of beams, which are optimized both spacially and temporally.

LLNL has pioneered this technology for more than a decade, and is presently using its capability in several projects, among them the Karmanos Breast Cancer Detection Initiative, and the Localized Wave project. This talk outlines the background of our present work, and shows a field application of the pre-processing capability.

This work was performed under the auspices of the Department of Energy by the Lawrence Livermore National Laboratory under contract W-7405-Eng-48.

Optimization of array generated fields for broad frequency band width

D. Kent Lewis
Strategic Systems Support Program

Accurate active beam forming methods depend on putting the right signal at the right place at the right time. Modern arrays are increasing dependant on individual source signals for each element or set of elements in a larger array. This capability allows generation of beams which are optimized both spacially and temporally.

LLNL has pioneered this technology for more than a decade, and is presently using its capability in several projects, among them the Karmanos Breast Cancer Detection Initiative, and the Localized Wave project. This talk outlines the background of our present work, and shows a field application of the pre-processing capability.

Background for Individually addressable array

Quantitative NonDestructive Evaluation Project
- '85-88 LLNL funded
- Signal Pre-Processing to generate arbitrary linear fields
- Spectral extrapolation post processing for sharpening

Localized Wave Project
- 89-present LLNL and Navy funded
- Multi-channel source electronics
- Individually addressable array materials
- Multi-channel beam forming and simulation

Alternate materials and fabrication
- PVDF and associated co-polymers
- PZT-N extruded and sintered arrays
- Si "drum-head" array elements
- Flexible piezo-electric "wires"

Quantitative NonDestructive Evaluation

Pre-processing of source waveforms
- Linear inverse filtering
- Correction for non-idealized element response
- Optimization for non-idealized media
- Correction of array structural resonances

Spectral extrapolation of received signals
- Similar to analytical continuation in complex plane
- Model based, part of the spectrum is "believed"
- Parameters control continuation area and time signal threshold

Localized Wave Pulse Beam

Localized Wave Pulses are wide band width, low diffraction pulse beams

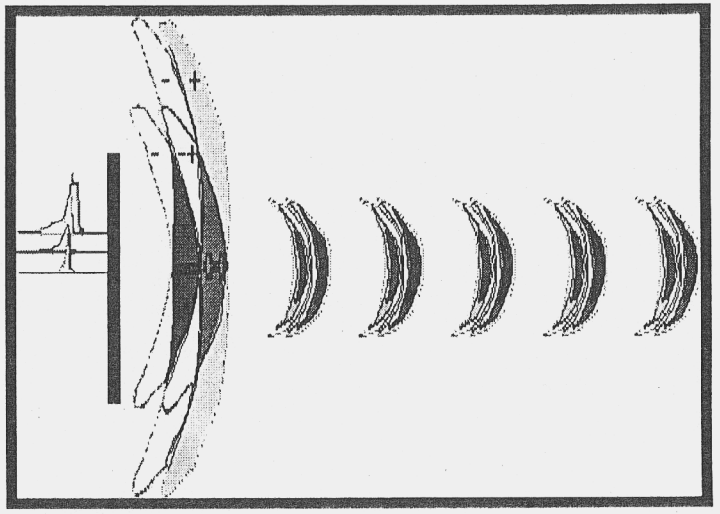

The Localized Wave (LW) pulse is created by linear superposition of a well characterized choice of basis functions.
It is <u>not</u> parametric generation or solitons

- Based on solid theoretical foundation spanning 1981 - 1998
  - Focused Wave Modes and Modified Pulse Spectrum
  - Gaussian packets optimized for each frequency
  - FWMs are solutions to the wave equation, a complete basis set, an orthogonal set
- Supported by a solid body of theory development coupled with experiment
  - First LW acoustic pulses launched, 8 experiments to date
  - First LW microwave pulses launched, planned for fall 1998
- Proven record of accomplishments
  - Discovered 2 of the first Low Diffraction, broad band width beams
  - Designed and performed original multi-channel proof of principle work, 8 to date
  - Designed and conducted several proof of principle experiments with contractors
    NUWC Keyport AdCap array, 1987
    UTx ARL 24 ring array, 1998
- LW beam requires individually addressable array elements and programmable, broad band width source generators

Time Line Summary, Localized Wave Pulse

'81 Brittingham finds the Focus Wave Modes (FWM)
'84 Ziolkowski builds the Modified Pulse Spectrum (MPS) Localized Wave
'87 Lewis and Cook launch LW waveforms, acousto-optics
'88 Lewis and Cook simulate 441 element 2D array
'89 Ziolkowski and Lewis create first real time LW pulse, 25 element array
'90 Ziolkowski and Lewis use 11 ring array for LW pulse
'91 Lewis sabbatica at U. Paris 6&7l, Ziolkowski moves to Tucson
'95 Work begins on ocean bottom penetration
'96 Work begins on microwave simulation
'96 Chambers builds the Superposed Gaussian Localized Wave
'96 Candy and Chambers preliminary resolution enhancement results
'97 Lewis and Chambers launch Localized Waves with 8X8 tonplitz head in Keyport, WA
'97 Planning for microwave experiment at Baltimore approved
'97 Plan for 1-3 composite array tests in Lake Travis approved
'98 Array design and experiments at Lake Travis

'98 Microwave linear antenna LW generation experiments

Localized Wave Ocean Applications

LW pulses are very broad frequency bandwidth, typically 3 or more octaves wide

Beam energy is highly localized on the axis, very low to no side lobe creation

LW capability enhances both active and passive beam forming

LW technology has proven useful in enhancing current Navy systems

Active:

- Highly directional, covert, broad band communication and location
- Covert broad band width scanning
- Tailored spectrum to optimize penetration of difficult media, e.g.. the ocean floor
- Improved clutter rejection in shallow water

Passive:

- Applied as a matched filter front end for enhanced sensitivity
- Improved noise rejection off axis, better directivity
- Higher spacial and temporal resolution

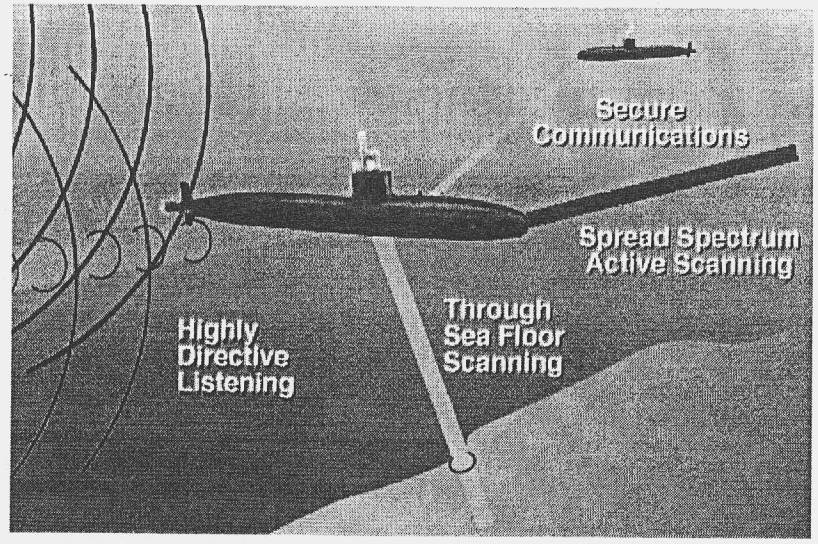

Localized Wave Passive Sensitivity

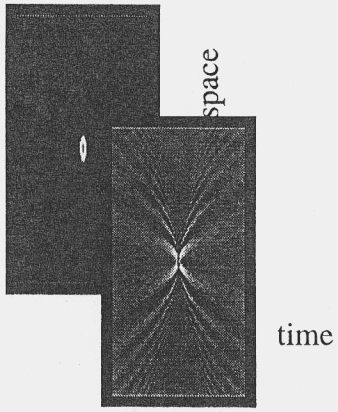

For Optimized Space-Time Filters

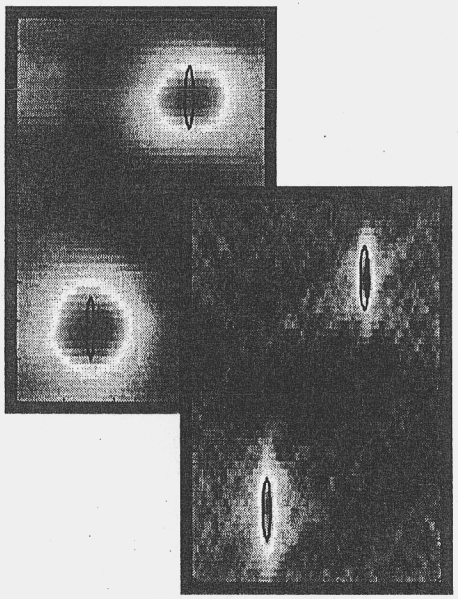

Spatial and Temporal Localization is as accurate as Optimized Gaussian Methods

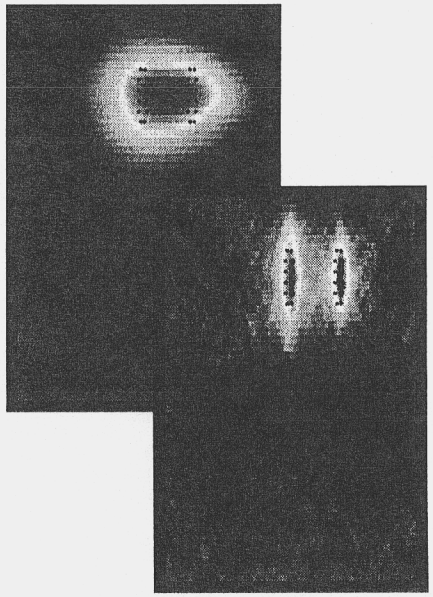

Resolution is enhanced using LW methods

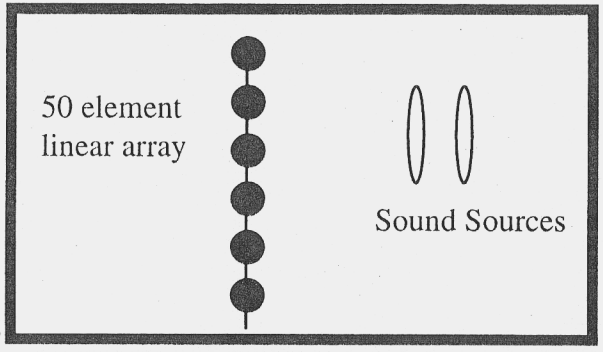

Model is a 50 element linear, broad band width array
Sources are separated in space and time
Range is vanishingly small, no range information is obtainable from this simulation

SSSP

Array Selection candidates

Requirements dictate multiple, individually addressable, broad band width elements

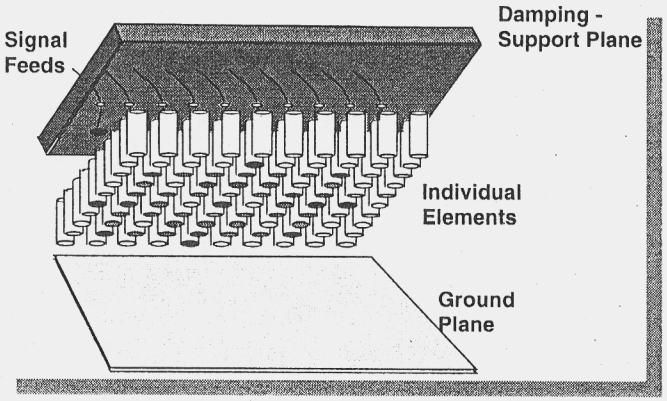

As a first cut, flat array panels will be used for PZT-N, Si, LiNb, etc.
Issues are bandwidth, radiation efficiency, detection sensitivity, cross talk suseptability, etc.
Goals are simplicity, economy, resolution, and contrast in mass production components.

Natural geometry selection is spherical (or spheroidal). Avoids most beam forming problems, and addresses the breast at normal incidence

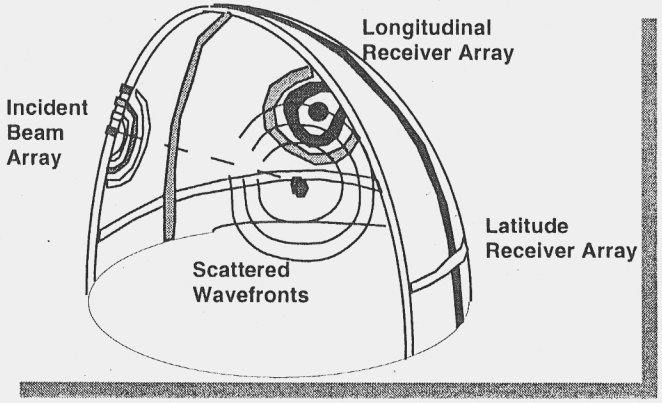

Individual addressability allows beam forming in any configuration. Perhaps overkill, it becomes a testbed for simulation, measurement, and imaging techniques.

Simple model of transducer system

Gaussian pulse input becomes first derivative (or velocity)in the water

Disk to disk coupling described by Rhyne yields a derivative

Receiver yields another derivative

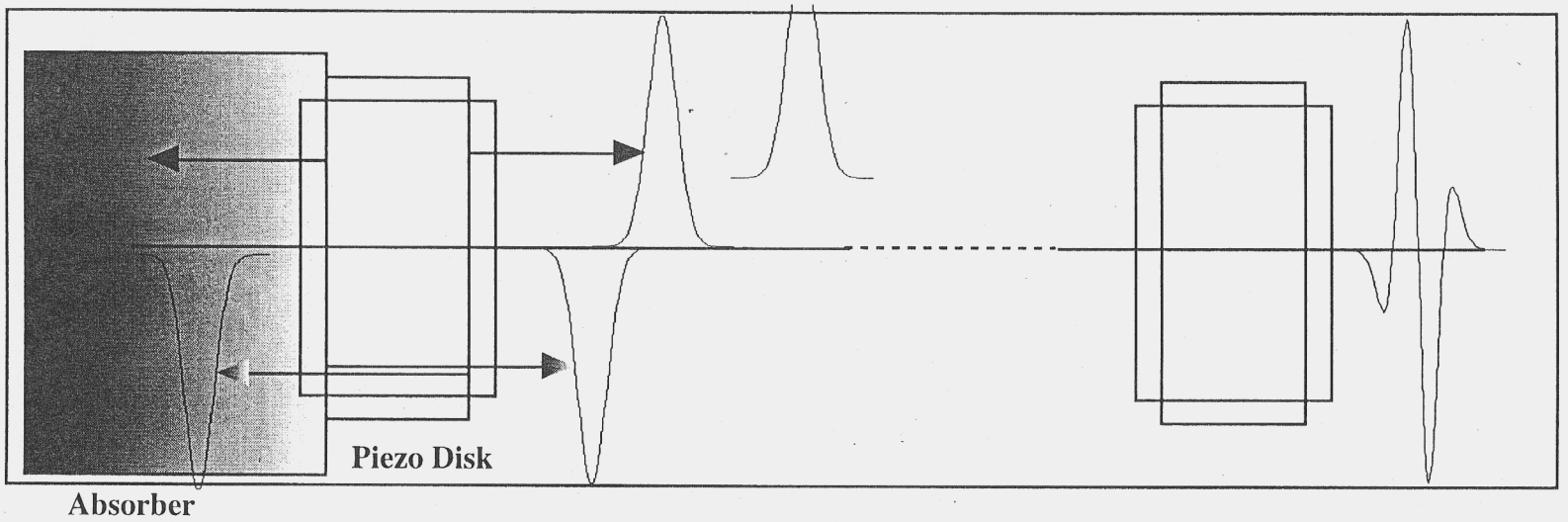

For far field measurements, we expect the third derivative of the input

First cut showed array problems

Our input signal is a broad band width Gaussian pulse, covering the frequency range of interest

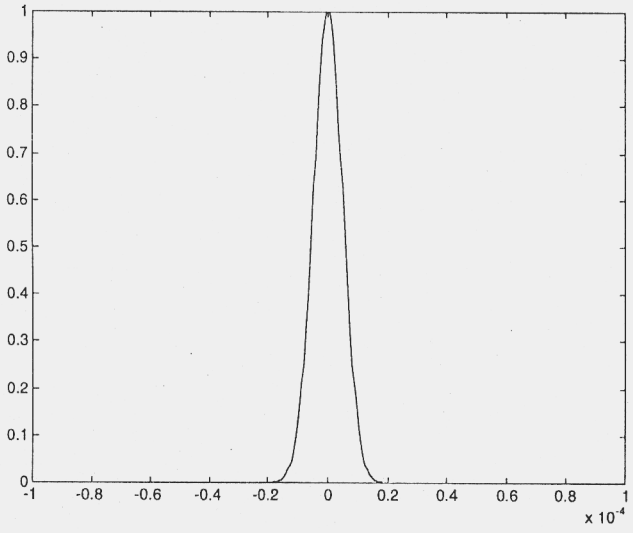

We expect to measure the 3rd derivative of this input signal

Comparing shows multiple signals overlap, and a frequency filtering

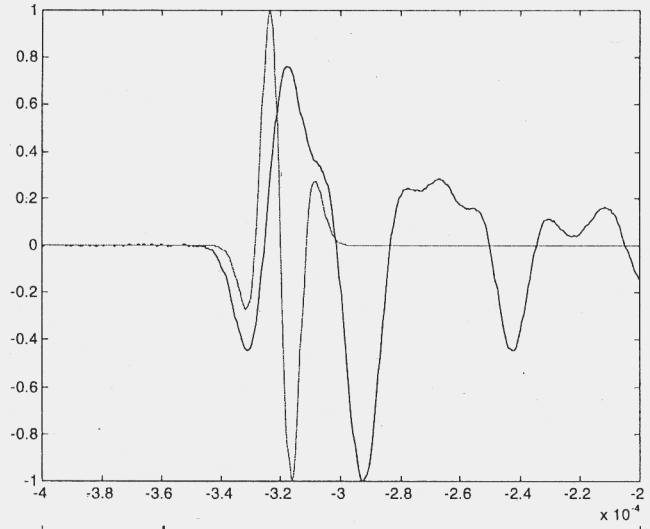

Full received response of system to Gaussian pulse

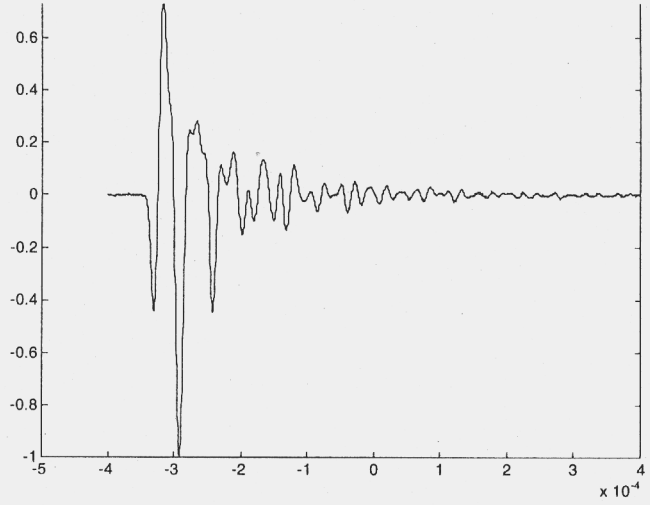

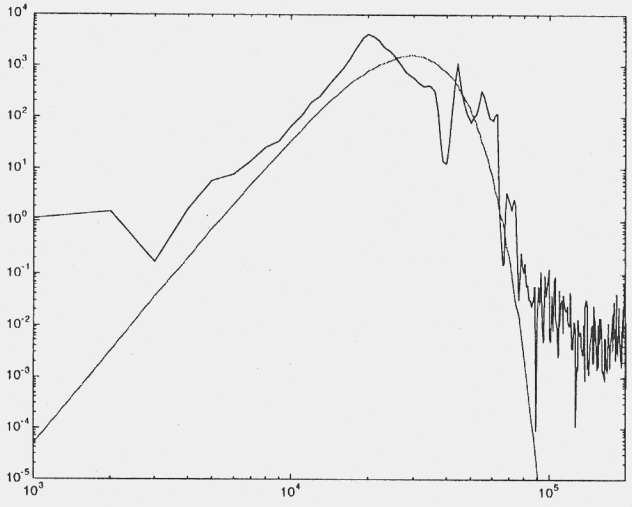
10^4
10^3
10^2
10^1
10^0
10^{-1}
10^{-2}
10^{-3}
10^{-4}
10^{-5}
10^3
10^4
10^5

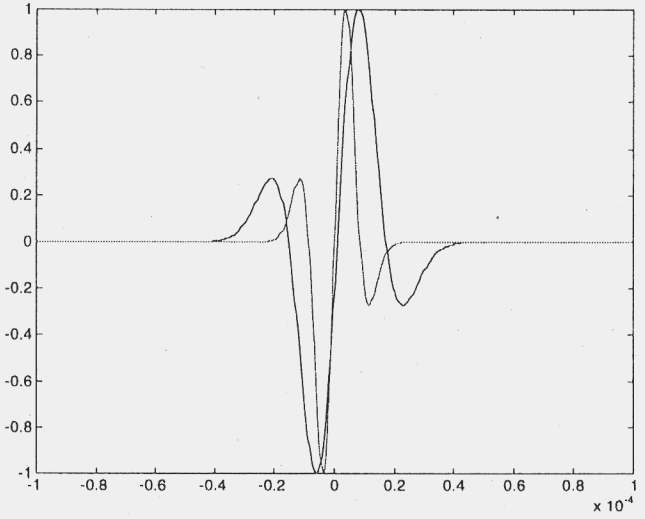
1
0.8
0.6
0.4
0.2
0
-0.2
-0.4
-0.6
-0.8
-1
-1
-0.8
-0.6
-0.4
-0.2
0
0.2
0.4
0.6
0.8
1
x 10^{-4}

The system inverse was inefficient but effective

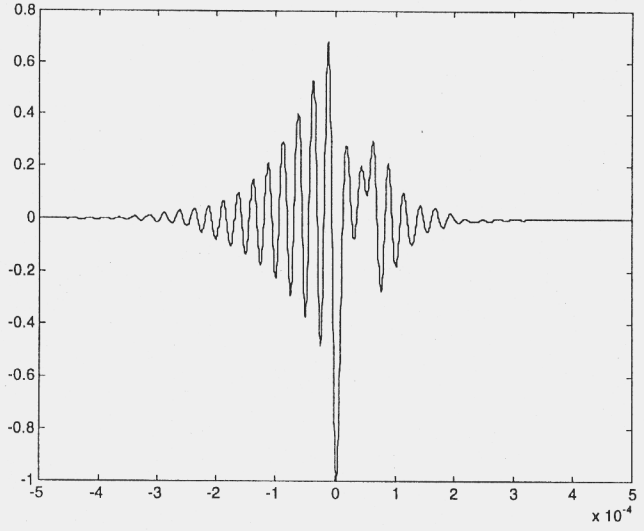

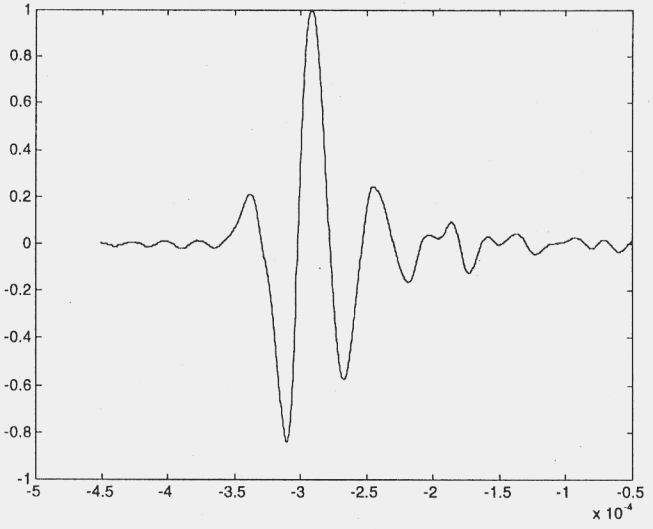

The system inverse (in time) was convolved with all the succeeding source signals

The resultant system response was cleaner, but not ideal. Further work was deemed too costly.

The data was acquired at 15 locations from 44" to 15'

Absolute value of the time records on axis

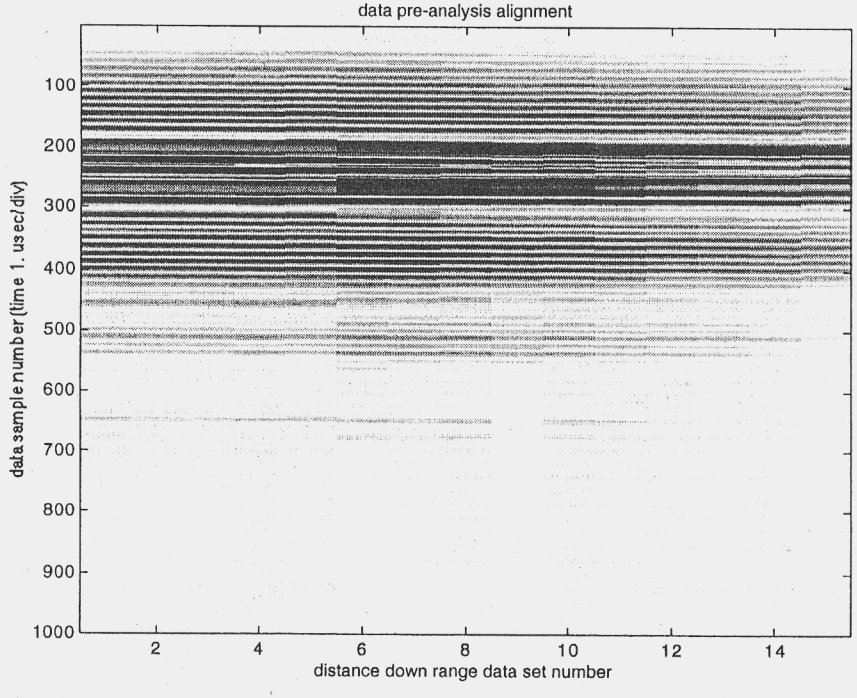

Time signals were lined up in relative time. The characteristic double peak structure in the absolute value time plot.

Representative time record for LW pulse on axis

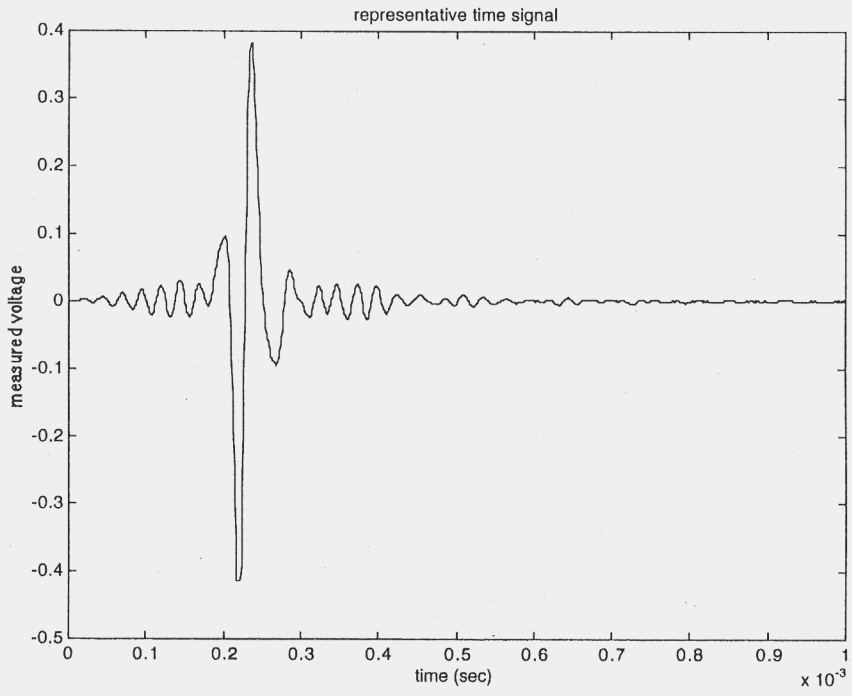

A measurement of the on axis time signal was made for each of the pulse sets at each of the down range positions

SSSP

Time window for time-frequency analysis

Time record and candidate Hanning window

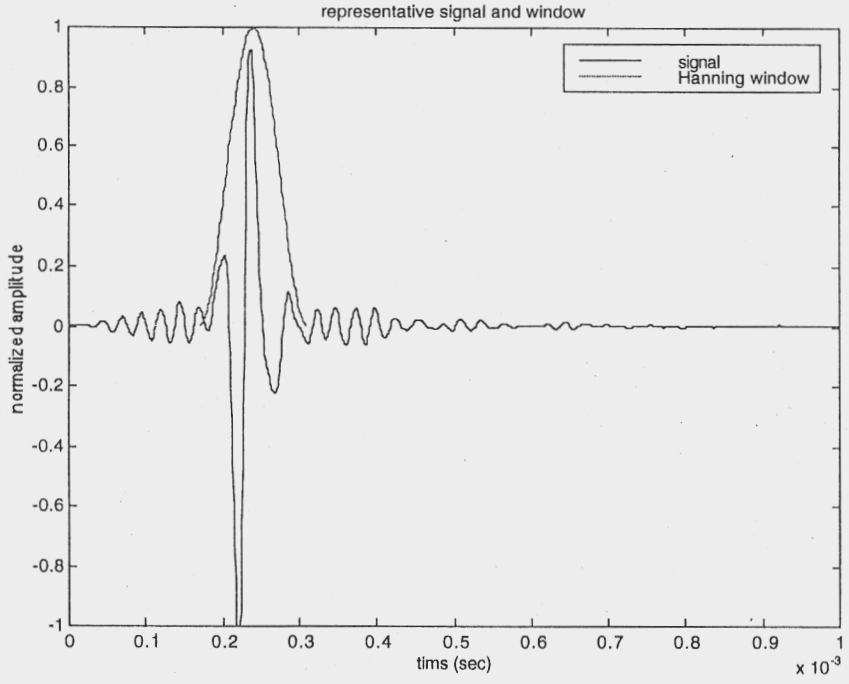

The Hanning window was chosed wide enough to allow a good representation of the main signal to pass relatively unchanged

Signal windowed at one step prepared for processing

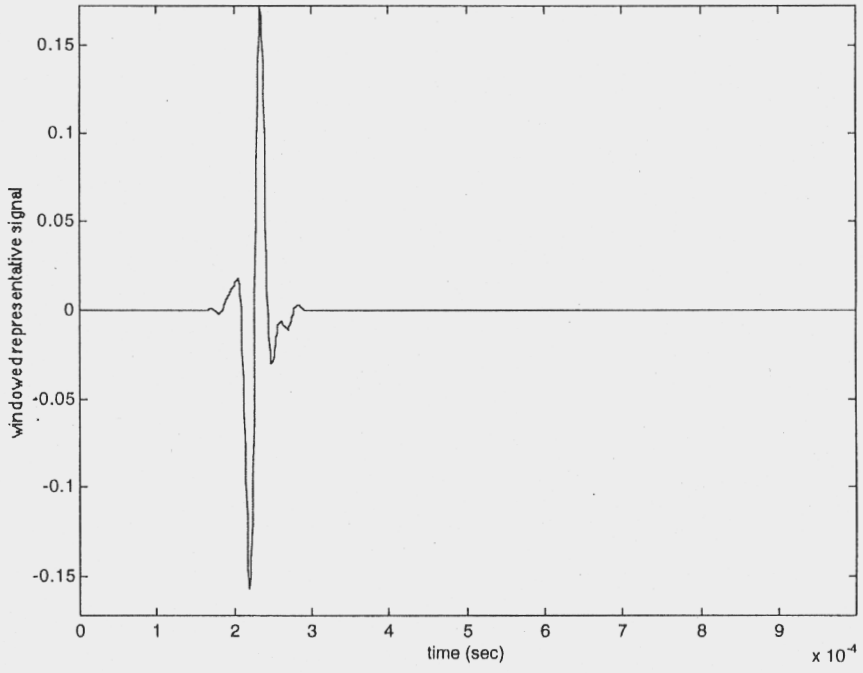

The chosen window was stepped through each data record by 1/20 of the window width. This choice was arbitrary.

SSSP

Time-frequency analysis shows uniform arrival of energy

The windowed data is Fourier transformed without further processing

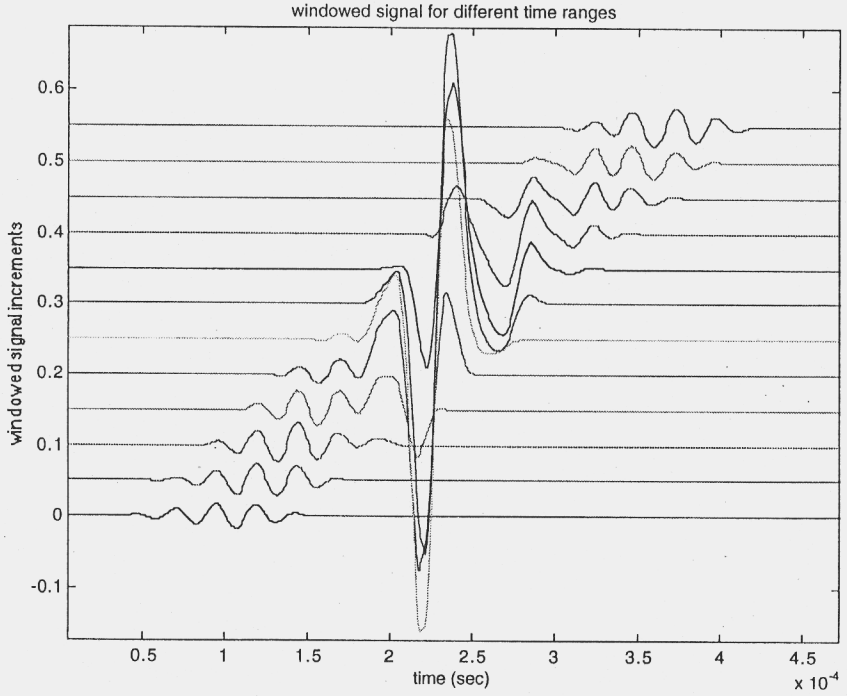

The power spectrum for time and frequency shows a broad bandwidth in the pulse

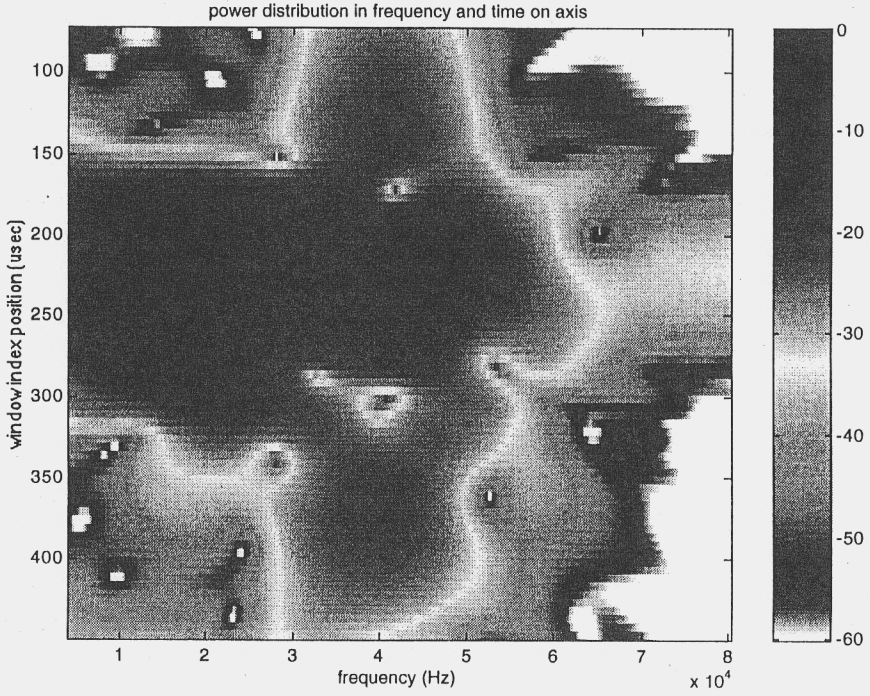

The compensation signal lead-in is clearly visible in the time signal segments

The time-frequency picture shows the lead-in and trailing signals are nearly single frequency

SSSP

Amplitude and phase surfaces vrs. time and frequency

The power spectrum for time and frequency shows a broad bandwidth in the pulse

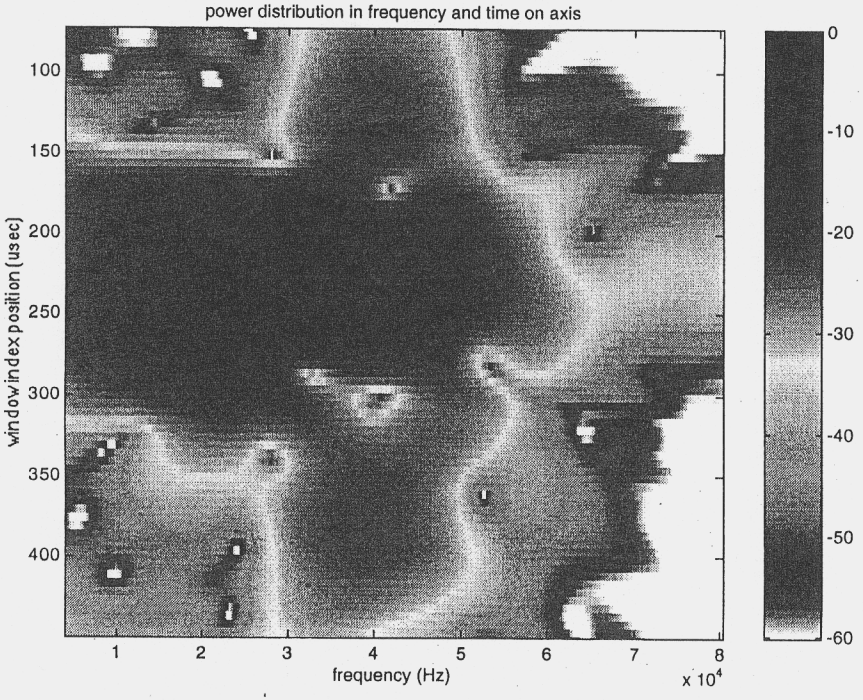

The phase surface for the region of pulse power (150 - 300 usec)

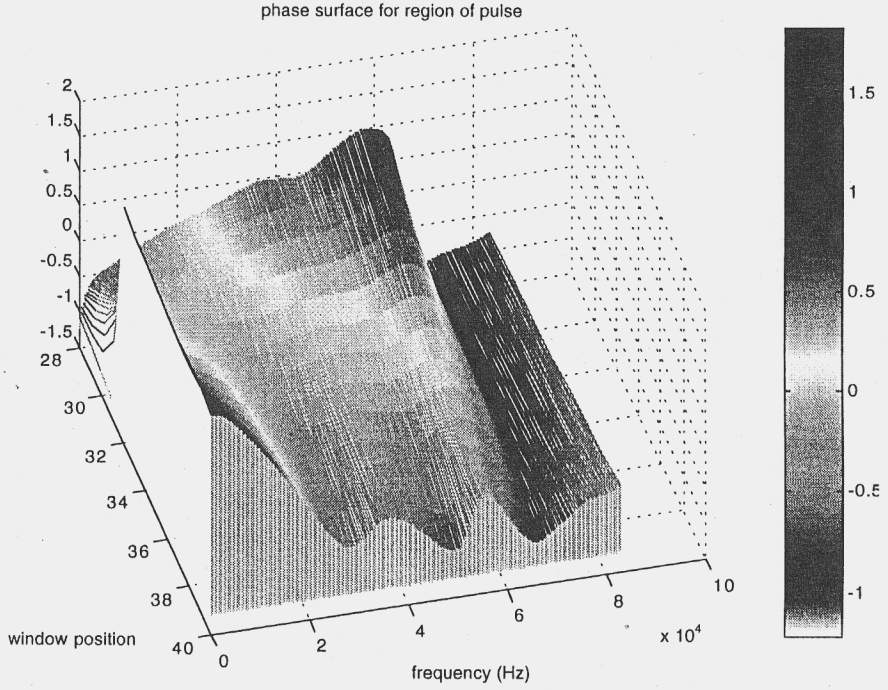

The time-frequency picture shows the lead-in and trailing signals are nearly single frequency

The phase surface has been unwrapped and detrended. It is presented for the region of significant power only

SSSP

Automatic Event Picking for Seismic Oil Exploration

Peter K.-Z. Cheng (U.C. Davis)
Gregory Clark (LLNL), and Gary Ford (U.C. Davis)

Velocity estimation is currently a "bottleneck," or barrier to progress in oil exploration, because the required seismic event picking step must be carried out manually at great cost in time and money. The goal of this research is to create 2D and 3D algorithms for automating the process of picking seismic events in pre-stack migrated gathers arranged in common reflection point (CRP) panels. The work has been funded through the DOE/NGOTP (National Gas and Oil Technology Program) and Shell E&P Technology Company. The approach uses supervised learning and statistical classification / neural network algorithms along with signal / image processing algorithms.

The most significant accomplishments during the first 2 years of work include the following: (i) Delivery of MATLAB code implementing the 2D automatic picking algorithms and a preliminary 3D algorithm. (ii) Excellent performance in picking events correctly in CRP panels, both during training and testing with a real data set. (iii) Excellent performance in reducing or eliminating the difficult loop skipping problem. (iv) Reduction of the time required to pick a data set from approximately one day (24 hours) to about 6 minutes, using a Shell implementation of the algorithm. Shell anticipates that with the 3D algorithms, the cost of picking a full seismic survey will be reduced from about 12 weeks and $75,000 to about 1 week and $6,000, for a factor of 12 savings. (v) Most recently, we have achieved significant results for the 3D problem of picking and tracking events from CRP panel to CRP panel to produce picked common offset panel (COP) displays of the full data set.

Explosive Detection and Discriminant Research for Civil Aviation Security†

Harry E. Martz, Derrill Rikard, Earl Updike, Clint Logan, and Sailes Sengupta
Lawrence Livermore National Laboratory

X- and gamma-ray imaging techniques in nondestructive evaluation (NDE) and assay (NDA) have seen increasing use in an array of industrial, environmental, military, and medical applications. Much of this growth in recent years is attributed to the rapid development of computed tomography (CT). A new application area for CT is civil aviation security explosives detection. The only Federal Aviation Administration (FAA) certified explosives detection system is a linear-array based x-ray CT scanner developed by InVision, Inc. Unfortunately the system's airport false-alarm rate performance is higher than the certification rate. We are working with the FAA William J. Hughes Technical Center to help them advance their explosives detection and discriminant research efforts. We have applied three x-ray CT scanners in four different data acquisition configurations to characterize explosives, distinguish between explosives and x-ray machine false-alarm items; and validate inert, non-hazardous materials that simulate the x-ray properties of explosives. I will describe the x-ray CT scanner configurations, their results and our preliminary analysis of the data.

† This work is funded by the FAA William J. Hughes Technical Center and is performed under the auspices of the U.S. Department of Energy by the LLNL under contract W-7405-ENG-48.

Grain Identification and Analysis of Shock Induced Damage of Sandstone

Carl Hagelberg
Los Alamos National Laboratory

Oil and gas wells are "completed" by sending a gun tool into the pipe to a particular pay-zone depth where shaped charges are used to perforate the well casing to allow the fluid to flow into the well for extraction. We are studying the microstructure damage and dynamics of what occurs when the rock is perforated in such a fashion. Gas gun recovery experiments are used to understand how rock is damaged under short duration shocks. The recovered samples are analyzed using a Scanning Electron Microscope (SEM). We also have an undamaged sample volume that has been imaged using X-ray Computed Micro Tomography (XCMT) providing a volume data set.

Image and volume analysis algorithms are being explored and developed to extract boundary and surface representations from the XCMT data and to characterize the SEM images. One of our goals is to use the data to create representations in two or three dimensions of a grain structure (e.g. sandstone) that can then be used in numerical simulations that model a shock applied to the material. Another goal is to develop analysis procedures that allow comparison of the experimental data and output from numerical simulations. Measures that can be used for comparison include a characterization of fractures in the rock using fractal analysis and grain size distributions.

The x-ray attenuation data is a (noisy) representation of a three-dimensional grain structure of a small core (1mm diameter) of sandstone. The process of extracting geometric information is essentially a two-tiered task: a multi-partition segmentation into individual grains, and a geometric representation of each grain. The segmentation into individual grains is the most difficult in that it involves categorizing each voxel into grain and non-grain material (relatively easy due to image contrast) and into distinct grains (relatively difficult due to ambiguity of the grain boundaries). Various approaches to segmenting the image data from a slice have been explored including edge finding, wavelet analysis, two-dimensional entropic segmentation, and region growing. A better understanding of how to manage ambiguities in grain boundaries in the CMT data is still needed. It seems evident that humans deduce structures from the images using multi-scale information suggesting that multi-scale analysis may be a necessary characteristic to include in algorithm designs.

Signal Design for Lithography

Jesse Kolman
Lawrence Livermore National Laboratory

We have developed an algorithm for designing input signals for a lithography system with the goal of printing prescribed patterns on semiconductor substrates. The input signal can represent various types of static masks and spatial light modulators. The forward model employed by the algorithm describes a partially coherent imaging system as well as a nonlinear photoresist. The imaging system is modeled by a bilinear transformation, which accounts for both the condenser and projection optics. Our algorithm attempts to work backwards, constructing an input signal, which yields the desired printed pattern, by evaluating the quality of the pattern and iteratively adjusting the input. The forward model is used to do the evaluation, and a constrained conjugate gradient optimizer solves the iterative problem.

Recent developments have included techniques for greatly speeding up the required calculations and extensions of the model. The fast computational techniques allow practical sized problems to be solved in a reasonable amount or time, with no reduction in quality. The model extensions consist of the consideration of arbitrary complex objects and constraints, which allow certain portions of the input signal to be fixed in value. This latter extension may be useful for modeling defects in multilayer masks. Another important avenue of future research is the development of an algorithm, which produces a binary input signal.

This work was performed under the auspices of the Department of Energy by the Lawrence Livermore National Laboratory under contract W-7405-Eng-48.

Fluoro Immuno Sensors for Biological Warfare Agents Detection and Identification

Kodumudi S. Venkateswaran[1], *Fred P. Milanovich*[2], *Raymond P. Mariella Jr.*[1,3] *and Richard G. Langlois*[1]

[1]*Biology and Biotechnology Research Program,* [2]*Nonproliferation, Arms Control and International Security Directorate,* [3]*Center for Microtechnology*

Lawrence Livermore National Laboratory

Advanced biodetector systems are of paramount importance for reducing the threat of biological weapons and also for containing the devastating effects of any incidence involving pathogenic microorganisms. Biological Defense Program at Lawrence Livermore National Laboratory is focussed in the development of rapid and sensitive detector/ identifier systems useful both in the battlefield and the urban settings. Under this program, pioneering development was made in the real time monitoring of nucleic acid amplification. Non-nucleic acid based fluoro immuno sensors are also being developed for simultaneous identification of multiple microbial agents in the sample. Fluorescent-labeled antibodies were used for detection of the microbial agents by flow cytometry. Blue or red laser was used as light source for excitation and sensitive photo detectors were used for fluorescence and light scatter measurement. Assays were standardized for the specific detection of simulants of biological warfare agents and tested using LLNL patented miniFlo flow cytometer and also with two different commercial flow cytometers. Four simulants used in this study were *Bacillus globigii* (Bg) for bacterial spore, *Erwinia herbicola* (EH) for vegetative bacteria, Ovalbumin (Ov) for protein toxin and bacteriophage MS2 (MS2) for virus. Flow cytometric detection is a sensitive, specific and reliable method and the fluoro immuno sensor will be very valuable for the rapid, simultaneous detection of different biological warfare agents.

Key Words: Fluoro immuno sensor, biological weapons, flow cytometry

This work was performed under the auspices of the Department of Energy by the Lawrence Livermore National Laboratory under contract W-7405-Eng-48.

Date: Mon, 26 Oct 1998 11:40:12 -0800 (PST)

UCRL-JC-131209 Abs

Preliminary results from an environmental geophysics project for improving geophysical imaging of fluid distribution in the shallow subsurface

By Patricia A. Berge, James G. Berryman,
Brian P. Bonner, Jeffery J. Roberts, Dorthe Wildenschild

The purpose of this project is to develop a computer code for joint inversion of seismic and electrical data to improve underground imaging for site characterization and remediation monitoring. The computer code developed in this project will invert geophysical data to obtain direct estimates of porosity and saturation underground, rather than inverting for seismic velocity and electrical resistivity or other geophysical properties.

This should improve the state-of-the-art of underground imaging significantly, so that interpretation of data collected at a contaminated site will be much less subjective. Potential users include DOE scientists and engineers responsible for characterizing contaminated sites and monitoring remediation of contaminated sites. In this three-year project, we use a multi-phase approach consisting of theoretical and numerical code development, laboratory investigations, tests on available laboratory and borehole geophysics data sets, and a controlled field experiment, to develop practical tools for joint electrical and seismic data interpretation. We are now in the second year of the project. We will present results to date from this work. Results from controlled laboratory experiments on sand-clay mixtures improve our understanding of the connections between measured geophysical properties and the parameters that control fluid distribution and flow (porosity, saturation, and permeability). Results from theoretical work include determining how to use appropriate effective medium theories and available physical properties information in algorithms for relating geophysical measurements to porosity, saturation, and permeability.

Other results include new guidelines for planning and carrying out geophysical field experiments for improved site characterization.

For more information on this project, please see the world-wide web page at:
http://www-ep.es.llnl.gov/www-ep/esd/expgeoph/Berge/EMSP/

This work was performed under the auspices of the U.S. Department of Energy by the Lawrence Livermore National Laboratory under contract No. W-7405-ENG-48 and supported specifically by the DOE Office of Energy Research within the Office of Basic Energy Sciences, Division of Engineering and Geosciences. This project is funded as part of the Environmental Management Science Program (EMSP), a pilot program managed jointly by the Office of Energy Research and the Office of Environmental Management.

UCRL-JC-131326

Surface and Borehole Electromagnetic Imaging of Conducting Contaminant Plumes

Authors:
James G. Berryman, H. Michael Buettner, Nathan J. Champagne II,
J. Brian Grant, Robert M. Sharpe
Lawrence Livermore National Laboratory

Co-Authors:
Oliver Dorn, George Papanicolaou
Mathematics Department, Stanford University

Electromagnetic induction tomography is a promising new tool for imaging electrical conductivity variations in the earth. The EM source field is produced by induction coil (magnetic dipole) transmitters deployed at the surface or in boreholes. Vertical and horizontal component magnetic field detectors are deployed in other boreholes or on the surface. Sources and receivers are typically deployed in a configuration surrounding the region of interest. The goal of this procedure is to image electrical conductivity variations in the earth, much as x-ray tomography is used to image density variations through cross-sections of the body. Although such EM field techniques have been developed and applied, the algorithms for inverting the magnetic field data to produce the desired images of electrical conductivity have not kept pace.

One of the main reasons for the lag in the algorithm development has been the fact that the magnetic induction problem is inherently three dimensional; other imaging methods such as x-ray and seismic can make use of two-dimensional approximations that are not too far from reality, but we do not have this luxury in EM induction tomography. In addition, previous field experiments were conducted at controlled test sites that typically do not have much external noise or extensive surface clutter problems often associated with environmental sites. To use the same field techniques in environments more typical of cleanup sites requires a new set of data processing tools to remove the effects of both noise and clutter. The goal of this project is to join theory and experiment to produce enhanced images of electrically conducting fluids underground, allowing better localization of contaminants and improved planning strategies for the subsequent remediation efforts. The poster first explains the physical context in more detail and then summarizes the progress made so far on this project: (1) on code development, (2) on field tests of these methods, and (3) data inversion methods.

This work was performed under the auspices of the Department of Energy by the Lawrence Livermore National Laboratory under contract W-7405-Eng-48.

Date: Tue, 20 Oct 1998 10:53:11 -0700 (PDT)

Clinical Access of PEREGRINE Dose Calculations

By Sarita S. May

The goal of the PEREGRINE Program is to improve the effectiveness of radiation therapy in the treatment of cancer, using Monte Carlo photon transport, by ensuring wide-spread rapid distribution of this technology to every cancer center that uses radiation therapy. In order for PEREGRINE to have the highest impact on the maximum number of patients, our program has the following objectives:

- Demonstrate that Monte Carlo dose calculations are fast and accurate
- Design an affordable package that is compatible with existing treatment systems
- Address intellectual property and copyright issues
- Prepare validation and verification package for FDA submission
- Develop and implement licensing strategy

Through these activities we believe we can fulfill the expectations of the medical community now and continue to advance the field of radiation therapy well into the 21st century.

UCRL-JC-132169 Abs
Clinical Access of PEREGRINE Dose Calculations
S. S. May

Sarita May
External and Regulatory Affairs
PEREGRINE Program Office
Lawrence Livermore National Laboratory (L-174)
7000 East Ave, Livermore, CA 94550

email: may1@llnl.gov
Phone: (925) 422-7473
Fax: 925-423-1447

Date: Mon, 26 Oct 1998 11:59:40 -0800 (PST)

UCRL-JC-131116 Abs

Direct observation of fluid-clay interactions with implications for mechanical and electrical properties

By C. Aracne-Ruddle, D. Wildenschild, B. Bonner, and P. Berge

When measuring sound speed in dilute sand-clay mixtures, observed changes in energy transmission have indicated that the pore fluid composition, as well as the amount of clay, may influence the acoustic properties of the medium. We devised an experiment to directly observe how sand and clay particles interact on the grain scale. An optical microscope was used to observe changes in clay morphology as a function of the chemistry of the pore fluid. We used a pure silica sand with grain sizes between 74-420 microns and a median diameter (d50) of 273 microns, mixed with 1, 3, and 10 weight-percent of sodium montmorillonite, a swelling clay. The wetting fluids were deionized water and a 0.1 N CaCl2 solution. For t5he dry sand-clay mixture, we observed that the clay particles would electrostatically cling to the sand grains, tending to bridge the gaps and thus influence the acoustic and electrical properties of the combined medium. As expected, due to the chemical interactions between the clay and the water, the clay particles swelled to occupy the available pore space between sand grains when wetted with deionized water. Subsequently, when wetted with CaCl2, the clay particles settled and clumped together to form larger clusters or flocs by a process called flocculation. The flocculation process depends mainly on the charge that may be present on the particles in solution. The charge on each particle may repel the other particles and keep the material in suspension, or it may cause the particles to be attracted to each other and form clusters (or flocs). The visual observation of these phenomena verifies our initial assumption that fluid-clay interactions can play a major role when making acoustic and electrical measurements on natural soils.

For more information, please visit our web-site at: http://www-ep.es.llnl.gov/www-ep/esd/expgeoph/Berge/EMSP/

This work was performed under the auspices of the U.S. Department of Energy by the Lawrence Livermore National Laboratory under contract No. W-7405-ENG-48 and supported specifically by the DOE Office of Energy Research within the Office of Basic Energy Sciences, Division of Engineering and Geosciences.

This project is funded as part of the Environmental Management Science Program (EMSP), a pilot program managed jointly by the Office of Energy Research and the Office of Environmental Management.

Ultrasonic Immunoassay for Detection of Breast Cancer Antigens*

By Amy Wang[1], Radwan Kiwan[2], Richard White[3]
[1]Lawrence Livermore National Laboratory
[2]Cancer Research Fund of Contra Costa
[3]University of California, Berkeley

ABSTRACT

Patients with active breast cancer exhibit elevated blood serum levels of breast epithelial mucin antigens (BrE-Ags). Currently, serum levels of BrE-Ags in breast cancer patients are monitored during follow-up of surgery or chemotherapy treatment, where a rise in blood antigen levels indicates the presence of residual tumors.

We present a silicon-micromachined immunosensor package that has been designed to detect a specific breast epithelial mucin antigen, non-penetrating glycoprotein (NPGP). We couple an acoustic sensor, the flexural plate wave (FPW) device, with a novel mass-amplifying label that increases sensor signal from that of previous acoustic immunoassays. The use of a gravimetric immunoassay provides an alternative to radioimmunoassay, eliminating the need for radioactive labels that require costly disposal. In addition to gravimetric sensing, the FPW device is also capable of providing a source of ultrasonic agitation, which results in localized mixing near the active immunoglobulin binding area of the device. We have observed increased antibody binding using ultrasonic agitation during immunoglobulin incubation periods. Consequently, with ultrasonic agitation, we are able to reduce the length of time necessary to complete the immunoassay, and also affect the amount of antibody binding.

Keywords: acoustic, breast cancer, immunosensor, ultrasonic, MEMS, micromachining

Amy Wang is an electrical engineer in the Center for Microtechnology at LLNL. She is also an adjunct professor in the Department of Applied Science at the University of California at Davis. Her research interests include the application of micro electro-mechanical systems (MEMS) to biological and medical applications. Amy received her
Ph. D. from the University of California at Berkeley.

* This work was performed at the University of California at Berkeley and the Cancer Research Fund of Contra Costa.